



HAL
open science

Modeling of time-dependent and anisotropic behavior of highly squeezing ground: Application to the Saint-Martin-la-Porte exploratory galleries of the Lyon-Turin link

Yichun Liu

► To cite this version:

Yichun Liu. Modeling of time-dependent and anisotropic behavior of highly squeezing ground: Application to the Saint-Martin-la-Porte exploratory galleries of the Lyon-Turin link. Géotechnique. Université Paris-Est, 2020. English. NNT : 2020PESC1028 . tel-03447636

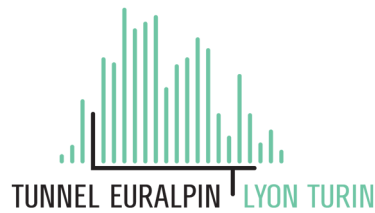
HAL Id: tel-03447636

<https://pastel.hal.science/tel-03447636>

Submitted on 24 Nov 2021

HAL is a multi-disciplinary open access archive for the deposit and dissemination of scientific research documents, whether they are published or not. The documents may come from teaching and research institutions in France or abroad, or from public or private research centers.

L'archive ouverte pluridisciplinaire **HAL**, est destinée au dépôt et à la diffusion de documents scientifiques de niveau recherche, publiés ou non, émanant des établissements d'enseignement et de recherche français ou étrangers, des laboratoires publics ou privés.



**Modeling of time-dependent and anisotropic behavior of highly squeezing ground
Application to the Saint-Martin-la-Porte exploratory galleries of the Lyon-Turin link**

Thèse soumise pour l'obtention du grade de

Docteur de l'Université Paris Est
Ecole Doctorale Sciences, Ingénierie et Environnement (SIE)
Spécialité : Géotechnique

présentée le 15 décembre 2020 à Champs-sur-Marne par

Yichun LIU

Laboratoire Navier, Equipe Géotechnique CERMES
Ecole des Ponts ParisTech, Université Gustave Eiffel, CNRS

JURY

Marco BARLA	Politecnico di Torino	Rapporteur
Mountaka SOULEY	INERIS	Rapporteur
Marc PANET	Ecole des Ponts ParisTech	Examineur
Amade POUYA	Ecole des Ponts ParisTech	Examineur
Jean SULEM	Ecole des Ponts ParisTech	Directeur de thèse
Didier SUBRIN	Centre d'Etudes des Tunnels	Co-encadrant de thèse
Emmanuel HUMBERT	Tunnel Euralpin Lyon Turin	Invité
Huy TRAN-MANH	ITASCA Consultants	Invité

To my family & friends...

ACKNOWLEDGMENTS

This research work has been carried out in the Geotechnical team (CERMES) of Laboratoire Navier at Ecole des Ponts ParisTech (ENPC), in partnership with Centre d'Etudes des tunnels (CETU) and Tunnel Euralpin Lyon Turin (TELT). I wish to thank all the people who have contributed to the completion of this project.

First and foremost, I would like to express my deep gratitude to my supervisor Prof. **Jean SULEM** for providing me the precious opportunity to join this interesting research project. His invaluable advice, brilliant ideas and continuous support have assisted me to successfully overcome the challenges we met. His trust, patience and kindness have encouraged me in my academic research and daily life during the past three years.

My sincere thanks also go to my co-supervisor Dr. **Didier SUBRIN**, who has shared with me his rich knowledge and experience in the domain of tunneling. His treasured comments and insight suggestions are always helpful to the progress of the project. I really appreciate the numerous discussions we had together and his availability at every stage of the research project.

This project would not have been possible without the support of TELT, which has financing this research work and providing the various field data of the Saint-Martin-la-Porte exploratory galleries. I wish to thank the engineers, in particular **Emmanuel HUMBERT**, for the interesting field visits and useful meetings, which have contributed a lot to the improvement of this work.

I would like to pay my special regards to ITASCA Consultants SAS for supporting this research project and for providing the software *FLAC3D*. I warmly thank Dr. **Daniel BILLAUX** for accepting me in the Itasca Educational Partnership (IEP) program and Dr. **Huy TRAN-MANH** for helping me to learn the *FLAC3D* code, sharing his treasured experience in numerical modeling and always being available to answer my questions.

Many thanks for the time they have devoted to me. It is a great pleasure for me to work with them.

I also wish to show my gratitude to Prof. **Marc PANET** and Prof. **Amade POUYA** for accepting to examine my thesis work and for the suggestions they proposed and the ideas they shared with me. I would like to extend my special thanks to the referees of this dissertation, Prof. **Marco BARLA** and Dr. **Mountaka SOULEY**, for their very detailed and useful comments and questions, which contribute to enrich the dissertation. I am appreciated for the interest they have shown in the regard to this work and the time they spent on reading my manuscript. It is an honor for me to have them in my jury committee and to receive their professional opinions on my work.

My gratitude extends to my friends and colleagues in the team CERMES. Thanks for the comfortable and friendly working environment and for the happy and unforgettable moments. In particular, I wish to thank Dr. **Lina María GUAYACAN CARRILLO** and Dr. **Manuel DE LA FUENTE MATA** for the interesting discussions on the understanding of tunneling aspects and numerical modeling.

Last but not least, I wish to acknowledge my family for their unconditional supports and my friends for their continuous encouragement during my long stay in France. This work would not have been possible without them.

ABSTRACT

Modeling of time-dependent and anisotropic behavior of highly squeezing ground Application to the Saint-Martin-la-Porte exploratory galleries of the Lyon-Turin link

Operational difficulties are frequently encountered during the excavation of tunnels in squeezing ground because of large, time-dependent and often anisotropic deformation. In the context of the future Lyon-Turin link, an access gallery (SMP2) and a survey gallery (SMP4) are excavated by conventional method in Saint-Martin-la-Porte (SMP) in France. A strongly tectonized Carboniferous formation was crossed which is highly fractured and heterogeneous. Squeezing behavior was observed and led to instability of support system and tunnel face. Specific excavation and support methods were adopted with an extensive field monitoring program. During the past years, several studies have been carried out to analyze the squeezing rock behavior and the interaction between the ground and the support system in SMP2: a processing procedure of anisotropic convergence data has been proposed and an anisotropic visco-elastic-plastic constitutive model has been developed and implemented in *Flac3D* code.

On the basis of the gained knowledge and the new available field data, developed tools for data processing and numerical simulation of SMP2 are extrapolated for longer-time scale and applied to the conditions encountered in SMP4, which is much deeper and excavated in another direction. By extending the proposed method and applying the obtained values of parameters, field data are studied for the anisotropic closure of different parts of SMP4 taking into account the stages of excavation and support installation to predict long-term convergence of the galleries. The developed anisotropic visco-elastic-plastic constitutive model in the previous studies is improved to simulate the mid-term and long-term behavior of SMP2 considering the excavation stages, the specific yielding support and the reprofiling process. Different excavation profiles of SMP4 are modeled. The constitutive parameters are identified and the ground and tunnel response is well reproduced.

Keywords: deep tunnels; squeezing rock; time-dependent behavior; anisotropic convergence; numerical modeling; yielding support; Saint-Martin-la-Porte galleries; Lyon-Turin link.

RESUME

Modélisation du comportement différé et anisotrope des terrains fortement tectonisés Application aux galeries de reconnaissances de Saint-Martin-la-Porte sur la liaison Lyon-Turin

Des difficultés opérationnelles sont fréquemment rencontrées lors de l'excavation de tunnels dans les terrains tectonisés à cause de déformations importantes, différées et souvent anisotropes. Dans le contexte de la future liaison Lyon-Turin, une descenderie (SMP2) et une galerie de reconnaissance (SMP4) sont excavées par la méthode conventionnelle à Saint-Martin-la-Porte (SMP) en France. Une formation de Houiller très fracturée, hétérogène et fortement tectonisée a été traversée. Le comportement poussant a été observé et a conduit à une instabilité du système de soutènement et du front de taille. Des méthodes spécifiques d'excavation et d'installation de soutènement ont été adoptées avec un programme exhaustif d'auscultation. Au cours des dernières années, de nombreuses études ont été menées pour analyser le comportement poussant du terrain et l'interaction entre le terrain et le soutènement dans SMP2 : une procédure de traitement des données de convergence anisotrope a été proposée et une loi de comportement visco-élastique-plastique anisotrope a été développée et implémentée dans le code *Flac3D*.

Sur la base des connaissances acquises et des nouvelles données disponibles, les outils développés pour le traitement de données et les simulations numériques de SMP2 sont extrapolés pour une échelle de temps plus longue et appliqués aux conditions rencontrées dans SMP4, ce qui est beaucoup plus profonde et excavée dans une autre direction. En étendant la méthode proposée et en appliquant les valeurs de paramètres obtenues, les mesures de convergences anisotropes sont étudiées pour de différents tronçons de la galerie SMP4 en tenant compte des procédures de reprofilage et de mise en place du soutènement pour la prédiction de la convergence à long terme. La loi de comportement visco-élastique-plastique anisotrope développée dans les études précédentes est améliorée pour simuler le comportement à moyen et long terme de la galerie SMP2 en considérant les phases d'excavation, le soutènement semi-rigide spécifique et le processus de reprofilage. Différents profils d'excavation de SMP4 sont modélisés. Les paramètres de la loi de comportement sont identifiés et la réponse globale du terrain et du tunnel est bien reproduite.

Mots-clés : tunnels profonds ; terrains tectonisés ; comportement différé ; convergence anisotrope ; modélisation numérique ; soutènement semi-rigide ; galeries de Saint-Martin-la-Porte ; liaison Lyon-Turin.

TABLE OF CONTENTS

ACKNOWLEDGMENTS	i
ABSTRACT	iii
RESUME	v
TABLE OF CONTENTS	vii
LIST OF TABLES	xi
LIST OF FIGURES	xiii
INTRODUCTION	1
1 STATE OF THE ART	5
1.1 Squeezing rock	6
1.1.1 Definition	6
1.1.2 Rock classification systems	7
1.1.3 Identification of squeezing behavior	11
1.2 Tunneling in squeezing ground	16
1.2.1 Excavation methods	16
1.2.2 Reinforcement and support systems	19
1.3 Rock mass behavior	21
1.3.1 Elastic and plastic responses	21
1.3.2 Time-dependent behavior	23
1.3.3 Anisotropic behavior	28
1.3.4 Ground response after tunneling	31
2 SMP EXPLORATORY GALLERIES	35
2.1 SMP field work	36
2.1.1 Lyon-Turin Link	36

2.1.2	Geological and geotechnical context	39
2.2	Excavation and support methods	40
2.2.1	Applied yielding support system	40
2.2.2	Tunneling of SMP2	42
2.2.3	Tunneling of SMP4	44
2.3	Monitoring	52
2.3.1	Convergence of tunnel cross-section	52
2.3.2	Extrusion of tunnel core	54
2.3.3	Extension around tunnel wall and stress in rock-bolts	54
2.3.4	Stress in final lining	56
2.3.5	Stress in shotcrete layer	56
3	FIELD DATA PROCESSING	59
3.1	Obtained knowledge of SMP2	60
3.1.1	Procedure of convergence data processing	60
3.1.2	Obtained parameters from SMP2	62
3.2	SMP4-GS	65
3.2.1	Geometrical processing considering the rock mass heterogeneity	68
3.2.2	Analysis of anisotropic convergence	70
3.3	SMP4-PS	72
3.3.1	Field monitoring data of SMP4-PS	72
3.3.2	Mean convergence	75
3.3.3	Anisotropic response	77
3.4	SMP4-RPS	82
3.4.1	Field monitoring data of SMP4-RPS	82
3.4.2	Mean convergence	84
3.4.3	Anisotropic response	85
3.5	Summary	89
4	NUMERICAL MODELING	91
4.1	Numerical models and parameters	92
4.1.1	Modeling assumptions and simplifications	92
4.1.2	Developed constitutive model for rock mass in SMP2	92
4.1.3	Obtained knowledge from numerical simulations of SMP2	93
4.1.4	Modeling of the reinforcement and support system	95
4.2	Long-term behavior of SMP2	97
4.2.1	Stress measurements in the final lining	98

4.2.2	Numerical model	98
4.2.3	Obtained results	101
4.2.4	Time-dependency of the viscosity	102
4.3	SMP4-PS	104
4.3.1	Numerical model	104
4.3.2	Results	107
4.4	SMP4-RPS	110
4.4.1	Stress measurements in the shotcrete	111
4.4.2	Numerical model	111
4.4.3	Numerical results	113
4.5	Summary	116
CONCLUSIONS AND FUTURE WORK		119
REFERENCES		123
APPENDIX		129
A	AVERAGE CONVERGENCE OF THE SECTIONS IN SMP4-PS	129
B	STRING CONVERGENCE OF THE SECTIONS IN SMP4-PS	133
C	AVERAGE CONVERGENCE OF THE SECTIONS IN SMP4-RPS	163
D	STRING CONVERGENCE OF THE SECTIONS IN SMP4-RPS	169

LIST OF TABLES

1.1	Relation between the RQD index and rock quality (Deere and Deere, 1988)	7
1.2	Guidelines for excavation and support based on the RMR system (Bieniawski, 1989)	9
1.3	Identification of squeezing degree (Goel et al., 1995)	12
1.4	Identification of squeezing degree (Singh and Goel, 1999)	12
1.5	Identification of squeezing degree (Jethwa et al., 1984)	13
1.6	Identification of squeezing degree (Aydan et al., 1993)	15
1.7	Identification of squeezing degree (Hoek and Marinos, 2000)	16
1.8	Characteristics of different TBM types (De La Fuente, 2018)	18
1.9	Kelvin and Maxwell model	25
1.10	Visco-elastic rheological models	25
1.11	Visco-plastic models	26
2.1	Assumption of the initial stress state in the Houiller formation	39
3.1	Obtained parameters of the geometrical processing in SMP2	63
3.2	Parameters of the convergence law in SMP2	64
3.3	Summary of convergence measurements in SMP4-GS	67
3.4	Position of monitoring points CT1-CT5	68
3.5	Fitted parameters with different fitting periods (chainages 10275 and 10280 m)	71
3.6	Fitted parameters on sections at chainages 10280 and 10290 m	71
3.7	Proposed parameters for the convergence law in SMP4	75
3.8	Obtained parameters of convergence law in SMP4-PS and predicted total convergence [Unit: m]	76
3.9	Proposed parameters of convergence law in SMP4-PS [Unit: m]	80
3.10	Parameters of convergence law in SMP4-RPS [Unit: m]	84
3.11	Parameters of convergence law in SMP4-RPS [Unit: m]	85
4.1	Principal stress conventions (Itasca, 2017)	93
4.2	Obtained parameters of the geometrical processing in SMP2 (after Tran-Manh, 2014)	94
4.3	Parameters of double-yield model to simulate the HiDCon elements	95

4.4	The hardening behavior of the cap pressure p_c	96
4.5	Elastic parameters of concrete used in SMP	97
4.6	Four stages of numerical simulation	100
4.7	Summary of the elements introduced in the numerical modeling of SMP2	100
4.8	Summary of the constitutive parameters in the numerical modeling of SMP2	101
4.9	Summary of the elements introduced in the numerical modeling of SMP4-PS	107
4.10	Summary of the constitutive parameters in the numerical modeling of SMP4-PS	107
4.11	Obtained parameters of the CVISC model for SMP4-PS	108
4.12	Four excavation stages at chainage 10344 m in SMP4-RPS	113
4.13	Summary of the elements introduced in the numerical modeling of SMP4-RPS	113
4.14	Summary of the constitutive parameters in the numerical modeling of SMP4-RPS	113
4.15	Obtained parameters of the CVISC model for SMP4-RPS	114
4.16	Summary of the obtained parameters for the CVISC model	117

LIST OF FIGURES

1.1	Rock support chart based on Q -values (NGI, 2015)	8
1.2	Characterization of rock masses on the basis of GSI (Hoek et al., 1998)	10
1.3	Prediction of squeezing conditions (Singh et al., 1992)	11
1.4	Prediction of squeezing conditions (Goel, 2000)	12
1.5	Prediction of pressure on tunnel lining in squeezing rock (Jethwa et al., 1984)	14
1.6	Prediction of squeezing condition (Aydan et al., 1993)	14
1.7	Five levels of squeezing (Hoek and Marinos, 2000)	15
1.8	Examples of conventional excavation techniques (photos from ITA-AITES)	16
1.9	Conventional excavation methods (after Kovári and Staus, 1996)	17
1.10	Spring line side drifts method (after Fujita, 1978)	17
1.11	Example of TBM types (images from Herrenknecht)	18
1.12	Schematics of CMC/CFC and DMFC rock-bolts (Bobet and Einstein, 2011)	19
1.13	TH type steel ribs with sliding joints	20
1.14	Yielding support concept using wood elements (Heise and Herbst, 1913)	20
1.15	Linear elasticity (a), non-linear elasticity (b) and plasticity (c)	21
1.16	Elasto-perfectly plastic (a) and elasto-plastic with hardening (b)	22
1.17	Three stages of creep	23
1.18	Viscous Abel dashpot (or “Scott-Blair element”)	24
1.19	Bingham model	26
1.20	Burgers-Mohr model available in <i>Flac3D</i> code	26
1.21	Limit surfaces and stress fields (Debernardi, 2008)	28
1.22	Experimental observation of anisotropic failure strength (McLamore and Gray, 1967)	29
1.23	Introduction of weak patches to simulate material anisotropy (Fjær and Nes, 2013)	31
1.24	Ubiquitous-joint approach	31
1.25	Modeling of tunnel face advance by increasing the deconfinement rate	32
1.26	Convergence-confinement method	32
1.27	Prediction of plastic zone based on the stability number (Panet, 1995)	34

2.1	Lyon Turin link in Ten-T project (from Iatransalpine)	36
2.2	Access galleries to the Lyon-Turin base tunnel	37
2.3	SMP survey project	37
2.4	SMP exploratory galleries: SMP2 and SMP4	38
2.5	Squeezing behavior observed in SMP2 (Mathieu, 2008; Barla et al., 2010)	38
2.6	Application and mechanical properties of HiDCon elements of Solexperts used in SMP	41
2.7	Technical characteristics of LSC elements (from DSI Underground)	41
2.8	Geological context of SMP2	42
2.9	Tunnel face lithology and support failure observed in SMP2 (chainage 1484 m) (Mathieu, 2008)	43
2.10	Tunnel face advance of SMP2	43
2.11	Profiles of support systems used in SMP2 from chainage 1267 m (Bonini and Barla, 2012)	44
2.12	Overburden of SMP4	44
2.13	Tunnel face advance of SMP4-GS	45
2.14	Lithology plane of SMP4-GS	45
2.15	Geological survey of the tunnel face of various sections in SMP4-GS	46
2.16	Support system applied in SMP4-GS	46
2.17	Tunnel face collapse occurred near chainage 10303 m	47
2.18	Different steps to cross the collapsed zone	47
2.19	Longitudinal map of the lithology SMP4-PS	48
2.20	Geological survey of the tunnel face of various sections in SMP4-PS	49
2.21	Tunnel face advance of SMP4-PS	49
2.22	Support system applied in SMP4-PS	50
2.23	Geological survey at the tunnel face and lithology map in the longitudinal direction in SMP4-RPS	50
2.24	Tunnel face advance of SMP4-RPS	51
2.25	Support systems applied in SMP4-RPS	51
2.26	Example of convergence measurement by five monitoring targets	53
2.27	Example of monitoring targets installed in SMP4-PS	53
2.28	Measurement of extrusion of tunnel core in SMP4-PS	54
2.29	Displacement recording by extensometers in SMP4-GS of ground at chainage 10281 m	55
2.30	Multipoint borehole extensometer	55
2.31	Vibrating wire strain gauge	55
2.32	Vibrating wire strain gauge	56
2.33	Stress measurement in the concrete ring at chainage 1383 m of SMP2	56
2.34	Stress measurements in the shotcrete in SMP4-RPS	57

3.1	Elliptical fitting of the deformed section	60
3.2	Circular fitting of the deformed section	61
3.3	Position of monitoring targets in SMP4-GS	65
3.4	Instrumented sections in SMP4-GS	65
3.5	Horizontal and vertical displacements of the monitoring points in SMP4-GS	66
3.6	Field monitoring of strings convergence in SMP4-GS	67
3.7	Evaluation the section ovalization at chainage 10275 m with respect to CT2, CT3 and CT4 in the upper Houiller part of the section	68
3.8	Inclination of the fitted ellipse θ	69
3.9	Major and minor semi-axes a and b of the fitted ellipse	69
3.10	Convergence fitting with different periods of data at chainages 10275 and 10280 m (x is the face advance from the considered section)	70
3.11	Convergence fitting of sections at chainages 10280 and 10290 m (x is the face advance from the considered section)	71
3.12	Monitoring targets and strings	72
3.13	Initial positions of the monitoring targets for all the sections of SMP4-PS	72
3.14	Convergence measurements in SMP4-PS	73
3.15	Convergence monitoring in SMP4-PS (example of chainage 10321 and 10326 m)	73
3.16	Recorded displacement of SMP4-PS (example of chainage 10321 and 10326 m)	74
3.17	Calibration of convergence data on 2 stages	75
3.18	Initial parameters of fitted circle in SMP4-PS	76
3.19	Obtained parameters of the convergence law and predicted long-term convergence	76
3.20	Convergence fitting (examples of sections at chainages 10316, 10321 and 10326 m)	77
3.21	Convergence fitting at chainage 10326 m	79
3.22	Parameters of the convergence law and predicted long-term convergence for string D3	82
3.23	Predicted long-term convergence	82
3.24	Initial coordinates of the monitoring targets for all the sections in SMP4-RPS	83
3.25	Convergence measurements of the sections in SMP4-RPS	83
3.26	Initial parameters of fitted circle in SMP4-RPS	84
3.27	Parameters of the convergence law and predicted long-term convergence	85
3.28	Convergence fitting at chainage 10344 m	88
3.29	Parameters of the convergence law and predicted long-term convergence D3	89
3.30	Predicted long-term convergence	89
3.31	Predicted long-term convergence normalized by the diameter of SMP4-PS and RPS	90
4.1	Mohr-Coulomb criterion with tension cut-off	93
4.2	3D mesh for the numerical simulation of SMP2 (Tran-Manh et al., 2015)	94

4.3	Numerical modeling of tunnel convergence (N) and comparison with field data (E) for SMP2 (after Tran-Manh et al., 2015)	95
4.4	The hardening behavior of the cap pressure p_c	96
4.5	Uniaxial compression tests of HiDCon elements (Barla et al., 2011) and numerical simulation	96
4.6	Profiles of support systems adopted in SMP2 (Bonini and Barla, 2012)	97
4.7	Stress measurement in the concrete ring at chainage 1383 m of SMP2	98
4.8	LDP and calculated deconfinement rate for the section at chainage 1383 m in SMP2	99
4.9	2D mesh for the section at chainage 1383 m in SMP2	99
4.10	Displacement contour before (a) and after (b) reprofiling process 94 days after excavation	101
4.11	Displacement and minimum (maximum in absolute value) principal stress in the final lining	102
4.12	Displacement and minimum principal stress in the final lining after modification of η^M	102
4.13	Fractional CVISC model	103
4.14	Variation of η^* versus computational time t	103
4.15	Numerical results of the stress in the final lining at chainage 1383 m in SMP2	104
4.16	Fitting of elasto-plastic parameters of SMP4-PS	105
4.17	Longitudinal displacement profile and calculated deconfinement rate in SMP4-PS	106
4.18	2D mesh for numerical simulation of SMP4-PS	107
4.19	Numerical simulation of mean behavior of SMP4-PS	108
4.20	Numerical results at 200 days after support installation of SMP4-PS	109
4.21	Numerical simulation of the strings at chainage 10326 m of SMP4-PS	110
4.22	Stress measurements in the shotcrete in SMP4-RPS	111
4.23	3D mesh for numerical simulation of SMP4-RPS	112
4.24	Tunnel face advance of SMP4-PS and SMP4-RPS	112
4.25	Numerical simulation of mean convergence of SMP4-RPS	114
4.26	Displacement magnitude contour at chainage 10344 m for different excavation stages in SMP4-RPS	115
4.27	Stress contour of the shotcrete in SMP4-RPS	116
4.28	Hoop stress evolution of the shotcrete in SMP4-RPS	116
A.1	Mean convergence fitting of the sections in SMP4-PS (The black lines show the tunnel face advance.)	132
B.1	Strings used for convergence measurements in SMP4-PS (The black lines show the tunnel face advance.)	133
B.2	Strings convergence fitting of the section at chainage 10312 m (C) in SMP4-PS (The black lines show the tunnel face advance.)	133
B.3	Strings convergence fitting of the section at chainage 10313 m (T) in SMP4-PS (The black lines show the tunnel face advance.)	134

B.4	Strings convergence fitting of the section at chainage 10316 m (C) in SMP4-PS (The black lines show the tunnel face advance.)	135
B.5	Strings convergence fitting of the section at chainage 10316 m (T) in SMP4-PS (The black lines show the tunnel face advance.)	136
B.6	Strings convergence fitting of the section at chainage 10321 m (C) in SMP4-PS (The black lines show the tunnel face advance.)	137
B.7	Strings convergence fitting of the section at chainage 10321 m (T) in SMP4-PS (The black lines show the tunnel face advance.)	139
B.8	Strings convergence fitting of the section at chainage 10326 m (T) in SMP4-PS (The black lines show the tunnel face advance.)	141
B.9	Strings convergence fitting of the section at chainage 10327 m (C) in SMP4-PS (The black lines show the tunnel face advance.)	143
B.10	Strings convergence fitting of the section at chainage 10335 m (T) in SMP4-PS (The black lines show the tunnel face advance.)	145
B.11	Strings convergence fitting of the section at chainage 10336 m (C) in SMP4-PS (The black lines show the tunnel face advance.)	146
B.12	Strings convergence fitting of the section at chainage 10341 m (T) in SMP4-PS (The black lines show the tunnel face advance.)	147
B.13	Strings convergence fitting of the section at chainage 10346 m (T) in SMP4-PS (The black lines show the tunnel face advance.)	148
B.14	Strings convergence fitting of the section at chainage 10350 m (T) in SMP4-PS (The black lines show the tunnel face advance.)	149
B.15	Strings convergence fitting of the section at chainage 10356 m (T) in SMP4-PS (The black lines show the tunnel face advance.)	150
B.16	Strings convergence fitting of the section at chainage 10361 m (T) in SMP4-PS (The black lines show the tunnel face advance.)	151
B.17	Strings convergence fitting of the section at chainage 10366 m (T) in SMP4-PS (The black lines show the tunnel face advance.)	152
B.18	Strings convergence fitting of the section at chainage 10371 m (B) in SMP4-PS (The black lines show the tunnel face advance.)	154
B.19	Strings convergence fitting of the section at chainage 10376 m (B) in SMP4-PS (The black lines show the tunnel face advance.)	156
B.20	Strings convergence fitting of the section at chainage 10381 m (B) in SMP4-PS (The black lines show the tunnel face advance.)	158
B.21	Strings convergence fitting of the section at chainage 10385 m (B) in SMP4-PS (The black lines show the tunnel face advance.)	160
B.22	Strings convergence fitting of the section at chainage 10390 m (B) in SMP4-PS (The black lines show the tunnel face advance.)	162
C.1	Mean convergence fitting of the sections in SMP4-RPS (The black lines show the tunnel face advance.)	167

D.1	Strings used for convergence measurements in SMP4-RPS (The black lines show the tunnel face advance.)	169
D.2	Strings convergence fitting of the section at chainage 10305 m (B) in SMP4-RPS (The black lines show the tunnel face advance.)	171
D.3	Strings convergence fitting of the section at chainage 10307 m (B) in SMP4-RPS (The black lines show the tunnel face advance.)	173
D.4	Strings convergence fitting of the section at chainage 10309 m (B) in SMP4-RPS (The black lines show the tunnel face advance.)	175
D.5	Strings convergence fitting of the section at chainage 10311 m (B) in SMP4-RPS (The black lines show the tunnel face advance.)	177
D.6	Strings convergence fitting of the section at chainage 10319 m (B) in SMP4-RPS (The black lines show the tunnel face advance.)	179
D.7	Strings convergence fitting of the section at chainage 10329 m (B) in SMP4-RPS (The black lines show the tunnel face advance.)	180
D.8	Strings convergence fitting of the section at chainage 10339 m (B) in SMP4-RPS (The black lines show the tunnel face advance.)	182
D.9	Strings convergence fitting of the section at chainage 10344 m (B) in SMP4-RPS (The black lines show the tunnel face advance.)	184
D.10	Strings convergence fitting of the section at chainage 10349 m (B) in SMP4-RPS (The black lines show the tunnel face advance.)	186
D.11	Strings convergence fitting of the section at chainage 10353 m (B) in SMP4-RPS (The black lines show the tunnel face advance.)	188
D.12	Strings convergence fitting of the section at chainage 10358 m (B) in SMP4-RPS (The black lines show the tunnel face advance.)	190
D.13	Strings convergence fitting of the section at chainage 10363 m (B) in SMP4-RPS (The black lines show the tunnel face advance.)	192
D.14	Strings convergence fitting of the section at chainage 10369 m (B) in SMP4-RPS (The black lines show the tunnel face advance.)	194
D.15	Strings convergence fitting of the section at chainage 10374 m (B) in SMP4-RPS (The black lines show the tunnel face advance.)	196
D.16	Strings convergence fitting of the section at chainage 10379 m (B) in SMP4-RPS (The black lines show the tunnel face advance.)	198
D.17	Strings convergence fitting of the section at chainage 10384 m (B) in SMP4-RPS (The black lines show the tunnel face advance.)	200

INTRODUCTION

Background

The Lyon-Turin railway link is highly strategic as it is a key element in the Mediterranean corridor of Trans-European Transport Network (TEN-T). It connects France and Italy through a 57.5 km bi-tube base tunnel under the Alps as its main part. The company Tunnel Euralpin Lyon Turin (TELT) is now responsible for the realization and operation of the cross-border section. Several excavation faces are processing at the same time by using the intermediate accesses, one of which is located in Saint-Martin-la-Porte (SMP) in France. During the excavation of the access gallery (SMP2), severe squeezing behavior was encountered due to the poor mechanical properties and the high stress state when the tunnel face entered in a Carboniferous formation – Productive Houiller at a depth of about 300 m. Then, the excavation was reoriented. The Houiller formation is highly fractured and heterogeneous, containing schists, sandstone, coal and a significant proportion of cataclastic rocks. The squeezing behavior is characterized by strong, time-dependent and anisotropic deformation of the rock mass around the tunnel, which can produce operational difficulties related to the excavation and support installation and cause instability problems. An ovalization of the section has been observed because of anisotropic convergence of the cross-section and failure of the temporary support system has occurred.

The encountered squeezing formation led to a significant delay of tunnel works and much higher costs. Specific excavation and support installation methods have been applied to overcome the operational difficulties: A dense reinforcement system is applied before excavation to improve the ground properties by rock-bolts installation and grouting; A yielding control temporary support system is installed close to the tunnel face with high deformable elements, which allows to accommodate the large convergence of the tunnel section; Reprofilng process has been performed to enlarged the section after strong convergence. Extensive monitoring programs have been carried out on site to record the ground response during and after tunnel excavation. Based on these measurements, numerous studies have been carried out to study the ground behavior, particularly on the large, time-dependent and anisotropic deformation.

Recently, another survey gallery (SMP4) began to be excavated at the depth and along the direction of the Southern tube of the future base tunnel (i.e. East-West direction), which allows to studies the geological condition at the level of the base tunnel. It crosses the same Houiller formation as SMP2 but much deeper, at a depth of about 600 m. The squeezing behavior had been predicted and has been encountered again. The specific excavation and support installation procedures adopted in SMP2 are used in SMP4, and the ground response in SMP4 is also extensively monitored, which contributes to investigate the squeezing behavior under the conditions encountered in SMP4. Excavation of SMP4 began with full size excavation. Because of the presence of a fault zone, collapse of the tunnel face has occurred and different profiles of excavation (e.g. full section – GS, small section – PS, reprofilng of

small section – RPS etc...) have been applied to overcome the collapsed zone.

The studies carried out for SMP cover different time scales with respect to the excavation and support installation stages:

- short-term: from the excavation of the section to the installation of the temporary support system (typically from several days to several weeks);
- mid-term: up to one to two years after the installation of the final lining;
- long-term: several years after the installation of the final lining.

Previous studies and objectives of the current work

The current thesis is the continuation of the thesis works of [Vu \(2010\)](#) and [Tran-Manh \(2014\)](#) within the context of the cooperation between Ecole des Ponts ParisTech (ENPC), Centre d'études des tunnels (CETU) and Tunnel Euralpin Lyon Turin (TELT). In these two previous theses, special tools have been developed for the field data processing and for the numerical modeling of excavation of SMP2.

In the thesis work of [Vu \(2010\)](#), a processing procedure of the geological information and the anisotropic convergence data recorded in SMP2 has been proposed. The deformed geometry of the cross-section after anisotropic closure is approached by an ellipse, and the major and minor elliptical axes are fitted by the semi-empirical convergence law ([Sulem et al., 1987a, 1987b](#)). The time-dependent behavior of the rock mass and the influence of the tunnel face advance are taken into account. The long-term convergence of the cross-section can be predicted. A non-linear anisotropic elastic model has been developed, and the 2D analytical solution of the stress and strain of ground around the gallery is obtained considering short-term and long-term mechanical parameters.

[Tran-Manh \(2014\)](#) has applied the processing procedure to complete the studies of the convergence measurements and geological data in SMP2, associated with the recorded displacement of rock mass and the stress in the lining. An anisotropic visco-elastic-plastic numerical model has been developed and implemented in *Flac3D* code. Numerical simulation of the ground response after excavation of SMP2 has been performed to validate the developed constitutive model in short-time scale taking into account the effects of excavation and time in the first months. The specific reinforcement and support systems are not introduced, and the obtained constitutive parameters represent the average behavior of the ground and support elements.

The present thesis work aims to complete the studies of squeezing Houiller formation encountered in SMP in the following ways:

- continue the studies of SMP2: examination of the capability of the developed numerical model and obtained values of constitutive parameters in SMP2 for longer-time scale based on the new available stress data in the final lining, introduction of the support system in the numerical modeling and improvement of the existing numerical model.
- apply the obtained knowledge and developed tools from SMP2 to SMP4, which is much deeper, excavated in another direction and with different excavation profiles: adaptation of the proposed processing procedure of convergence data to SMP4 condition, and numerical simulation of the different excavation stages taking into account the excavation method and the specific support system.

Structure of the dissertation

The present manuscript is organized in four chapters.

Chapter one is a general presentation of the state of the art. The definition and identification criteria of squeezing are first summarized based on different rock classification systems. The excavation methods and the reinforcement and support systems applied during tunnel excavation under squeezing condition are documented, and the developed procedure for convergence data processing is then recalled. After that, various rock mass behaviors (e.g. elasticity, plasticity, time-dependency and anisotropy) are discussed, and modeling of the interaction between the ground and the support system using the convergence-confinement method is presented.

Chapter two gives details about the field works of the SMP exploratory galleries. The context of the Lyon-Turin link and of the SMP survey project are first presented. Then, the specific yielding support system containing high deformable elements is described and the information about the excavation of SMP2 and different parts of SMP4 (full section – GS, small section – PS, reprofiling of small section – RPS) are provided (e.g. overburden, geological context, tunnel face advance, support system etc...). Finally, the monitoring programs are presented: convergence measurements, extensometric data, stresses in the rock-bolts, the shotcrete layer and the final lining.

In Chapter three, the field data of SMP4 are analyzed after a brief presentation of the proposed procedure and the obtained parameters of SMP2. After presenting the recorded data, the convergence measurements of different parts of SMP4 are studied and fitted by using a convergence law. Special attention is given to the anisotropy of the convergence data.

Chapter four presents numerical studies performed for SMP2 and SMP4 including the modeling of the specific support system. The computations are performed with *Flac3D* (Itasca, 2017) as in the thesis of Tran-Manh (2014). The constitutive model is based on the CVISC visco-elastic-plastic law with ubiquitous joints. The mid-term and long-term response of SMP2 is simulated in a 2D configuration and compared to the newly available data of stress measurements (up to 10 years) in the concrete lining. 2D and 3D modeling of SMP4 PS and RPS permits to adjust the model parameters to the conditions encountered at greater depth and to discuss the heterogeneity of the rock mass and the performance of the excavation and support method.

CHAPTER 1

STATE OF THE ART

“Squeezing behavior” refers to the phenomenon of large, time-dependent and often anisotropic deformation observed during and after tunneling in deep rock formation with low strength and high deformability. It can lead to operational difficulties related to high convergence of tunnel cross-section, stability problems and excessive loading on support system, which require adaptation of the excavation and support methods.

A number of studies have been carried out to analyze the squeezing behavior encountered in tunneling work and to overcome the relevant problems. In the present chapter, a brief state of the art is presented. After clarifying the definition and identification of squeezing, the specific tunneling procedure is documented. Then, the existing analytical and numerical tools to study the time-dependent and anisotropic ground response and the interactions between the ground and the support structures are summarized.

1.1 Squeezing rock

The problems encountered in tunneling work due to squeezing ground require careful studies. The definition of squeezing has been given after several years of observations and analyses of phenomena. Different identification criteria have been proposed on the basis of various rock classification systems.

1.1.1 Definition

The squeezing behavior of rock was first recognized during the tunneling work in the Alps between 1860 and 1910 (Kovári and Staus, 1996), which resulted in great delay and high costs to complete the construction works. However, the term “*squeezing*” was often confused with “*swelling*” and misused in the following years. The phenomenal definition of squeezing is first described by Terzaghi (1946) to distinguish with swelling:

- “*Squeezing rock is merely rock which contains a considerable amount of clay. The clay may have been present originally, as in some shales, or it may be an alteration product. The rock may be dominated by the inoffensive members of the Kaolinite group or it may have the vicious properties of the Montmorillonites. Therefore, the properties of squeezing rock may vary within as wide a range as those of clay;*”
- “*The term swelling rock refers to rocks the squeeze of which is chiefly due to swelling. Swelling rocks are always at least moderately dense, having the consistency of stiff or hard, preloaded clays.*”

Terzaghi (1946) has also pointed out that:

- “*Squeezing rock slowly advances into the tunnel without perceptible volume increase. Prerequisite for squeezing is a high percentage of microscopic and submicroscopic particles of micaceous minerals or of clay with a low swelling capacity;*”
- “*Swelling rock advances into the tunnel chiefly on account of expansion. The capacity to swell seems to be limited to those rocks which contain clay minerals such as montmorillonite, with a high swelling capacity.*”

After several years of observations, developments and studies (Gioda, 1982; O’Rourke, 1984; Jethwa et al., 1984; Kovári, 1986; Einstein, 1989; Singh et al., 1992; Aydan et al., 1993), the definition of squeezing is given by Commission on Squeezing Rocks in Tunnels of International Society for Rock Mechanics (ISRM) (Barla, 1995):

“Squeezing of rock is the time-dependent large deformation which occurs around the tunnel and is essentially associated with creep caused by exceeding a limiting shear stress. Deformation may terminate during construction or continue over a long-time period.”

In tunneling work, the effects of squeezing ground on support system were also remarked:

“Squeezing is closely related to the excavation and support techniques and sequences adopted in tunneling. If the support installation is delayed, the rock mass moves into the tunnel and a stress redistribution takes place around it. Conversely, if the rock deformations are constrained, squeezing will lead to long-term load build-up of rock support.”

After analyzing numerous cases of tunneling in squeezing ground, Steiner (1996) has summarized the factors which influence squeezing conditions: rock type (lithology), strength and fragmentation of the rock mass, orientation of the rock structure, stress state (overburden), water pressure, construction

procedures, support systems etc.

1.1.2 Rock classification systems

Rock classification systems play an essential role in rock engineering. Various qualitative or quantitative classification systems have been developed in the past years to describe rock properties, and based on which several identification criteria of squeezing are proposed.

The main objective of rock classification is to divide a particular rock mass formation into groups of similar behavior (Bieniawski, 1989), which is mainly related to strength of the intact rock material, fracture degree, mechanical behavior of the discontinuities, stress state and hydrogeological conditions. It permits to provide quantitative information for engineering judgment and design.

Rock Quality Designation (RQD)

The RQD index was introduced by Deere (1964) when rock quality information was usually available only from the geologists' descriptions and the percentage of core recovery. It is defined as the percentage of intact core pieces longer than 100 mm in the total length of a core diameter of at least 54.7 mm. The calculation procedure is clarified by Deere and Deere (1988) with Equation 1.1 and the engineering quality of rock is represented by the following values of RQD index (Table 1.1).

$$\text{RQD} = \frac{\Sigma \text{ length of core pieces } > 10 \text{ cm}}{\text{total length of the core}} \times 100\% \quad (1.1)$$

Table 1.1: Relation between the RQD index and rock quality (Deere and Deere, 1988)

RQD (%)	Rock Quality
0 - 25	Very poor
25 - 50	Poor
50 - 75	Faire
75 - 90	Good
90 - 100	Excellent

Palmstrom (1982) has proposed an estimation of RDQ when the information of core is unavailable, which is based on the number of joints per cubic meter J_v :

$$\text{RQD} = \begin{cases} 0 & J_v \geq 35 \\ 115 - 3.3J_v & 4.5 < J_v < 35 \\ 100 & J_v \leq 4.5 \end{cases} \quad (1.2)$$

The evaluation method of J_v is presented in the paper of Palmstrom (1982)

Q -systems

The Q -system of rock mass classification is developed on the basis of an analysis of 212 tunnel case histories of Scandinavia by Norwegian Geotechnical Institute (NGI) between 1971 and 1974 (Barton et

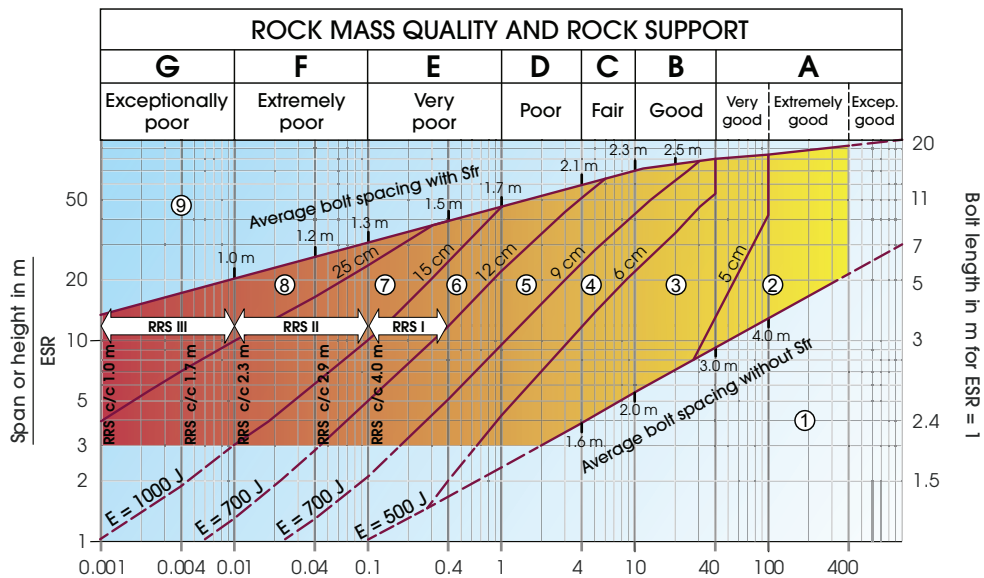
al., 1974). It is a quantitative classification combined in the following way:

$$Q = \frac{RQD}{J_n} \times \frac{J_r}{J_a} \times \frac{J_w}{SRF} \tag{1.3}$$

with

- J_n joint set number;
- J_r joint roughness number;
- J_a joint alteration number;
- J_w joint water reduction factor;
- SRF stress reduction factor.

Detailed determination procedures of the parameters are presented in NGI (2015). Figure 1.1 shows the recommendations of the support design on the basis of the Q -values and the equivalent dimension, which is defined as the ratio between the excavation span or height (in m) and the excavation support ratio (ESR).



$$\text{Rock mass quality } Q = \frac{RQD}{J_n} \times \frac{J_r}{J_a} \times \frac{J_w}{SRF}$$

Support categories

- ① Unsupported or spot bolting
- ② Spot bolting, **SB**
- ③ Systematic bolting, fibre reinforced sprayed concrete, 5-6 cm, **B+Sfr**
- ④ Fibre reinforced sprayed concrete and bolting, 6-9 cm, **Sfr (E500)+B**
- ⑤ Fibre reinforced sprayed concrete and bolting, 9-12 cm, **Sfr (E700)+B**
- ⑥ Fibre reinforced sprayed concrete and bolting, 12-15 cm + reinforced ribs of sprayed concrete and bolting, **Sfr (E700)+RRS I +B**
- ⑦ Fibre reinforced sprayed concrete >15 cm + reinforced ribs of sprayed concrete and bolting, **Sfr (E1000)+RRS II+B**
- ⑧ Cast concrete lining, **CCA** or **Sfr (E1000)+RRS III+B**
- ⑨ Special evaluation

Bolts spacing is mainly based on Ø20 mm
 E = Energy absorption in fibre reinforced sprayed concrete
 ESR = Excavation Support Ratio
 Areas with dashed lines have no empirical data

RRS - spacing related to Q-value

- I** **Si30/6 Ø16 - Ø20 (span 10m)**
D40/6+2 Ø16-20 (span 20m)
- II** **Si35/6 Ø16-20 (span 5m)**
D45/6+2 Ø16-20 (span 10m)
D55/6+4 Ø20 (span 20m)
- III** **D40/6+4 Ø16-20 (span 5 m)**
D55/6+4 Ø20 (span 10 m)
Special evaluation (span 20 m)

Si30/6 = Single layer of 6 rebars,
 30 cm thickness of sprayed concrete
 D = Double layer of rebars
 Ø16 = Rebar diameter is 16 mm
 c/c = RSS spacing, centre - centre

Figure 1.1: Rock support chart based on Q -values (NGI, 2015)

Rock Mass Rating (RMR)

The Rock Mass Rating (RMR) system (or “Geomechanics classification”) was initially developed at the South African Council of Scientific and Industrial Research (CSIR) by Bieniawski (1973). Several modifications have been carried out and the definition of RMR can be expressed as the following formula (Bieniawski, 1989):

$$RMR = A1 + A2 + A3 + A4 + A5 + B \quad (1.4)$$

with

- $A1$ uniaxial compressive strength of intact rock;
- $A2$ RQD;
- $A3$ spacing of discontinuities;
- $A4$ condition of discontinuities;
- $A5$ groundwater conditions;
- B orientation of discontinuities.

Detailed explications of each parameter are presented in Bieniawski (1989). The rock mass can be classified by the total rating notes, and the excavation and support installation methods are proposed for different classes (Table 1.2).

Table 1.2: Guidelines for excavation and support based on the RMR system (Bieniawski, 1989)

Rock mass class	Excavation	Rock bolts (20 mm diameter, fully grouted)	Shotcrete	Steel sets
I- Very good rock RMR: 81–100	Full face, 3 m advance	Generally, no support required except spot bolting		
II- Good rock RMR: 61–80	Full face, 1–1.5 m advance complete support 20 m from the face.	Locally, bolts in crown 3m long, spaced 2.5 m with occasional wire mesh	50 mm in crown where required	None
III- fair rock RMR: 41–60	Top heading and bench 1.5–3 m advance in top heading. Commence support after each blast. Complete support 10 m from the face.	Systematic bolts 4 m long, spaced 1.5–2 m in crown and walls with wire mesh in the crown.	50–100 mm in crown and 30 mm in sides	None
IV- Poor rock RMR: 21–40	Top heading and bench 1.0–1.5 m advance in top heading Install support currently with excavation, 10 m from the face.	Systematic bolts 4–5 m long, spaced 1–1.5 m in crown and wall with wire mesh	100–150 mm in crown and 100 mm in sides	Light to medium ribs spaced 1.5 m where required.
V- Very poor rock RMR: <20	Multiple drifts 0.5–1.5 m advance in top heading. Install support currently with excavation. Shotcrete as soon as possible after blasting.	Systematic bolts 5–6 m long, spaced 1–1.5 m in crown and walls with wire mesh, Bolt invert	150–200 m in the crown, 150 mm in sides, and 50 mm on the face.	Medium to heavy ribs spaced 0.75 m with steel lagging and forepoling if required. Close invert.

Geological Strength Index (GSI)

Geological Strength Index (GSI) was introduced by Hoek (1994) and developed by Hoek et al. (1998). It aims to estimate the reduction in rock mass strength on the basis of rock mass structure and surface discontinuity condition (Figure 1.2).

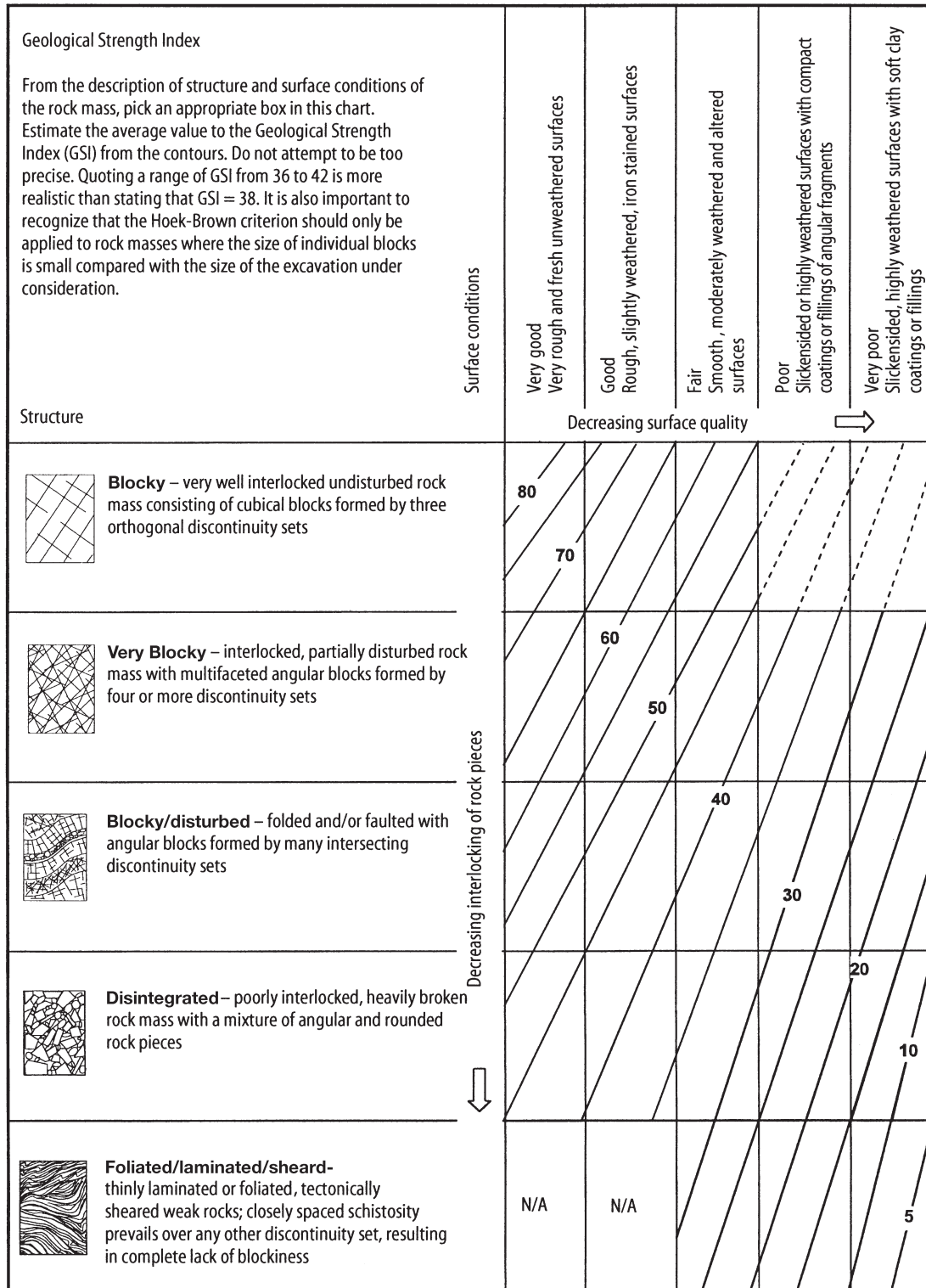


Figure 1.2: Characterization of rock masses on the basis of GSI (Hoek et al., 1998)

1.1.3 Identification of squeezing behavior

The identification of squeezing conditions has great importance before the execution of the tunneling work. Several empirical (Singh et al., 1992; Goel et al., 1995) and semi-empirical (Jethwa et al., 1984; Aydan et al., 1993; Hoek and Marinos, 2000) approaches have been developed to identify the squeezing condition. Barla (2001) has summarized the most commonly used identification methods, which are presented in the following.

Empirical approaches

The empirical approaches are proposed essentially in terms of the tunnel depth and rock mass quality to predict squeezing.

Singh et al. (1992) have analyzed 39 case histories to relate squeezing behavior to Q -values (Barton et al., 1974) and the overburden H (Figure 1.3). The linear function $H = 350Q^{1/3}$ was proposed to separate squeezing and non-squeezing conditions.

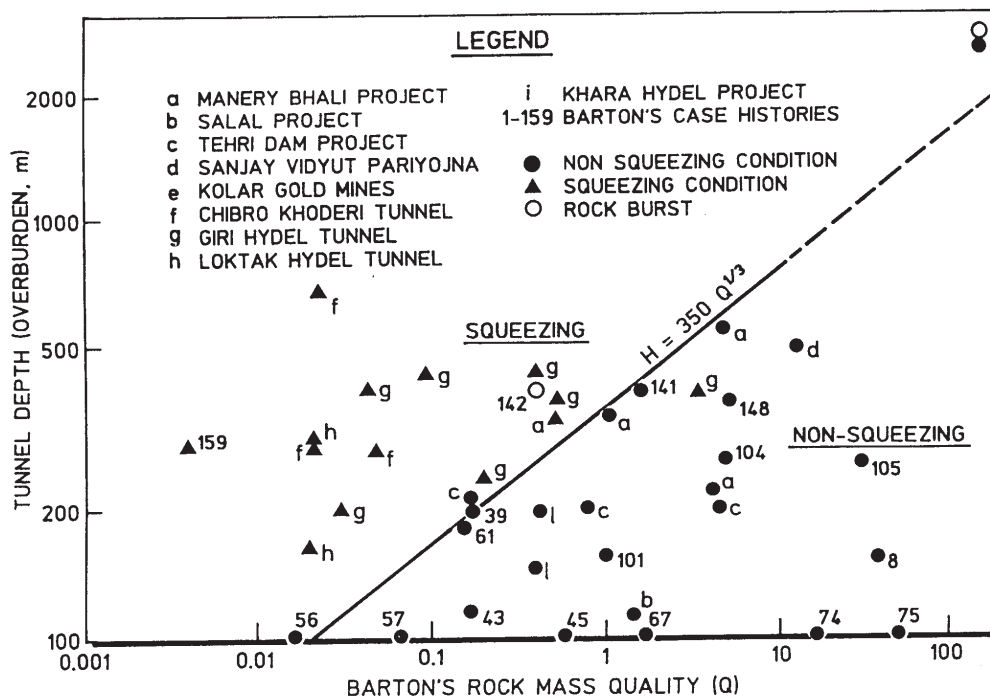


Figure 1.3: Prediction of squeezing conditions (Singh et al., 1992)

After studying 99 tunnel sections, Goel et al. (1995) and Goel (2000) developed an empirical approach on the basis of the rock mass number N , which is defined as stress-free Q value:

$$N = (Q)_{SRF=1} = \frac{RQD}{J_n} \frac{J_r}{J_a} J_w \quad (1.5)$$

Figure 1.4 shows the data analyzed by Goel et al. (1995) and Goel (2000) considering the rock mass number N , the tunnel depth H and the tunnel span or diameter B . Squeezing condition can be identified and squeezing degree can also be predicted with the formulas proposed in Table 1.3.

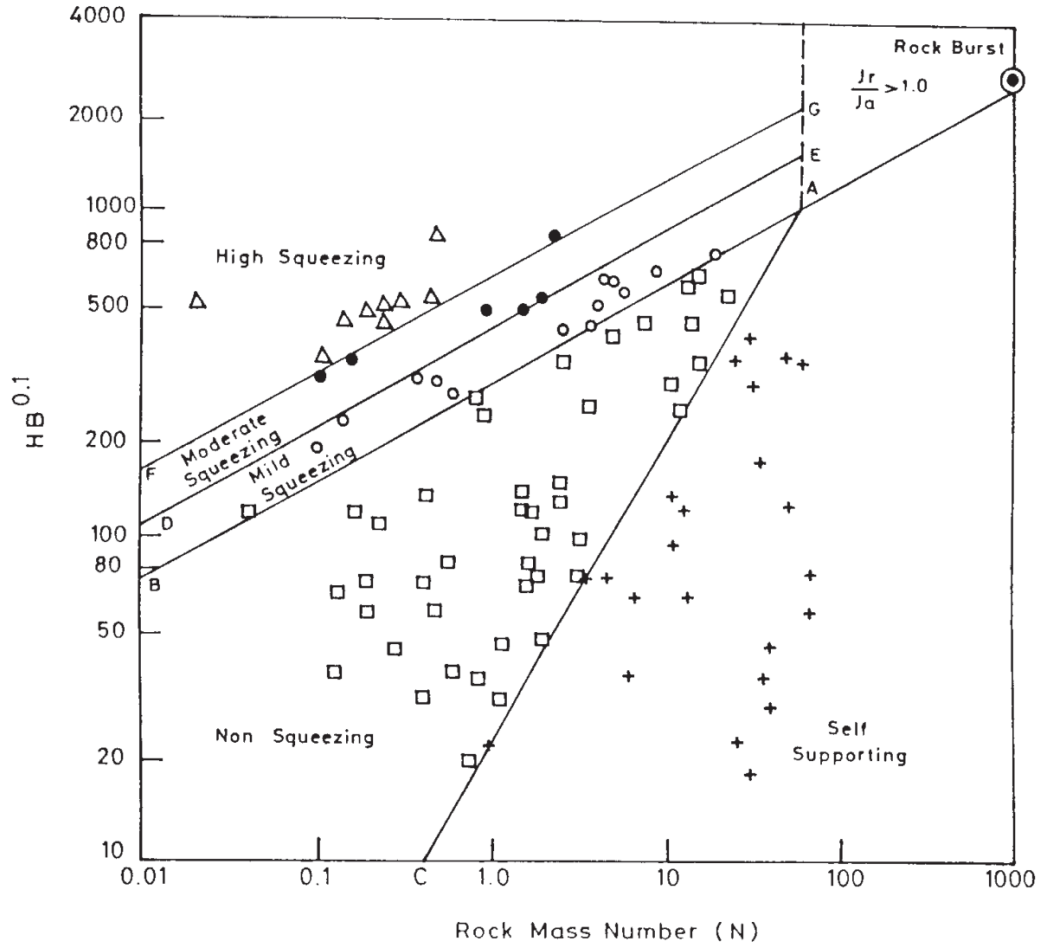


Figure 1.4: Prediction of squeezing conditions (Goel, 2000)

Table 1.3: Identification of squeezing degree (Goel et al., 1995)

Squeezing degree	H [m]
Non	$H < (275N^{0.33})B^{-0.1}$
Mild	$(275N^{0.33})B^{-0.1} < H < (450N^{0.33})B^{-0.1}$
Moderate	$(450N^{0.33})B^{-0.1} < H < (630N^{0.33})B^{-0.1}$
High	$H > (630N^{0.33})B^{-0.1}$

For both empirical approaches, the squeezing degree (Table 1.4) can be described by tunnel cross-section convergence normalized with diameter (Singh and Goel, 1999):

Table 1.4: Identification of squeezing degree (Singh and Goel, 1999)

Squeezing degree	Convergence/tunnel diameter (%)
Mild	1-3
Moderate	3-5
High	> 5

Semi-empirical approaches

The semi-empirical approaches cannot only identify potential squeezing behavior but also help to predict squeezing degree, estimate the ground deformation around the tunnel or the loading on support system.

The concept of competency factor (or “stability factor”) N_c is defined as the ratio of the uniaxial compressive strength of the ground σ_{cm} to the net pressure of the overburden $\sigma_0 = \gamma H$, both at the level of the tunnel (Muir Wood, 1972):

$$N_c = \frac{\sigma_{cm}}{p_0} = \frac{\sigma_{cm}}{\gamma H} \quad (1.6)$$

Ground behavior can be predicted according to the N_c values:

- $N_c < 2$, the ground will be over-stressed immediately;
- $2 < N_c < 10$, the stability of the ground around tunnel will depend on time and ground brittleness (i.e. the extent to which the stress-strain curve shows a sharp peak at initial failure);
- $N_c > 10$, the ground is able to stand unsupported if intact and unaffected by the disturbance of tunneling.

Squeezing degree can be predicted with different N_c values proposed by Jethwa et al. (1984) as is shown in Table 1.5.

Table 1.5: Identification of squeezing degree (Jethwa et al., 1984)

Squeezing degree	N_c
Non	> 2.0
Mild	0.4-0.8
Moderate	0.8-2.0
High	< 0.4

The ultimate rock pressure on the tunnel lining p_u is defined as the radial rock pressure acting on the lining until the tunnel wall displacement rate becomes zero. Jethwa et al. (1984) have proposed a method to estimate p_u base on the hypothesis that a compacting zone is formed around tunnel supports under squeezing rock conditions. Estimation of the radius of compacting zone R_c has been given (Jethwa et al., 1984). In case of an elasto-plastic rock formation, p_u can be calculated by using an analytical closed-form solution for a circular tunnel under a hydrostatic stress field:

$$\frac{p_u}{p_0} = DM_\phi (1 - \sin \phi_p) \left(1 - \frac{\sigma_{cm}}{2p_0} \right) \quad (1.7)$$

where

$$D = \frac{(R_c/R)^\alpha - (R/R_c)^2}{1 - (R/R_c)^2} \quad (1.8)$$

$$M_\phi = (R/R_{pl})^\alpha \quad (1.9)$$

$$\sigma_{cm} = \frac{2c_p \cos \phi_p}{1 - \sin \phi_p} \quad (1.10)$$

$$\alpha = \frac{2 \sin \phi_r}{1 - \sin \phi_r} \quad (1.11)$$

with R tunnel radius; R_{pl} radius of plastic zone; and c_p, c_r and ϕ_p, ϕ_r rock mass cohesion and friction

angle (peak and residual values respectively). Figure 1.5 shows p_u/p_0 versus ϕ_p for different values of $\sigma_{cm}/2p_0$ considering the residual cohesion c_r equal to zero (Jethwa et al., 1984).

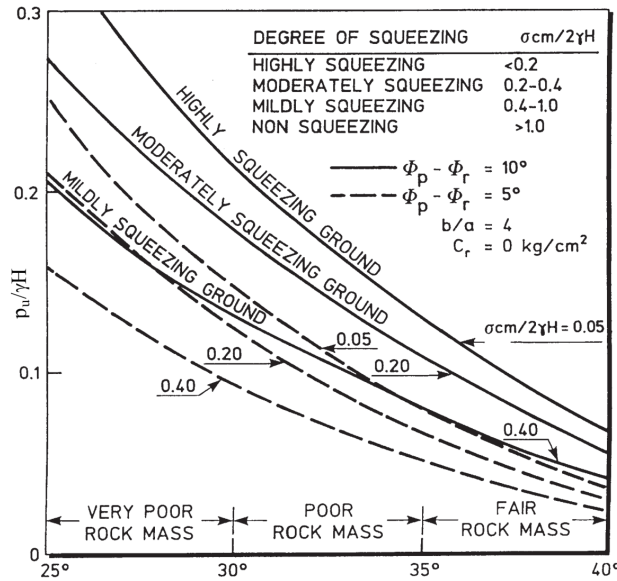


Figure 1.5: Prediction of pressure on tunnel lining in squeezing rock (Jethwa et al., 1984)

Aydan et al. (1993) have studied a number of case histories of tunnels in Japan and defined the stability factor α on the basis of the uniaxial compressive strength of intact rock σ_{ci} instead of σ_{cm} , which is used in the previous methods (Muir Wood, 1972; Jethwa et al., 1984). The definition of α is shown in Equation 1.12. When $\alpha > 2$, squeezing behavior will occur (Figure 1.6).

$$\alpha = \frac{\sigma_{ci}}{p_0} = \frac{\sigma_{ci}}{\gamma H} \tag{1.12}$$

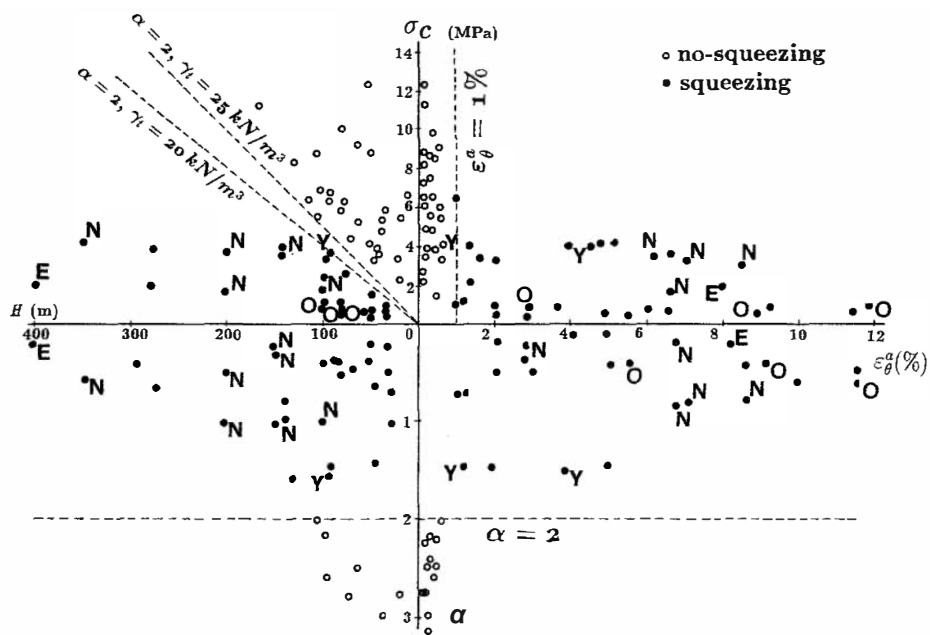


Figure 1.6: Prediction of squeezing condition (Aydan et al., 1993)

Five squeezing degrees is proposed according to the normalized deformation on the tunnel wall $\varepsilon_{\theta}^a/\varepsilon_{\theta}^e$ (Table 1.6), with

- ε_{θ}^a the tangential deformation around the tunnel defined as the ratio of the radial displacement around the tunnel to the tunnel radius;
- ε_{θ}^e the limit elastic deformation.

Table 1.6: Identification of squeezing degree (Aydan et al., 1993)

Class number	Squeezing degree	Theoretical expression
1	Non	$\varepsilon_{\theta}^a/\varepsilon_{\theta}^e \leq 1$
2	Light	$1 < \varepsilon_{\theta}^a/\varepsilon_{\theta}^e \leq \eta_p$
3	Fair	$\eta_p < \varepsilon_{\theta}^a/\varepsilon_{\theta}^e \leq \eta_s$
4	Heavy	$\eta_s < \varepsilon_{\theta}^a/\varepsilon_{\theta}^e \leq \eta_f$
5	Very heavy	$\eta_f < \varepsilon_{\theta}^a/\varepsilon_{\theta}^e$

The three normalized deformations can be calculated with the uniaxial compressive strength of intact rock σ_{ci} : $\eta_p = 2\sigma_{ci}^{-0.17}$, $\eta_s = 3\sigma_{ci}^{-0.25}$ and $\eta_f = 5\sigma_{ci}^{-0.32}$.

On the basis of axisymmetric finite element analysis and a range of different rock masses, in-situ stresses p_0 and support pressures p_i , Hoek (2001) proposed the following expression to approximate the deformation around tunnel ε_t , which is defined as the ratio of the radial displacement around the tunnel to the tunnel radius:

$$\varepsilon_t(\%) = 0.15 \left(1 - \frac{p_i}{p_0} \right) \frac{\sigma_{cm}}{p_0} - \left(3 \frac{p_i}{p_0} + 1 \right) / \left(3.8 \frac{p_i}{p_0} + 0.54 \right) \quad (1.13)$$

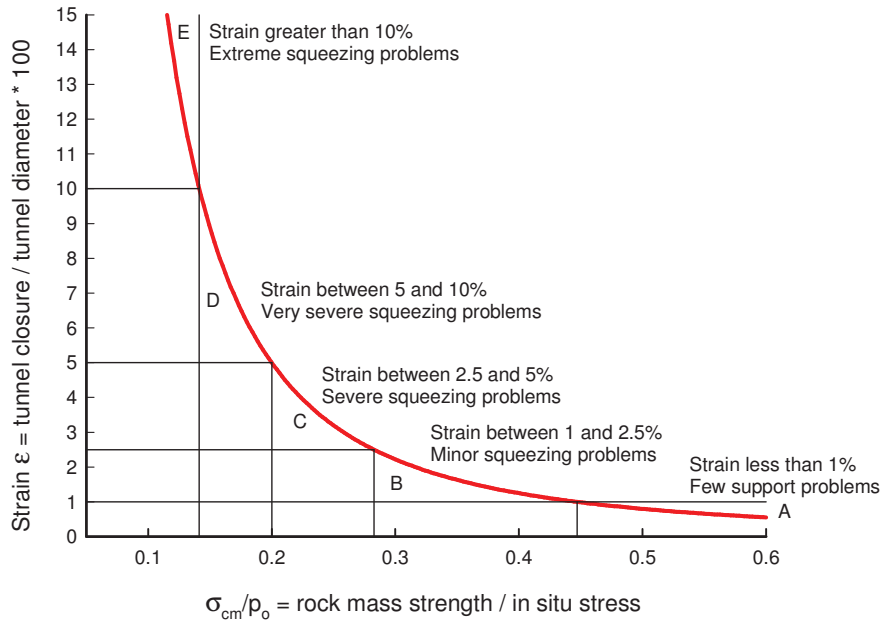


Figure 1.7: Five levels of squeezing (Hoek and Marinos, 2000)

The identification methods proposed by Hoek and Marinos (2000) and by Aydan et al. (1993) are both based on the rock deformation around the tunnel. The method of Hoek and Marinos (2000) covers a larger range of squeezing behavior in comparison with the method of Aydan et al. (1993). Considering

case histories for a number of tunnels, the squeezing degree can be classed to five levels (Figure 1.7) according to different values of ε_t as shown in Table 1.7.

Table 1.7: Identification of squeezing degree (Hoek and Marinos, 2000)

Class number	Squeezing degree	Theoretical expression
1	few support problems	$\varepsilon_t \leq 1$
2	minor squeezing	$1 < \varepsilon_t \leq 2.5$
3	severe squeezing	$2.5 < \varepsilon_t \leq 5.0$
4	very severe squeezing	$5.0 < \varepsilon_t \leq 10.0$
5	extreme squeezing	$\varepsilon_t > 10.0$

1.2 Tunneling in squeezing ground

Because of the large, time-dependent and often anisotropic closure of cross-section induced by the squeezing ground, the excavation and support installation methods need to be adapted to the local geological and geotechnical context. The conventional and mechanized excavation methods and commonly used reinforcement and support systems are presented in this section.

1.2.1 Excavation methods

Several excavation methods are applied for the tunneling work in squeezing ground, which can be classified into two categories: conventional excavation methods carried out by successive excavation steps and mechanized excavation method using a tunnel boring machine (TBM).

Conventional tunneling

The conventional tunneling are based on drill and blast excavation mainly applied in hard rock ground conditions (Figure 1.8a), and mechanical excavation using roadheaders, excavators with shovels, rippers, hydraulic breakers etc., mainly applied in soft ground and in weak rock conditions (Figure 1.8b).



(a) Drill and blast excavation



(b) Roadheader excavation

Figure 1.8: Examples of conventional excavation techniques (photos from ITA-AITES)

Kovári and Staus (1996) has summarized the basic conventional excavation methods for the tunnels

whose cross-sections are in the range of 90 – 150 m² and presented three widely used excavation profiles of conventional tunneling (Figure 1.9):

- Side drift method: two side drifts are first excavated before the opening of the full cross-section to ensure the stability of tunnel face. This method leads to very slow tunnel face advance;
- Top heading / benching down method: the excavation is performed first for the heading and then for the benching;
- Full face excavation: the whole section is opened in a single excavation step.

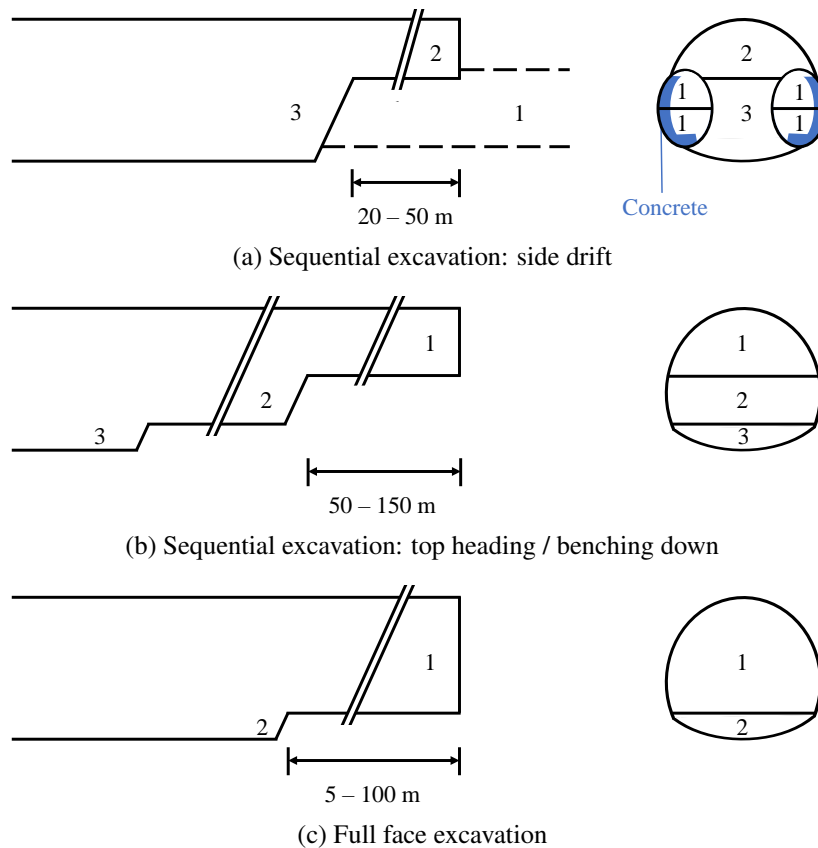


Figure 1.9: Conventional excavation methods (after Kovári and Staus, 1996)

There exist also several kinds of excavation profiles according to the specific requirements of field work. For example, a special sequential excavation method (Figure 1.10) was applied in Seikan tunnel of Japan (Fujita, 1978). Two side drifts are first excavated and completely filled by concrete before excavation of the heading and benching. The concrete body acts as a foundation and ensures the stability of tunnel wall during excavation (Kovári and Staus, 1996).

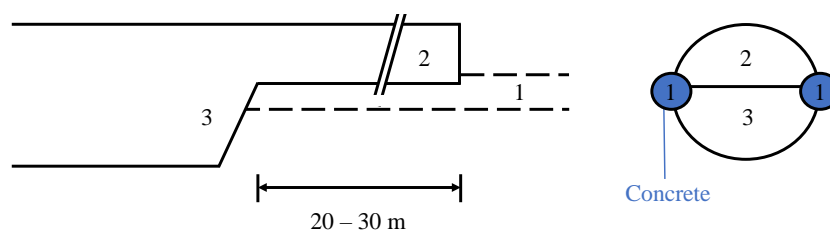


Figure 1.10: Spring line side drifts method (after Fujita, 1978)

Mechanized tunneling

In the context of excavation of long tunnels, TBMs are more and more widely used as they permit to reduce the construction time and costs. TBMs excavate circular tunnels through a variety of soil and rock strata, for a diameter from 1 to 17.5 m. Three TBM types are distinguished based on the thrusting system, the type of support and the existence or not of a shield (Ramoni and Anagnostou, 2008): gripper TBMs, single shield TBMs and double shield TBMs (Figure 1.11). Characteristics of these TBM types are summarized in Table 1.8.

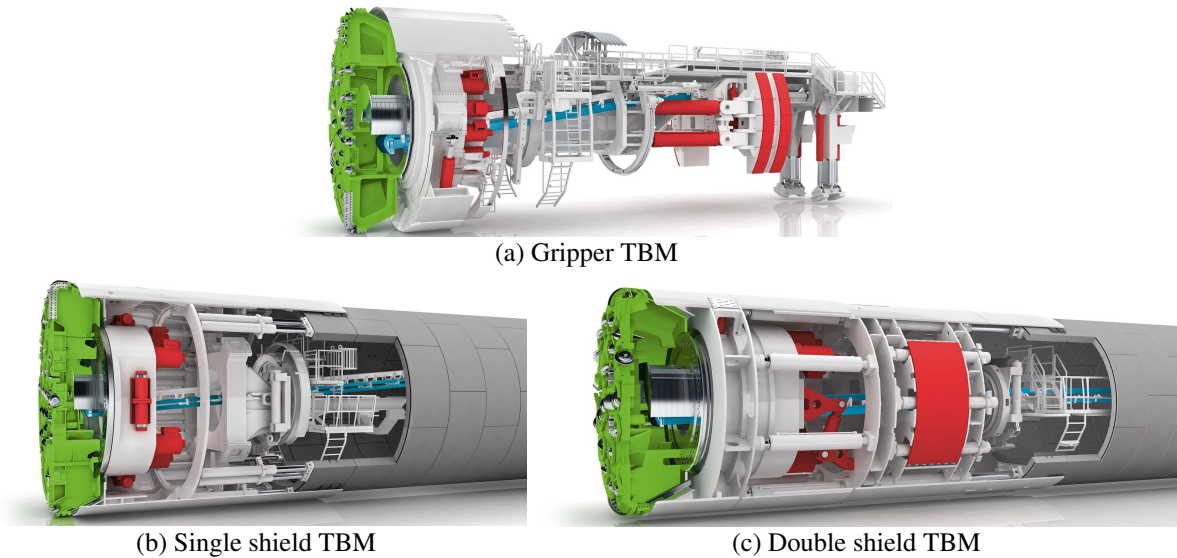


Figure 1.11: Example of TBM types (images from Herrenknecht)

Table 1.8: Characteristics of different TBM types (De La Fuente, 2018)

Type of machine	Risk of shield jamming	Advance rate	Support system	Thrusting and torque system
Gripper TBMs	Low (short shield)	Low in poor ground	Grippers	Gripper forces are transmitted to the ground which must be able to provide a sufficient reaction to them
Single shield TBMs	Moderate (medium length shield)	High in poor ground	Longitudinal support	The TBM is jacked against the segmental lining
Double shield TBMs	High (long shield)	Very high in poor ground (simultaneous installation of the lining and excavation)	Mix-support	Grippers on the lining and longitudinal hydraulic jacks

TBM performance depends on the interaction between the machine, the support and the ground, so that many problems may occur when tunneling with TBM in squeezing ground (Barla et al., 2014; Hasanpour et al., 2015). Due to excessive tunnel convergence under high in-situ stress, the support can be overloaded. Shielded TBMs can get stuck when the available thrust is not sufficient to maintain TBM advancement or to allow for TBM restart. Long-time stoppages need to be avoided as the time factor plays a major role on the costs of the works.

1.2.2 Reinforcement and support systems

Reinforcement of squeezing ground is required before and during excavation to modify the ground behavior by installation of structural elements within the rock mass in order to ensure the stability of tunnel face and around tunnel wall. After opening of the section, support systems are installed according to the rock response. Support system provides surface restraint to rock mass by installation of structural elements on the tunnel wall.

Rock reinforcement

The objective of rock reinforcement is to improve the shear and tensile strength or decrease the deformability characteristics of rock mass (Windsor and Thompson, 1994). Two techniques are widely used for ground reinforcement: installation of rock-bolts and injection of grouts.

When using rock-bolts, the choice of the bolt types depends on the geological context and the field work requirements. Based on the way how the element load is transferred to the rock (Bobet and Einstein, 2011) (Figure 1.12), the rock-bolts can be classed into three categories (Windsor and Thompson, 1994):

- Continuously Mechanically Coupled (CMC);
- Continuously Frictionally Coupled (CFC);
- Discretely Mechanically or Frictionally Coupled (DMFC).

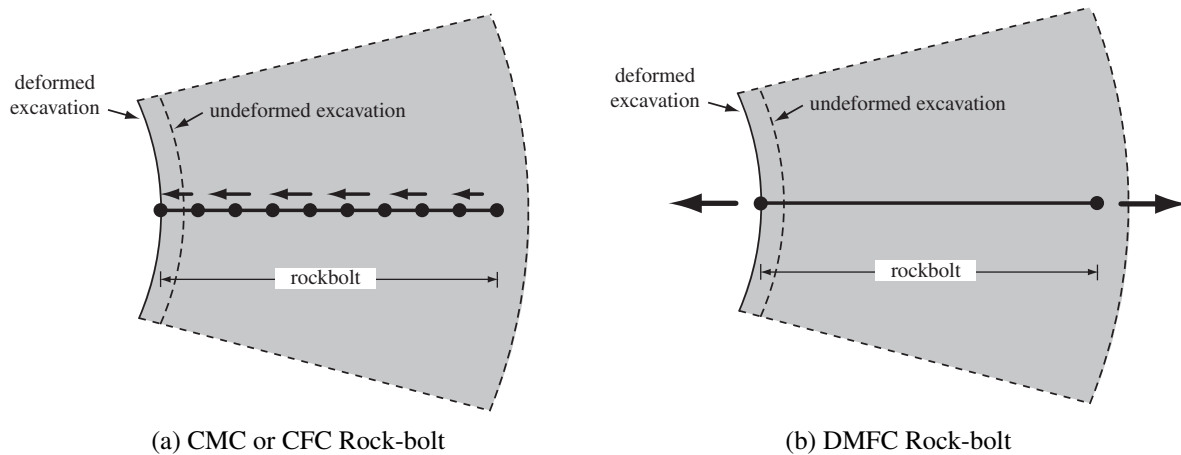


Figure 1.12: Schematics of CMC/CFC and DMFC rock-bolts (Bobet and Einstein, 2011)

Reinforcement by injection considers injecting mortar, cement grout or resin into the ground to improve its stiffness and strength, and to reduce its permeability. The following types of injection are often used:

- Low pressure injection: the injected product propagates through the pores;
- High pressure injection: the injected product creates and fills cracks;
- Jet-grouting: a jet of fluid with high kinetic energy is used to break down the ground and mixed with the grouting material.

Support system

The support system aims at stabilizing the tunnel wall and providing secured working environment of excavation. Two types of support systems are adopted for tunneling in squeezing ground: active and passive approaches.

The active approach (“heavy method” or “resistance principle”) consists to prevent ground deformations by installing heavy support system, for example, steel ribs of HEB type and shotcrete. It allows very small ground deformation and results in strong loading on the support.

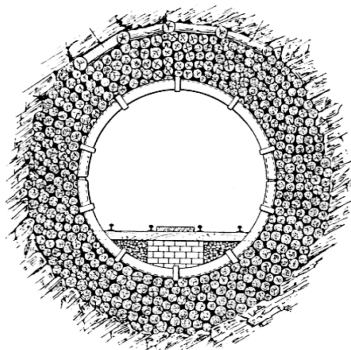
The passive approach (“light method” or “yielding principle”) permits to accommodate the large deformation before stabilizing the convergence of cross-section. This method shows advantages in case of high deformable ground and is often applied with the following techniques:

- Over-excavation and reprofiling process: Because of the delayed cross-section closure induced by squeezing behavior, the section often needs to be over-excavated to a larger size in order to preserve the place for high convergence of the section and for support or lining installation. If the section size becomes too small after deformation, the reprofiling process can be applied to enlarge the cross-section.
- Steel rib with sliding joints: Introduction of sliding joints in the steel ribs permits the different elements of the steel ribs to slide between each other when the hoop stress exceeds a certain level (Figure 1.13). The sliding joints help to avoid the failure and ensure the good performance of steel ribs.

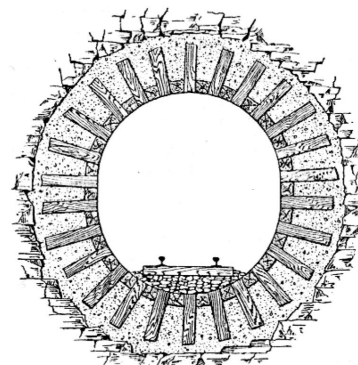


Figure 1.13: TH type steel ribs with sliding joints

- High compressible elements: The concept of using compressible material for tunneling in squeezing or swelling ground allows to accommodate larger deformation of tunnel wall. Heise and Herbst (1913) have presented the use of wood radially between rock and support and in the circumference of the concrete lining to permit large section convergence without failure of the support (Figure 1.14).



(a) Layer of wood between rock and steel support



(b) Concrete with wood interlayers

Figure 1.14: Yielding support concept using wood elements (Heise and Herbst, 1913)

1.3 Rock mass behavior

The ground response and the interactions between the rock mass and the support structure during and after tunneling have been widely studied by considering different ground behaviors. The time-dependent and anisotropic response is important to be taken into account in squeezing condition.

1.3.1 Elastic and plastic responses

Elastic and plastic behaviors of material are widely applied to analyze the ground behavior for their simplicity. A material is elastic if the stress – strain relation is reversible, which can be linear or non-linear. The plastic behavior of the material is described by the development of irreversible deformations (Figure 1.15).

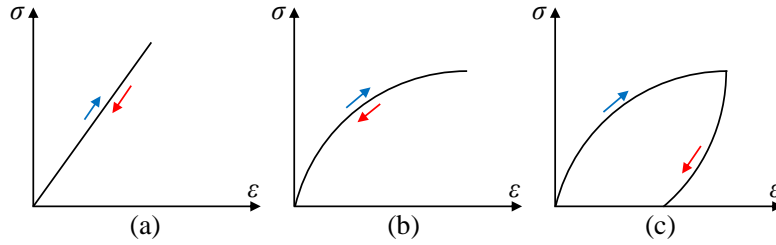


Figure 1.15: Linear elasticity (a), non-linear elasticity (b) and plasticity (c)

Elasticity

In small deformation, the stress – strain relation is given by Hooke's law as a function of Young's modulus E and Poisson's ratio ν in the following two index forms:

$$\sigma_{ij} = \frac{E}{1+\nu} \varepsilon_{ij} + \frac{\nu E}{(1+\nu)(1-2\nu)} \varepsilon_{kk} \delta_{ij} \quad (1.14)$$

$$\varepsilon_{ij} = \frac{1+\nu}{E} \sigma_{ij} - \frac{\nu}{E} \sigma_{kk} \delta_{ij} \quad (1.15)$$

It can be presented with matrix format considering $\gamma_{ij} = 2\varepsilon_{ij}$:

$$\begin{pmatrix} \varepsilon_{xx} \\ \varepsilon_{yy} \\ \varepsilon_{zz} \\ \gamma_{yz} \\ \gamma_{xz} \\ \gamma_{xy} \end{pmatrix} = \frac{1}{E} \begin{pmatrix} 1 & -\nu & -\nu & 0 & 0 & 0 \\ -\nu & 1 & -\nu & 0 & 0 & 0 \\ -\nu & -\nu & 1 & 0 & 0 & 0 \\ 0 & 0 & 0 & 2(1+\nu) & 0 & 0 \\ 0 & 0 & 0 & 0 & 2(1+\nu) & 0 \\ 0 & 0 & 0 & 0 & 0 & 2(1+\nu) \end{pmatrix} \begin{pmatrix} \sigma_{xx} \\ \sigma_{yy} \\ \sigma_{zz} \\ \tau_{yz} \\ \tau_{xz} \\ \tau_{xy} \end{pmatrix} \quad (1.16)$$

Plasticity

Two types of plastic behavior can be distinguished: perfect elasto-plasticity and elasto-plasticity with strain hardening (Figure 1.16).

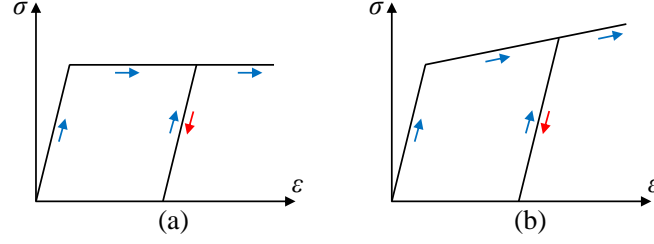


Figure 1.16: Elasto-perfectly plastic (a) and elasto-plastic with hardening (b)

A number of different yield criteria have been developed for geological application, for example, the Mohr-Coulomb criterion and the Hoek-Brown criterion, which are most widely used.

The Mohr-Coulomb criterion is commonly used for soils and rocks and is defined, in the plane of principal maximal stress σ_1 and minimal stress σ_3 , as a function of the friction parameter K_p and the uniaxial compressive strength R_c :

$$\sigma_1 = K_p \sigma_3 + R_c \quad (1.17)$$

where

$$K_p = \tan^2 \left(\frac{\pi}{4} + \frac{\phi}{2} \right) \quad (1.18)$$

$$R_c = 2c \frac{\cos \phi}{1 - \sin \phi} \quad (1.19)$$

The Hoek-Brown empirical yield criterion (Hoek and Brown, 1980) for rock matrix introduces two material parameters: the uniaxial compressive strength R_c and parameter related to rock nature m :

$$\sigma_1 - \sigma_3 = \sqrt{m \sigma_3 R_c + R_c^2} \quad (1.20)$$

The discontinuities of rock mass are later introduced (Hoek and Brown, 1980; Hoek et al., 2002) by applying the GSI index to modify the yield criterion:

$$\sigma_1 - \sigma_3 = \sigma_{ci} \left(m_b \frac{\sigma_3}{\sigma_{ci}} + s \right)^a \quad (1.21)$$

where

- σ_1, σ_3 major and minor principle stress;
- σ_{ci} uniaxial compressive strength of intact rock;
- m_b, s and a coefficients of rock with

$$m_b = m_i \exp \left(\frac{GSI - 100}{28 - 14D} \right) \quad (1.22)$$

$$s = \exp \left(\frac{GSI - 100}{9 - 3D} \right) \quad (1.23)$$

$$a = \frac{1}{2} + \frac{1}{6} \left[\exp \left(-\frac{GSI}{15} \right) - \exp \left(-\frac{20}{3} \right) \right] \quad (1.24)$$

The state of stress inside the yield surface is elastic and the material becomes plastic when the stress state lies on the surface. The evolution of plastic deformation is described by the flow rule depending

on the plastic potential g as shown in Equation 1.25. The flow rule can be associated ($\frac{\partial g}{\partial \sigma} = \frac{\partial f}{\partial \sigma}$) or non-associated ($\frac{\partial g}{\partial \sigma} \neq \frac{\partial f}{\partial \sigma}$).

$$\varepsilon_p = \dot{\lambda} \frac{\partial g}{\partial \sigma} \quad (1.25)$$

1.3.2 Time-dependent behavior

Time-dependent response of rock mass are important to be taken into account in rock engineering, particularly when squeezing behavior is encountered. Creep of rock mass is a complex phenomenon that depends upon the rock mass type, the stress state, the hydrological conditions, the temperature, the chemical interactions etc... In a creep test, when constant loading is applied, the strain evolution of rock mass is typically composed of three stages (Figure 1.17):

- primary (transient) stage: the strain rate is high and decreases with time;
- secondary (steady-state) stage: the strain rate is constant and the curve is nearly linear. This stage can last for long period;
- tertiary (accelerated) stage: the strain rate accelerates exponentially up to possibly ultimate failure.

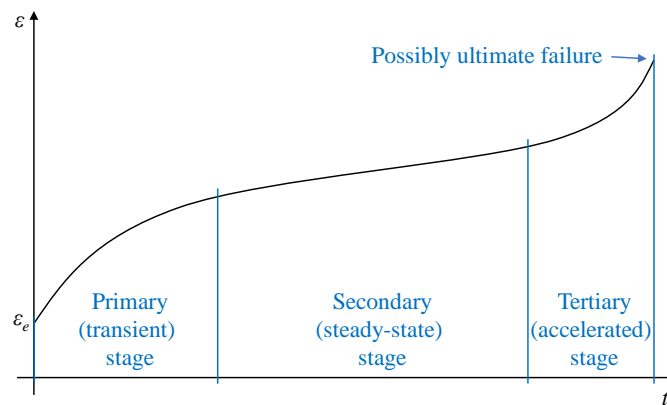


Figure 1.17: Three stages of creep

Different kinds of models have been developed and studied to approximate time-dependency of rock behaviors. The most widely used models for tunneling in squeezing condition (the analogical approaches and the models based on general overstress theory) are presented in the following.

Basic analogical elements

Rheological models are often used to describe the time-dependent behavior of material by assembling analogical elements in parallel ($\sigma = \Sigma \sigma_i$ and $\varepsilon = \varepsilon_i$), in series ($\varepsilon = \Sigma \varepsilon_i$ and $\sigma = \sigma_i$) or in mixed grouping. The most common basic analogical elements are the following:

- Hooke element: linear elastic spring;

$$\begin{array}{c} E \\ \text{---} \text{---} \text{---} \text{---} \text{---} \\ \text{---} \end{array} \rightarrow \sigma \quad \sigma = E\varepsilon$$

- Newton element: linear viscous dashpot (damper);

$$\begin{array}{c} \eta \\ \text{---} \boxed{\text{---}} \text{---} \end{array} \rightarrow \sigma \quad \sigma = \eta \dot{\varepsilon}$$

– Saint-Venant element: slider (sliding block representing a stress threshold);

$$\begin{array}{c} \sigma_s \\ \text{---} \text{---} \boxed{\text{---}} \text{---} \end{array} \rightarrow \sigma \quad -\sigma_s < \sigma < \sigma_s$$

In addition to the above basic analogical elements, the viscous Abel dashpot (or “Scott-Blair element”) is more and more used for geotechnical applications (Figure 1.18) by introducing the fractional calculus to simulate the non-linear deformation-time relation of rock (Mainardi and Spada, 2011; Kabwe et al., 2020).

$$\begin{array}{c} \eta, \alpha \\ \text{---} \boxed{\text{---}} \text{---} \end{array} \rightarrow \sigma \quad \sigma = \eta^\alpha D^\alpha \varepsilon$$

Figure 1.18: Viscous Abel dashpot (or “Scott-Blair element”)

The fractional calculus is an extension of the traditional definition of integration and differentiation. It permits to solve physical and mechanical modeling problems. Several kinds of definitions are proposed and the most widely used is the Riemann-Liouville approach (Mainardi, 2010), which is based on the well-known Cauchy formula of the definition of integration:

$$I^n f(t) := f_n(t) = \frac{1}{(n-1)!} \int_0^t (t-\tau)^{n-1} f(\tau) d\tau, \quad n \in \mathbb{N} \quad (1.26)$$

where $t > 0$ and n belongs to the set of positive integers \mathbb{N} . In the Riemann-Liouville definition, the Cauchy formula is extended to any positive real value by using the Gamma function. The Riemann-Liouville fractional integral is defined for $\alpha > 0$ in the set of positive real numbers \mathbb{R}^+ :

$$I^\alpha f(t) := \frac{1}{\Gamma(\alpha)} \int_0^t (t-\tau)^{\alpha-1} f(\tau) d\tau, \quad \alpha \in \mathbb{R}^+ \quad (1.27)$$

and the Riemann-Liouville fractional derivative is defined:

$$D^\alpha f(t) = \begin{cases} \frac{1}{\Gamma(m-\alpha)} \frac{d^m}{dt^m} \int_0^t \frac{f(\tau) d\tau}{(t-\tau)^{\alpha+1-m}} & m-1 \leq \alpha \leq m \\ \frac{d^m}{dt^m} f(t) & \alpha = m \end{cases} \quad (1.28)$$

Based on the Riemann-Liouville definition, the strain-stress relation in the Abel element for $0 \leq \alpha \leq 1$ can be determined with the characterized creep time $\tau = \frac{\eta}{E}$:

$$\sigma(t) = C \frac{d^\alpha \varepsilon}{dt^\alpha} = E \tau^\alpha \frac{d^\alpha \varepsilon}{dt^\alpha} \quad (1.29)$$

In a creep test, the strain ε and the strain rate $\dot{\varepsilon}$ on time t of the Abel element can be calculated with the following formulas:

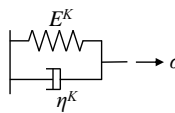
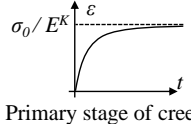
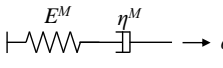
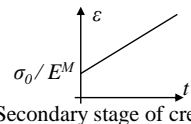
$$\varepsilon(t) = \frac{1}{E} \frac{\sigma}{\Gamma(1+\alpha)} \left(\frac{t}{\tau}\right)^\alpha \quad (1.30)$$

$$\dot{\varepsilon}(t) = \frac{1}{E\tau} \frac{\alpha\sigma}{\Gamma(1+\alpha)} \left(\frac{t}{\tau}\right)^{\alpha-1} \quad (1.31)$$

Visco-elastic models

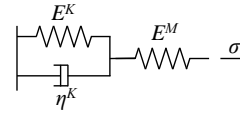
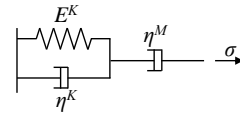
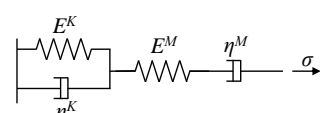
Two simple rheological models (Table 1.9) are commonly used to simulate visco-elastic behavior by coupling the elastic spring and the viscous dashpot in parallel and in series: Kelvin model and Maxwell model. They permit to simulate different stages of creep and can be extended to produce more complex models. The Kelvin element allows to reproduce the ground behavior in case of a decreasing deformation rate with time. However, it cannot simulate instantaneous deformation under loading. The Maxwell element has a linear strain-time behavior and cannot model the commonly observed non-linear behavior.

Table 1.9: Kelvin and Maxwell model

Model	Analogical presentation	Strain-stress relationship	Creep test $\sigma = \sigma_0$
Kelvin model		$\varepsilon(t) = \frac{1}{\eta^K} \int_0^t \sigma(t - \theta) e^{-\frac{E^K \theta}{\eta^K}} d\theta$ <p>When $\sigma = \sigma_0 = \text{constant}$: $\varepsilon(t) = \frac{\sigma_0}{E^K} \left(1 - e^{-\frac{E^K}{\eta^K} t} \right)$</p>	 <p>Primary stage of creep</p>
Maxwell model		$\varepsilon(t) = \frac{\sigma(t)}{E^M} + \frac{1}{\eta^M} \int_0^t \sigma(\theta) d\theta$ <p>When $\sigma = \sigma_0 = \text{constant}$: $\varepsilon(t) = \frac{\sigma_0}{E^M} \left(1 + \frac{E^M}{\eta^M} t \right)$</p>	 <p>Secondary stage of creep</p>

Based on these two models, several visco-elastic model are constructed, for example, the generalized Kelvin model (or “Kelvin-Voigt model” or “Zener model”), the generalized Maxwell model and the Burgers model (Table 1.10), which have better performance in modeling the divers behavior of rocks. The Burgers model allows to simulate the time-dependent behavior of sedimentary rocks and can be used to capture both the primary creep and the secondary creep.

Table 1.10: Visco-elastic rheological models

Model	Analogical presentation	Strain-stress relationship
Generalized Kelvin (Kelvin-Voigt or Zener) model		$\varepsilon(t) = \frac{\sigma(t)}{E^M} + \frac{1}{\eta^K} \int_0^t \sigma(t - \theta) e^{-\frac{E^K \theta}{\eta^K}} d\theta$ <p>When $\sigma = \sigma_0 = \text{constant}$: $\varepsilon(t) = \frac{\sigma_0}{E^M} + \frac{\sigma_0}{E^K} \left(1 - e^{-\frac{E^K}{\eta^K} t} \right)$</p>
Generalized Maxwell model		$\varepsilon(t) = \frac{1}{\eta^K} \int_0^t \sigma(t - \theta) e^{-\frac{E^K \theta}{\eta^K}} d\theta + \frac{1}{\eta^M} \int_0^t \sigma(\theta) d\theta$ <p>When $\sigma = \sigma_0 = \text{constant}$: $\varepsilon(t) = \frac{\sigma_0}{E^K} \left(1 - e^{-\frac{E^K}{\eta^K} t} \right) + \frac{\sigma_0}{\eta^M} t$</p>
Burgers model		$\varepsilon(t) = \frac{1}{\eta^K} \int_0^t \sigma(t - \theta) e^{-\frac{E^K \theta}{\eta^K}} d\theta + \frac{\sigma(t)}{E^M} + \frac{1}{\eta^M} \int_0^t \sigma(\theta) d\theta$ <p>When $\sigma = \sigma_0 = \text{constant}$: $\varepsilon(t) = \frac{\sigma_0}{E^K} \left(1 - e^{-\frac{E^K}{\eta^K} t} \right) + \frac{\sigma_0}{E^M} \left(1 + \frac{E^M}{\eta^M} t \right)$</p>

Visco-plastic models

In addition to the visco-elastic models, the plasticity can be introduced with viscous damper like the visco-plastic Bingham model (Figure 1.19), which couples a plastic Saint-Venant element and a viscous Newton element in parallel. In this model, strain occurs when the applied stress is equal or greater than the capacity of the slider. The Bingham model can help to describe the tertiary creep stage of rock behavior.

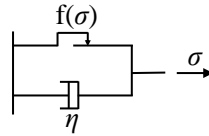


Figure 1.19: Bingham model

By attaching Bingham model with the other elements, more complex visco-plastic models can be produced to simulate various deformation modes of rocks (Table 1.11). The model of Lombardi (1977) reproduced well the convergence data of the Saint-Gothard tunnel up to a period of several months using two yielding criteria. The models proposed by Gioda (1981), Gioda and Cividini (1996) and Sterpi and Gioda (2009) allow to simulate the tertiary creep stage of rocks.

Table 1.11: Visco-plastic models

Model	Analogical presentation
Modified Bingham model	
Lombardi (1977)	
Gioda (1981), Gioda and Cividini (1996)	
Sterpi and Gioda (2009)	
Sterpi and Gioda (2009)	

A visco-elastic-plastic model (CVISC or Burgers-Mohr model) has been developed (Itasca, 2017) by using the Mohr-Coulomb model for the volumetric behavior and by combining the Burgers model and the Mohr-Coulomb model for deviatoric behavior (Figure 1.20). The deviatoric strain rate is partitioned into three parts, in Kelvin element, in Maxwell element and in Mohr-Coulomb element: $\dot{e}_{ij} = \dot{e}_{ij}^K + \dot{e}_{ij}^M + \dot{e}_{ij}^P$.

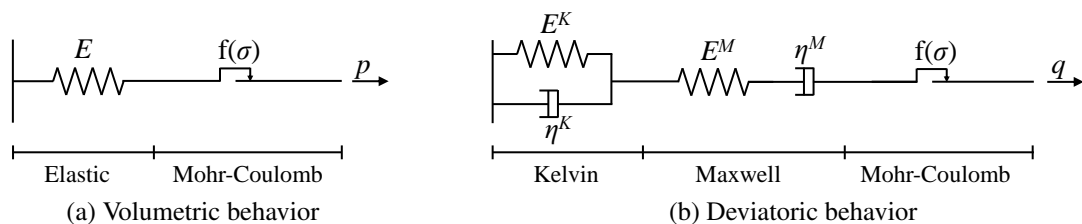


Figure 1.20: Burgers-Mohr model available in *Flac3D* code

This model has been widely used in many numerical simulations of rock squeezing behavior (Tran-Manh, 2014; Bonini et al., 2009; De La Fuente et al., 2019). It is characterized by 9 parameters for the rock mass, and Young's modulus E and Poisson's ratio ν can be used to define the elasticity instead of bulk modulus K and shear modulus G^M :

- elastic bulk modulus K , elastic shear modulus G^M , Maxwell dynamic viscosity η^M ,
- Kelvin shear modulus G^K , Kelvin viscosity η^K ,
- cohesion c , friction angle ϕ , tension limit σ_t , dilation angle ψ .

The overstress theory is based upon a static yield surface in the stress domain assuming that the point presenting the state of stress can cross the yield surface during loading. The yield function f can be positive or negative, and the consistency conditions of the classical theory of elasto-plasticity are not satisfied. The yield surface separates two different fields in the stress space:

- an elastic field inside the yield surface ($f < 0$). The deformation is elastic and can be determined using the generalized Hooke's law of elasticity.
- an elasto-visco-plastic field external to the yield surface ($f > 0$). The deformation is elasto-visco-plastic and the strain rate $\dot{\epsilon}_{ij}$ can be divided into an elastic component $\dot{\epsilon}_{ij}^e$ and a visco-plastic component $\dot{\epsilon}_{ij}^{vp}$:

$$\dot{\epsilon}_{ij} = \dot{\epsilon}_{ij}^e + \dot{\epsilon}_{ij}^{vp} \quad (1.32)$$

The elastic strain rate $\dot{\epsilon}_{ij}^e$ can be determined using the generalized Hooke's law of elasticity, and the visco-plastic component $\dot{\epsilon}_{ij}^{vp}$ can be evaluated by the following non-associated general flow rule:

$$\dot{\epsilon}_{ij}^{vp} = \gamma \cdot \Phi(F) \cdot \frac{\partial g}{\partial \sigma_{ij}} \quad (1.33)$$

with γ is a fluidity parameter, $\Phi(F)$ is the viscous nucleus, F is the overstress function presenting a measure of the unbalanced forces in the material, g is the visco-plastic potential function defining the direction of the visco-plastic strain rate, and σ_{ij} is the state of stress.

On the basis of the overstress theory from Perzyna (1966), the SHELVIP (Stress Hardening ELastic Viscous Plastic) model has been proposed and validated for tunnel excavation under squeezing condition encountered in SMP2 (Debernardi, 2008; Debernardi and Barla, 2009).

In the SHELVIP model, the strain rate $\dot{\epsilon}_{ij}$ is divided into three parts: elastic component $\dot{\epsilon}_{ij}^e$, plastic component $\dot{\epsilon}_{ij}^p$ and visco-plastic component $\dot{\epsilon}_{ij}^{vp}$:

$$\dot{\epsilon}_{ij} = \dot{\epsilon}_{ij}^e + \dot{\epsilon}_{ij}^p + \dot{\epsilon}_{ij}^{vp} \quad (1.34)$$

In the principal stress space, an external plastic yield surface and an internal visco-plastic yield surface are defined (Figure 1.21a). The plastic yield surface defines the stress locus for onset of plastic strains according to the classical theory of elasto-plasticity. The visco-plastic yield surface defines the stress threshold for development of visco-plastic strains, according to the overstress theory of Perzyna.

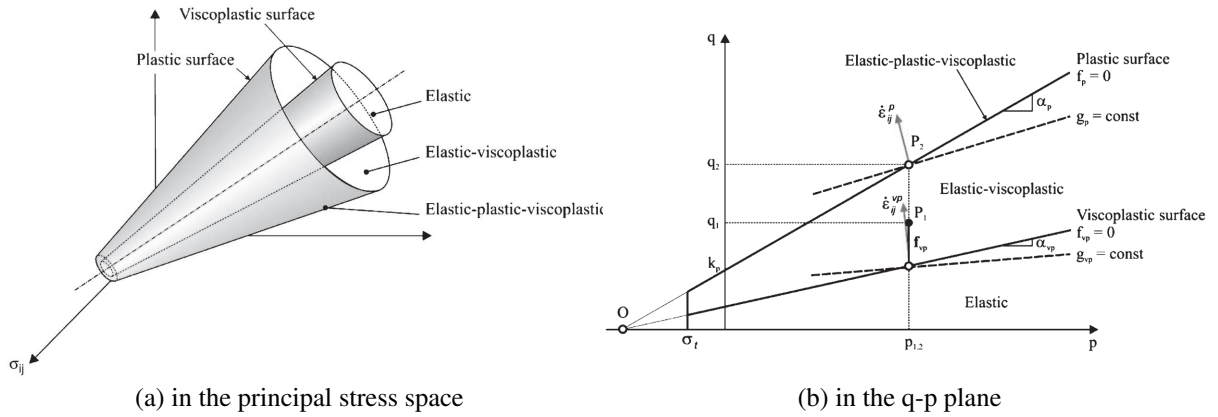


Figure 1.21: Limit surfaces and stress fields (Debernardi, 2008)

The surfaces are defined using Drucker-Prager's criterion in the $p - q$ stress plane (Figure 1.21b):

- the plastic yield surface $f_p = q - \alpha_p \cdot p - k_p$ for $p \geq \sigma_t$ where α_p and k_p are respectively the slope and the intercept with the q -axis and σ_t is the volumetric tension cut-off;
- the visco plastic yield surface $f_{vp} = q - \alpha_{vp} \cdot \left(p + \frac{k_p}{\alpha_p}\right)$ for $p \geq \sigma_t$ where α_{vp} defines the slope of the linear criterion.

1.3.3 Anisotropic behavior

The perfectly isotropic rock mass is seldom encountered due to mineral structure and discontinuities. A material is anisotropic if the behavior depends on the direction of sollicitation.

Elasticity

In general, the anisotropic elastic behavior is characterized by a constitutive relation with 21 parameters. Symmetrical planes can reduce the number of parameters. When the rock mass has two symmetrical planes, only 9 independent parameters are sufficient to describe the constitutive relation:

$$\begin{pmatrix} \epsilon_{xx} \\ \epsilon_{yy} \\ \epsilon_{zz} \\ \gamma_{yz} \\ \gamma_{xz} \\ \gamma_{xy} \end{pmatrix} = \begin{pmatrix} \frac{1}{E_x} & -\frac{\nu_{xy}}{E_y} & -\frac{\nu_{xz}}{E_z} & 0 & 0 & 0 \\ -\frac{\nu_{xy}}{E_x} & \frac{1}{E_y} & -\frac{\nu_{yz}}{E_z} & 0 & 0 & 0 \\ -\frac{\nu_{xz}}{E_x} & -\frac{\nu_{yz}}{E_y} & \frac{1}{E_z} & 0 & 0 & 0 \\ 0 & 0 & 0 & \frac{1}{G_{yz}} & 0 & 0 \\ 0 & 0 & 0 & 0 & \frac{1}{G_{zx}} & 0 \\ 0 & 0 & 0 & 0 & 0 & \frac{1}{G_{xy}} \end{pmatrix} \begin{pmatrix} \sigma_{xx} \\ \sigma_{yy} \\ \sigma_{zz} \\ \tau_{yz} \\ \tau_{xz} \\ \tau_{xy} \end{pmatrix} \quad (1.35)$$

In the case of transverse isotropy, for example vertically stratified rocks, the physical properties of rock mass are symmetric about an axis and any plane passing through the axis is a symmetric plane. The

constitutive relation depends only on 5 independent parameters:

$$\begin{pmatrix} \epsilon_{xx} \\ \epsilon_{yy} \\ \epsilon_{zz} \\ \gamma_{yz} \\ \gamma_{xz} \\ \gamma_{xy} \end{pmatrix} = \begin{pmatrix} \frac{1}{E_h} & -\frac{\nu_{hv}}{E_v} & -\frac{\nu_h}{E_h} & 0 & 0 & 0 \\ -\frac{\nu_{hv}}{E_h} & \frac{1}{E_v} & -\frac{\nu_{hv}}{E_h} & 0 & 0 & 0 \\ -\frac{\nu_h}{E_h} & -\frac{\nu_{hv}}{E_v} & \frac{1}{E_h} & 0 & 0 & 0 \\ 0 & 0 & 0 & \frac{1}{G_{hv}} & 0 & 0 \\ 0 & 0 & 0 & 0 & \frac{1}{G_h} & 0 \\ 0 & 0 & 0 & 0 & 0 & \frac{1}{G_{hv}} \end{pmatrix} \begin{pmatrix} \sigma_{xx} \\ \sigma_{yy} \\ \sigma_{zz} \\ \tau_{yz} \\ \tau_{xz} \\ \tau_{xy} \end{pmatrix} \quad (1.36)$$

where $G_h = \frac{E_h}{2(1+\nu_h)}$.

The modulus E_θ in the inclined direction θ with the symmetric axis can be determined:

$$\frac{1}{E_\theta} = \frac{\cos^4 \theta}{E_v} + \left(\frac{1}{G_{vh}} - \frac{2\nu_{vh}}{E_v} \right) \sin^2 \theta \cos^2 \theta + \frac{\sin^4 \theta}{E_h} \quad (1.37)$$

Plasticity

Experimental investigations show that the failure of material can also be anisotropic (McLamore and Gray, 1967; Oka et al., 2002; Duveau et al., 1998). Failure strength can vary strongly according to the direction.

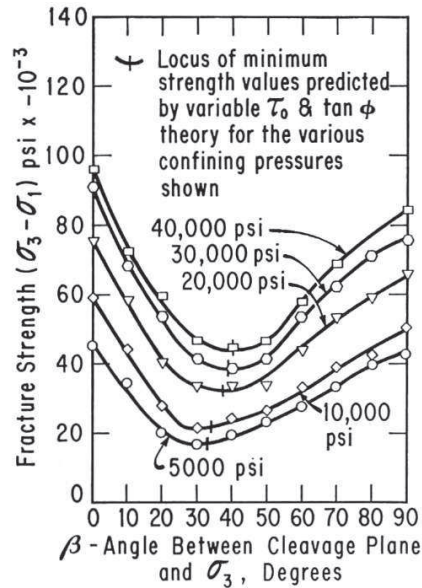


Figure 1.22: Experimental observation of anisotropic failure strength (McLamore and Gray, 1967)

A number of anisotropic yield criteria have been proposed, which can be classified into two categories (Duveau et al., 1998): continuous criteria (mathematical and empirical approaches) and discontinuous criteria.

Continuous criteria

Continuum-based approaches for elasto-plastic behavior of anisotropic geomaterials are carried out by means of strength parameters, fourth-order projection tensor or second-order microstructure tensor

(Semnani et al., 2016).

Strength parameters approaches are first introduced for ductile metal and cohesive frictionless materials (Hill, 1948, 1949, 1950). Pariseau (1968) has applied this technique to frictional material like rocks and soils whose mechanical behaviors are sensitive to the mean stress, and the following yield criterion is define with the characteristic constants of anisotropy F , G , M , U and V :

$$[F(\sigma_{22} - \sigma_{33})^2 + G\{(\sigma_{33} - \sigma_{11})^2 + (\sigma_{11} - \sigma_{22})^2\} + (2G + 4F)\sigma_{23}^2 + M(\sigma_{31}^2 + \sigma_{12}^2)]^{\frac{n}{2}} - [U\sigma_{11} + V(\sigma_{22} + \sigma_{33})] = 1 \quad (1.38)$$

On the basis of the general form of yield surface using strength tensors (Gol'denblat and Kopnov, 1966):

$$(F_i \sigma_i)^\alpha + (F_{ij} \sigma_i \sigma_j)^\beta + (F_{ijk} \sigma_i \sigma_j \sigma_k)^\gamma + \dots = 1 \quad (1.39)$$

Tsai and Wu (1971) have proposed an anisotropic yield surface as:

$$f(\sigma_k) = F_i \sigma_i + F_{ij} \sigma_i \sigma_j = 1 \quad (1.40)$$

with strength tensors $F_i = \begin{pmatrix} F_1 \\ F_2 \\ F_3 \\ F_4 \\ F_5 \\ F_6 \end{pmatrix}$ and $F_{ij} = \begin{pmatrix} F_{11} & F_{12} & F_{13} & F_{14} & F_{15} & F_{16} \\ & F_{22} & F_{23} & F_{24} & F_{25} & F_{26} \\ & & F_{33} & F_{34} & F_{35} & F_{36} \\ & & & F_{44} & F_{45} & F_{46} \\ & & & & F_{55} & F_{56} \\ & & & & & F_{66} \end{pmatrix}$.

Pietruszczak and Mroz (2000) introduced the material anisotropy by using an orientation-dependent parameter η :

$$F = F(\sigma_{ij}, \eta) = 0 \quad (1.41)$$

where $\eta = a_{ij} l_i l_j$ is the projection of the microstructure fabric tensor a_{ij} which is a measure of the material fabric, on the loading direction l_i .

Jaeger (1960) has defined the failure condition with shear stress τ , as a function of shear strength S and coefficient of internal friction $\mu = \tan \phi$:

$$\tau = S + \mu N \quad (1.42)$$

Then an empirical approach has been proposed to approximate continuously variable shear strength:

$$S = S_1 + S_2 \cos 2(\alpha - \beta) \quad (1.43)$$

where β is the direction of the least shear strength referenced to the major principle stress and α is the direction of studied plan.

Discontinuous criteria

Discontinuous approach has also been used by Jaeger (1960) by introducing a single plane of weakness with S' and $\mu' = \tan \phi'$.

In the context of Mancos shales study, Fjær and Nes (2013) considered the heterogeneity of the weak

planes and existence of the weak patches (Figure 1.23).

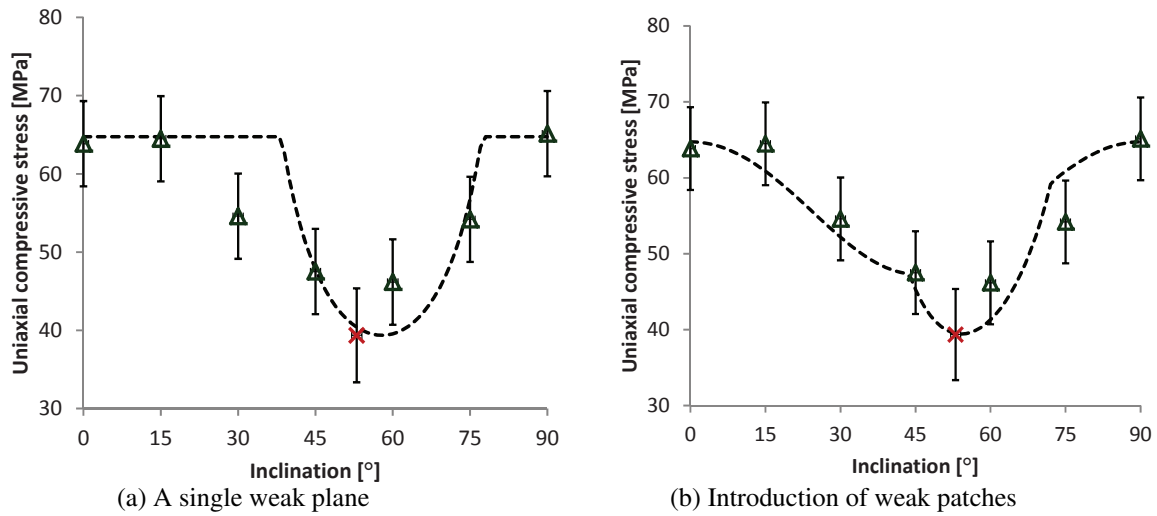


Figure 1.23: Introduction of weak patches to simulate material anisotropy (Fjær and Nes, 2013)

The ubiquitous-joint model is available in *Flac3D*, which permits to simulate the material anisotropy by introducing weakness planes with given orientation θ (Figure 1.24). The yield criterion on the plane consists of a Mohr-Coulomb envelope with tension cut-off. It depends on 4 parameters for the behavior of the weakness planes:

- joint cohesion c_j ,
- joint friction angle ϕ_j ,
- joint tension limit σ_{tj} ,
- joint dilation angle ψ_j .

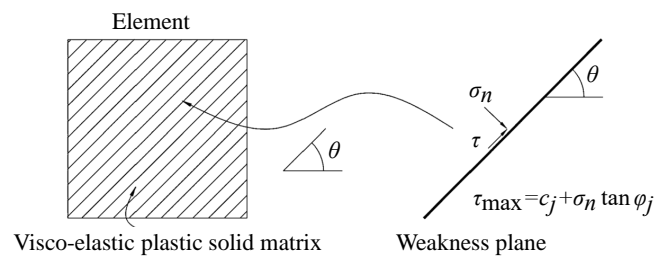


Figure 1.24: Ubiquitous-joint approach

1.3.4 Ground response after tunneling

The interactions between the ground and the support structure during tunneling is an important factor to be considered. The convergence-confinement method is a basic tool for preliminary design of support system introducing the concept of deconfinement rate.

Deconfinement rate

The tunnel face advance has a great influence on the tunnel convergence. In planar strain analyses, the tunnel face advance can be taken into account by progressive reduction of the radial stress applied on

the tunnel wall (Figure 1.25):

$$\Delta\sigma_R = -\lambda\sigma_0 \quad (1.44)$$

where λ is the deconfinement rate and σ_0 the initial stress (Panet, 1995).

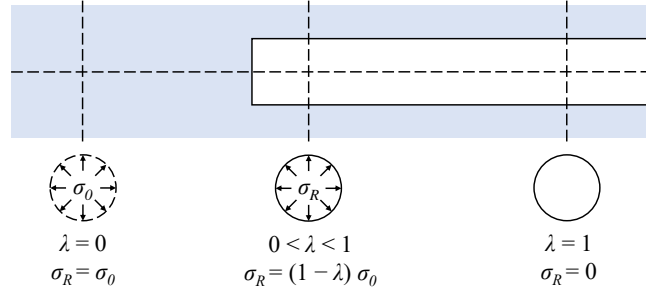


Figure 1.25: Modeling of tunnel face advance by increasing the deconfinement rate

Convergence-confinement method

The principle of the convergence-confinement method (Figure 1.26) is to combine two characteristic curves: ground reaction curve (GRC) and support confining curve (SCC).

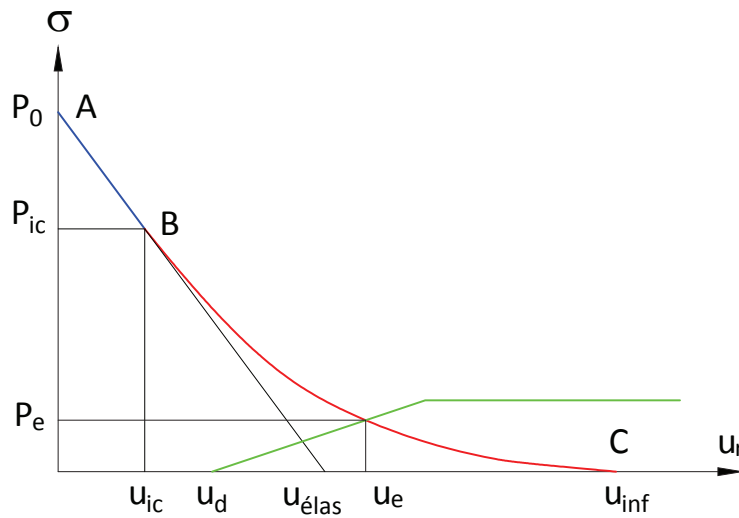


Figure 1.26: Convergence-confinement method

The following assumptions are considered (Panet, 1995):

- circular tunnel section;
- two-dimensional problem in plane deformation;
- homogeneous and isotropic material;
- hydrostatic initial stress state;
- deep tunnel;
- uniform loading on the support.

GRC characterizes the ground behavior after tunnel excavation. In elastic rock mass, the displacement u and the stress σ_R and σ_θ on the tunnel wall can be calculated by introducing the deconfinement rate λ :

$$u = \lambda \frac{\sigma_0 R}{2G} \quad (1.45)$$

$$\sigma_R = (1 - \lambda) \sigma_0 \quad (1.46)$$

$$\sigma_\theta = (1 + \lambda) \sigma_0 \quad (1.47)$$

Considering elasto-plastic ground behavior with the Mohr-Coulomb criterion, when the value of λ reaches λ_e , the tunnel wall enters in plasticity:

$$f[(1 + \lambda_e) \sigma_0, (1 - \lambda_e) \sigma_0] = 0 \quad (1.48)$$

λ_e can be evaluated using the following formula:

$$\lambda_e = \frac{1}{K_p + 1} \left[K_p - 1 + \frac{\sigma_c}{\sigma_0} \right] \quad (1.49)$$

The radius of plastic zone R_p can be determined:

$$\frac{R_p}{R} = \left[\frac{2\lambda_e}{(K_p + 1)\lambda_e - (K_p - 1)\lambda} \right]^{\frac{1}{K_p - 1}} \quad (1.50)$$

The displacement of the tunnel wall u can be obtained as:

$$\frac{2G}{\sigma_0} \frac{u}{R} = \lambda_e \left[F_1 + F_2 \left(\frac{R}{R_p} \right)^{K_p - 1} + F_3 \left(\frac{R_p}{R} \right)^{K_\psi + 1} \right] \quad (1.51)$$

where

$$F_1 = - (1 - 2\nu) \frac{K_p + 1}{K_p - 1} \quad (1.52)$$

$$F_2 = 2 \frac{1 + K_\psi K_p - \nu(K_p + 1)(K_\psi + 1)}{(K_p - 1)(K_\psi + K_p)} \quad (1.53)$$

$$F_3 = 2(1 - \nu) \frac{K_p + 1}{K_p + K_\psi} \quad (1.54)$$

with $K_p = \frac{1 + \sin \phi}{1 - \sin \phi}$ and $K_\psi = \frac{1 + \sin \psi}{1 - \sin \psi}$.

The characterized curve of rock mass can be then constructed:

$$\frac{2G}{\sigma_0} \frac{u}{R} = \begin{cases} \lambda & 0 \leq \lambda \leq \lambda_e \\ \lambda_e \left[F_1 + F_2 \left(\frac{R}{R_p} \right)^{K_p - 1} + F_3 \left(\frac{R_p}{R} \right)^{K_\psi + 1} \right] & \lambda_e \leq \lambda \leq 1 \end{cases} \quad (1.55)$$

SCC is obtained based on the support property. In an elastic support, the normal pressure p_s can be determined as a function of the normal stiffness K_s and the displacement at the tunnel wall at the time of

support installation u_d :

$$p_s = K_s \frac{u - u_d}{R} \quad (1.56)$$

$$K_s = \frac{2G_s(R_o^2 - R_i^2)}{(1 - 2\nu_s)R_o^2 + R_i^2} \quad (1.57)$$

In case of thin support, calculation of K_s can be simplified to:

$$K_s = \frac{E_s}{1 - \nu_s^2} \frac{e}{R} \quad (1.58)$$

By combining GRC and SCC, the final displacement at the tunnel wall and the loading on the support system can be calculated, which give an indication for support conception. In the classical convergence-confinement method, u_d of a supported tunnel is assumed to be equal to that of an unsupported tunnel without taking into account the stiffness of the support system, which cause errors in the evaluation of the loading on the support and the long-term convergence at the tunnel wall. Several improvements have been proposed to modify the value of u_d by resorting to the so-called implicit methods (Bernaud and Rousset, 1992, 1996; Nguyen-Minh and Guo, 1996).

Panet (1995) has also defined the stability number N as:

$$N = \frac{2\sigma_0}{\sigma_c} = \frac{2}{N_c} \quad (1.59)$$

which permits the evaluation of the tunnel face stability for three different levels (Figure 1.27):

- $N < 2$ the plastic zone appears after the tunnel face;
- $2 < N < 5$ intermediate case;
- $N > 5$ the tunnel face is totally in the plastic zone and the instability of the tunnel face may occur.

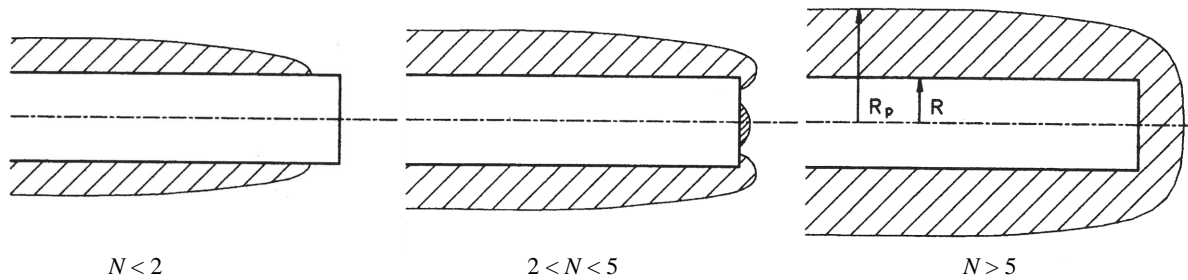


Figure 1.27: Prediction of plastic zone based on the stability number (Panet, 1995)

CHAPTER 2

SMP EXPLORATORY GALLERIES

Squeezing ground behavior has been observed during the excavation of SMP exploratory galleries due to the presence of productive Houiller in a Carboniferous formation. Several operational difficulties related to the excavation and support process have been encountered.

In this chapter, a general presentation of the field work of SMP survey project in a complex geological context is first given. Then, we focus on the applied excavation and support installation methods and on the in-situ monitoring process.

2.1 SMP field work

One of the objectives of the excavation of SMP exploratory galleries is to study the geological, hydrogeological and geotechnical conditions of the ground for the design of the Lyon-Turin base tunnel.

2.1.1 Lyon-Turin Link

In order to build up a more efficient connection of the European countries, the European Commission has launched the Trans-European Transport Network (Ten-T) project. The new Lyon-Turin railway link is highly strategic as it is a key element in the Mediterranean corridor (Figure 2.1), which connects southwestern, central and eastern Europe. The Lyon-Turin link is a 270 km long high-speed rail line project under construction between France and Italy. It contains a 57.5 km long base tunnel as its main part, 45 km in the French side and 12.5 km in the Italian side. It will cross the Alps from St-Jean-de-Maurienne in Savoy (France) to Susa Valley in Piedmont (Italy). The studies and preliminary works of the cross-border section of Lyon-Turin line were carried out by LTF (Lyon Turin Ferroviare) from October 2001 to February 2015; then, LTF was replaced by TELT (Tunnel Euralpin Lyon Turin) who is now responsible for the realization and operation of the cross-border section.



Figure 2.1: Lyon Turin link in Ten-T project (from latransalpine)

Since 1872, the Turin-Modane railway connects Lyon with Turin via the 13.7 km long Fréjus rail tunnel. However, the capability of the historical line is limited because of the poor profile of Fréjus tunnel: high elevation (1338 m), sharp curves and steep gradients (a maximum gradient of 30 ‰). The line is close to saturation and does not meet current international safety standards. In the context of growing traffic between France and Italy, the construction of the new Lyon-Turin railway link will allow to:

- provide faster transport thanks to its reduced gradients and much wider curves;
- transfer freight traffic across the Alps from trucks to rail in order to reduce energy costs, air pollution and CO₂ emissions.

The construction period of the Lyon-Turin base tunnel is estimated to be around 10 years. Several excavation faces are processing at the same time by using intermediate accesses (Figure 2.2): three of them are situated in the French side for a total length of about 9 km (Saint-Martin-la-Porte, La Praz and Villarodin-Bourget / Modane), and one of them is situated in the Italian side with a length of about 7.6 km (La Maddalena).

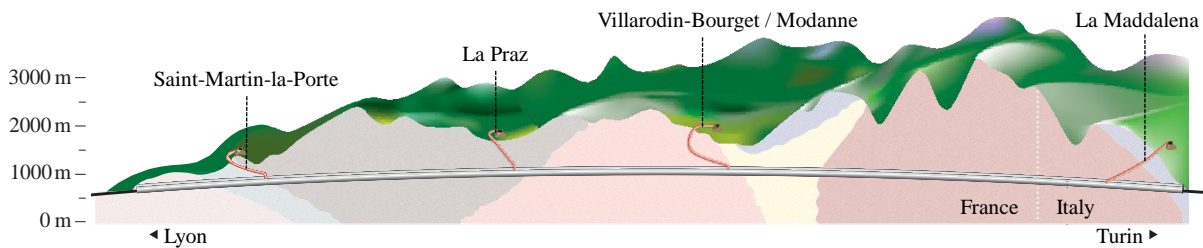


Figure 2.2: Access galleries to the Lyon-Turin base tunnel

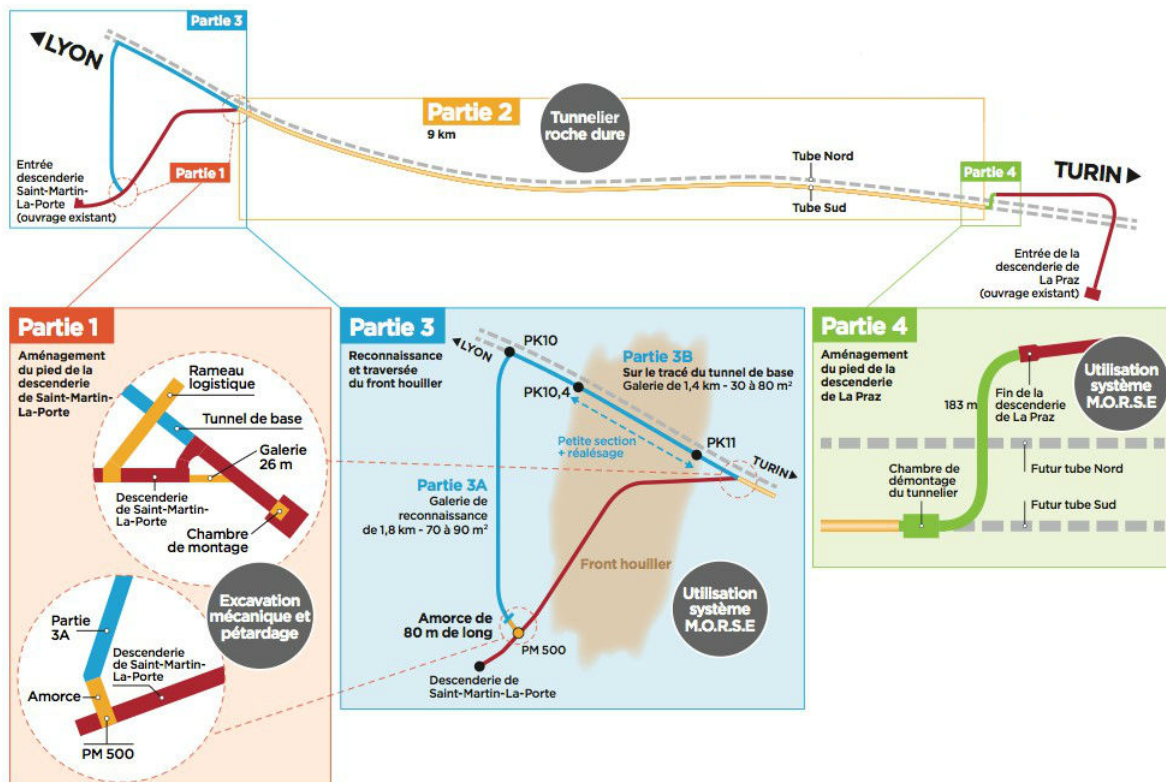


Figure 2.3: SMP survey project

During the excavation of the access gallery in Saint-Martin-la-Porte (SMP2), squeezing behavior has been encountered and caused operational problems in a Carboniferous formation. In order to study the geological context for the future based tunnel, which will cross the squeezing rock formation at a depth of near 600 m, a new survey project has been launched by TELT in May 2014 (Figure 2.3), including 4 parts:

- Part 1: development of the foot of Saint-Martin-La-Porte access gallery;
- Part 2: construction of a 9 km survey tunnel in the axis and with the diameter of the southern tube in hard rock. The TBM “Federica” started the excavation at the end of August 2016 and has completed it in September 2019;
- Part 3: excavation of a 1.8 km long complementary survey gallery to avoid Houiller formation, and excavation of another survey gallery across Houiller formation along the axis of the future tunnel (Figure 2.4);
- Part 4: development of the foot of La Praz access gallery.

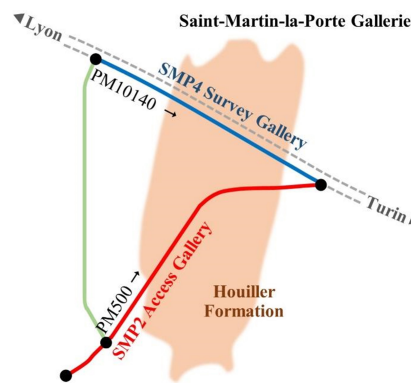


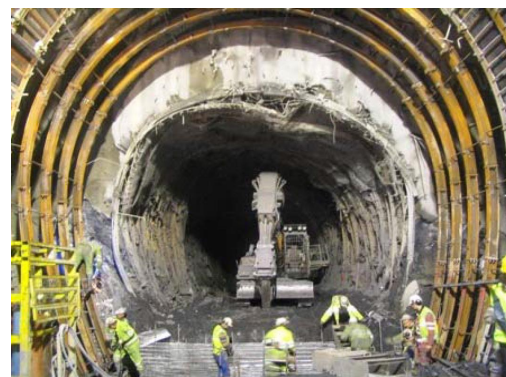
Figure 2.4: SMP exploratory galleries: SMP2 and SMP4

The excavation of SMP2 entered in the Houiller formation at a depth of more than 250 m from chainage 1250 m. Squeezing behavior has been observed during and after excavation (Figure 2.5), which is characterized by:

- metric radial convergences associated with a thick decompressed zone around the gallery;
- time-dependent behavior with difficulty to stabilize the deformation using conventional support profiles;
- anisotropic deformation with inclined orientation of large convergence.



(a) Large and anisotropic cross-section closure



(b) Failure of the support

Figure 2.5: Squeezing behavior observed in SMP2 (Mathieu, 2008; Barla et al., 2010)

Several studies have been carried out to analyze the squeezing ground behavior of SMP2, particularly on the time-dependent and anisotropic deformation and on the specific excavation and support method applied to overcome the operational problems (e.g. Barla et al., 2007; Rettighieri et al., 2008; Subrin et al., 2009; Russo et al., 2009; Barla et al., 2010; Vu, 2010; Barla et al., 2011, 2012; Tran-Manh, 2014; Monin et al., 2014; Descoeurdes et al., 2015). As SMP4 is crossing the same tectonized Houiller formation, squeezing behavior is also encountered.

2.1.2 Geological and geotechnical context

The geological and geotechnical context of Houiller formation encountered in SMP is very complex, and it has been carefully studied during the excavation of SMP2. Several formations not clearly separated are crossed by the two exploratory galleries and result in multiple geological phenomena (Barla et al., 2010; Vu et al., 2013).

As no reliable measurement of the initial stress state is available in the Houiller formation, it is assumed that the initial stress state is geostatic and isotropic in the following studies, with $\sigma_v = \sigma_H = \sigma_h = \gamma h$ and $\gamma = 27 \text{ kN/m}^3$ as shown in Table 2.1. Thus, the in-situ stress in Houiller formation is assumed to be 8.5 MPa for SMP2 and 16.2 MPa for SMP4. This is in accordance with the assumptions made by the project engineers in the design reports of these galleries.

Table 2.1: Assumption of the initial stress state in the Houiller formation

	SMP2	SMP4
Depth (m)	315 (300 - 330)	600
Initial stress state (MPa)	8.5	16.2

The productive Houiller met in the Carboniferous formation exhibits a very heterogeneous, stratified and fractured structure, consisting of schists or carboniferous schists (45–55 %), sandstone (40–50 %) and also a significant proportion of cataclastic rocks (up to 15 %) (Barla et al., 2010). Heterogeneity of the rock mass is present in both longitudinal and cross-section directions.

For the Carboniferous formation encountered in SMP2, the average value of the RQD is about 45% and the average value of the RMR is about 35-40, which corresponds to poor quality rock (Barla et al., 2010). The quality index obtained after measuring wave speeds in ground at different depths shows an average to very high fractured degree.

As the Houiller formation is very heterogeneous and fractured containing different kinds of rocks, laboratory tests can not be carried out to study the behavior of Houiller. Typical properties of the “intact” rock mass have been evaluated from samples taken from the tunnel face by Barla et al. (2007). For the weak rock components (coal, shales and cataclastic rock), these authors have determined the Hoek and Brown parameters:

- strength under uniaxial compression test $\sigma_{ci} = 15.3 \text{ MPa}$;
- $m_i = 8.97$.

The short-term GSI value is in the range of 20–30.

Based on GSI value, the uniaxial strength of the rock mass σ_{cm} is very low (between 1.2 to 1.6 MPa).

The stability factor N_c (Muir Wood, 1972) is defined as:

$$N_c = \frac{\sigma_{cm}}{\gamma H} = 0.17 \sim 0.24 \quad (2.1)$$

On the basis of the semi-empirical approach to identify the squeezing, the squeezing potential of the Houiller formation encountered in SMP2 is very high.

The stability number N (Panet, 1995) can also be determined:

$$N = \frac{2\sigma_0}{\sigma_c} = 8.3 \sim 11.8 \gg 5 \quad (2.2)$$

which indicates very poor rock mass conditions and possible occurrence of instability of the tunnel. Thus, the squeezing potential of the Houiller formation encountered in SMP2 is very high.

During excavation work, a number of continuous measurements have been performed to follow the water flow. In general, no significant water flow is remarked: the observed flow rate is very low. The tunnel faces are general slightly wet and several faces in Houiller are totally dry as the permeability of the Carboniferous formation is very low.

2.2 Excavation and support methods

The galleries are excavated by the conventional method, locally by drill and blast and mainly using mechanical shovels and hydraulic hammers in the Houiller zone. Because of the operational difficulties induced by the squeezing condition and the necessary specific excavation and support system, the tunnel face advances slowly in the Carboniferous formation.

2.2.1 Applied yielding support system

In order to accommodate larger convergence and stabilize the deformation around the tunnel wall under squeezing condition encountered in SMP, yielding support system has been adopted in the zones of high deformation generally, following three stages (Bonini and Barla, 2012):

- Stage 1: After reinforcement of tunnel core with bolts, the section is excavated and a flexible support is placed immediately behind the tunnel face. This support consists of a layer of fiber-reinforced shotcrete, reinforced with a welded safety mesh on the intrados, bolts around the tunnel wall, a steel rib with sliding joints (TH type) every meter;
- Stage 2: A yielding support is then placed. It consists of a shotcrete layer and a number of high compressible elements between the steel ribs installed in Stage 1;
- Stage 3: The final lining was installed when the convergence rate became small enough (few millimeters per day), which blocks totally the deformation.

The most commonly used compressible elements in SMP are the high deformable concrete (HiDCon) blocks of Solexperts (Figure 2.6a). These blocks are composed of high strength concrete matrix with porous aggregates reinforced with steel fibers, stirrups, rings and plates. The pores close successively with prevention of lateral strain under loading. After exceeding the elastic range, a practically constant load can be resisted up to a compression range of around 50 % to 60 % of the original element height (Figure 2.6b). Once the compression limit of the elements is exhausted, the support system will exhibit normal shotcrete characteristics. The dimensions of these elements are 40 cm high, 80 cm long and 20

cm thick. The number and the position of the compressible blocks are adjusted along the gallery to adapt to the observed convergence.

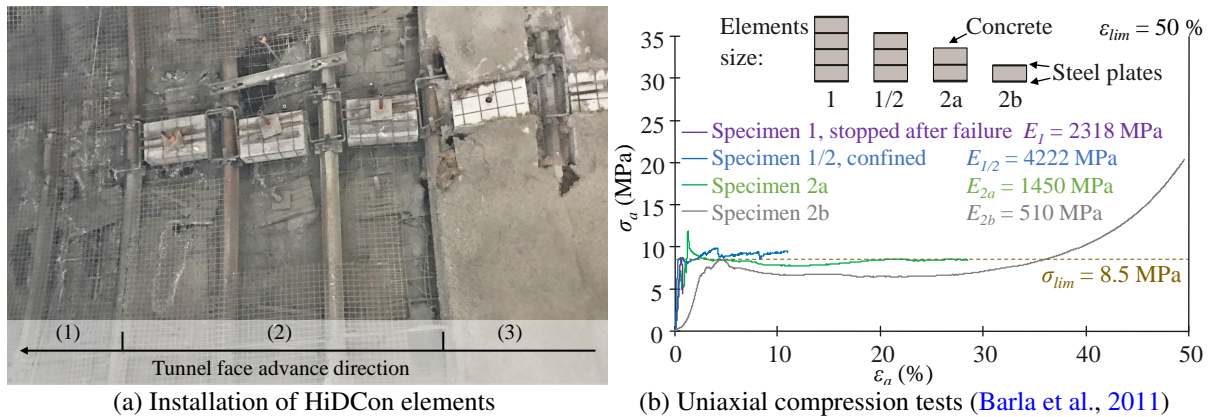


Figure 2.6: Application and mechanical properties of HiDCon elements of Solexperts used in SMP

In addition to HiDCon elements, lining stress controllers (LSC) have also been used in a part of SMP4 in order to test their efficiency (Figure 2.7).

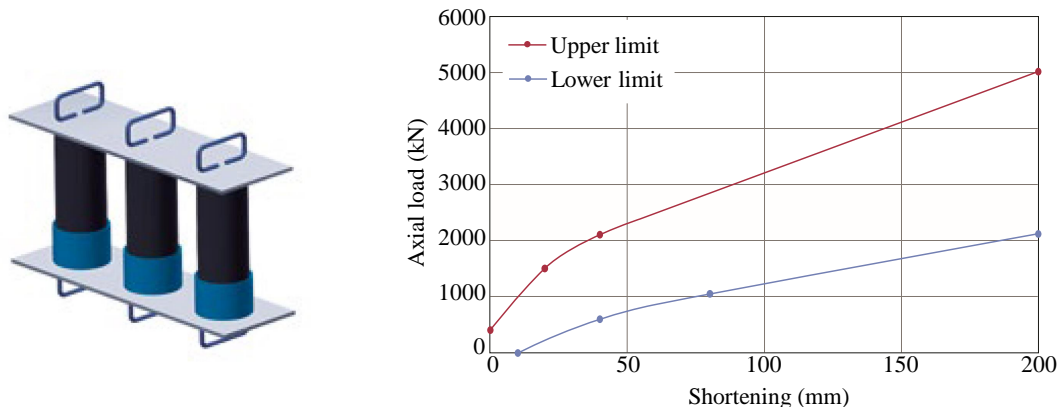


Figure 2.7: Technical characteristics of LSC elements (from DSI Underground)

LSC steel elements (provided by DSI Underground) allow to:

- Maintain the loading on the support, optimize the use of the primary lining and control stress release and deformability to avoid excessive overstressing on the tunnel support;
- Quickly increase the support strength in slowly increasing deformations and provide steady increase of the support strength while undergoing large deformations.

In a LSC element, single yielding elements are aligned between base plates. These plates fix the position of the yielding elements and limit LSC elements towards the tunnel lining. Each yielding element has a factory-set imperfection where controlled deformations start in case of excessive loading. Load-deformation characteristics of the LSC system with three yielding elements (type 3) are defined with upper and lower limits as shown in Figure 2.7.

2.2.2 Tunneling of SMP2

SMP2 was first excavated from Vallée de l'Arc in 2003 and was completed in July 2010 with a final length of 2.33 km up to the depth of the base tunnel. The objectives of SMP2 can be described for three stages (Triclot et al., 2007):

- before excavation of the base tunnel: SMP2 can help to obtain information about the excavation conditions until several-hundred meters depth, in particular, variety of rock mass around the future tunnel like structural, geological and geotechnical context. It contributes to define the excavation and support method and prepare for the expected technical difficulties.
- during excavation of the base tunnel: SMP2 offers intermediate faces for excavation. It allows to access to the underground working field and provides ventilation.
- after excavation of the base tunnel: it will serve as an emergency and maintenance access as well as for ventilation and smoke evacuation of the final structure.

The ground exhibited high heterogeneity from the entrance (Figure 2.8). The proposed initial direction of SMP2 was perpendicular to the axis of the Lyon-Turin base tunnel. Because of the presence of tectonized Carboniferous formation from the Houiller front at chainage 800 m the gallery was reoriented from chainage 1450 m (see Figure 2.3).

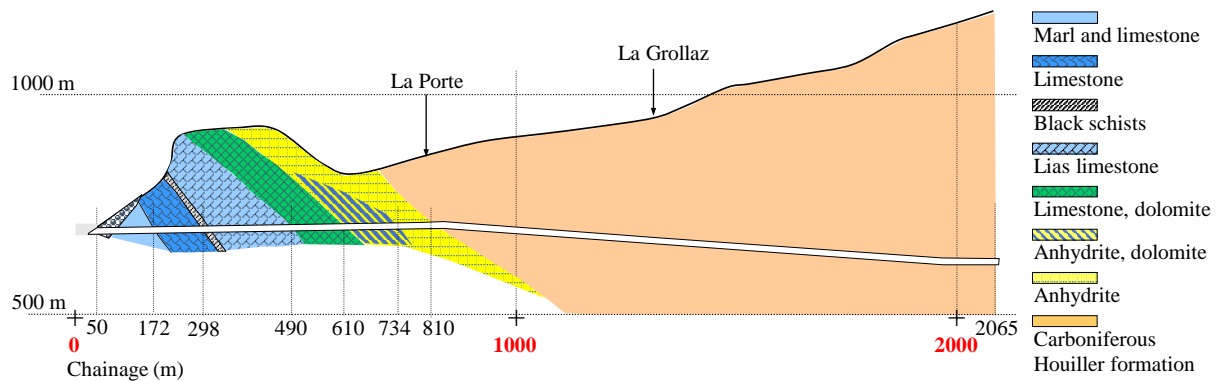
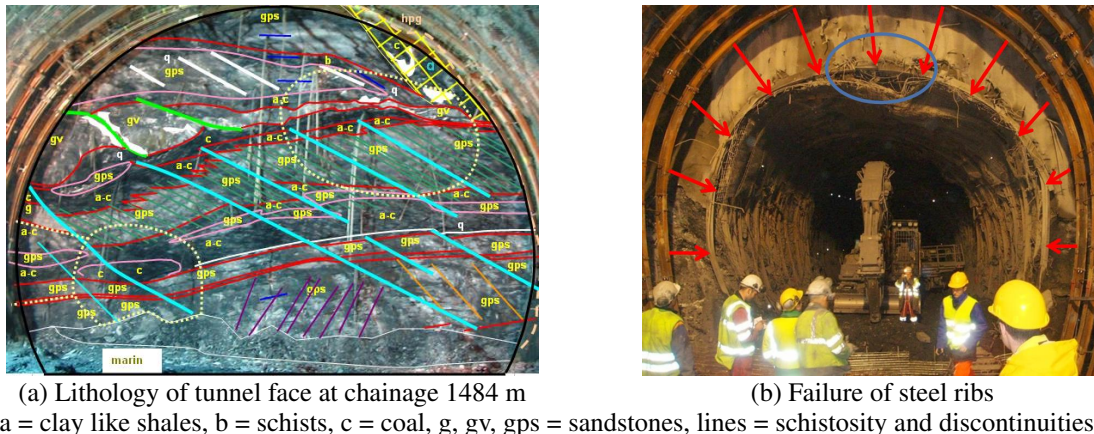


Figure 2.8: Geological context of SMP2

The heterogeneity of rock mass is illustrated in Figure 2.9a showing one example of the geological survey as recorded at the tunnel face. This section at chainage 1484 m presents different kinds of rock mass and several fractures (Mathieu, 2008). Schists, coal and sandstone appear alternately with a significant degree of discontinuities. Because of the poor mechanical properties of ground and the material heterogeneity, large and anisotropic closure occurs, which lead to failure of the support in the zone of large deformation (Figure 2.9b).



(a = clay like shales, b = schists, c = coal, g, gv, gps = sandstones, lines = schistosity and discontinuities, etc.)

Figure 2.9: Tunnel face lithology and support failure observed in SMP2 (chainage 1484 m) (Mathieu, 2008)

Figure 2.10 shows the excavation progress of SMP2. Tunnel face advance got much slower when the excavation entered in Houiller formation near chainage 810 m. The observed squeezing behavior delayed greatly the field work.

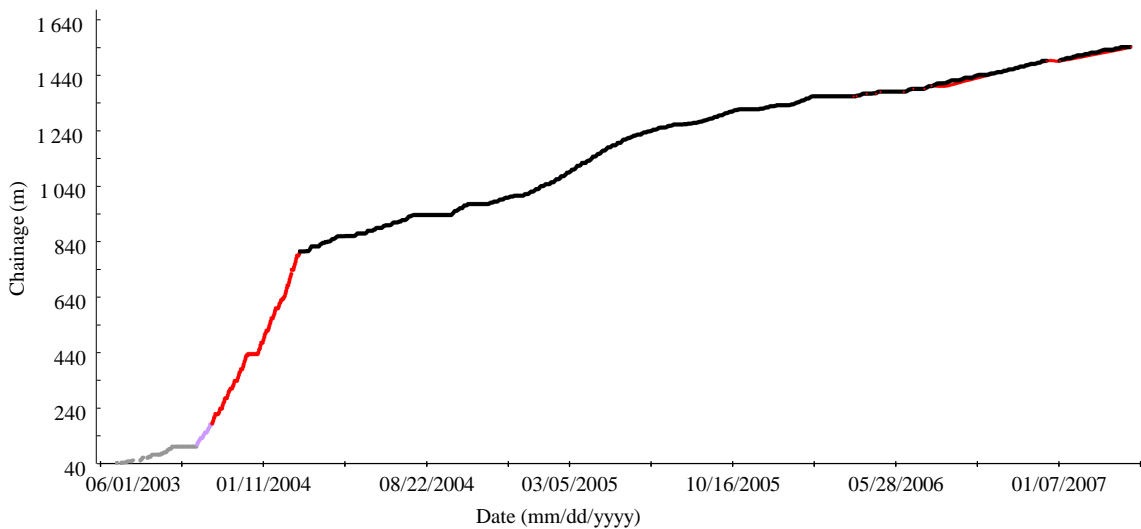


Figure 2.10: Tunnel face advance of SMP2

The support profiles were adapted to the ground properties and were changed for different parts of SMP2. In the zones of large convergence, yielding support system began to be applied after a transition zone:

- from chainage 1267 to 1324 m: P7-3 support system was used (Figure 2.11a);
- from chainage 1325 to 1384 m: In this transition zone, P7-3 support system was first installed. As the convergence was much larger than expected, reprofiling was carried out to reopen the section and the support system P7-3 was replaced by DSMxx containing yielding elements (Figure 2.11b);
- from chainage 1385 m: DSMxx system was used with eight HiDCon elements;
- from chainage 1440 m: Another HiDCon element was added in the invert.

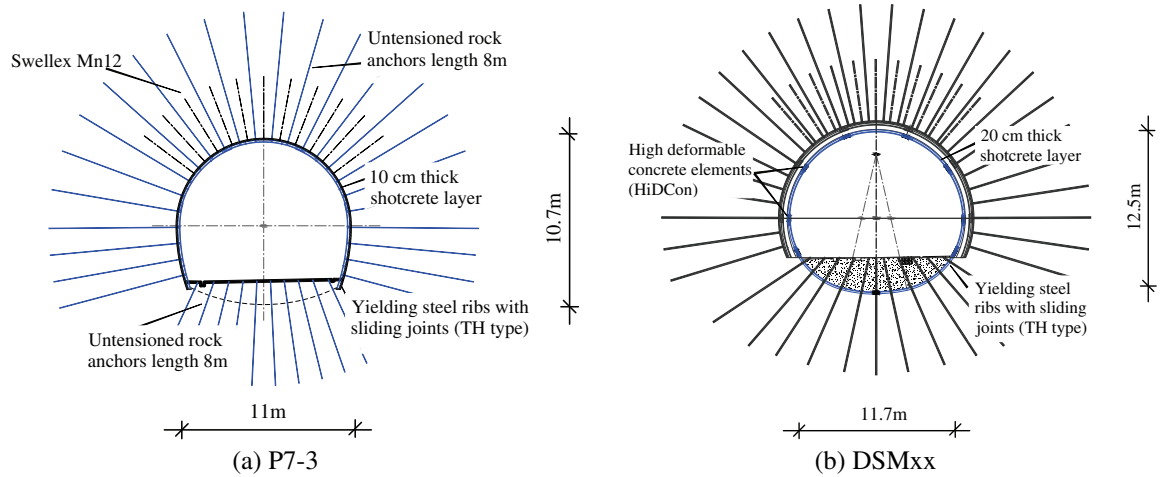


Figure 2.11: Profiles of support systems used in SMP2 from chainage 1267 m (Bonini and Barla, 2012)

2.2.3 Tunneling of SMP4

SMP4 is being excavated with conventional technique since 2017 from West to East along the axis of the Southern tube of base tunnel at a depth of about 600 m (Figure 2.12). It crosses the same squeezing formation as SMP2 from chainage 10267 m. Excavation of SMP4 allows to study the rock mass properties in the axis of the future base tunnel. Different parts of SMP4 with different excavation and support profiles are presented in the following.

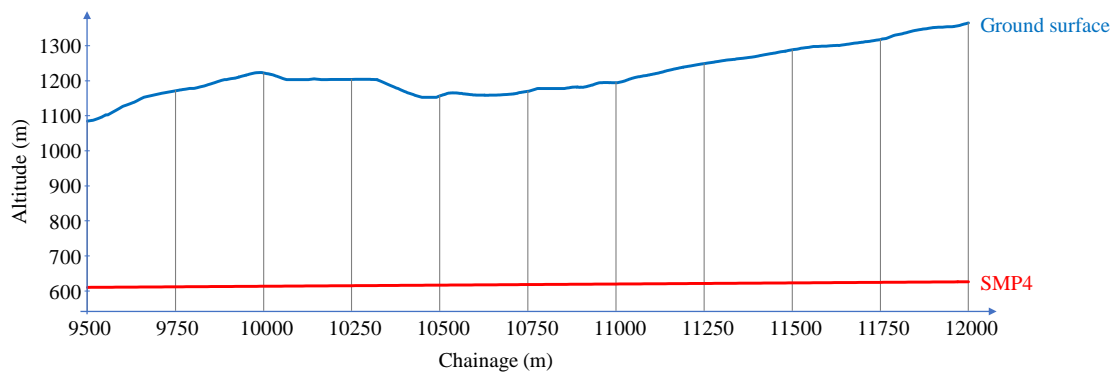


Figure 2.12: Overburden of SMP4

SMP4-GS

Tunneling works of SMP4 started with a full-face excavation (SMP4-GS) from West to East. The diameter of the excavated section is about 13 m and the rate of excavation is low, from 0.5 m/day to 0.7 m/day (Figure 2.13).

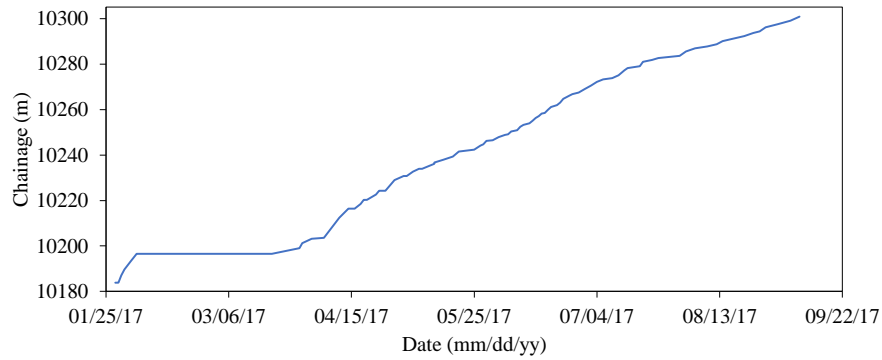


Figure 2.13: Tunnel face advance of SMP4-GS

The ground is highly heterogeneous in both longitudinal and cross-section directions (Figure 2.14). The top side of the tunnel entered in the Houiller area at chainage 10267 m. From chainage 10267 to 10287 m, the Houiller is present in the upper part of the section whereas a layer of anhydrite is located in the lower part of the section. The encountered anhydrite is much stiffer than the Houiller. As the tunnel face advances, the proportion of anhydrite is lower and lower. The full section was in the Houiller formation from chainage 10287 m.

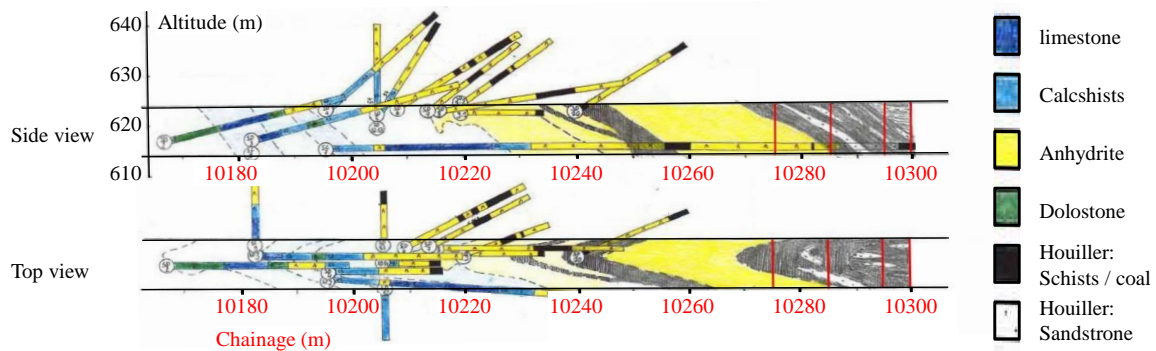
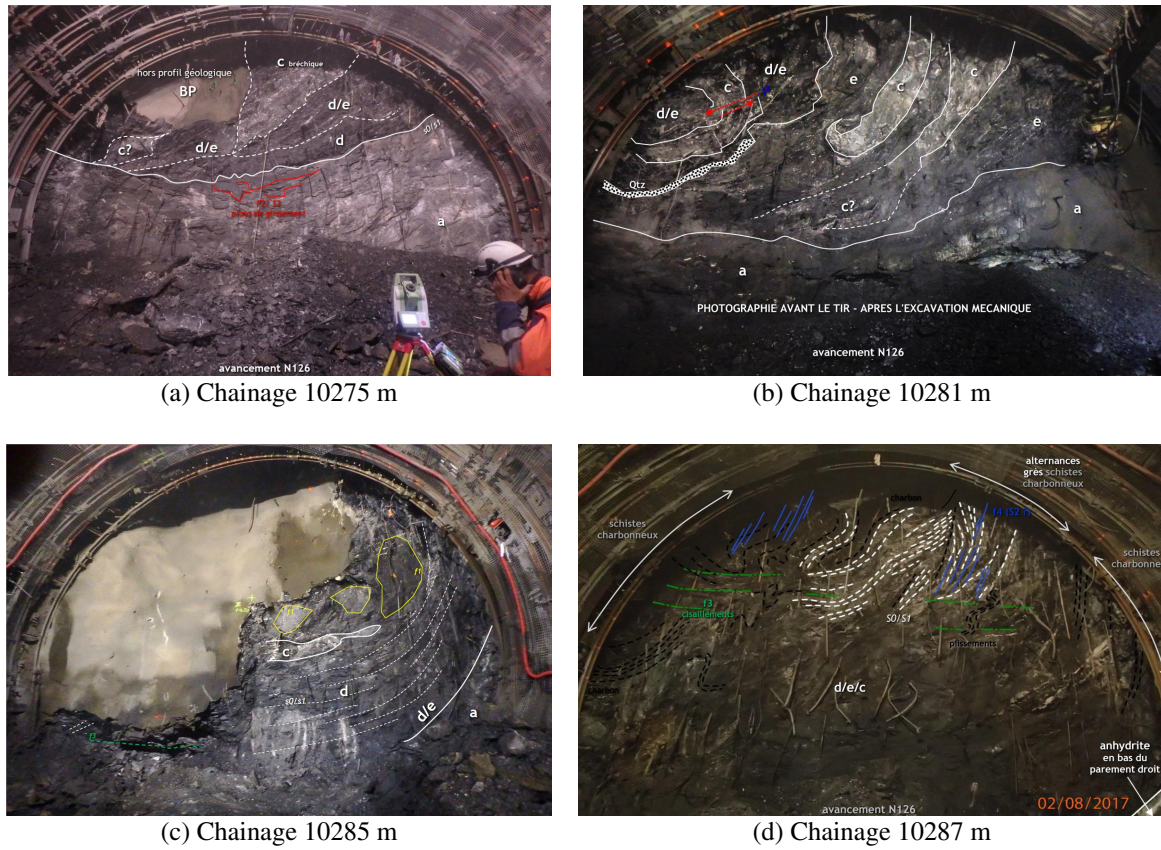


Figure 2.14: Lithology plane of SMP4-GS

The heterogeneity of rock mass and the variation of the proportion of Houiller and of anhydrite can also be observed on the tunnel face, as shown in Figure 2.15.



Lithology: a Anhydrite; c Sandstone; d Coal; e Carboniferous schists

Figure 2.15: Geological survey of the tunnel face of various sections in SMP4-GS

The yielding support applied in SMP4-GS contains 8 or 10 HiDCon elements for the zones located in Houiller formation (Figure 2.16). Final concrete lining had not been installed before the collapse of tunnel face near chainage 10303 m.

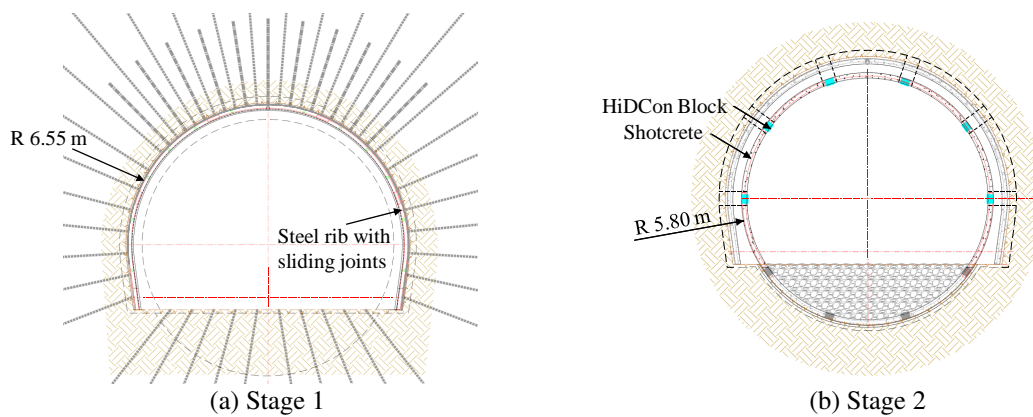


Figure 2.16: Support system applied in SMP4-GS

Tunnel face collapse

The tunnel face collapsed on September 8, 2017 near chainage 10303 m because of the presence of a fault zone (Figure 2.17). Before collapse, the ground around the tunnel wall has been reinforced by bolts

and the tunnel face was reinforced by shotcrete. The steel ribs have been installed near tunnel face as flexible support, and the yield-control support was installed at 25 m from tunnel face. The convergence rate of cross-sections became larger and larger. The collapse of tunnel face occurred first (Figure 2.17a), and then the TH type steel ribs with sliding joints from chainage 10298 to 10300 m were destroyed later (Figure 2.17b).

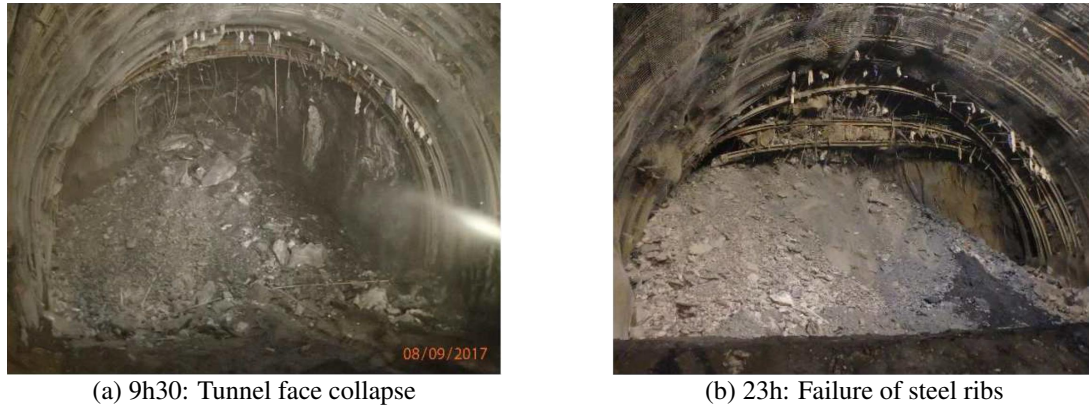


Figure 2.17: Tunnel face collapse occurred near chainage 10303 m

In order to cross the collapsed zone, the excavated part of SMP4 was filled from chainage 10275 m and the following procedure of excavation was performed (Figure 2.18):

- excavation of a small size gallery (GTE) with $R_{GTE} \approx 2.3$ m in the upper part of the tunnel to reinforce the rock mass in the collapsed zone from chainage 10275 to 10310 m;
- GTE was followed by an axial survey gallery (GRA) with $R_{GRA} \approx 2.3$ m from chainage 10310 to 10330 m to study the rock mass properties. Rigid support system is used for GTE and GRA, and they were filled later with concrete and foam;
- excavation with a reduced size section (SR) with $R_{SR} \approx 4.36$ m from chainage 10275 to 10310 m;
- excavation with a small size section (PS) with $R_{PS} \approx 3.15$ m from chainage 10310 to 10410 m;
- reprofiling SR to full size section (RSR) with $R_{RSR} \approx 6.5$ m from chainage 10275 to 10310 m;
- reprofiling PS to full size section (RPS) with $R_{RPS} \approx 6.5$ m from chainage 10310 to 10410 m.

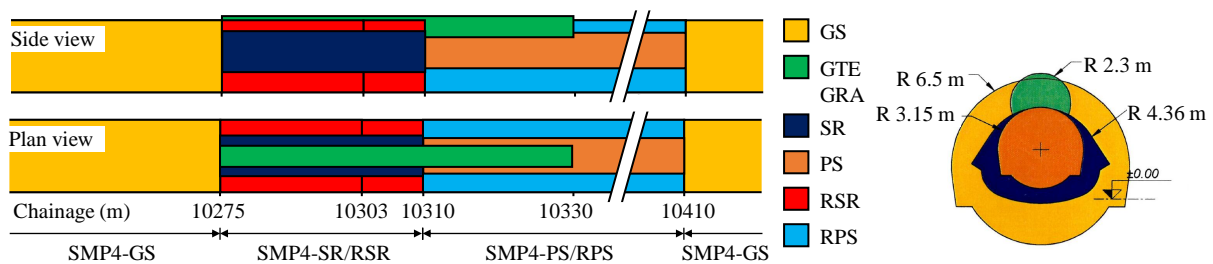


Figure 2.18: Different steps to cross the collapsed zone

The portion of SMP4 from chainage 10275 to 10310 m is not studied in the present work, as the excavation and back-fill process of this part is complex, and that the surrounding rock mass is highly reinforced to cross the fault zone, which represents no longer the nature of ground.

The studies of SMP4-PS and RPS do not consider specifically SMP4-GRA, because the surrounding ground material is various and highly heterogeneous, the back-fill of SMP4-GRA can be consider as another kind of material. Its impact is taken into account in the homogenization process of the analyses.

SMP4-PS

SMP4-PS is excavated from chainage 10310 to 10410 m with an equivalent radius of tunnel section about 3.15 m to ensure the security of field work and propose solution for operational problems. The rock mass is very heterogeneous on this stretch and several discontinuity planes are present (Figure 2.19). Four zones can be identified according to the composition of rock mass:

- zone 1 from chainage 10310 to 10337 m: very high proportion of Carboniferous shales/coal;
- zone 2 from chainage 10337 to 10365 m: low proportion of Carboniferous shales/coal;
- zone 3 from chainage 10365 to 10392 m: high proportion of Carboniferous shales/coal;
- zone 4 from chainage 10392 to 10410 m: low proportion of Carboniferous shales/coal.

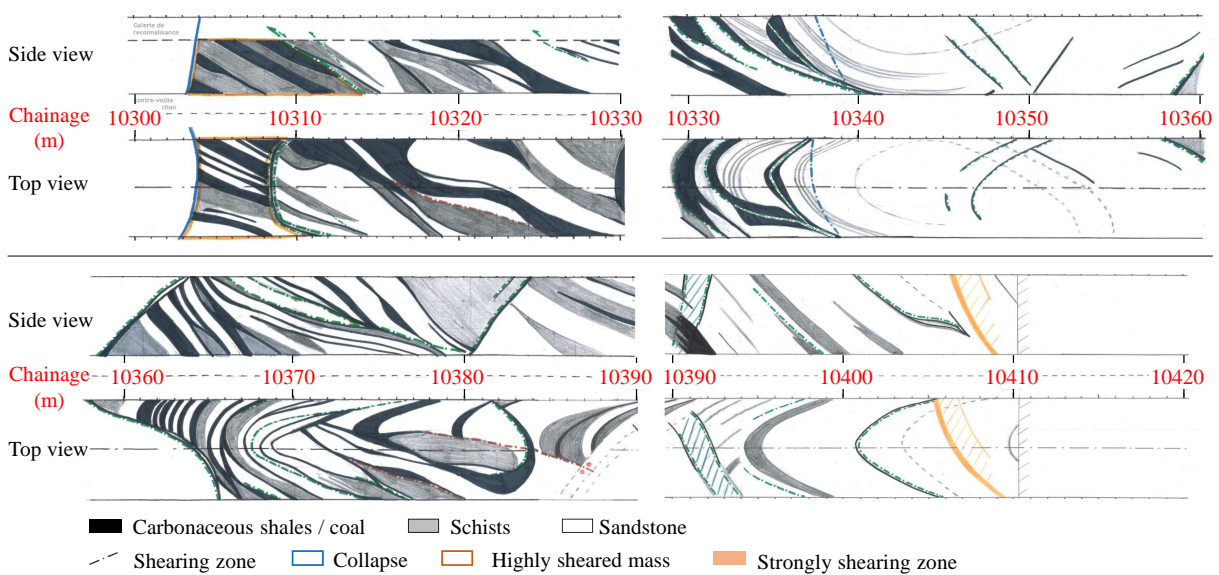
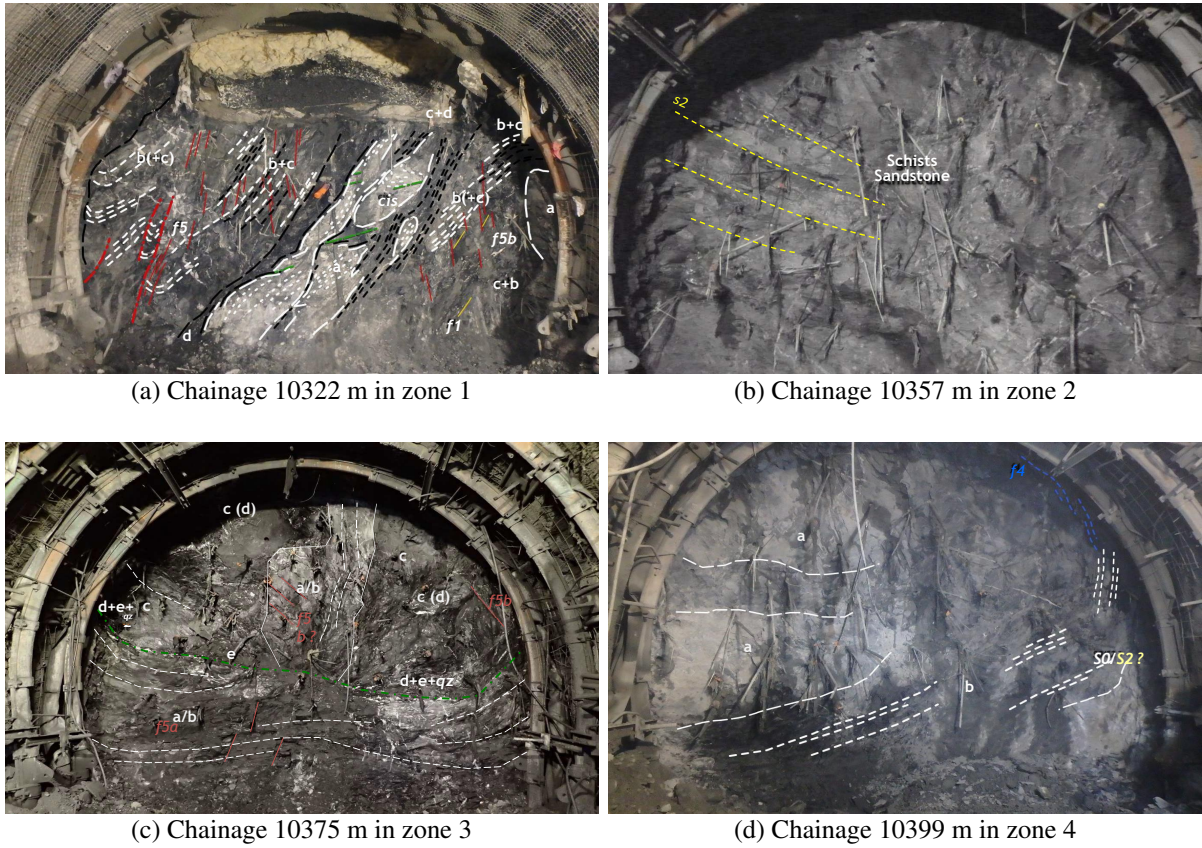


Figure 2.19: Longitudinal map of the lithology SMP4-PS

The heterogeneity of rock mass is also shown on the tunnel face. Figure 2.20 shows the tunnel face lithology in four different zones. The filled GRA can be seen at the vault of the tunnel face at chainage 10322 m. The distribution of the Houiller in zones 1 and 3 is complex and one dominant direction of stratification cannot be identified.



Lithology: a = Sandstone; b = Schists; c = Black Schists; d,e = Carbonaceous schists / Coal

Figure 2.20: Geological survey of the tunnel face of various sections in SMP4-PS

The excavation of SMP4-PS began on July 3, 2018 and was completed in 150 days (Figure 2.21). The tunnel face advanced regularly with an excavation rate of about 0.6 m/day. The temporary support system (Stage 2) was installed at about 12 m from the tunnel face. No final lining was installed in SMP4-PS as this part would be enlarged to full size later.

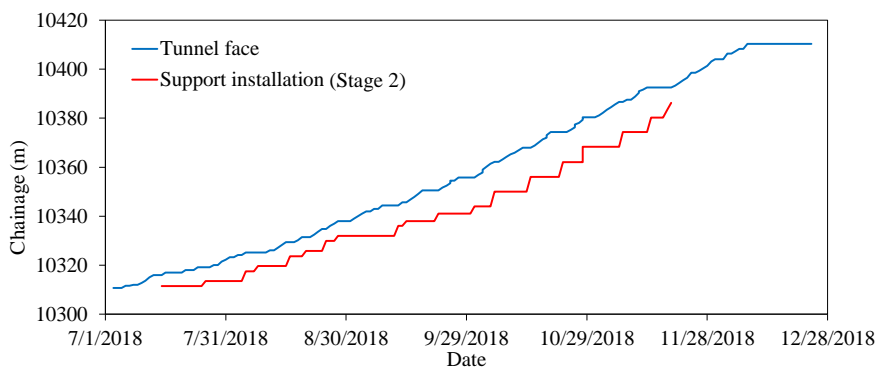


Figure 2.21: Tunnel face advance of SMP4-PS

The yielding support system used in SMP4-PS is presented in Figure 2.22. Four to eight HiDCon elements are installed depending on the amount of deformation.

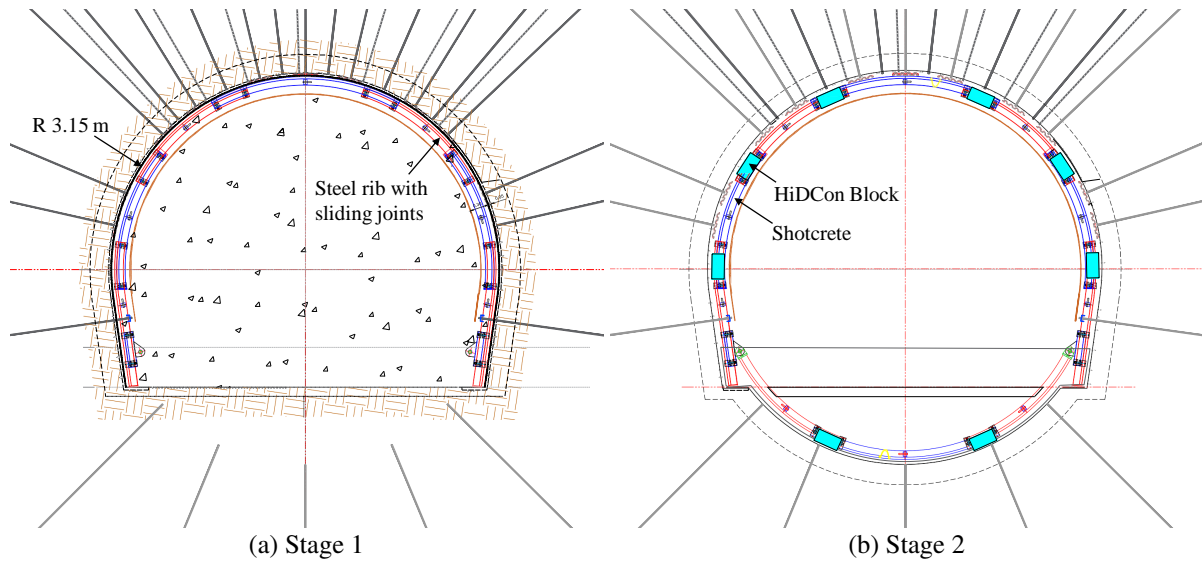


Figure 2.22: Support system applied in SMP4-PS

SMP4-RPS

SMP4-PS was then enlarged to full size section (SMP4-RPS). The rock mass is highly heterogeneous in SMP4-RPS as can be seen in Figure 2.23. It is noted that the legends in Figure 2.23 are different from that in Figure 2.19 for SMP4-PS. The proportion of the Carboniferous shales/coal becomes lower and lower from West to East with tunnel face advancing.

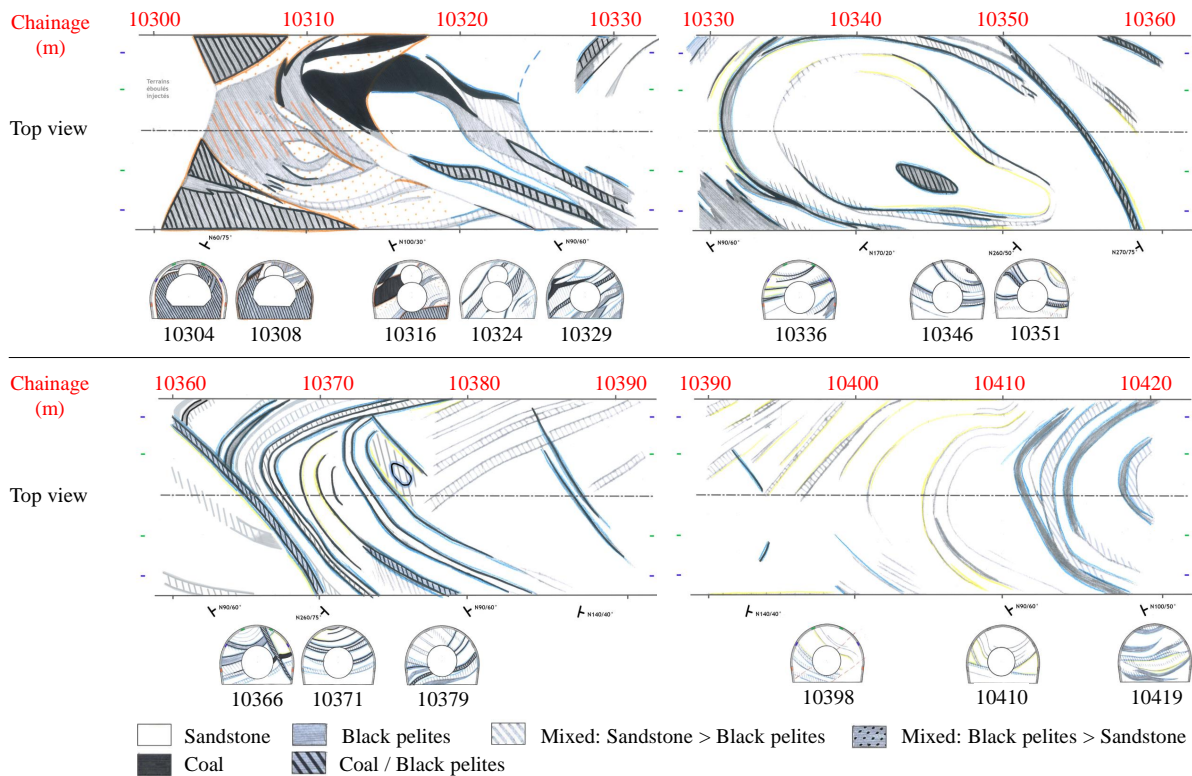


Figure 2.23: Geological survey at the tunnel face and lithology map in the longitudinal direction in SMP4-RPS

The material heterogeneity is remarkable in the cross-section direction. Location of SMP4-PS can be seen in the geological survey at the tunnel face of SMP4-RPS. The information about the lithology of SMP4-PS does not allow to imagine the lithology of SMP4-RPS. As for SMP4-PS a dominant direction of stratification cannot be identified due to the complexity of the distribution of the various materials and discontinuities.

The excavation rate of SMP4-RPS was about 0.75 m/day (Figure 2.24). The support system (Stage 2) was first installed at 5 m from the tunnel face until chainage 10330, and then at 30 m because of lower convergence of the tunnel section. The information of support installation is available until chainage 10351 m.

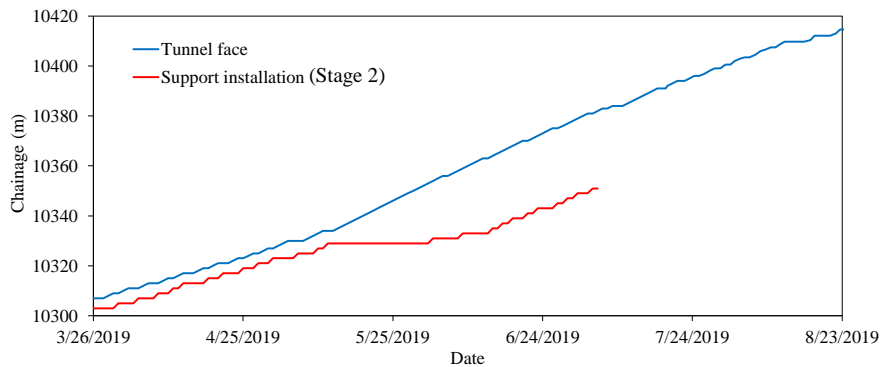


Figure 2.24: Tunnel face advance of SMP4-RPS

The excavation and support system are shown in Figure 2.25b.

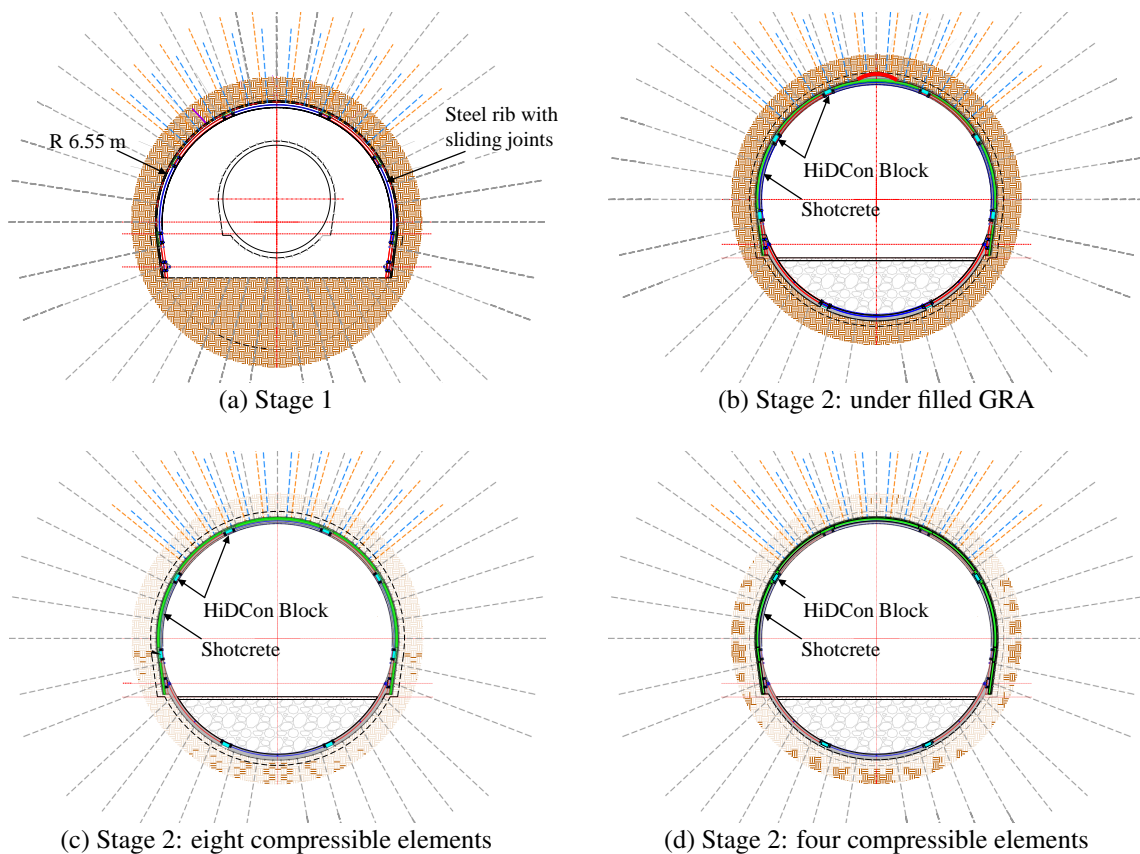


Figure 2.25: Support systems applied in SMP4-RPS

The Final lining will be installed in the future when the convergence rate becomes sufficiently small. The information on the design of the final lining is not yet available. The profile of yielding support system changes according to the different sections:

- from chainage 10310 to 10330 m: presence of filled GRA, eight HiDCon elements (Figure 2.25b);
- from chainage 10330 to 10355 m: eight HiDCon elements (Figure 2.25c);
- from chainage 10355 to 10385 m: eight LSC elements (Figure 2.25c);
- from chainage 10385 to 10402 m: eight HiDCon elements (Figure 2.25c);
- from chainage 10402 to 10410 m: four HiDCon elements (Figure 2.25d).

Summary

Because of the high heterogeneity presenting in both longitudinal and cross-section directions, difficulties have been encountered in interpreting the geological survey data. The variety of the rock mass material and the discontinuity of the mechanical characteristics cannot be accurately taken into account: the spatial distribution of different materials is complex and the mechanical properties of all the existing materials are not identified. The homogenization process is necessary for the studies of the highly heterogeneous zones of the galleries.

2.3 Monitoring

Observation and monitoring are important during tunneling for the following objectives (Barla, 2001; AFTES, 2005):

- evaluate the long-term stability of the tunnel face and around the tunnel wall;
- extrapolate observed behavior to sections to be excavated;
- adapt support system or change excavation technique;
- provide factual documentation of tunnel performance as a function of rock conditions and adopted construction methods;
- provide valuable data for interpretation and back analysis in order to clarify design assumptions and improve constitutive models for rock mass and the interactions between the rock and the support structure.

The monitoring in conventional tunneling is carried out mainly on ground deformation (convergence measurement of cross-section, radial extension around the tunnel and extrusion of the tunnel face) and stress in support system (stress in shotcrete support or in concrete ring measured with strain gauges).

The excavation of SMP galleries is associated with extensive geological survey and monitoring of the ground deformation and the stress in the support system in order to adjust the excavation and support method based on the local ground response. Several monitoring processes of SMP2 have been presented in the previous theses (Vu, 2010; Tran-Manh, 2014).

2.3.1 Convergence of tunnel cross-section

Convergence measurement at the tunnel wall is the most common monitoring applied in tunneling works as it gives a direct vision of the cross-section closure.

By following the displacements of the monitoring points and the evolution of the distance between

two points (Figure 2.26), convergence measurements of a given section can be carried out for different periods of construction:

- before construction: the convergence of a survey gallery helps to understand the ground behavior;
- during construction: the performance of the support system can be checked and adjusted;
- after construction: it provides hint on the long-term response of the tunnel.

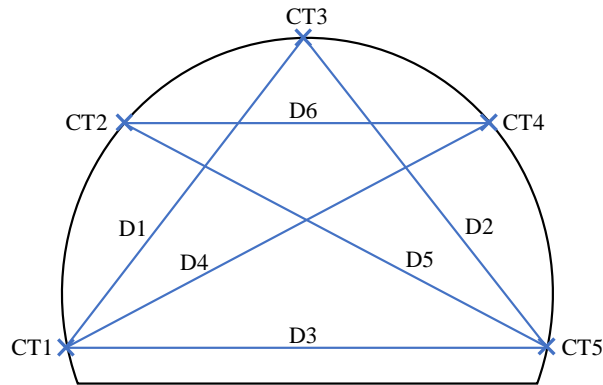


Figure 2.26: Example of convergence measurement by five monitoring targets

In SMP4 exploratory galleries, total station of Leica TS15 type has been used for convergence measurements. Five to seven measuring points have been installed every 5 m to follow the cross-section convergence (Figure 2.27). The targets can be installed on the tunnel wall (T), on the head of bolts (B) and on the steel ribs with sliding joints (C). Convergence measurements were carried out by following the horizontal, vertical and axial displacements of monitoring points.

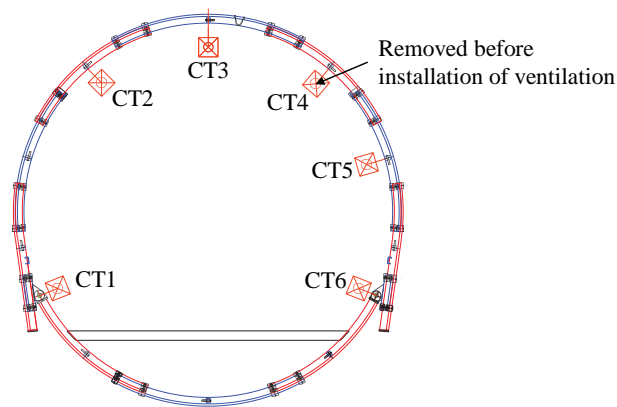


Figure 2.27: Example of monitoring targets installed in SMP4-PS

The convergence of tunnel cross-section $C(t)$ is defined as the evolution of the distance between two monitoring targets on time t :

$$C(t) = D_0 - D(t) \quad (2.3)$$

with

- D_0 initial distance between two targets (when the first measurement);
- $D(t)$ distance between two targets for a given time t .

As described by [Sulem \(1983\)](#), the tunnel convergence is influenced by the tunnel face advance and

the time-dependent behavior of the rock mass. The tunnel face advance has more effect when it is close to the section under study. If the tunnel face is far enough, the convergence depends mainly on the time-dependent behavior of the ground.

2.3.2 Extrusion of tunnel core

By installing extensometers before the tunnel face, the extrusion in axial direction of the tunnel core can be followed during excavation. The extrusion becomes higher and higher when the tunnel face approaches. This technique helps to control the tunnel face stability. For example, in SMP4-PS, the extrusion of the tunnel core is measured for several sections using Modular Reverse-Head Extensometer provided by Solexperts (Figure 2.28).

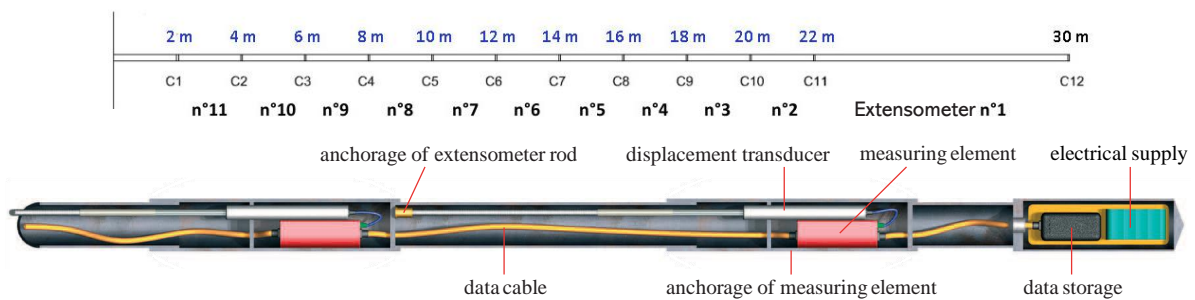


Figure 2.28: Measurement of extrusion of tunnel core in SMP4-PS

The system consists of a series of connected simple extensometers. In the case of a small borehole diameter, this set-up facilitates the arrangement of a large number of measuring points. The continuous measurement is guaranteed, despite the tunnel advance and a stepwise reduction of the number of measuring points. The measured values of the individual displacement transducers are stored at selected time intervals.

2.3.3 Extension around tunnel wall and stress in rock-bolts

The displacement measurement in the rock mass around the tunnel wall is carried out using multi-point extensometers. The relative displacement between two points in a borehole along its axial direction is determined. This technique helps to identify the evolution of the yielded zone. A single borehole can have from 3 to 6 bases and the distance between the continuous bases is 3 meters. In SMP4-GS, the displacements of ground (for example, at chainage 10281 m) are recorded (Figure 2.29).

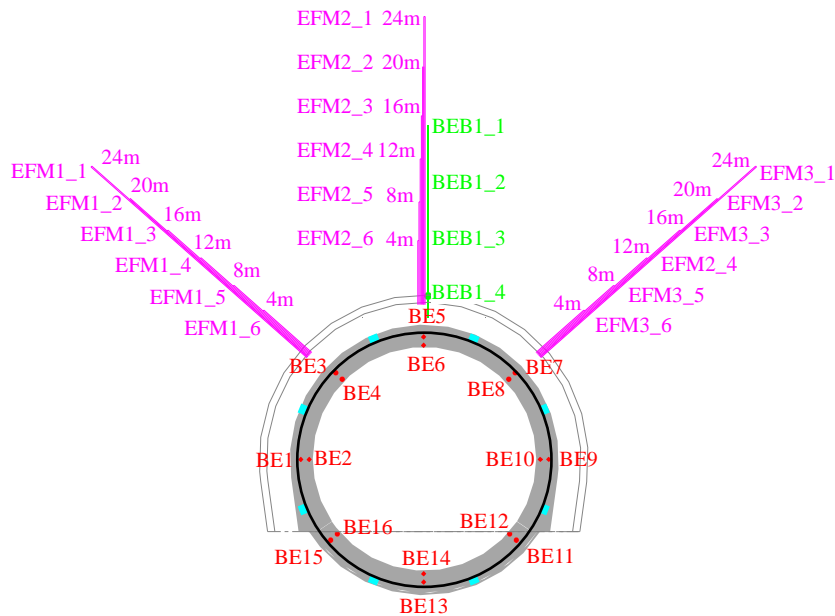


Figure 2.29: Displacement recording by extensometers in SMP4-GS of ground at chainage 10281 m

Multipoint borehole extensometer (MPBX) with stainless steel rods provided by SISGEO (EFM) are used for the measurements of the ground deformation (Figure 2.30). MPBX is designed to monitor changes in the distance between downhole anchors, each set at a specified depth in the borehole, and a measurement head at the surface. Rods extend upward from the anchors to the head, where measurements are made with a depth micrometer or displacement transducers.

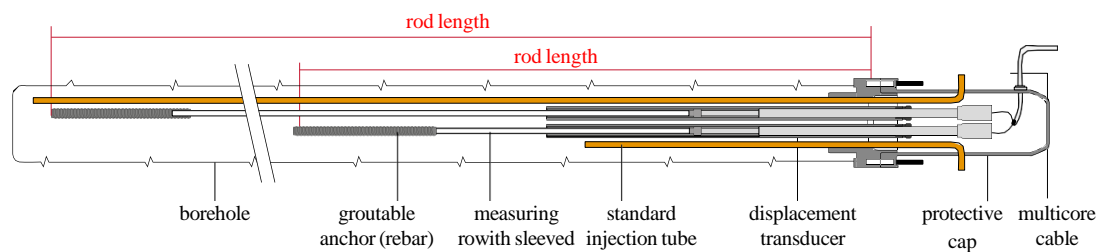


Figure 2.30: Multipoint borehole extensometer

The stress in the rock-bolts are followed with vibrating wire spot-weldable strain gauges provided by SISGEO (BEB) (Figure 2.31). It is designed to measure strain on steel-structure surface with the following characteristics: 64.7 mm long, measurement range up to $1500 \mu\epsilon$ and with a sensibility of $1 \mu\epsilon$. The gauge consists of a steel wire tensioned between two plates which can be either spot-welded or epoxy bonded to the surface in question.

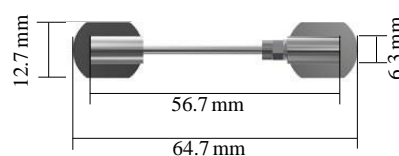


Figure 2.31: Vibrating wire strain gauge

2.3.4 Stress in final lining

Vibrating wire strain gauges provided by SISGEO (BE) (Figure 2.32) are used to measure the strain in concrete structures like shotcrete in the support system and concrete ring as final lining. It has the same measurement range and sensibility as BEB but longer (165 mm). The measurements are used to calculate structural loads or stresses.

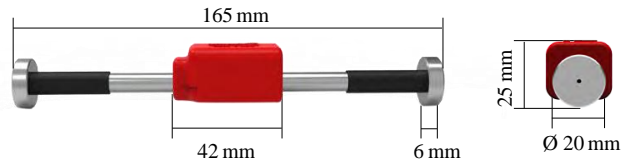


Figure 2.32: Vibrating wire strain gauge

The hoop stress in the final lining was monitored in SMP2 during more than 10 years at chainage 1383 m using BE (Figure 2.33). The stress in the final lining increases quickly after installation of the concrete ring and tends to stabilize after 5 years.

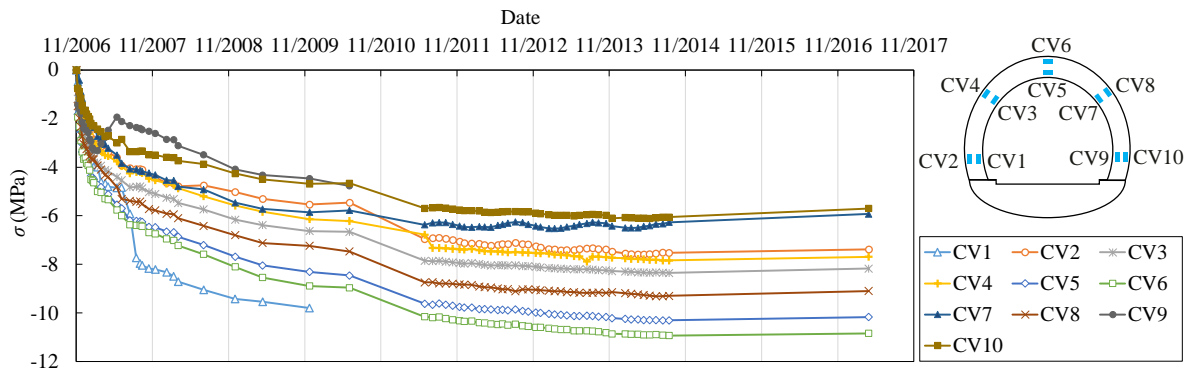
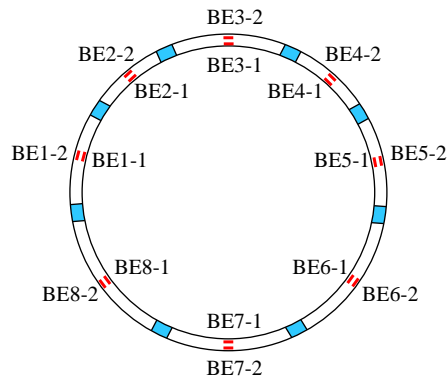


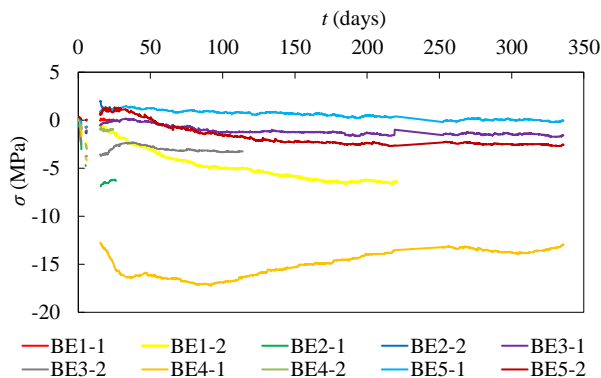
Figure 2.33: Stress measurement in the concrete ring at chainage 1383 m of SMP2

2.3.5 Stress in shotcrete layer

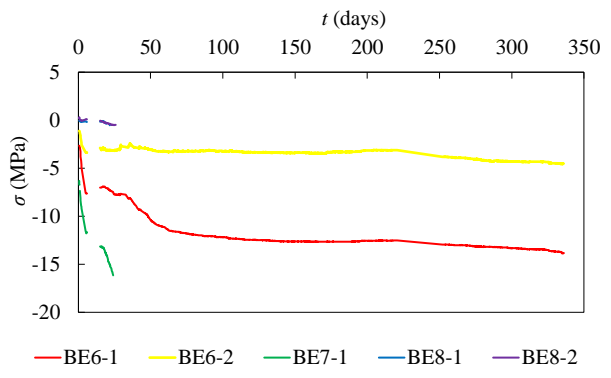
Hoop stress measurements have been recorded in the shotcrete lining in two sections at chainage 10325 and 10383 m. 16 gauges have been installed in the inner and outer sides of the shotcrete in the yielding support (Figure 2.34). These measurements show that the stress can reach values over 15 MPa in the shotcrete.



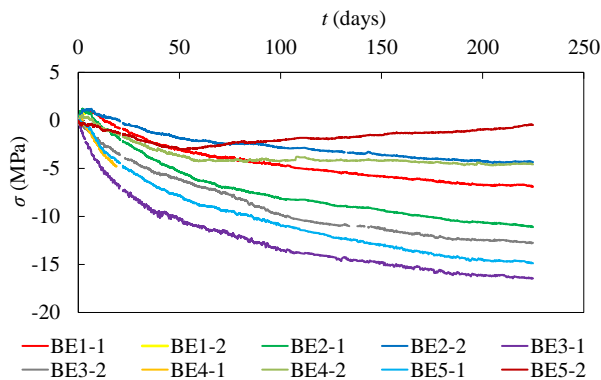
(a) Gauges in the shotcrete of the yielding support



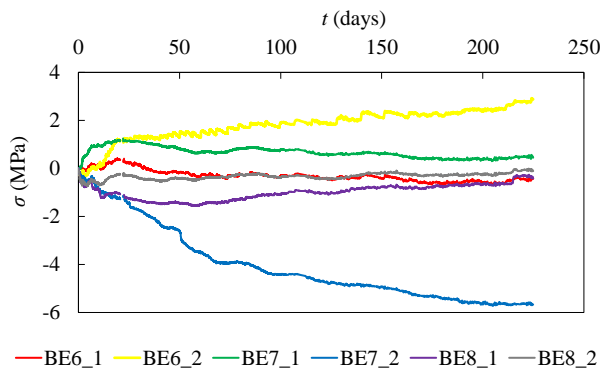
(b) Chainage 10325 m: upper part



(c) Chainage 10325 m: lower part



(d) Chainage 10383 m: upper part



(e) Chainage 10383 m: lower part

Figure 2.34: Stress measurements in the shotcrete in SMP4-RPS

CHAPTER 3

FIELD DATA PROCESSING

In SMP exploratory galleries, various field measurements have been carried out in order to follow the rock deformation around the tunnel wall during and after excavation. Several studies have been carried out for SMP2 particularly to analyze the observed squeezing behavior based on the field monitoring data. Vu (2010) has proposed a method to analyze the large and anisotropic closure of SMP2, which will be examined and applied for SMP4 at the depth and along the orientation of the base tunnel in the present work.

In this chapter, the available information obtained from SMP2 and the proposed data processing procedure are first presented. After that, the convergence measurements are analyzed for different parts of SMP4 (GS, PS and RPS) to help the understanding of the deformation mode of rock mass and to predict the long-term tunnel convergence.

3.1 Obtained knowledge of SMP2

In previous thesis works (Vu, 2010; Vu et al., 2013; Tran-Manh, 2014), a geometrical processing procedure has been proposed to describe the anisotropic deformation observed in SMP2. The convergence law proposed by Sulem et al. (1987a, 1987b) has been applied to fit the monitoring data which allows to predict the long-term convergence. The parameters values of the convergence law obtained for SMP2 are first tested to fit the convergence measurements of SMP4.

3.1.1 Procedure of convergence data processing

With the help of the monitoring targets installed on the tunnel wall, the convergence of a given section is recorded by following the displacements of these points and the evolution of the distance between two targets. The field data of the convergence measurement show that the deformation of the section is highly anisotropic in SMP2. The gallery is excavated with initial circular section and an ovalization has been observed in the site during and after excavation.

Geometrical processing of tunnel section deformation

In order to study the anisotropic convergence observed in SMP2, a geometrical processing procedure of tunnel cross-section convergence has been proposed (Vu, 2010; Vu et al., 2013) and applied later in different research works (Tran-Manh, 2014; Guayacán-Carrillo, 2016; De La Fuente, 2018).

The convergence measurements and visual observations in the field evidenced that the deformation of the tunnel section is highly anisotropic in SMP2. An ovalization has been observed on site after excavation. The displacements of the monitoring targets in longitudinal direction are ignored and the points are first projected on the mean vertical plane of the considered cross-section. The anisotropic deformation is represented by a 2D elliptical closure of the section (Figure 3.1).

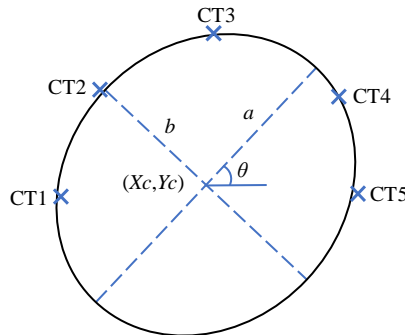


Figure 3.1: Elliptical fitting of the deformed section

An elliptical shape of the considered section can be fitted from the current position of the monitoring targets. The maximal and minimal convergences are obtained from the shortening of the minor and major axes respectively. The general equation of an ellipse is written as a function of the coordinates of the ellipse center (X_c, Y_c) , the two semi-axes lengths a and b and the orientation of the ellipse θ :

$$\left(\frac{x - X'_c}{a}\right)^2 + \left(\frac{y - Y'_c}{b}\right)^2 = 1 \quad (3.1)$$

with $X'_c = X_c \cos \theta + Y_c \sin \theta$ and $Y'_c = Y_c \cos \theta - X_c \sin \theta$.

The fitting procedure of the five ellipse parameters has been performed following three steps for SMP2 in the previous studies (Vu, 2010; Vu et al., 2013):

- step 1: fitting of the 5 parameters (X_c , Y_c , a , b and θ);
- step 2: fitting on 4 parameters (X_c , a , b and θ) with the coordinate Y_c fixed to its initial value based on the fitting of Step 1;
- step 3: fitting on 3 parameters (X_c , a and b) with the inclination θ fixed to its final value (it is generally observed in Step 2 that θ tends to stabilize to a fixed value).

In several situations, the deformation mode cannot be simply represented by an elliptical convergence the section, for example when:

- the convergence is almost isotropic;
- the convergence is anisotropic but due to a highly heterogeneous rock mass, a stable orientation of the fitted ellipse at large convergence cannot be identified. The convergence of each individual string has to be analyzed.

In the present study, the anisotropic convergence observed in SMP4-PS and RPS is produced by the heterogeneous rock mass and can not be studied by fitting an ellipse for the deformed section. In the cases, the average deformation of the considered tunnel section is analyzed by simply considering an isotropic closure. In doing so, although the anisotropic effects are ignored, one can access to the average behavior of the system (Figure 3.2). After projecting the monitoring targets on the mean vertical plane, the deformed section can be fitted by a circle and the evolution of the radius represents the mean convergence of the section. A circle is characterized by the following equation:

$$(x - X_c)^2 + (y - Y_c)^2 = r^2 \quad (3.2)$$

where (X_c, Y_c) are the coordinates of the circle center and r is the radius of the circle. It is noted that different origins of coordinates are used for the geometrical fitting processes of SMP2 and SMP4.

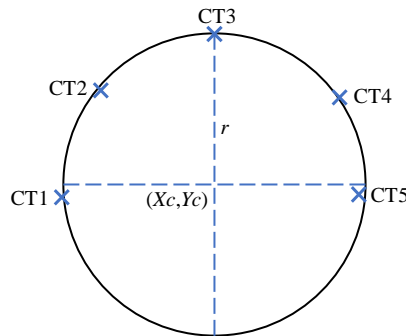


Figure 3.2: Circular fitting of the deformed section

Semi-empirical convergence law

The convergence of strings, of the major and minor axes of fitted ellipse and of the circle radius can be studied with the semi-empirical convergence law proposed by Sulem et al. (1987a, 1987b). The deformation of ground after tunneling can be described as the sum of instantaneous deformation ε_i and delayed (or time-dependent) deformation ε_d :

$$\varepsilon = \varepsilon_i + \varepsilon_d \quad (3.3)$$

The convergence of the tunnel section is considered to be influenced by tunnel face distance x and time t : $C(x,t) = C_1(x) + C_2(t)$ and these two parts of convergence are approximated :

$$C_1(x) = C_{\infty x} \left[1 - \left(\frac{X}{x+X} \right)^2 \right] \quad (3.4)$$

$$C_2(t) = A \left[1 - \left(\frac{T}{t+T} \right)^n \right] \quad (3.5)$$

The semi-empirical convergence law has then been proposed:

$$C(x,t) = C_{\infty x} \left[1 - \left(\frac{X}{x+X} \right)^2 \right] \left\{ 1 + m \left[1 - \left(\frac{T}{t+T} \right)^n \right] \right\} \quad (3.6)$$

This convergence law depends on 5 parameters:

- T is a characteristic time related to the time-dependent properties of the system;
- X is a parameter related to the distance of influence of the tunnel face;
- $C_{\infty x}$ is the instantaneous convergence obtained in the case of an infinite rate of face advance;
- m is a parameter related to the ratio between the time-dependent convergence and the instantaneous convergence;
- n is a constant, usually taken equal to 0.3.

The total convergence can be calculated with the following formula:

$$C_{\infty} = C_{\infty x} (1 + m) \quad (3.7)$$

The interpretation of the measured convergence must take into account the displacement that has occurred between the opening of the section and the installation of the convergence targets (i.e. the “lost convergence”) (Guayacán-Carrillo et al., 2016). The recorded convergence is thus:

$$\Delta C(x_i, t_i) = C(x_i, t_i) - C(x_0, t_0) \quad (3.8)$$

where x_0 is the face distance for the first record reading and t_0 is the time elapsed since the face crossed the considered section.

The real geometry of the tunnel section is complex. In the previous (Vu et al., 2013; Tran-Manh et al., 2015) and present studies of SMP galleries, the initial section shape is assumed to be circular ignoring the secondary effect of the geometry and focusing on the time-dependent behavior of the rock mass.

3.1.2 Obtained parameters from SMP2

The results of the geometrical processing in terms of the elliptical characteristics are obtained (Tran-Manh, 2014; Addante, 2016) as shown in the Table 3.1, where CT3 is consider as the origin of the coordinates ($*_i$ and $*_f$ correspond to the initial and final monitoring values respectively). After that, convergence fitting with the convergence law (explained in Section 3.1.1) (Sulem et al., 1987a, 1987b) has been performed for the sections between chainage 1272 and 1384 m considering 11 zones of ground (Table 3.2) in the previous studies.

Table 3.1: Obtained parameters of the geometrical processing in SMP2

Profile	Chainage (m)	θ ($^{\circ}$)	Y_c (m)	a_i (m)	b_i (m)	a_f (m)	b_f (m)
P2	1006	80	-5.2	5.18	4.96	5.16	4.93
	1133	-89	-5.16	5.16	4.97	5.15	4.95
P7-2	1223	-77	-5.15	6.55	5.21	6	5.05
	1228	86	-5.58	6.6	5.44	6.12	5.2
	1245	50	-5.42	5.57	5.53	5.35	5.04
	1253	75	-6.25	6.31	5.56	6.17	5.33
	1260	87	-5.39	5.39	5.06	5.32	4.92
	1265	-88	-5.41	5.41	5.05	5.4	4.85
P7-3	1272	10	-5.18	5.26	5.2	4.76	4.19
	1278	-10	-5.26	5.14	5.28	4.36	4.13
	1284	5	-5.26	5.21	5.26	4.46	3.68
	1291	20	-5.51	5.26	5.47	4.43	3.96
	1297	0	-5.13	5.22	5.13	4.4	3.47
	1311	15	-5.35	5.34	5.37	4.41	4
	1322	75	-5.25	5.28	5.06	4.57	4.16
	1342	55	-5.1	5.18	5.09	4.39	4.26
	1367	60	-5.4	5.4	5.23	5.06	4.55
	1375	50	-5.2	4.93	5.14	4.66	4.51
	1384	-25	-4.96	5.14	4.94	4.74	4.22
	1394	25	-5.41	6.33	5.45	6.1	4.75
DSM	1399	25	-5.62	6.43	5.7	6.31	5.01
	1413	25	-6.28	6.55	6.22	6.55	5.36
	1421	25	-5.39	5.62	5.39	5.59	5.2
	1438	20	-5.96	6.24	5.94	6.04	5.35
	1443	30	-6.26	6.43	6.27	6.31	5.77
	1450	10	-5.91	6.3	5.94	6.1	5.6
	1458	15	-6.88	6.43	6.91	6.23	6.59
	1470	30	-5.97	6.19	5.89	6.04	5.67
	1493	30	-6.34	6.35	6.25	6.23	5.89
	1507	10	-6.13	6.33	6.19	6.1	5.66
	1531	10	-6.8	6.49	6.84	6	6.33
	1538	10	-5.67	6.11	5.67	5.83	5.43
	1589	60	-6.33	6.38	6.28	6.37	6.13
	1598	70	-6.48	6.5	6.3	6.42	6.17
	1650	-80	-6.66	6.7	6.42	6.63	6.32
	1842	14	-5.52	5.82	5.51	5.64	5.36
	1948	-76	-6.23	6.29	5.8	6.25	5.71
	1953	0	-5.09	5.52	5.09	5.49	5.03
	1981	-78	-5.81	5.85	5.58	5.8	5.56
	1996	75	-5.56	5.58	5.12	5.55	5.08
	2012	-90	-6.24	6.25	5.35	6.21	5.23
	2017	-90	-5.6	5.68	5.25	5.66	5.17
	2037	47	-5.03	5.13	5.02	5.14	4.84
	2042	0	-4.3	5.05	4.37	4.92	4.27
2228	-6	-4.74	5.91	4.92	5.9	4.91	
2306	-54	-5.74	5.78	5.66	5.76	5.65	
2312	85	-6.26	6.28	5.78	6.28	5.76	
2318	-85	-7.79	7.84	6.21	7.83	6.2	

Table 3.2: Parameters of the convergence law in SMP2

Zone	Chainage (m)	T (days)	m (\circ)	Major axis			Minor axis		
				X (m)	$C_{\infty x}$ (m)	C_{∞} (m)	X (m)	$C_{\infty x}$ (m)	C_{∞} (m)
1	1006	1	1	23	0.029	0.05	23	0.039	0.08
	1133			*	*	*	11	0.044	0.08
2	1223	25	18	15	0.199	3.78	15	0.055	1.05
	1228			15	0.182	3.46	15	0.09	1.71
	1245			15	0.093	1.75	15	0.207	3.94
3	1260	20	18	15	0.023	0.44	15	0.073	1.39
	1265			*	*	*	15	81.32	1.55
4	1272	16	9	24	0.2	1.97	39	0.43	4.23
	1278			34	0.33	3.2	36	0.49	4.74
	1284			16	0.32	3.12	46	0.7	6.78
	1291			15	0.32	3.15	39	0.64	6.23
	1297			14	0.32	3.15	22	0.66	6.39
5	1311	71	10	13	0.5	5.31	13	0.75	7.99
	1322			24	0.48	5.12	24	0.6	6.36
	1331			34	0.46	4.88	57	0.62	6.57
	1342			14	0.48	5.13	14	0.61	6.46
6	1367	117	11	37	0.3	3.74	37	0.61	7.67
	1375			6	0.24	2.93	6	0.54	6.72
	1384			32	0.4	4.93	32	0.75	9.4
7	1399	25	13	3	0.07	0.07	19	0.46	0.46
	1406			4	0.04	0.04	10	0.37	0.37
	1413			*	*	*	32	0.63	0.63
	1438			4	0.14	0.14	4	0.39	0.39
	1443			*	*	*	28	0.45	0.45
8	1463	6.7	10	2	0.17	0.17	47	0.65	0.65
	1470			34	0.33	0.33	47	0.68	0.68
	1493			6	0.08	0.08	*	*	*
	1507			29	0.33	0.33	1	0.73	0.73
9	1589	5	10	*	*	*	25	0.071	0.78
	1598			*	*	*	25	0.05	0.55
	1650			25	0.037	0.41	25	0.05	0.55
	1841,5			8	0.079	0.87	6	0.066	0.72
10	1948	3	10	8	0.018	0.2	24	0.028	0.3
	1953			*	*	*	8	0.022	0.24
	1981			10	0.016	0.18	21	0.006	0.07
	1996			5	0.008	0.1	17	0.021	0.23
	2012			10	0.01	0.11	*	*	*
	2017			7	0.012	0.13	21	0.032	0.35
	2037			*	*	*	25	0.056	0.62
2042	17	0.041	0.45	20	0.024	0.26			
11	2228	5	2	*	*	*	*	*	*
	2306			25	0.027	0.08	*	*	*
	2312			*	*	*	10	0.026	0.08
	2318			5	0.027	0.08	*	*	*

Various values of the parameters of the convergence law have been obtained for different zones in SMP2 (Tran-Manh et al., 2015), in which Zone 3 shows similar geological context as SMP4. In the present study, the average values obtained from Zone 3 of SMP2 of 4 parameters of the convergence law are applied: $T = 20$ days; $X = 15$ m; $m = 18$ and $n = 0.3$. The only parameter to fit is the instantaneous convergence $C_{\infty X}$. The experience obtained from SMP2 will be applied to SMP4 which is much deeper and in another direction.

3.2 SMP4-GS

In SMP4-GS, 5 monitoring targets (CT1 to CT5) have been installed every 5 meters along the gallery on the upper part of the tunnel, on the bolt head (B), steel ribs (C) or tunnel wall (T). Due to the lack of detailed information on the position of these targets, we assume that they are situated as shown in Figure 3.3 based on a diagram from the convergence measurement files provided by TELT. The origin of the coordinates is the center of the initial circular section.

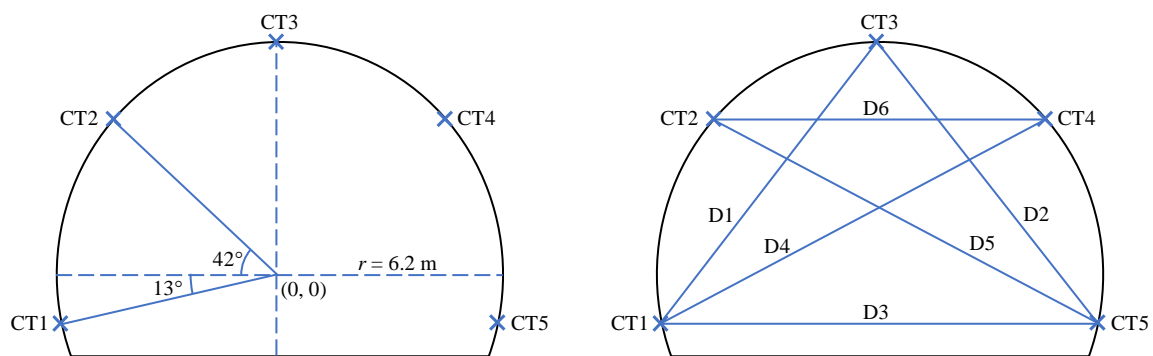


Figure 3.3: Position of monitoring targets in SMP4-GS

The convergence is recorded from chainage 10160 m (Figure 3.4). The convergence was very low as the excavation was in the stiff rock until chainage 10270 m, then, the tunnel began to enter into the Houiller formation and the convergence became much higher. In the present work, we focus on 4 sections between chainage 10275 and 10290 m. In this zone, the Houiller formation is encountered and squeezing behavior has been observed.

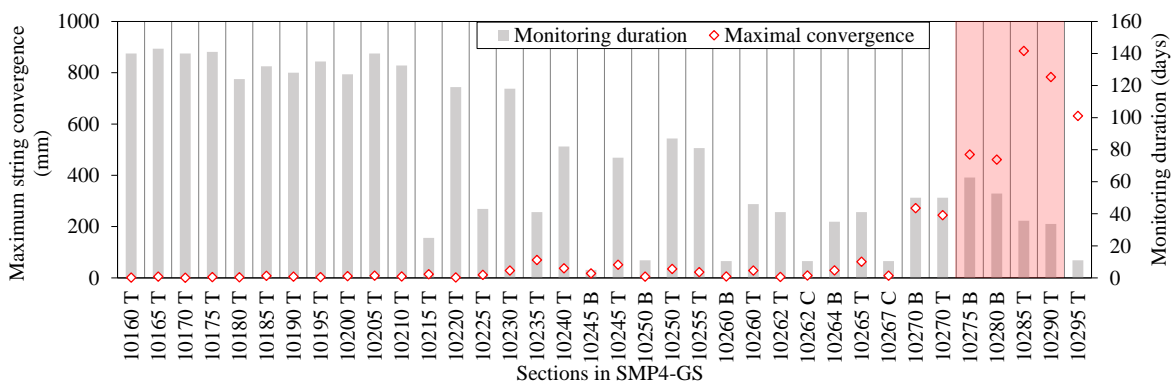


Figure 3.4: Instrumented sections in SMP4-GS

The displacements of the monitoring targets (Figure 3.5) and the shortening of the 6 strings between targets (D1 to D6) (Figure 3.6) have been recorded.

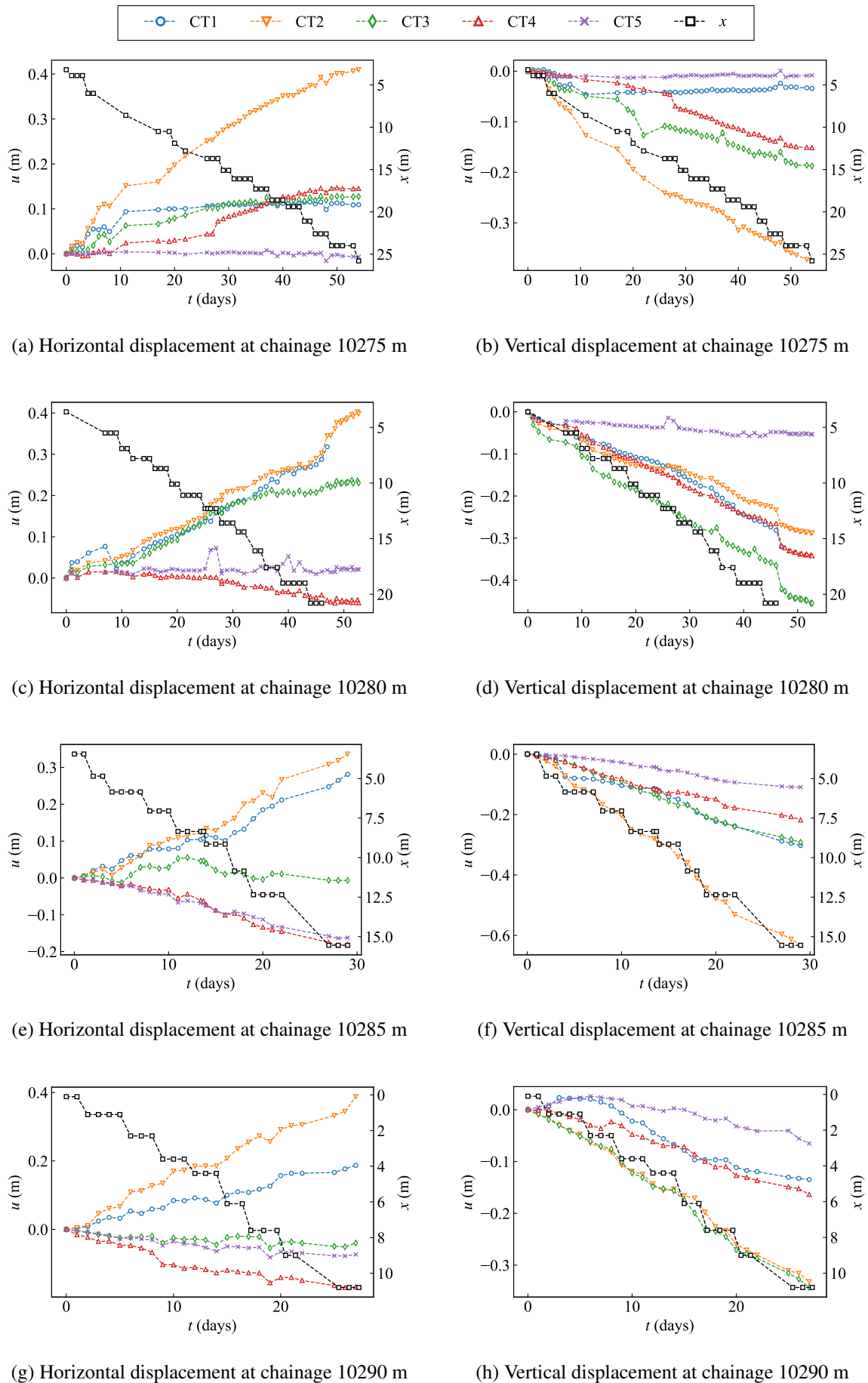


Figure 3.5: Horizontal and vertical displacements of the monitoring points in SMP4-GS

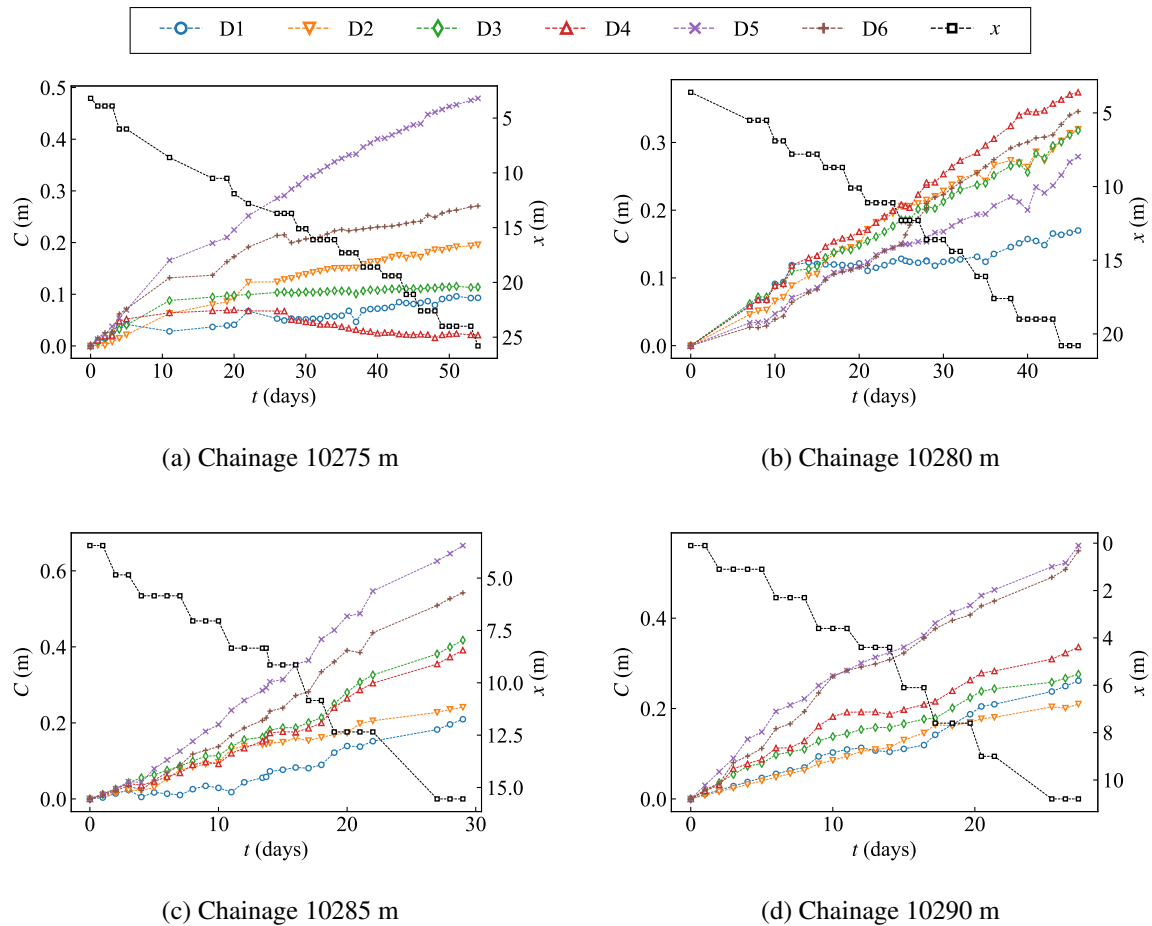


Figure 3.6: Field monitoring of strings convergence in SMP4-GS

The duration of measurements is limited to 34 to 54 days because of the collapse of the face that occurred at chainage 10303 m. The recorded maximal strings convergence can reach more than 0.8 m within the four analyzed sections (Table 3.3). The deformation mode is different from one section to another. For example, at chainage 10275 m, D5 shortens much more than D4 (Figure 3.6a), and CT2 moves more than CT4 (Figures 3.5a and 3.5b), which indicate that the convergence is highly anisotropic and that the top left part of the tunnel section deforms much more. This anisotropy can also be observed at chainages 10285 and 10290 m. However, at chainage 10280 m (Figure 3.6b), D4 and D5 show almost the same convergence. The convergence at chainages 10285 and 10290 m are much higher than those at chainages 10275 and 10280 m. These field monitoring data of convergence measurements are analyzed in the following.

Table 3.3: Summary of convergence measurements in SMP4-GS

Chainage (m)	Recording duration (days)	Maximal strings convergence (m)
10275 B	54	0.479
10280 B	53	0.461
10285 T	36	0.857
10290 T	34	0.783

3.2.1 Geometrical processing considering the rock mass heterogeneity

The rock mass is highly heterogeneous around SMP4-GS: an inclined layer of anhydrite crosses the lower part of the tunnel section and a zone of carboniferous schists (Houiller formation) is encountered in the upper part of the tunnel. The extension of the Houiller formation is increasing from chainage 10267 to 10287 m as the tunnel advances. This heterogeneous character of the rock mass is clearly shown on the geological survey of the tunnel face (Figure 2.15). In the Houiller formation, coal and/or schists dominate, and several inclined bands of sandstone are embedded.

Due to the presence of the Houiller formation in the upper part of the tunnel, large deformations are recorded in this zone whereas the lower part of the tunnel which is in the Anhydrite formation exhibits smaller deformation. The monitoring points are located in different rock mass types (Table 3.4).

Table 3.4: Position of monitoring points CT1-CT5

Section	Upper part (Houiller)	Lower part (Anhydrite)
Chainage 10275 m (B)	CT2; CT3; CT4	CT1; CT5
Chainage 10280 m (B)	CT2; CT3; CT4	CT1; CT5
Chainage 10285 m (T)	CT1; CT2; CT3; CT4	CT5
Chainage 10290 m (T)	CT1; CT2; CT3; CT4; CT5	

Visual observation and convergence data show a higher deformation and an ovalization of the upper part of the section in Houiller formation. In the following, the study focuses on the upper part of the section by fitting the deformed shape of the upper part only. For example (Figure 3.7), at chainage 10275 m, CT1 and CT5 are disregarded in the fitting procedure since they are both localized in the anhydritic lower part of the section.

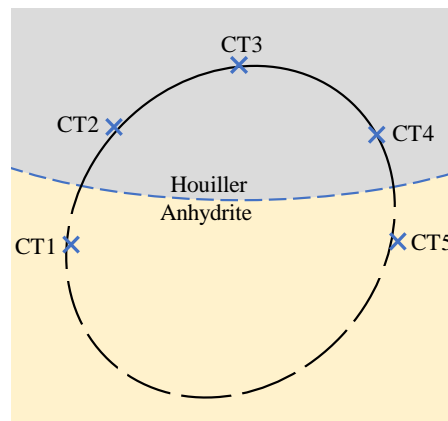
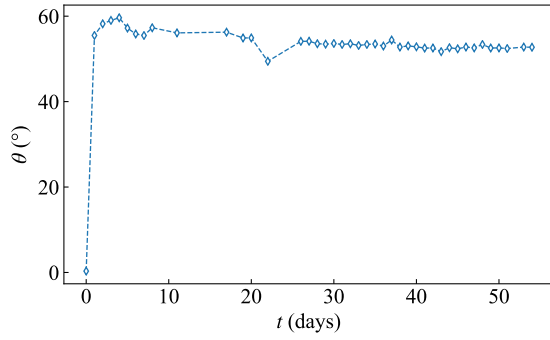
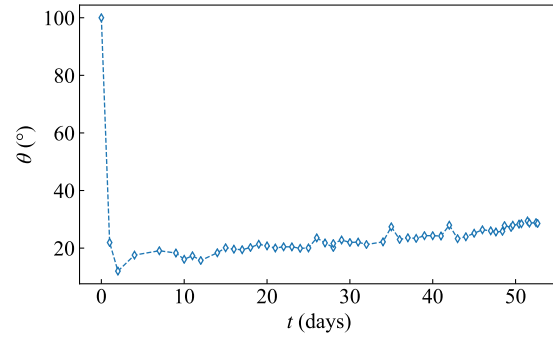
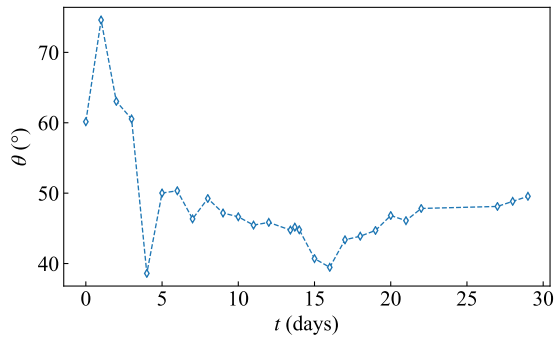
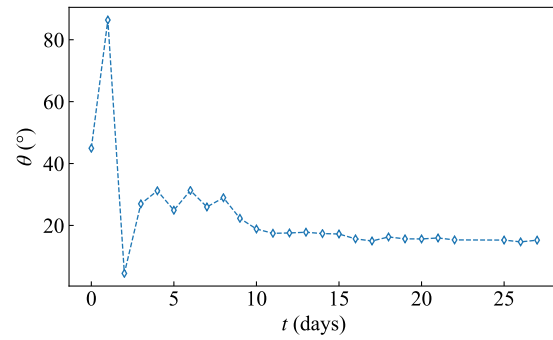
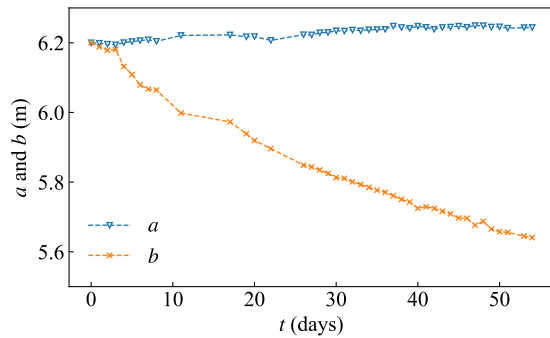
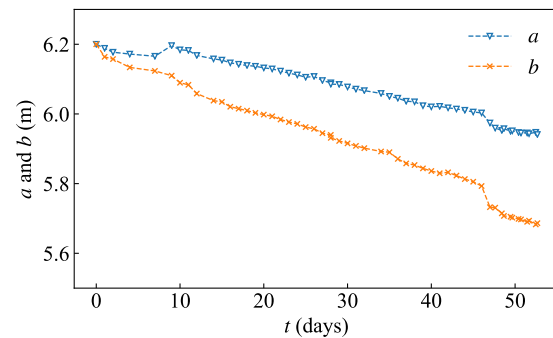


Figure 3.7: Evaluation the section ovalization at chainage 10275 m with respect to CT2, CT3 and CT4 in the upper Houiller part of the section

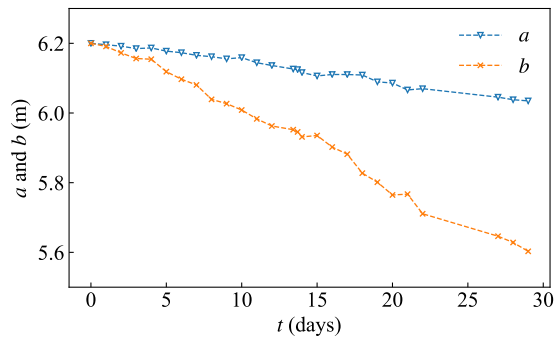
An ellipse is fitted to describe the anisotropic deformation of the upper part of the section. It is assumed that the coordinates of the ellipse center (X_c, Y_c) are fixed, so that only 3 parameters are needed to be fitted: the two semi-axes lengths (a and b) and the orientation of ellipse (θ). In every section under study, the orientation of the ellipse tends to stabilize to θ_f as deformations develop because of the significant movement of the top left side of tunnel (Figure 3.8).

(a) Chainage 10275 m ($\theta_f = 53^\circ$)(b) Chainage 10280 m ($\theta_f = 26^\circ$)(c) Chainage 10285 m ($\theta_f = 50^\circ$)(d) Chainage 10290 m ($\theta_f = 15^\circ$)Figure 3.8: Inclination of the fitted ellipse θ 

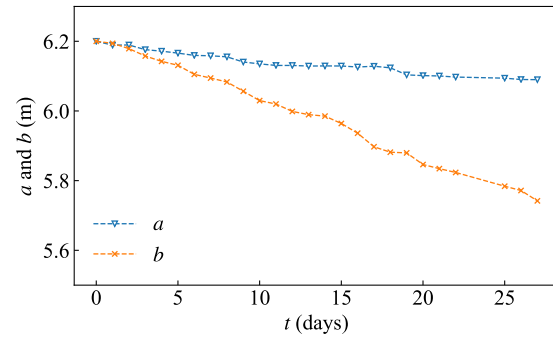
(a) Chainage 10275 m



(b) Chainage 10280 m



(c) Chainage 10285 m



(d) Chainage 10290 m

Figure 3.9: Major and minor semi-axes a and b of the fitted ellipse

Fixing the orientation at its final value θ_f , the tunnel convergence is fitted again by computing the 2 parameters (a and b) (Figure 3.9). A high anisotropy of the cross-section convergence can be observed: the minor axis, which gives the direction of the maximal convergence, shortens much more than the major axis. The convergences of the sections at chainage 10285 and 10290 m are larger than at chainage 10275 and 10280 m.

3.2.2 Analysis of anisotropic convergence

The convergence analysis is carried out in each section of SMP4-GS by studying the maximal convergence. The proposed convergence law and the obtained parameters of the average of the anisotropic behavior of SMP2 ($T = 20$ days; $X = 15$ m; $m = 18$ and $n = 0.3$) are tested. These values of parameters are thus fixed for analyzing the convergence of SMP4-GS from chainage 10275 to 10290 m. The only parameter to be evaluated for each section is the instantaneous convergence $C_{\infty x}$. We also test, in a second stage, the predicted long-term convergence by restricting the fitting of $C_{\infty x}$ to the first 20 days of measurements.

The calculation is firstly performed on the two sections at chainages 10275 and 10280 m (Figure 3.10). As shown in these figures, the recorded data are well reproduced by the convergence law when the fitting is performed both on the complete set of data and only on the first 20 days of measurements. The instantaneous convergence and the predicted total (long-term) convergence C_{∞} obtained from the two fitting procedures are close as shown in Table 3.5. This capability of prediction allows to obtain accurate parameters of the convergence law within a few weeks behind the face.

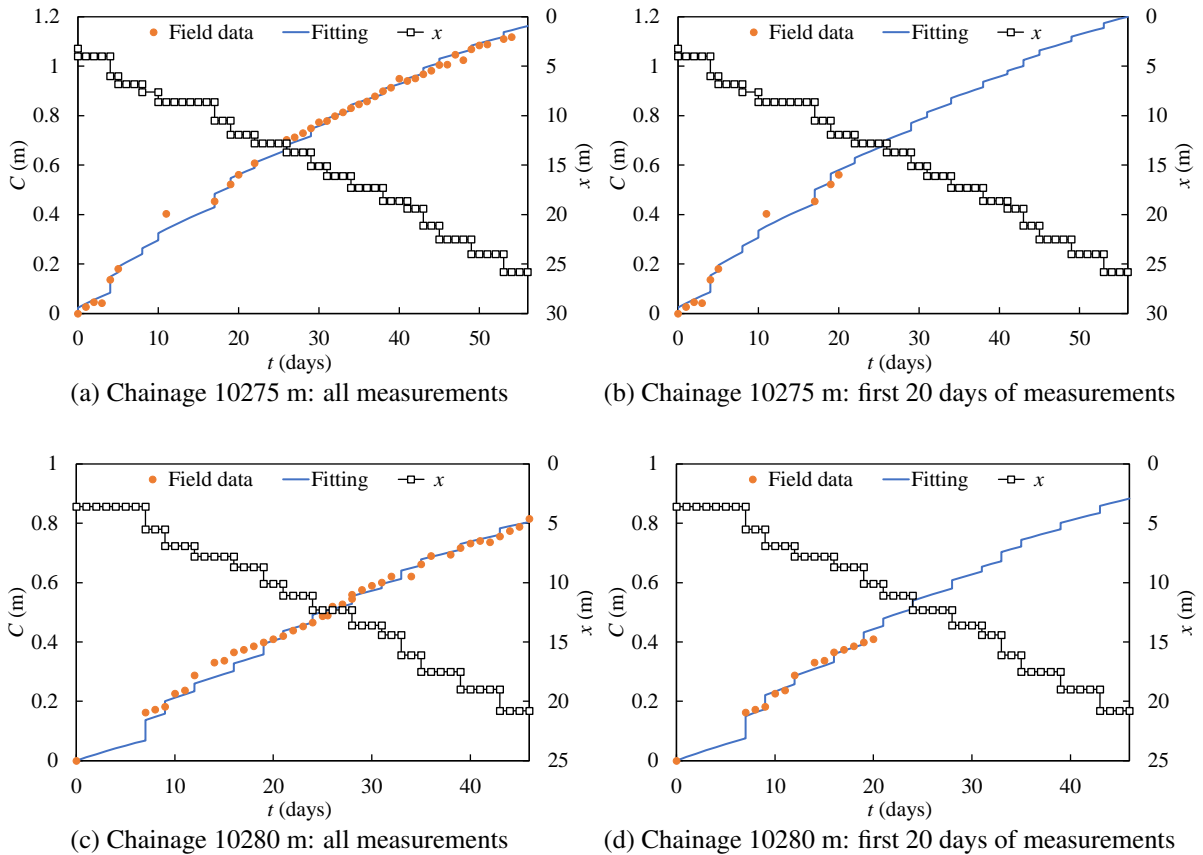


Figure 3.10: Convergence fitting with different periods of data at chainages 10275 and 10280 m (x is the face advance from the considered section)

Table 3.5: Fitted parameters with different fitting periods (chainages 10275 and 10280 m)

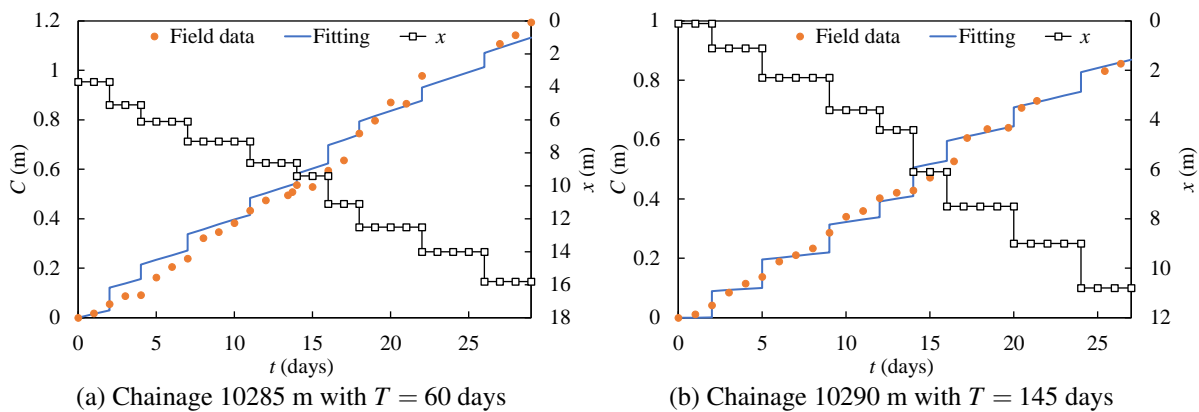
Section	All measurements		20 days of measurements	
	$C_{\infty x}$ (m)	C_{∞} (m)	$C_{\infty x}$ (m)	C_{∞} (m)
Chainage 10275 m (B)	0.21	3.98	0.22	4.12
Chainage 10280 m (B)	0.17	3.25	0.19	3.54

The predictive capability of the convergence law proposed for SMP2 and the typical values of parameters are thus relevant for the sections at chainages 10275 and 10280 m in SMP4-GS which is much deeper and in different orientation. The parameters of the convergence law retrieved from SMP2 are applicable in SMP4 and only 20 days of continuous recording of the data are sufficient for accurate predictions of the convergence at least up to 50 days, corresponding to the last available measure. The predictive capability of the convergence law allows to estimate the mid-term and long-term convergence of the cross-section with the field measurements of a short period.

The same process is applied to the two following sections situated at chainage 10285 and 10290 m respectively. In this case, it was observed that the measured data cannot be reproduced by keeping the parameters of SMP2. A larger value of the characteristic time parameter T is obtained (Table 3.6): $T = 60$ days for the section at chainage 10285 m (Figure 3.11a) and $T = 145$ days for the section at chainage 10290 m (3.11b). This indicates that the time-dependent deformation of these two sections is significantly higher than the two previous ones. The values of C_{∞} (total convergence) are very high (more than 10 m) for these two sections and correspond to full closure of the tunnel. It reflects the highly damaged state of the rock mass around these 2 sections and could be interpreted as an indicator of the collapse that occurred near chainage 10303 m.

Table 3.6: Fitted parameters on sections at chainages 10280 and 10290 m

Section	T (days)	$C_{\infty x}$ (m)	C_{∞} (m)
Chainage 10285 m (T)	60	0.56	10.63
Chainage 10290 m (T)	145	0.70	13.28

Figure 3.11: Convergence fitting of sections at chainages 10280 and 10290 m (x is the face advance from the considered section)

3.3 SMP4-PS

SMP4-PS is excavated from chainage 10310 to 10410 m with an average radius of 3.15 m in a very heterogeneous rock formation with several fault zones. From chainage 10310 to 10330 m, the top of tunnel is reinforced by GRA which is filled with concrete. Near chainage 10310 m, the material is stratified and the proportion of coal and of carbon schist is higher than the following sections. From chainage 10337 to 10360 m, the material appears stiffer from the geological face surveys and the interpreted longitudinal geological profile (Figure 2.19), while after chainage 10360 m, the material becomes stratified again. The available field monitoring data of SMP4-PS are analyzed in the present section.

3.3.1 Field monitoring data of SMP4-PS

The tunnel convergence during and after excavation are followed in 44 sections from chainage 10310 to 10410 m. For each section, 5 or 6 monitoring points are installed on the tunnel wall to record the displacements of each monitoring points and the evolution of the string length between 2 targets (Figure 3.12). The coordinates of the monitoring targets for the first measurement (i.e. initial position) are available for all the sections and they vary from one section to another (Figure 3.13).

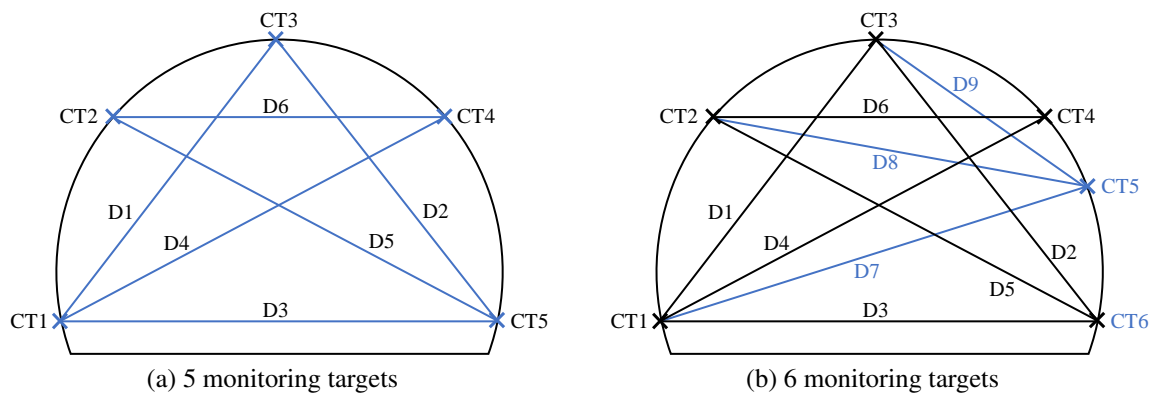


Figure 3.12: Monitoring targets and strings

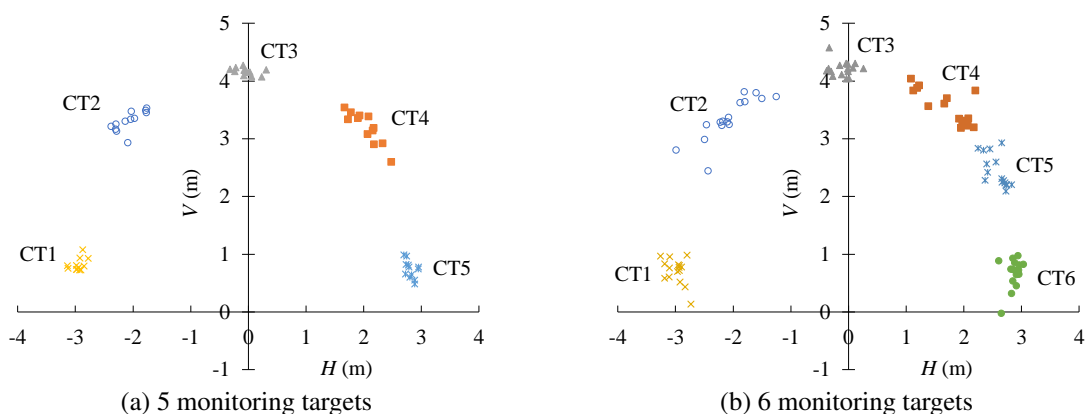


Figure 3.13: Initial positions of the monitoring targets for all the sections of SMP4-PS

The convergence magnitude recorded in SMP4-PS is much smaller than in SMP4-GS. The convergence is recorded during more than 200 days for most of the sections where the targets are installed on

the bolts or on the tunnel wall. For most of the other sections, where the targets are installed on the steel ribs, the convergence data are available only for a rather short period (from 12 to 25 days). The sections of SMP4-PS can be classified into 4 zones with two zones of higher deformation and two zones of limited convergence (Figure 3.14):

- from chainage 10312 to 10327 m: the convergence is very high up to 0.25 m at the end of the monitoring period (about 200 days);
- from chainage 10330 to 10371 m: the convergence is smaller (below 0.1 m);
- from chainage 10376 to 10386 m: the convergence is high again;
- from chainage 10399 to 10410 m: the convergence is very low (few centimeters).

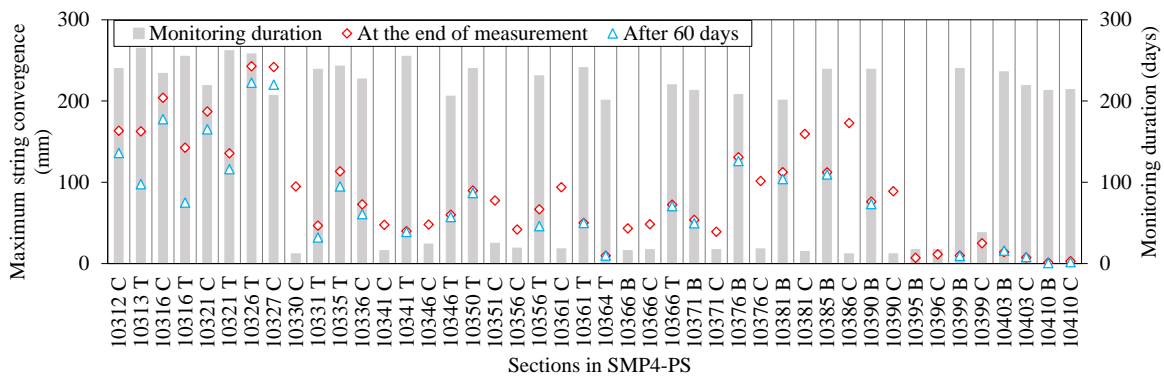


Figure 3.14: Convergence measurements in SMP4-PS

The convergence measurements for SMP4-PS cover the 2 stages of excavation and support installation (Figure 3.15). The convergence increases quickly after excavation of the section and the installation of the semi-rigid support system limits the convergence magnitude and convergence rate. In the zones of strong convergence, high anisotropic deformation can be observed. For example, at chainage 10326 m, which has the highest convergence, the strings D2, D3 and D5 shorten much more than the other strings because the target CT6 moves significantly to the left and down (Figure 3.16).

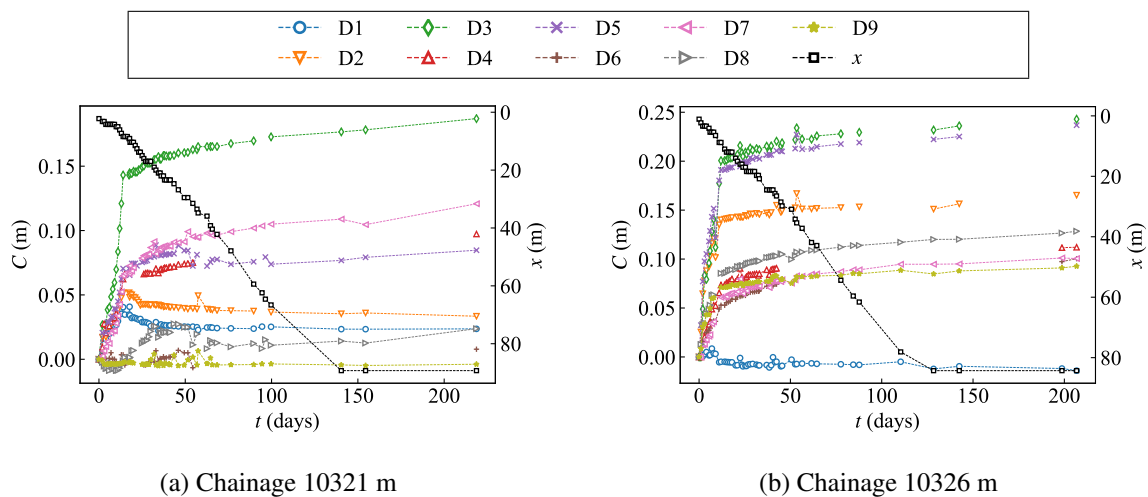


Figure 3.15: Convergence monitoring in SMP4-PS (example of chainage 10321 and 10326 m)

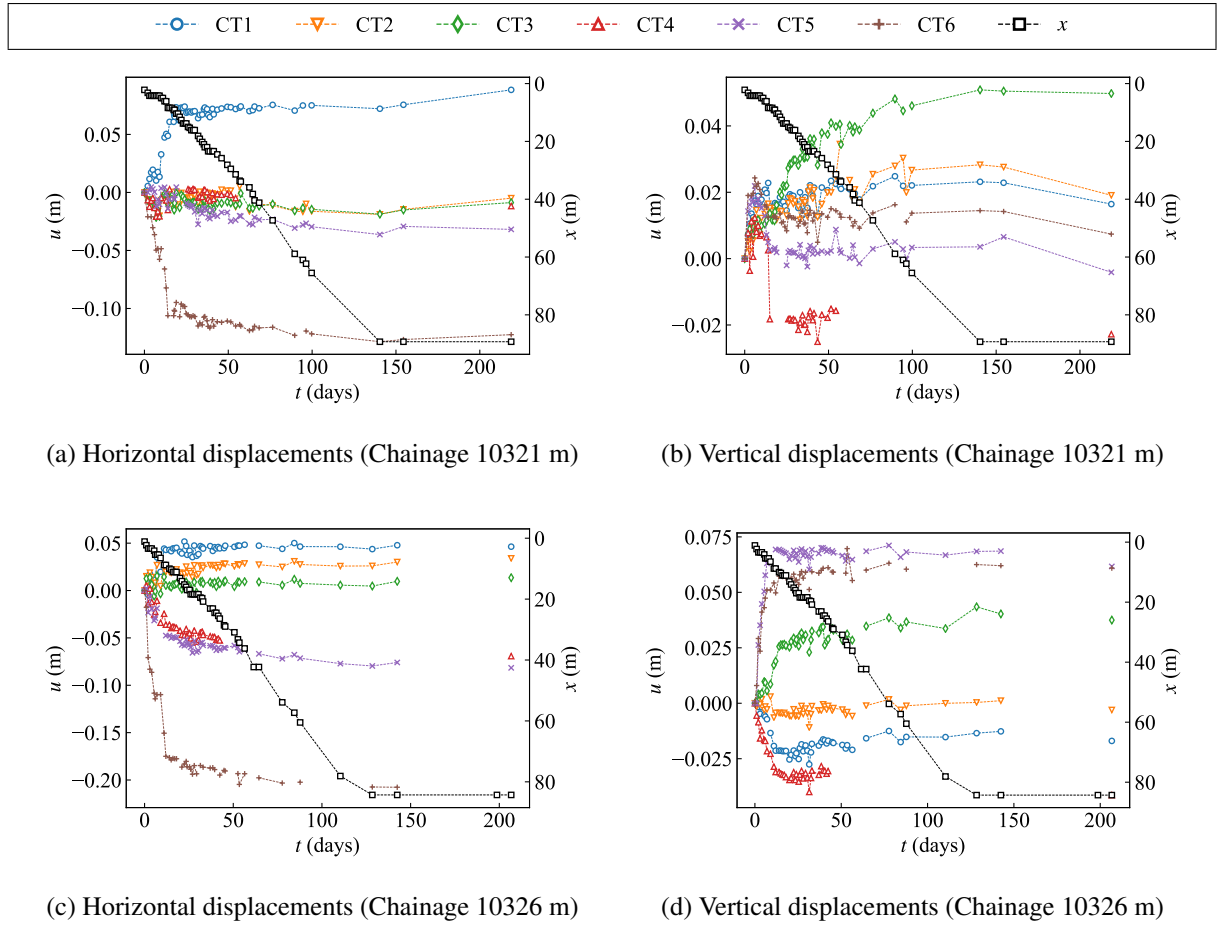


Figure 3.16: Recorded displacement of SMP4-PS (example of chainage 10321 and 10326 m)

The rock mass is very heterogeneous and stratified. Even though the convergence is anisotropic, a single direction cannot be identified and the deformed section cannot be simply represented as an ellipse. Therefore, the section convergence can be characterized by the mean convergence and the maximal convergence. The mean convergence is studied by fitting of a circle and evaluating the 3 parameters (X_c , Y_c and r) and the maximal convergence is studied by analyzing the string with largest convergence (D3 in most cases).

The convergence of the tunnel section is then approximated by using the proposed convergence law. As the measured data cover 2 stages of excavation and support procedure, the present study accounts for these 2 stages and the fitting needs to be performed separately (Figure 3.17):

- stage A: excavation of the tunnel section;
- stage B: installation of the semi-rigid support system.

The recorded convergence in stage A is thus:

$$\Delta C_A(x_i, t_i) = C_A(x_i, t_i) - C_A(x_0, t_0) \quad (3.9)$$

where x_0 is the face distance for the first record reading and t_0 is the time elapsed since the face crossed the considered section.

In stage B:

$$\Delta C_B(x_i, t_i) = C_B(x_i, t_i) - C_B(x_B, t_B) + C_{AB} \quad (3.10)$$

where x_B is the distance to the tunnel face when the second support system is installed, t_B is the corresponding time and C_{AB} is the corresponding measured convergence. The final convergence can be evaluated by

$$C_{\infty} = C_{\infty B} - C_B(x_B, t_B) + C_{AB} \quad (3.11)$$

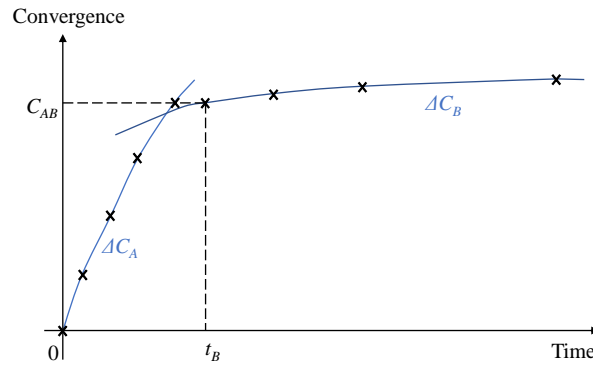


Figure 3.17: Calibration of convergence data on 2 stages

The mean parameters of convergence law obtained in SMP4-GS are applied to the first sections of SMP4-PS which are close to SMP4-GS and in similar geological units and with similar support system. The size effect is taken into account in the present study: $C_{\infty x}$ and X are assumed proportional to tunnel diameter (Guayacán-Carrillo et al., 2018). The following values of parameters are then proposed for SMP4-PS (Table 3.7) and the only parameter to evaluate is $C_{\infty x}$ for each section.

Table 3.7: Proposed parameters for the convergence law in SMP4

Profile	Diameter (m)	Stage	X (m)	T (days)	m	n
SMP4-GS	12.4	*	15	20	18	0.3
SMP4-PS	6.3	A	7.6	20	18	0.3
		B	7.6	20	18	0.3

3.3.2 Mean convergence

As mentioned before, in order to analyze the mean convergence, the section is fitted by a circle and the 3 parameters (X_c , Y_c and r) are evaluated for both zones with high convergence (Figure 3.14). In the other zones, the convergences are so small that the fitting process is inefficient. The initial values of the circle parameters for each section are shown in Figure 3.18.

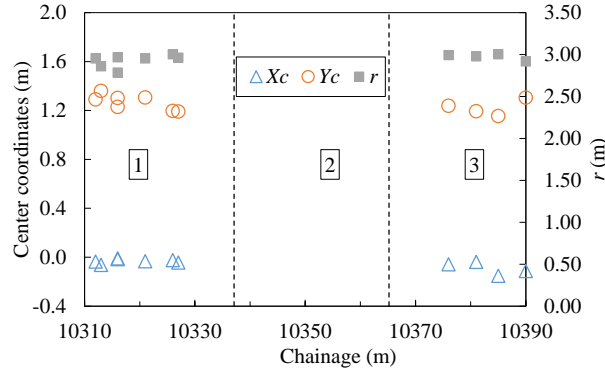


Figure 3.18: Initial parameters of fitted circle in SMP4-PS

From the fitting, we can observe that the center of the circle moves up with respect to its initial location, which indicates a global displacement of the section. The obtained parameters and predicted long-term convergence are shown in Table 3.8.

Table 3.8: Obtained parameters of convergence law in SMP4-PS and predicted total convergence [Unit: m]

Section	$C_{\infty xA}$	$C_{\infty xB}$	C_{lostA}	C_{AB}	C_{∞}
10312 C	0.0220	0.0047	0.0105	0.0414	0.1262
10313 T	0.0334	0.0071	0.0311	0.0548	0.2011
10316 C	0.0316	0.0091	0.0104	0.1032	0.2513
10316 T	0.0237	0.0060	0.0499	0.0457	0.1868
10321 C	0.0338	0.0034	0.0203	0.0919	0.1656
10326 T	0.0679	0.0037	0.0203	0.1593	0.2376
10327 C	0.0517	0.0052	0.0013	0.1324	0.2175
10376 B	0.0336	0.0009	0.0163	0.0993	0.1287
10381 B	0.0343	0.0018	0.0218	0.0970	0.1461
10385 B	0.0450	0.0018	0.0215	0.0983	0.1479
10390 B	0.0299	0.0003	0.0195	0.0617	0.0864

The obtained values of parameters $C_{\infty xA}$ and $C_{\infty xB}$ significantly vary from chainage 10310 to 10390 m (Figure 3.19). The predicted final convergence varies from 0.08 to 0.25 m. The instantaneous convergence $C_{\infty x}$ for the stages A and B and the long-term convergence C_{∞} are slightly higher in the first zone, which corresponds to a higher proportion of Carboniferous schists and coal.

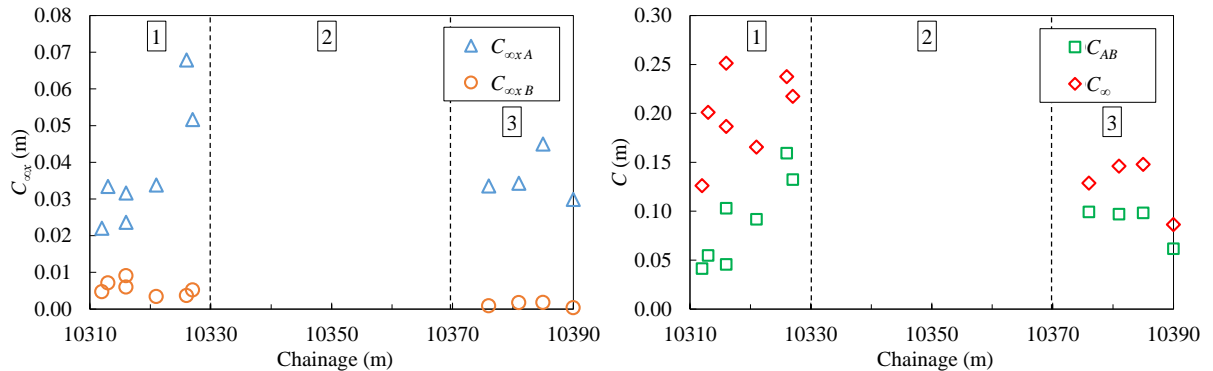
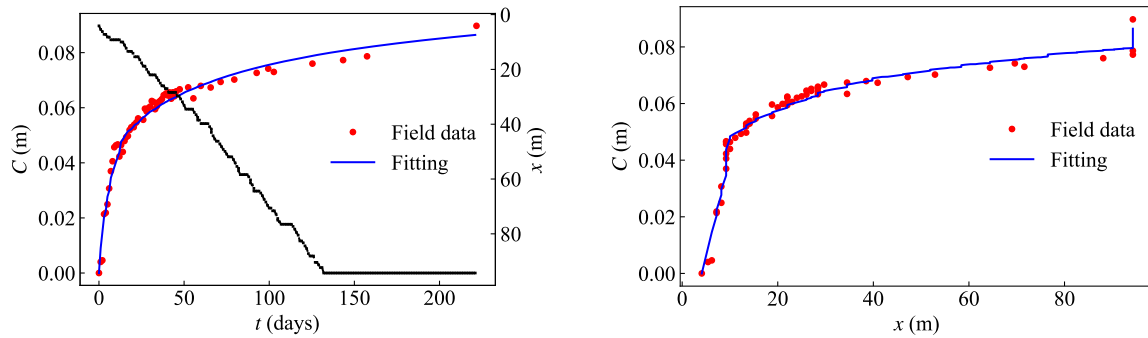
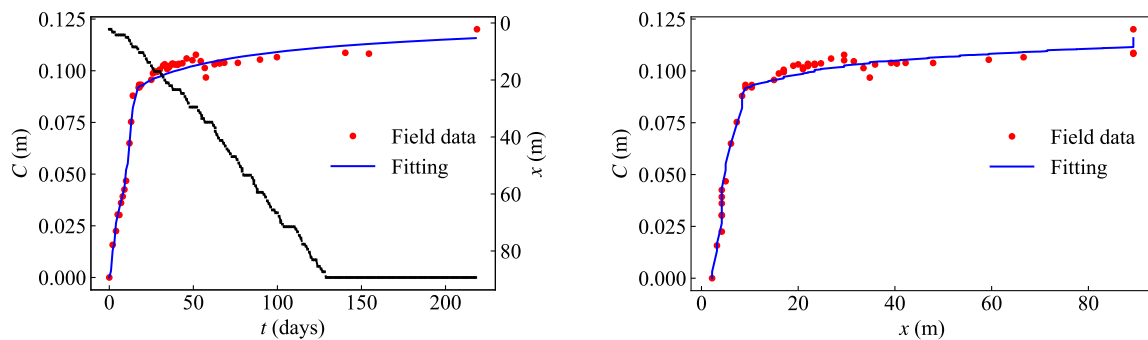


Figure 3.19: Obtained parameters of the convergence law and predicted long-term convergence

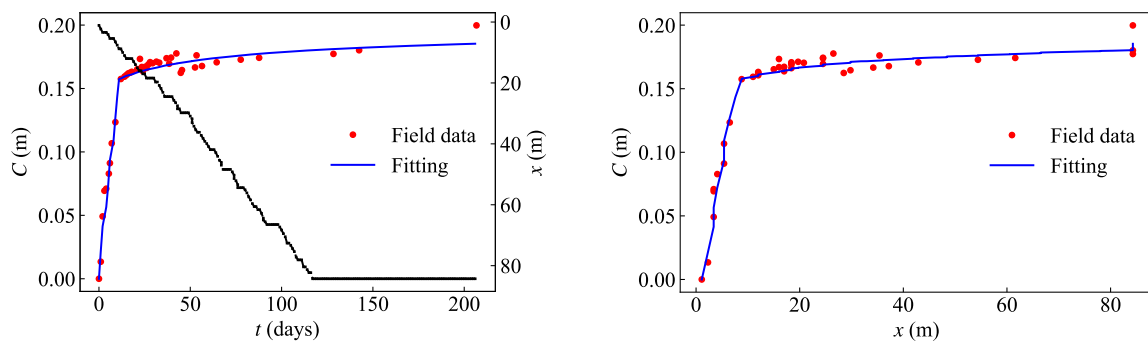
With the obtained parameters, the convergence measurements can be well reproduced. The detailed fitting results of all the studied sections are shown in Appendix A. The sections at chainages 10316, 10321 and 10326 m, which have higher convergence, are shown in Figure 3.20 as examples. The time-dependent behavior of the rock mass and the influence of the tunnel face advance are well approximated for more than 200 days.



Chainage 10316 m



Chainage 10321 m



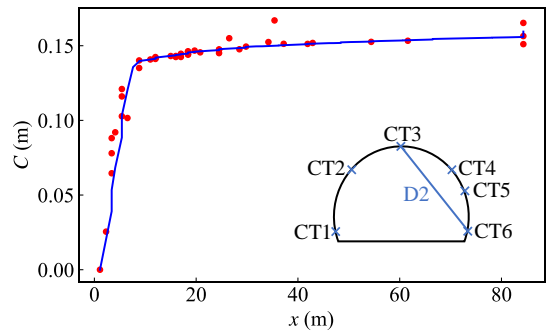
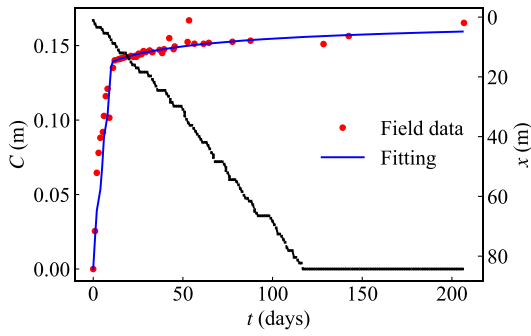
Chainage 10326 m

Figure 3.20: Convergence fitting (examples of sections at chainages 10316, 10321 and 10326 m)

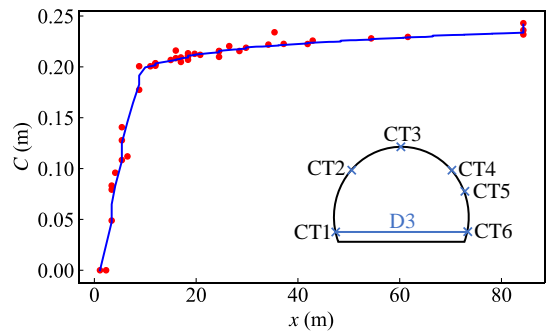
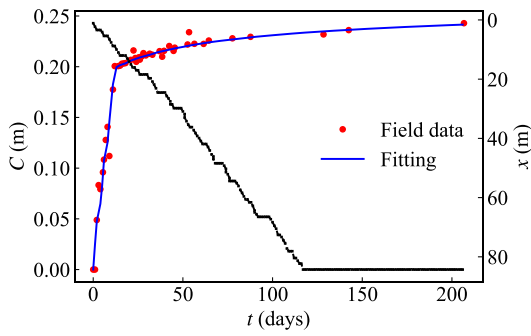
3.3.3 Anisotropic response

In order to understand the anisotropic deformation of the rock mass, the strings convergences are studied individually. The fitting of the convergence law parameters is performed for every section following the 2 stages of excavation and support installation. As for example, the section at chainage 10326

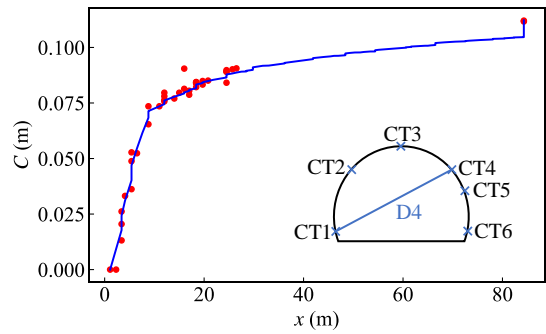
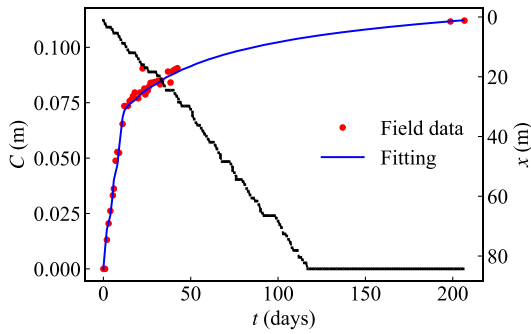
m is shown in Figure 3.21). The detailed fitting results of all the studied sections are shown in Appendix B.



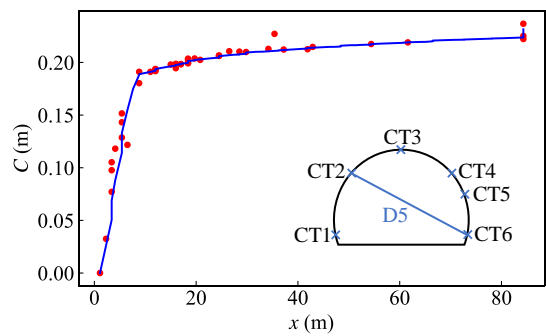
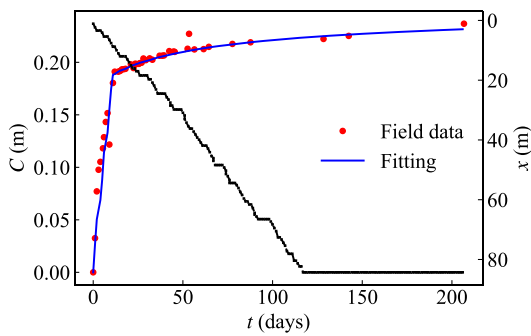
String D2



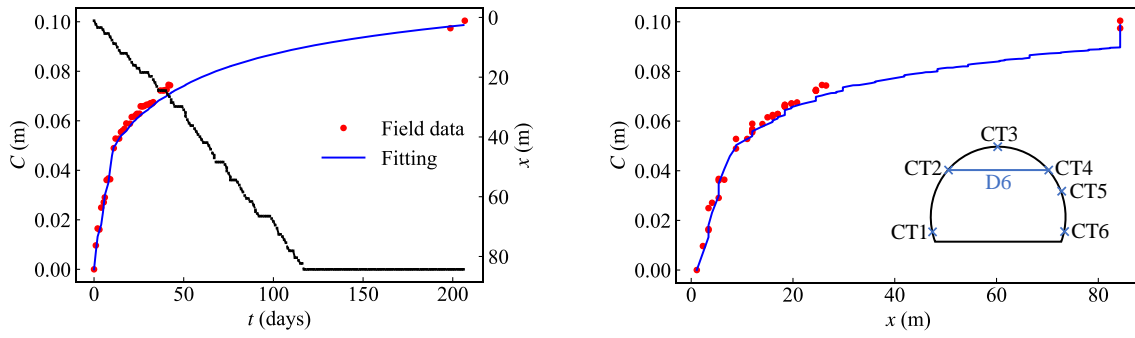
String D3



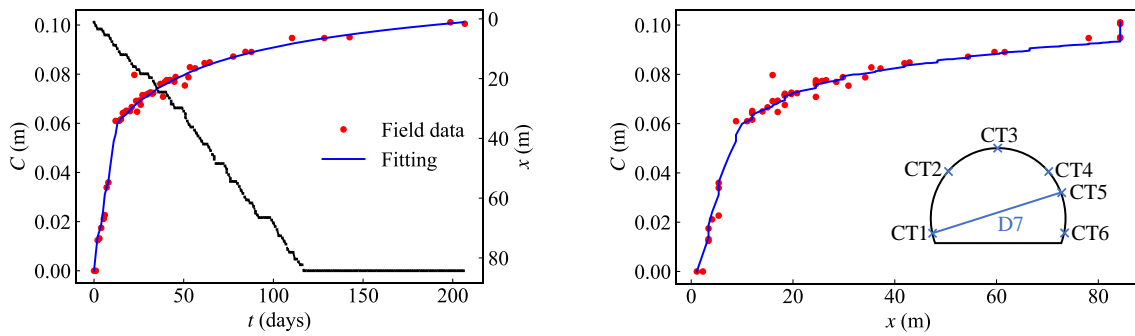
String D4



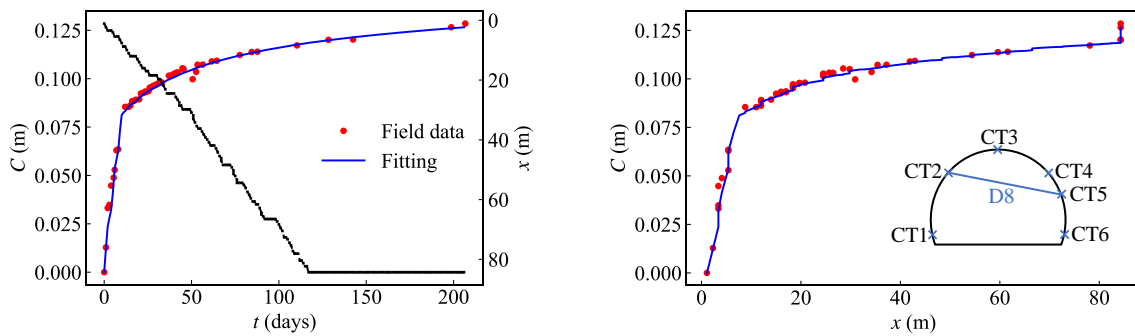
String D5



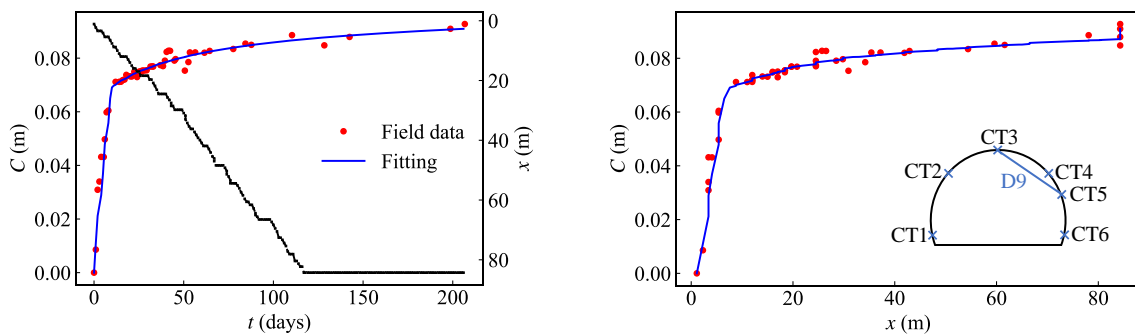
String D6



String D7



String D8



String D9

Figure 3.21: Convergence fitting at chainage 10326 m

The convergence of different strings can be well reproduced by fitting only the instantaneous convergence for the two excavation stages $C_{\infty xA}$ and $C_{\infty xB}$ respectively. The obtained parameters and the predicted long-term convergence for different strings of the sections in SMP4-PS are shown in Table 3.9. The monitoring targets are installed on the steel ribs [C], on the tunnel wall [T] or on the head of bolts [B]. The parameters of the convergence law vary from one to another section.

Table 3.9: Proposed parameters of convergence law in SMP4-PS [Unit: m]

Section	String	$C_{\infty xA}$	$C_{\infty xB}$	C_{lostA}	C_{AB}	C_{∞}
10312 C	D3	0.0456	0.0070	0.0218	0.1086	0.2402
10313 T	D3	0.0384	0.0072	0.0358	0.0635	0.2157
	D4	0.0260	0.0087	0.0242	0.0459	0.2104
	D5	0.0202	0.0049	0.0188	0.0340	0.1315
	D6	0.0124	0.0052	0.0115	0.0222	0.1184
10316 C	D5	0.0270	0.0058	0.0089	0.0939	0.1914
	D6	0.0082	0.0048	0.0027	0.0274	0.1037
10316 T	D1	0.0239	0.0062	0.0503	0.0330	0.1785
	D3	0.0215	0.0056	0.0453	0.0348	0.1652
	D4	0.0346	0.0076	0.0728	0.0478	0.2370
	D6	0.0072	0.0054	0.0151	0.0127	0.1109
10321 C	D3	0.0530	0.0060	0.0318	0.1431	0.2685
	D4	0.0256	0.0044	0.0154	0.0662	0.1500
	D7	0.0230	0.0073	0.0138	0.0665	0.1945
10321 T	D2	0.0229	0.0021	0.0226	0.0525	0.1082
	D3	0.0430	0.0053	0.0424	0.0982	0.2221
	D4	0.0298	0.0077	0.0294	0.0636	0.2116
	D5	0.0338	0.0049	0.0333	0.0825	0.1920
	D6	0.0348	0.0069	0.0344	0.0711	0.2119
10326 T	D2	0.0642	0.0026	0.0192	0.1408	0.2016
	D3	0.0779	0.0058	0.0232	0.2006	0.3152
	D4	0.0292	0.0055	0.0087	0.0735	0.1687
	D5	0.0828	0.0057	0.0247	0.1911	0.3060
	D6	0.0217	0.0065	0.0065	0.0528	0.1617
	D7	0.0226	0.0057	0.0067	0.0610	0.1575
	D8	0.0389	0.0058	0.0116	0.0854	0.1889
	D9	0.0347	0.0028	0.0104	0.0712	0.1257
10327 C	D2	0.0334	0.0014	0.0009	0.0708	0.0934
	D3	0.0797	0.0061	0.0021	0.1961	0.2963
	D4	0.0153	0.0037	0.0004	0.0449	0.1041
	D5	0.0603	0.0062	0.0016	0.1447	0.2451
	D6	0.0101	0.0043	0.0003	0.0310	0.1000
	D7	0.0322	0.0055	0.0008	0.0929	0.1826
	D8	0.0223	0.0053	0.0006	0.0649	0.1505
10335 T	D1	0.0041	0.0035	0.0035	0.0092	0.0667
	D3	0.0359	0.0045	0.0303	0.0794	0.1800
	D4	0.0281	0.0068	0.0237	0.0607	0.1889
	D5	0.0049	0.0039	0.0041	0.0137	0.0788
	D6	0.0217	0.0050	0.0183	0.0468	0.1430
	D7	0.0356	0.0058	0.0300	0.0775	0.1974
	D8	0.0286	0.0048	0.0241	0.0619	0.1600
	D9	0.0318	0.0036	0.0268	0.0676	0.1495

Section	String	$C_{\infty xA}$	$C_{\infty xB}$	C_{lostA}	C_{AB}	C_{∞}
10336 C	D1	0.0063	0.0009	0.0035	0.0156	0.0335
	D2	0.0088	0.0038	0.0050	0.0158	0.0794
	D3	0.0240	0.0046	0.0135	0.0455	0.1307
	D7	0.0112	0.0045	0.0063	0.0282	0.1041
10341 T	D4	0.0081	0.0021	0.0052	0.0279	0.0641
	D7	0.0089	0.0020	0.0057	0.0279	0.0640
	D8	0.0082	0.0017	0.0053	0.0228	0.0543
10346 T	D2	0.0113	0.0002	0.0097	0.0450	0.0576
	D3	0.0163	0.0007	0.0140	0.0576	0.0809
10350 T	D2	0.0083	0.0018	0.0077	0.0278	0.0605
	D3	0.0208	0.0020	0.0191	0.0809	0.1281
	D5	0.0123	0.0021	0.0113	0.0377	0.0784
	D6	0.0083	0.0015	0.0077	0.0287	0.0576
10356 T	D5	0.0104	0.0015	0.0105	0.0286	0.0613
	D6	0.0061	0.0011	0.0062	0.0162	0.0390
10361 T	D3	0.0083	0.0024	0.0026	0.0345	0.0731
	D4	0.0085	0.0009	0.0027	0.0340	0.0509
	D6	0.0027	0.0007	0.0008	0.0137	0.0249
10366 T	D3	0.0152	0.0025	0.0107	0.0404	0.0878
	D4	0.0120	0.0014	0.0084	0.0306	0.0593
	D5	0.0163	0.0028	0.0115	0.0403	0.0928
	D6	0.0110	0.0016	0.0077	0.0277	0.0587
10371 B	D1	0.0113	0.0006	0.0115	0.0368	0.0574
	D2	0.0056	0.0011	0.0057	0.0193	0.0409
	D4	0.0110	0.0014	0.0112	0.0459	0.0782
	D5	0.0097	0.0017	0.0099	0.0274	0.0627
	D6	0.0132	0.0006	0.0135	0.0523	0.0746
10376 B	D1	0.0117	0.0007	0.0057	0.0339	0.0495
	D2	0.0409	0.0009	0.0199	0.1272	0.1607
	D3	0.0297	0.0007	0.0144	0.0962	0.1212
	D4	0.0185	0.0013	0.0090	0.0618	0.0900
	D5	0.0305	0.0006	0.0149	0.0897	0.1139
10381 B	D1	0.0182	0.0012	0.0115	0.0454	0.0748
	D2	0.0261	0.0015	0.0166	0.0659	0.1050
	D3	0.0379	0.0015	0.0241	0.0976	0.1454
	D4	0.0379	0.0013	0.0241	0.1054	0.1497
	D5	0.0312	0.0013	0.0198	0.0782	0.1179
	D6	0.0366	0.0004	0.0233	0.0975	0.1265
10385 B	D1	0.0212	0.0021	0.0101	0.0406	0.0828
	D2	0.0328	0.0021	0.0156	0.0717	0.1200
	D3	0.0473	0.0020	0.0226	0.1014	0.1556
	D4	0.0365	0.0022	0.0174	0.0861	0.1374
	D5	0.0414	0.0018	0.0198	0.0895	0.1378
	D6	0.0270	0.0039	0.0129	0.0641	0.1387
10390 B	D1	0.0255	0.0009	0.0166	0.0513	0.0821
	D2	0.0246	0.0008	0.0160	0.0509	0.0789
	D3	0.0263	0.0001	0.0172	0.0546	0.0726
	D4	0.0373	0.0006	0.0244	0.0734	0.1061
	D5	0.0246	0.0009	0.0161	0.0506	0.0809
	D6	0.0190	0.0007	0.0124	0.0353	0.0577

In most sections, the horizontal string D3 presents the largest convergence of the section. The fitting of the shortening of string D3 is validated in more sections than of the mean convergence. This allows to compare the parameters of the convergence law and predicted long-term convergence for a larger range (Figure 3.22). The same conclusion is obtained that the convergence in the first zone of SMP4-PS is much larger, which corresponds to the higher proportion of Carboniferous schists and coal. The final convergence in this case are much smaller than in SMP4-GS, and varies from 0.07 to 0.32 m.

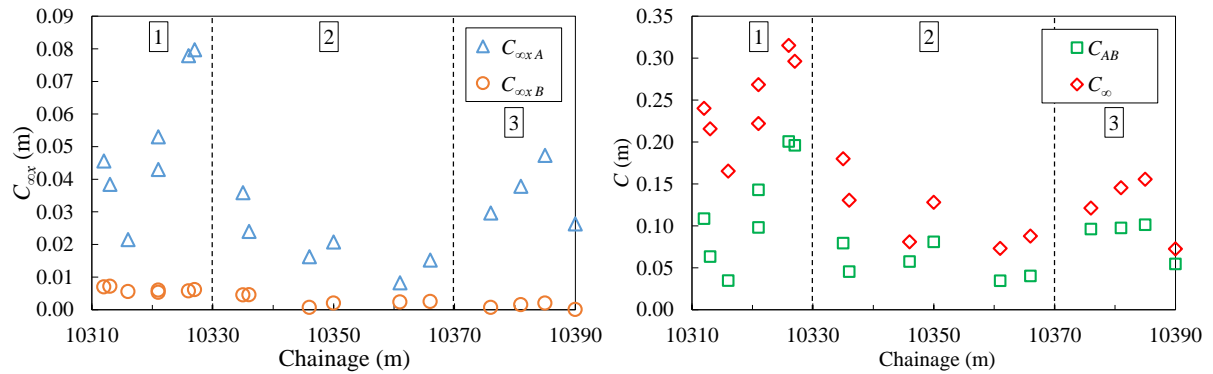


Figure 3.22: Parameters of the convergence law and predicted long-term convergence for string D3

The predicted long-term convergences of the fitted circle and of the string D3 are compared (Figure 3.23). In general, the D3 string shows almost the same convergence as the diameter of the fitted circle in the zones 1 and 3 where the fitting results are available for both these two cases.

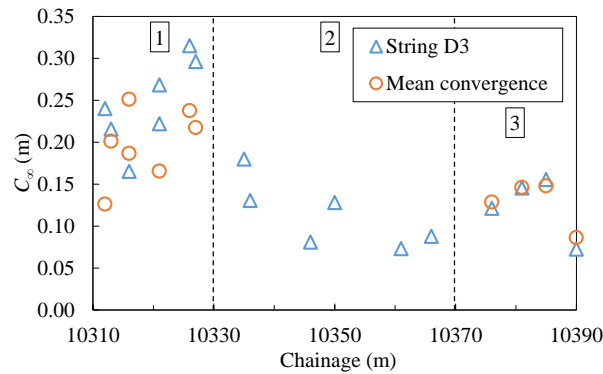


Figure 3.23: Predicted long-term convergence

3.4 SMP4-RPS

In a later stage, the part of tunnel that has been excavated in small dimension has been enlarged to the full section (SMP4-RPS) with a radius of 6.5 m. The convergence data are available for this part and analyzed with the proposed procedure for SMP4-PS.

3.4.1 Field monitoring data of SMP4-RPS

Five monitoring targets are installed on the tunnel wall or on the steel rib with sliding joints. The coordinates of these targets at the first convergence measurement are available (Figure 3.24). The initial

coordinates of the monitoring targets are different from one section to another. With the help of these targets, the tunnel convergence is recorded by the displacement of the targets and shortening of the strings between the targets.

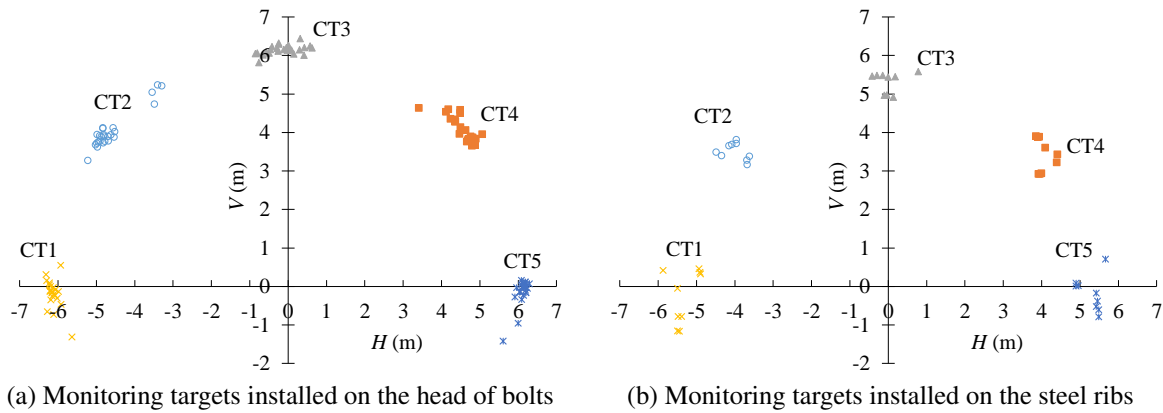


Figure 3.24: Initial coordinates of the monitoring targets for all the sections in SMP4-RPS

The convergence is monitored for more than 400 days and the maximal strings convergence recorded reaches more than 0.3 m (Figure 3.25a). The convergence is much higher for the targets installed on the tunnel wall than for those on the steel ribs. The sections with few measurements or with very low convergence are not analyzed. Therefore, 22 sections with the targets installed on the tunnel wall are studied (Figure 3.25b).

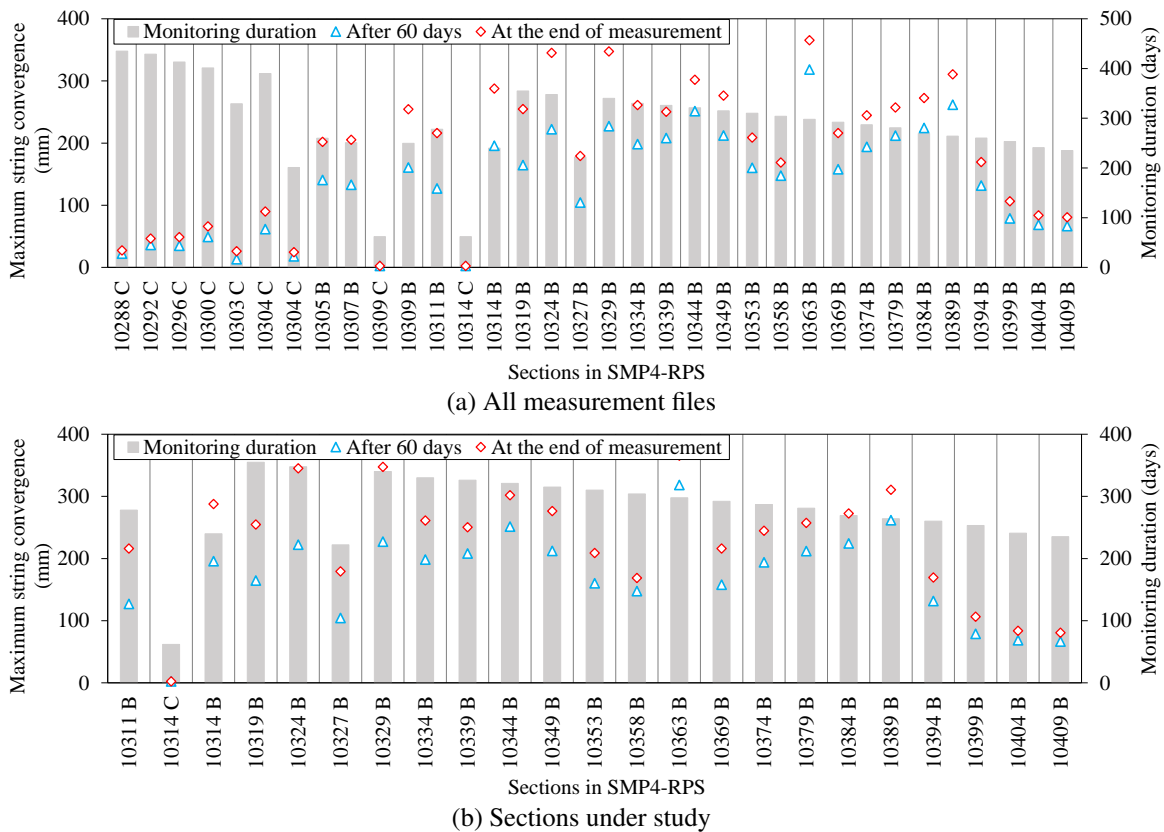


Figure 3.25: Convergence measurements of the sections in SMP4-RPS

3.4.2 Mean convergence

The mean convergence is studied for SMP4-RPS by fitting a circle with 3 parameters (X_c , Y_c and r). The initial values of the parameters are shown in Figure 3.26. As the center of the fitted circle does not move too much, the coordinates of the circle center are then fixed to their initial values and the only parameter to be fitted is the circle radius r . It is noted that SMP4-RPS begins at chainage 10310 m after SMP4-RSR.

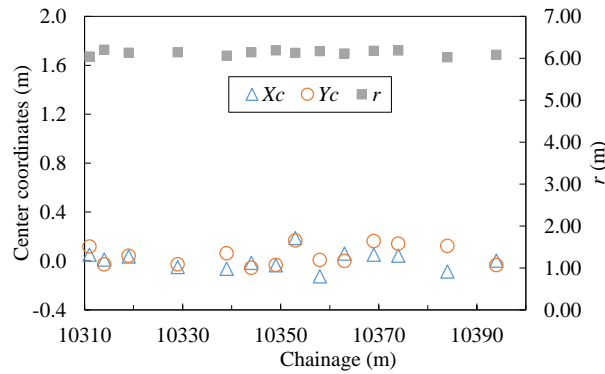


Figure 3.26: Initial parameters of fitted circle in SMP4-RPS

Then, the evolution of the circle radius is analyzed by fitting the convergence law in two stages following the same procedure as SMP4-PS. 4 parameters of the convergence law are fixed ($T = 20$ days; $X = 15$ m; $m = 18$ and $n = 0.3$) and the only parameters to evaluate is $C_{\infty x}$ for the two stages of excavation and support installation.

The parameters and the predicted long-term convergence are obtained and shown in Table 3.10. The detailed fitting results of all the studied sections are shown in Appendix C. The final convergences of these sections are various from one section to another (Figure 3.27). The second zone shows smaller convergence than the first zone because of stiffer ground, even though the temporary support system is installed farther from the tunnel face in the second zone.

Table 3.10: Parameters of convergence law in SMP4-RPS [Unit: m]

Section	$C_{\infty xA}$	$C_{\infty xB}$	C_{lostA}	C_{AB}	C_{∞}
10305 B	0.0450	0.0138	0.0195	0.0733	0.3241
10307 B	0.0558	0.0133	0.0215	0.0403	0.2980
10311 B	0.0251	0.0220	0.0507	0.0187	0.4287
10314 B	0.0449	0.0223	0.0082	0.0756	0.4657
10319 B	0.0439	0.0197	0.0169	0.0262	0.3982
10329 B	0.0552	0.0278	0.0116	0.0605	0.5623
10339 B	0.0433	0.0157	0.0145	0.1805	0.4182
10344 B	0.0541	0.0160	0.0181	0.2329	0.4715
10349 B	0.0455	0.0106	0.0242	0.2009	0.3704
10353 B	0.0302	0.0153	0.0180	0.1507	0.3694
10358 B	0.0235	0.0124	0.0173	0.1030	0.2895
10363 B	0.0276	0.0103	0.0203	0.1204	0.2811
10369 B	0.0245	0.0213	0.0146	0.1305	0.4205
10374 B	0.0201	0.0118	0.0078	0.0953	0.2546
10384 B	0.0383	0.0122	0.0443	0.1835	0.3850
10394 B	0.0219	0.0076	0.0073	0.1198	0.2256

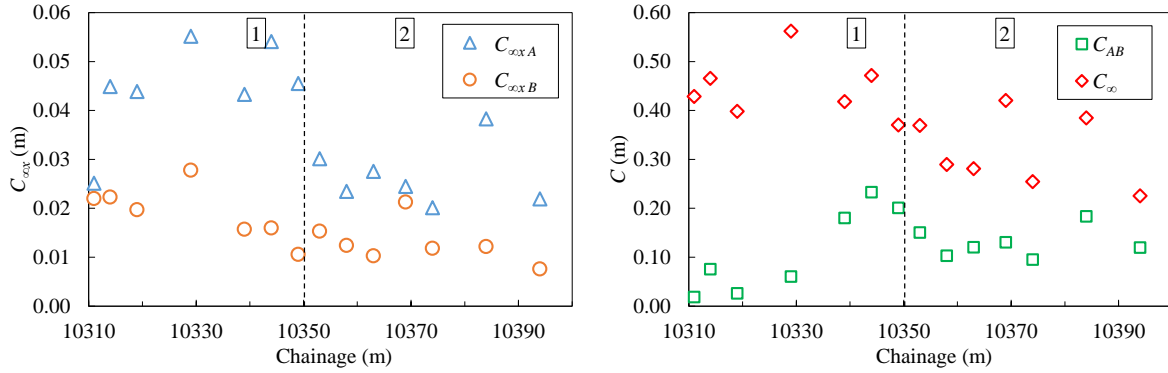


Figure 3.27: Parameters of the convergence law and predicted long-term convergence

3.4.3 Anisotropic response

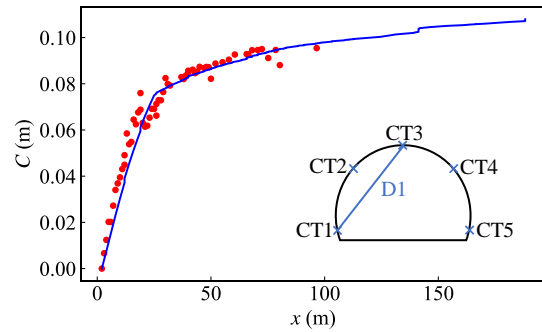
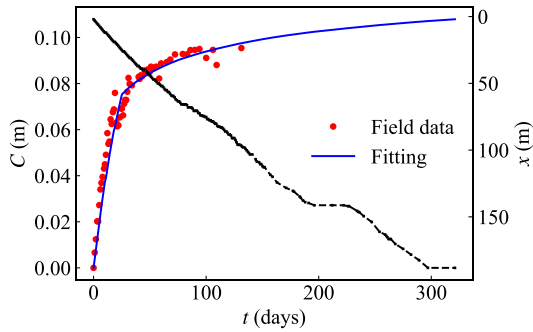
Following the same procedure as SMP4-PS, the anisotropic convergence of RPS is studied. The strings shortenings are fitted by the convergence law in two stages and the obtained values of the convergence law parameters are shown in Table 3.11 for the section between chainage 10305 and 10384. The detailed fitting results of all the studied sections are shown in Appendix D. Fitting of the strings convergence at chainage 10344 m is shown as an example (Figure 3.28).

Table 3.11: Parameters of convergence law in SMP4-RPS [Unit: m]

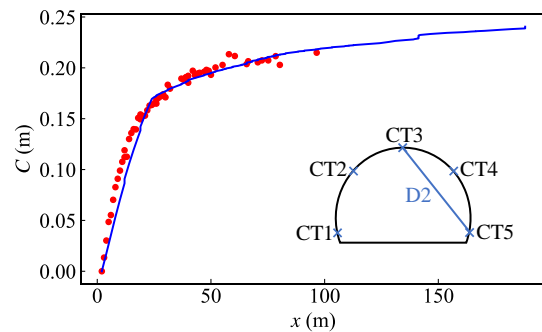
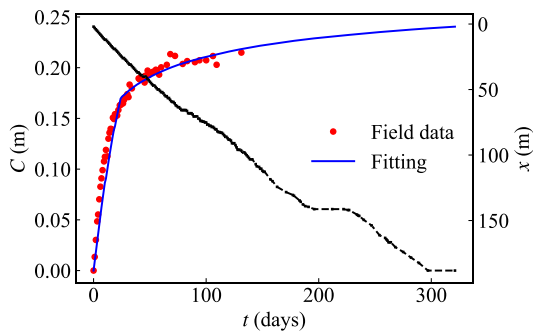
Section	String	$C_{\infty xA}$	$C_{\infty xB}$	C_{lostA}	C_{AB}	C_{∞}
10305 B	D1	0.0444	0.0091	0.0192	0.0698	0.2412
	D2	0.0159	0.0064	0.0069	0.0238	0.1388
	D3	0.0436	0.0136	0.0189	0.0700	0.3179
	D4	0.0511	0.0140	0.0221	0.0844	0.3410
	D5	0.0382	0.0131	0.0166	0.0629	0.2995
	D6	0.0389	0.0123	0.0169	0.0672	0.2898
10307 B	D1	0.0460	0.0123	0.0177	0.0331	0.2695
	D2	0.0384	0.0099	0.0148	0.0264	0.2175
	D3	0.0593	0.0165	0.0228	0.0420	0.3590
	D4	0.0531	0.0155	0.0205	0.0433	0.3391
	D5	0.0411	0.0185	0.0158	0.0288	0.3737
	D6	0.0318	0.0163	0.0122	0.0277	0.3307
10309 B	D1	0.0379	0.0142	0.0127	0.0374	0.3018
	D2	0.0432	0.0105	0.0144	0.0263	0.2263
	D3	0.0764	0.0209	0.0255	0.0450	0.4408
	D4	0.0524	0.0191	0.0175	0.0324	0.3878
	D5	0.0743	0.0220	0.0248	0.0474	0.4611
	D6	0.0507	0.0193	0.0169	0.0343	0.3927
10311 B	D1	0.0157	0.0164	0.0317	0.0116	0.3118
	D2	0.0122	0.0101	0.0247	0.0092	0.1993
	D3	0.0249	0.0223	0.0502	0.0186	0.4333
	D4	0.0203	0.0189	0.0410	0.0143	0.3637
	D5	0.0232	0.0231	0.0468	0.0187	0.4429
	D6	0.0189	0.0199	0.0380	0.0147	0.3787

Section	String	$C_{\infty xA}$	$C_{\infty xB}$	C_{lostA}	C_{AB}	C_{∞}
10319 B	D1	0.0176	0.0182	0.0068	0.0123	0.3476
	D2	0.0308	0.0118	0.0119	0.0171	0.2414
	D3	0.0457	0.0221	0.0176	0.0273	0.4431
	D4	0.0279	0.0189	0.0107	0.0167	0.3681
	D5	0.0446	0.0183	0.0172	0.0272	0.3738
	D6	0.0298	0.0147	0.0115	0.0186	0.2955
10329 B	D3	0.0543	0.0281	0.0114	0.0619	0.5684
	D4	0.0398	0.0220	0.0084	0.0460	0.4426
	D5	0.0516	0.0286	0.0109	0.0595	0.5745
	D6	0.0440	0.0227	0.0093	0.0513	0.4606
10339 B	D1	0.0117	0.0040	0.0039	0.0560	0.1161
	D2	0.0378	0.0088	0.0126	0.1414	0.2787
	D3	0.0420	0.0123	0.0140	0.1753	0.3635
	D4	0.0368	0.0121	0.0123	0.1545	0.3388
	D5	0.0410	0.0088	0.0137	0.1640	0.3030
	D6	0.0310	0.0082	0.0103	0.1254	0.2524
10344 B	D1	0.0186	0.0047	0.0062	0.0792	0.1507
	D2	0.0434	0.0100	0.0145	0.1796	0.3326
	D3	0.0532	0.0121	0.0178	0.2266	0.4118
	D4	0.0471	0.0106	0.0157	0.2051	0.3670
	D5	0.0472	0.0103	0.0158	0.2011	0.3590
	D6	0.0385	0.0092	0.0129	0.1679	0.3080
10349 B	D1	0.0159	0.0068	0.0085	0.0738	0.1763
	D2	0.0303	0.0032	0.0161	0.1162	0.1770
	D3	0.0445	0.0126	0.0236	0.1959	0.3921
	D4	0.0398	0.0112	0.0212	0.1730	0.3485
	D5	0.0388	0.0090	0.0206	0.1632	0.3076
	D6	0.0367	0.0094	0.0195	0.1520	0.3010
10353 B	D2	0.0195	0.0079	0.0116	0.1053	0.2209
	D3	0.0277	0.0127	0.0166	0.1425	0.3249
	D4	0.0126	0.0089	0.0076	0.0676	0.1921
	D5	0.0282	0.0106	0.0169	0.1410	0.2967
	D6	0.0103	0.0057	0.0061	0.0459	0.1264
10358 B	D1	0.0174	0.0082	0.0128	0.0743	0.1988
	D2	0.0302	0.0100	0.0223	0.1290	0.2874
	D3	0.0245	0.0112	0.0181	0.1077	0.2781
	D4	0.0265	0.0097	0.0196	0.0961	0.2478
	D5	0.0247	0.0111	0.0182	0.1125	0.2824
	D6	0.0203	0.0083	0.0150	0.0685	0.1967
10363 B	D1	0.0178	0.0100	0.0131	0.0732	0.2235
	D2	0.0360	0.0088	0.0266	0.1537	0.3011
	D3	0.0265	0.0113	0.0195	0.1163	0.2907
	D4	0.0557	0.0148	0.0411	0.2312	0.4751
	D5	0.0289	0.0121	0.0213	0.1265	0.3138
	D6	0.0652	0.0172	0.0481	0.2716	0.5541

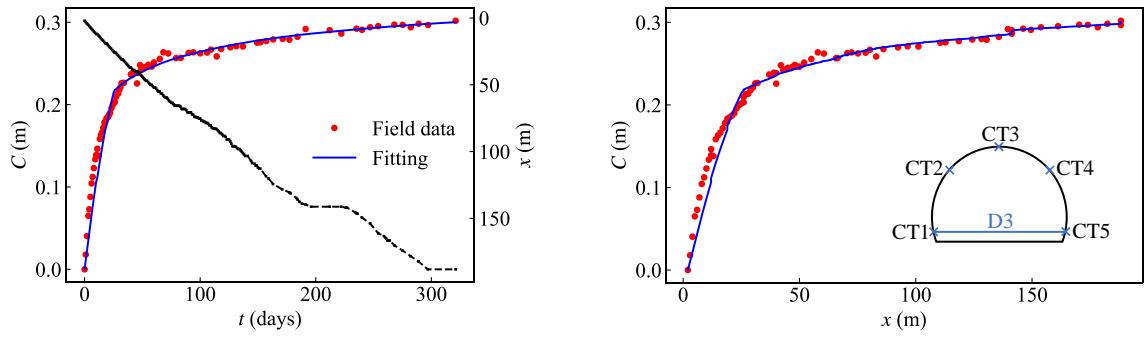
Section	String	$C_{\infty xA}$	$C_{\infty xB}$	C_{lostA}	C_{AB}	C_{∞}
10369 B	D1	0.0227	0.0072	0.0136	0.1049	0.2113
	D2	0.0243	0.0085	0.0145	0.1397	0.2645
	D3	0.0227	0.0128	0.0136	0.1268	0.3062
	D4	0.0261	0.0094	0.0156	0.1440	0.2814
	D5	0.0259	0.0154	0.0155	0.1411	0.3560
	D6	0.0292	0.0079	0.0174	0.1525	0.2726
10374 B	D1	0.0327	0.0115	0.0126	0.1720	0.3318
	D2	0.0197	0.0094	0.0076	0.0995	0.2280
	D3	0.0202	0.0105	0.0078	0.1134	0.2556
	D4	0.0348	0.0124	0.0134	0.1833	0.3558
	D5	0.0217	0.0071	0.0084	0.1123	0.2120
	D6	0.0284	0.0073	0.0109	0.1466	0.2506
10379 B	D1	0.0269	0.0061	0.0104	0.1414	0.2309
	D2	0.0258	0.0094	0.0099	0.1377	0.2688
	D3	0.0304	0.0105	0.0117	0.1606	0.3082
	D4	0.0372	0.0122	0.0143	0.2001	0.3724
	D5	0.0246	0.0070	0.0095	0.1344	0.2349
	D6	0.0256	0.0092	0.0099	0.1404	0.2694
10384 B	D1	0.0294	0.0109	0.0340	0.1696	0.3439
	D3	0.0371	0.0145	0.0430	0.1753	0.4053
	D4	0.0423	0.0143	0.0490	0.2066	0.4405
	D5	0.0276	0.0090	0.0319	0.1312	0.2790
	D6	0.0280	0.0091	0.0324	0.1413	0.2908



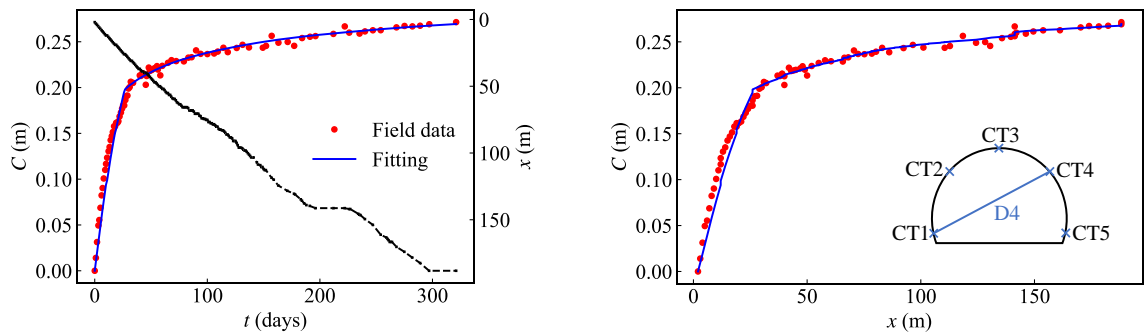
String D1



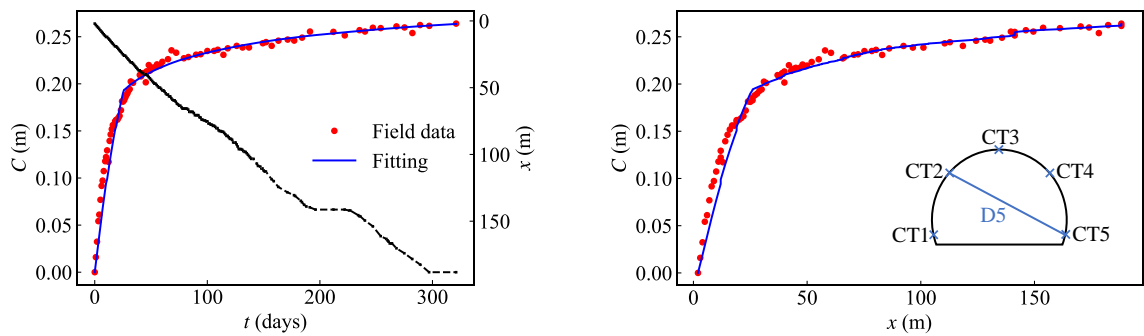
String D2



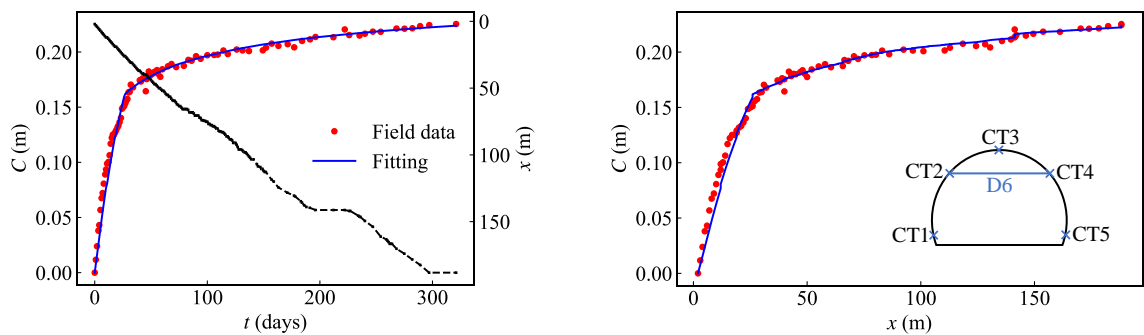
String D3



String D4



String D5



String D6

Figure 3.28: Convergence fitting at chainage 10344 m

The field data of SMP4-RPS can be well reproduced by fitting only the parameters of instantaneous convergence for two stages $C_{\infty XA}$ and $C_{\infty XB}$ of the convergence law. The fitting results of string D3 is also studied in SMP4-RPS. The same conclusion can be obtained that the final convergence of different sections varies from one to another section and is higher before chainage 10350 m (Figure 3.29).

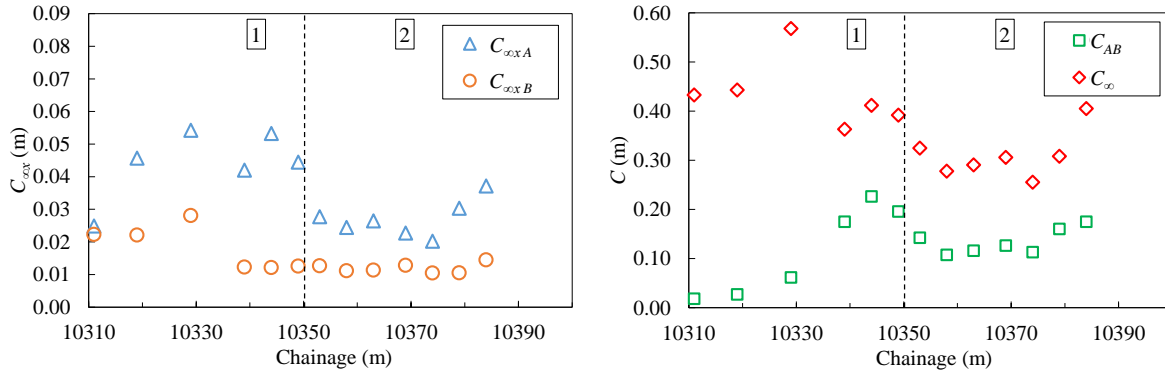


Figure 3.29: Parameters of the convergence law and predicted long-term convergence D3

Comparison of the values of the final convergence C_{∞} has been carried out between the fitting results of the mean convergence and of the shortening of the string D3. The final convergence is very close in these two cases and the string D3 can be representative for the mean convergence in SMP4-RPS (Figure 3.30).

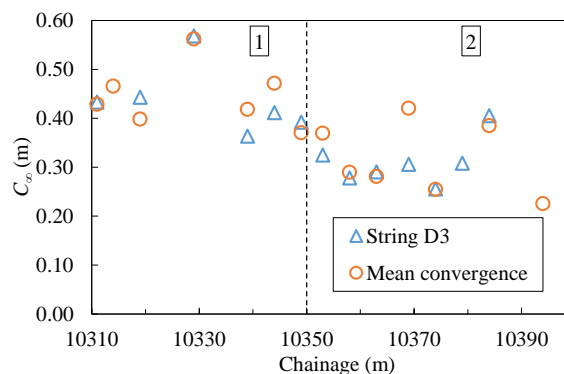


Figure 3.30: Predicted long-term convergence

3.5 Summary

In this chapter, the developed methods to analyze the monitoring convergence data and the obtained parameter values of the proposed convergence law in SMP2 is applied to SMP4, which is much deeper and excavated in another direction.

In SMP4-GS, the sections with large convergence are studied. The present work accounts for the material heterogeneity in radial direction by separating the monitoring data for different rock materials and only the upper part of the section situated in the Houiller formation is studied. The anisotropy of section closure is identified by the consideration of a preferred orientation of the tunnel deformation for each section. The top left side of the section deforms more. The deformed shape of the cross section can be fitted with an ellipse, which permits to simplify and describe the observed anisotropic closure of

the section. With the parameters obtained from SMP2, the convergence can be reproduced for the first studied sections, and the monitoring data of a short period is sufficient to accurately predict long-term convergence. However, when the tunnel approaches to the collapse section at chainage 10303 m, the convergence becomes much higher and higher. Larger and larger values of the parameter T are required to fit the convergence data. This high value of parameter T reflects the damaged state of the rock mass and is seen as an indicator of the collapse.

In SMP4-PS and RPS, the measured convergences are much smaller than those in SMP4-GS as the material is stiffer. A single orientation cannot be identified for the anisotropic convergence because the rock mass is highly heterogeneous. In the present work, the mean convergence and the strings convergence are studied and are reproduced by fitting the convergence law. The mean convergence is studied by fitting a circle for the deformed section. As the convergence measurements cover two stages of excavation and support installation, fitting is performed separately for these two stages with the new proposed procedure. The same values of parameters of the convergence law are kept as for SMP4-GS taking into account the size effect on the parameter X , which permits to fit only $C_{\infty x}$ of the two stages for each section. In these two cases, the convergence of the horizontal string D3 can represent the mean convergence of the section.

The long-term convergences normalized by the tunnel section diameter of SMP4-PS and RPS are compared (Figure 3.31). The normalized predicted convergences are similar for these two profiles for the most sections, except from chainage 10340 to 10370 m, the normalized convergence is larger for SMP4-RPS than for SMP4-PS. This reflects the heterogeneity of the rock mass not only in longitudinal direction but also in the radial direction. The comparison of the final convergence shows that the excavating method with first a small size section and then reprofiling dose not have significant advantages on reducing the long-term convergence.

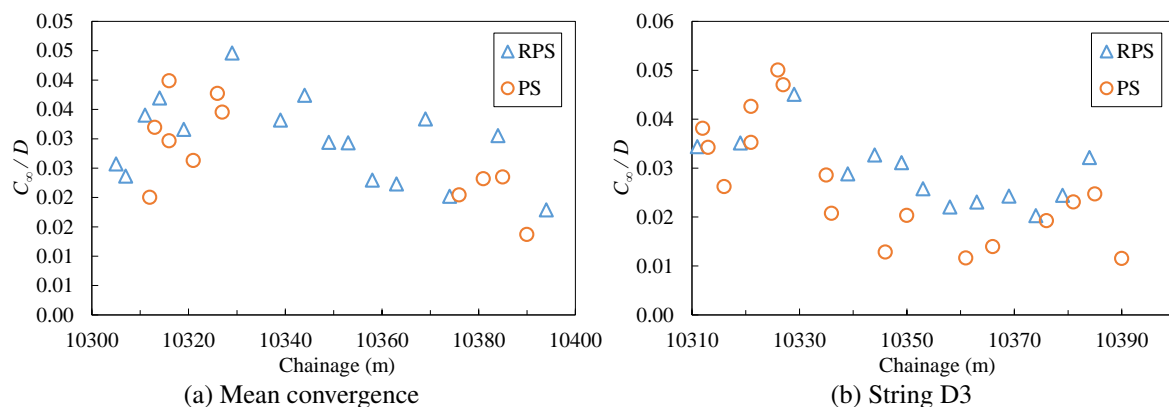


Figure 3.31: Predicted long-term convergence normalized by the diameter of SMP4-PS and RPS

CHAPTER 4

NUMERICAL MODELING

Numerical simulations have been carried out to complete the analysis of the squeezing behavior observed during and after excavation of the SMP exploratory galleries in the encountered tectonized Houiller formation. In the thesis of [Tran-Manh \(Tran-Manh, 2014; Tran-Manh et al., 2015\)](#), a constitutive model has been developed and implemented in the calculation code *FLAC3D* ([Itasca, 2017](#)) for SMP2 to simulate the short-term time-dependent and anisotropic convergence of rock mass at the time scale of the excavation work. This constitutive law combines the CVISC visco-elastic-plastic model and the ubiquitous-joint model.

Based on the studies performed for SMP2 in the previous thesis, the present work aims at extending the numerical simulations to large time scale (ten years) and also at performing new computations to simulate the behavior of SMP4. The developed model and obtained parameters are first tested. The validity of the model for mid-term and long-term response is first examined for SMP2 with respect to the stresses accumulated over time in the final lining several years after installation. The same constitutive parameters of the rock mass are applied and the specific support system and the reprofiling process are considered. As a single anisotropic direction cannot be identified in SMP4 (PS and RPS), the average response of SMP4 is simulated by considering an isotropic behavior of the rock mass (i.e. without introducing the ubiquitous joints) and new values of the constitutive parameters are fitted for the rock mass encountered in SMP4.

4.1 Numerical models and parameters

A numerical model has been proposed to simulate time-dependent and anisotropic behavior of rock and has been validated through SMP2 data (Tran-Manh, 2014; Tran-Manh et al., 2015). The typical values of constitutive parameters have been obtained and the convergence data have been well reproduced for several sections in SMP2. This model is applied in the present work with several assumptions and adaptations taking into account the excavation procedure and the support system of the galleries.

4.1.1 Modeling assumptions and simplifications

The real conditions of the SMP field works are complex. In the modeling we focus on the dominant features of the tunnel excavation conditions. Therefore, several assumptions have been considered in the present study and secondary effects have been purposely neglected.

First, as no reliable measurement of the initial stress state is available in the Houiller formation, it is assumed that the initial stress state is geostatic and isotropic with $\sigma_v = \sigma_H = \sigma_h = \gamma h$ and $\gamma = 27 \text{ kN/m}^3$. The Houiller formation was encountered at a depth of near 315 m in SMP2 and at 600 m in SMP4. Thus, the in-situ stress in Houiller formation is assumed to be 8.5 MPa for SMP2 and 16.2 MPa for SMP4. This is in accordance with the assumptions made by the project engineers in the design reports of these galleries.

In the field work, excavation of the section is performed first for the upper part and then for the lower part. The real geometry of the cross section is complex. We ignore the influence of the section geometry to focus on the ground and support behavior after excavation. We assume that the galleries are circular and opened in one step. This allows us to avoid geometrical problems in largestrain modeling and singular points which may accumulate computational errors.

The ground is very heterogeneous. Reinforcement system including bolts and anchors is applied to improve the properties of the highly fractured ground. This reinforcement system is not explicitly modeled. Steel ribs with sliding joints are not introduced. The influence of these elements is included in the properties of the equivalent homogenized ground. This allows us to focus on the long-term response of ground and support. Sliding between the support system and the ground is not allowed.

4.1.2 Developed constitutive model for rock mass in SMP2

FLAC3D is a three-dimensional numerical code that can simulate a full range of nonlinear static and dynamic problems. In this code, continua are simulated with the finite volume method: generalized finite difference method with arbitrary element shapes. Materials are represented by polyhedral elements within a three-dimensional grid. Each element behaves according to a prescribed linear or nonlinear stress-strain law in response to applied forces or boundary restraints. For both dynamic and quasi-static problems, *FLAC3D* solves the full dynamic equations of motion. To model the quasi-static response of a system, damping is used to absorb kinetic energy. *FISH* is a programming language embedded in *FLAC3D*, which gives access to all internal variables and allows custom-written functions.

Different from the general usage in geotechnical domain, the sign conventions in *FLAC3D* are used in the following studies:

- Positive stresses indicate tension; negative stresses indicate compression;
- Positive strain indicates extension; negative strain indicates compression.

And the principal stresses are defined with $\sigma_1 \leq \sigma_2 \leq \sigma_3$ by default (Table 4.1).

Table 4.1: Principal stress conventions (Itasca, 2017)

<i>FLAC3D</i>	minimum	intermediate	maximum
Symbol	σ_1	σ_2	σ_3

The CVISC model (presented in Section 1.3.2) and ubiquitous-joint approach (presented in Section 1.3.3) have been combined and implemented in *FLAC3D* code to simulate the time-dependent and anisotropic deformation observed in SMP2 (Tran-Manh, 2014; Tran-Manh et al., 2015). Using the developed combined model, both the yield criteria of solid matrix (CVISC model) and of weakness planes (ubiquitous-joint model) are checked for every calculation step. Yielding can be detected in solid matrix or on weakness planes.

The available Mohr-Coulomb failure criterion using in the CVISC model is combined with tension yield function (tension cut-off) in *Flac3D* (Figure 4.1). The Mohr-Coulomb yield function f^s and the tension yield function f^t are defined by the following equations:

$$f^s = -\sigma_1 + \sigma_3 N_\phi - 2c\sqrt{N_\phi}, \text{ with } N_\phi = \frac{1 + \sin \phi}{1 - \sin \phi} \quad (4.1)$$

$$f^t = \sigma_3 - \sigma^t \quad (4.2)$$

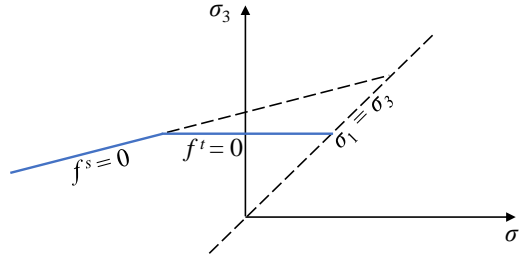


Figure 4.1: Mohr-Coulomb criterion with tension cut-off

4.1.3 Obtained knowledge from numerical simulations of SMP2

The time-dependent and anisotropic convergence of the sections in SMP2 between chainage 1272 and 1384 m has been studied by Tran-Manh et al. (2015). Based on the field data processing, an elliptical deformation of the tunnel section is considered and the evolution of the major and minor axes of the ellipse is studied by performing 3D numerical simulations of the tunnel excavation.

The initial state of stress was considered as isotropic: $\sigma_x = \sigma_y = \sigma_z = 8.5$ MPa. Only the ground has been considered in the modeling (Figure 4.2); the reinforcement (bolts, shotcrete) and support system (steel ribs with sliding joints) were not explicitly included in the computations. Thus, the obtained constitutive parameters of ground include the influence of the reinforcement and support system.

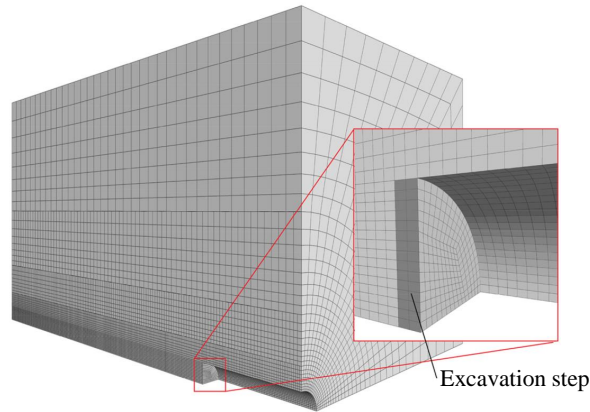


Figure 4.2: 3D mesh for the numerical simulation of SMP2 (Tran-Manh et al., 2015)

Three different zones have been identified along the tunnel between chainage 1272 and 1384 m and the values of constitutive parameters are shown in Table 4.2. The details of the calibration process can be found in Tran-Manh (2014). Several model parameters (E , ν , ϕ , σ_t , ψ , ϕ_j , σ_{tj} and ψ_j) are fixed for all the sections under study. The parameters describing the visco-elastic behavior of the ground (G^K , η^K and η^M) keep constant values in each zone and the cohesion of rock mass and of the weakness planes (c and c_j) were calibrated in each section.

Table 4.2: Obtained parameters of the geometrical processing in SMP2 (after Tran-Manh, 2014)

Solid matrix					Joint		
E	ν	ϕ	σ_t	ψ	ϕ_j	σ_{tj}	ψ_j
(MPa)	()	($^\circ$)	(kPa)	($^\circ$)	($^\circ$)	(kPa)	($^\circ$)
650	0.3	26	8.5	0	23	8.5	0

Chainage (m)	Solid matrix			Joint	
	G^K (MPa)	η^K (GPa.day)	η^M (GPa.day)	c (MPa)	c_j (MPa)
1272				0.8	0.25
1278				0.45	0.35
1284	250	6.25	35	0.4	0.18
1291				0.42	0.25
1297				0.45	0.2
1311				0.65	0.45
1331	250	1.25	10	0.7	0.5
1342				0.73	0.7
1367				1.55	0.4
1375	550	2.2	13.75	1.3	0.35
1384				1.2	0.42

The comparison between the numerical results and the field data for the maximum and minimum convergence of the sections at chainages 1367 and 1375 m are shown in Figure 4.3 as for example. The large and anisotropic convergence can be well simulated for a duration of several months.

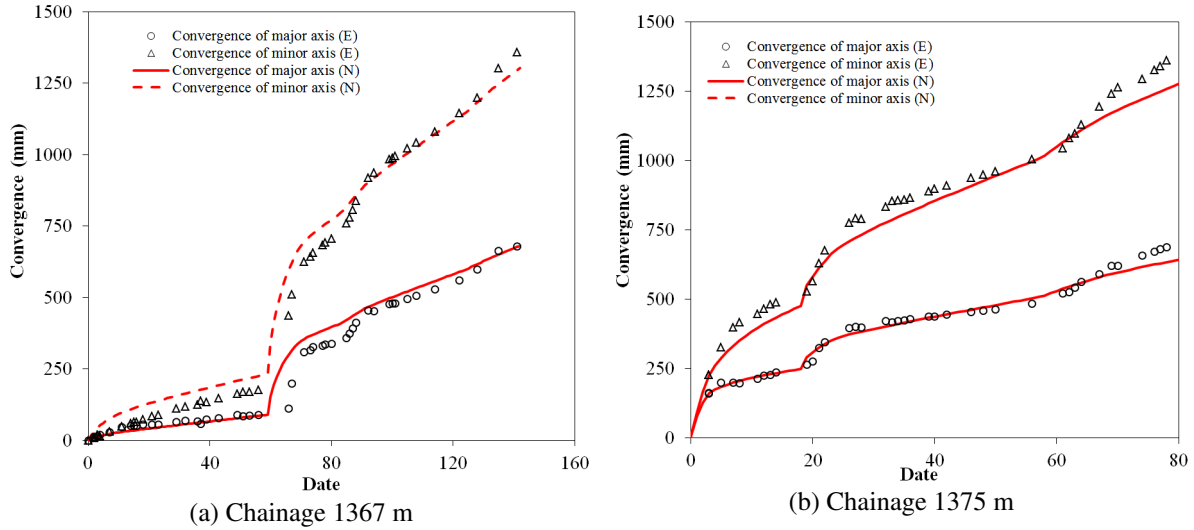


Figure 4.3: Numerical modeling of tunnel convergence (N) and comparison with field data (E) for SMP2 (after [Tran-Manh et al., 2015](#))

4.1.4 Modeling of the reinforcement and support system

The present study takes into account the used support system. In the SMP field work, a specific reinforcement and support system is adopted to overcome the severe problems caused by the squeezing Carboniferous formation ([Barla et al., 2012](#)):

- The rock mass is first reinforced by bolts ahead and around the tunnel;
- Then, the section is excavated and supported by yielding steel ribs with sliding joints (TH type);
- After that, the HiDCon elements are installed between sliding joints and the support is filled with shotcrete;
- A concrete ring is installed as the final lining when the convergence rate become low enough.

The used HiDCon elements are simulated with the double-yield model available in *FLAC3D* code ([Itasca, 2017](#)). A volumetric yield surface (or cap surface) is taken into account in this model to simulate the permanent volume changes caused by the application of isotropic pressure. The cap surface is defined by the cap pressure p_c and is independent of shear stress. The tangential bulk and shear moduli evolve as plastic volumetric strain takes place according to a special law defined in terms of a factor R and defined as the ratio of elastic bulk modulus to plastic bulk modulus. The parameter values as proposed by Itasca France are listed in Table 4.3. As these blocks contain porous aggregates and the pores close successively with prevention of lateral strain under loading, the Poisson's ratio is taken equal to 0. The shearing behavior of the deformable blocks is not considered and a very large value of cohesion is used in the modeling as these blocks works mainly work in compression.

Table 4.3: Parameters of double-yield model to simulate the HiDCon elements

Young's modulus	E	(MPa)	550
Poisson's ratio	ν	(-)	0
Cohesion	c	(MPa)	10^{20}
Tension limit	σ^t	(MPa)	0
Multiplier	R	(-)	1000
Cap pressure	p_c	(MPa)	2.83

The hardening behavior of the cap pressure is activated by the volumetric plastic strain, and follows a piecewise-linear law (Table 4.4 and Figure 4.4).

Table 4.4: The hardening behavior of the cap pressure p_c

e^{pv}	(-)	0	1.00	1.41
p_c	(MPa)	2.83	2.86	8.33

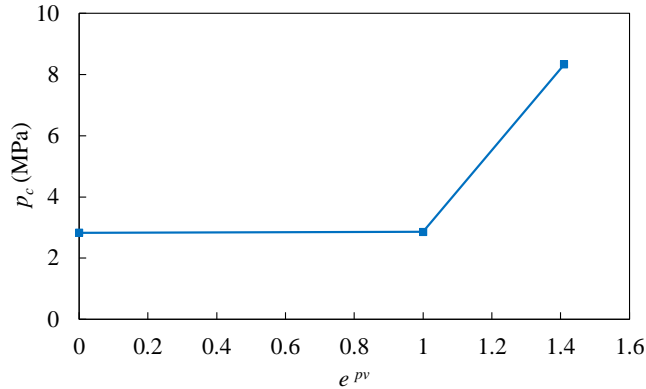


Figure 4.4: The hardening behavior of the cap pressure p_c

The stress-strain curves of HiDCon elements are obtained in laboratory uniaxial compression tests for different kinds of specimens (Barla et al., 2011) (Figure 4.5). The blocks are nearly elastic perfectly plastic until $\epsilon_a = 35\%$ with $\sigma_{lim} = 8.5$ MPa, and then a hardening behavior is observed until the strain limit $\epsilon_{lim} = 50\%$. With the proposed model and parameters (Tables 4.3 and 4.4), the uniaxial behavior of the HiDCon elements are well simulated.

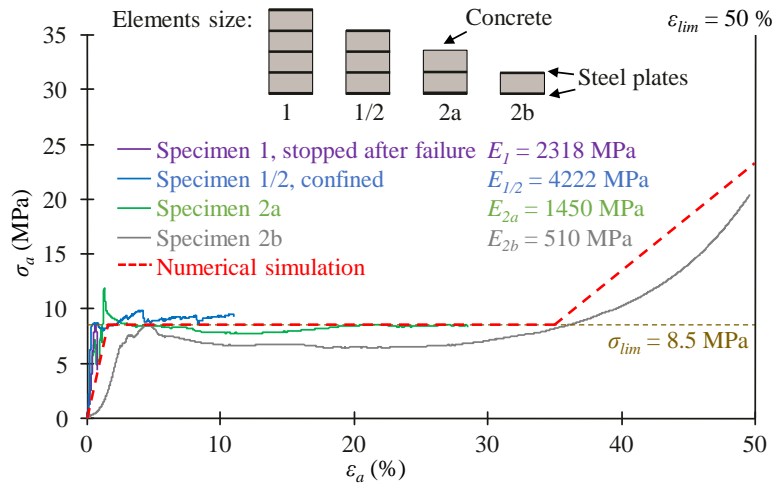


Figure 4.5: Uniaxial compression tests of HiDCon elements (Barla et al., 2011) and numerical simulation

The shotcrete used for the yielding support and the concrete for the final ling are modeled with elastic elements whose parameters are shown in Table 4.5. The time-dependent properties of the concrete are not taken into account in the numerical simulations and the considered elastic parameters are representative of the long-term behavior of the concrete several years after lining installation.

Table 4.5: Elastic parameters of concrete used in SMP

Parameters		Shotcrete	Final lining
Young's modulus	E (GPa)	10	20
Poisson's ratio	ν (-)	0.2	0.2

4.2 Long-term behavior of SMP2

SMP2 is excavated by conventional method with an equivalent radius of 5.5 m and the support profile changes depending on the ground mechanical properties and response (Bonini and Barla, 2012). P7-3 support system (Figure 4.6a) is applied from chainage 1267 to 1324 m and DSM profile (Figure 4.6b) is used from chainage 1385 m after a transition zone.

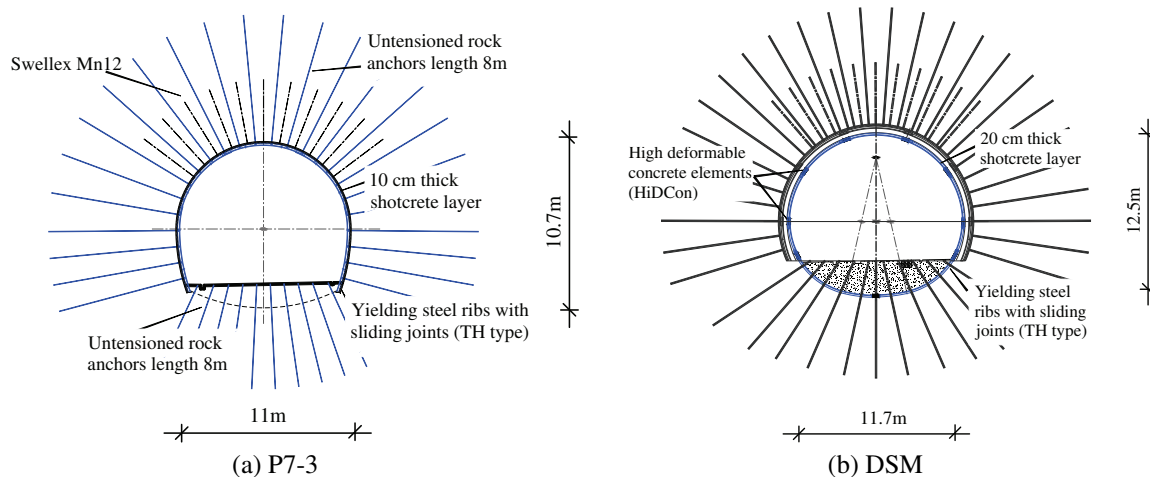


Figure 4.6: Profiles of support systems adopted in SMP2 (Bonini and Barla, 2012)

In the transition zone from chainage 1325 to 1384 m, excavation and support procedure is performed in 3 steps:

- Stage A: the tunnel is excavated in the upper cross section with an equivalent radius of 5.5 m, reinforced by bolts and supported by steel ribs with sliding joints (P7-3 profile);
- Stage B: as the convergence is larger than expected, the tunnel section is then enlarged to a radius of near 5.7 m and supported by yielding support system (DSM profile), which contains HiDCon elements and shotcrete between steel ribs with sliding joints.
- Stage C: when the convergence rate is small enough, a concrete ring of 80-100 cm is installed as the final lining of the tunnel.

The section at chainage 1383 m located in this transition zone and in Houiller formation is studied in the present work because mid-term and long-term stress measurement of the final lining is recently available for this section. Reprofiting process and installation of the yielding support system occurred near 3 months after the opening of section and the final lining is installed nearly 5 months later.

4.2.1 Stress measurements in the final lining

Ten gauges have been installed in the inner and outer sides of the upper part of the final lining to follow the strain evolution in the circumferential direction and to monitor the hoop stress during more than 10 years (Figure 4.7) (presented in Section 2.3.4). The stress increases quickly right after lining installation and the increasing rate becomes smaller and smaller. The gauges CV1 and CV9 are no longer available near 3 years after installation of the concrete ring. Near 6 years later, the stress tends to stabilize. The recorded stress in the concrete ring at the end of monitoring period varies from 6 to 11 MPa. These new data permit to analyze the ground behavior for much longer time as compared to the initial computations of Tran-Manh (2014) and to examine if the considered constitutive model (CVISC model combined with ubiquitous-joint model) is applicable to simulate the mid-term and long-term behavior.

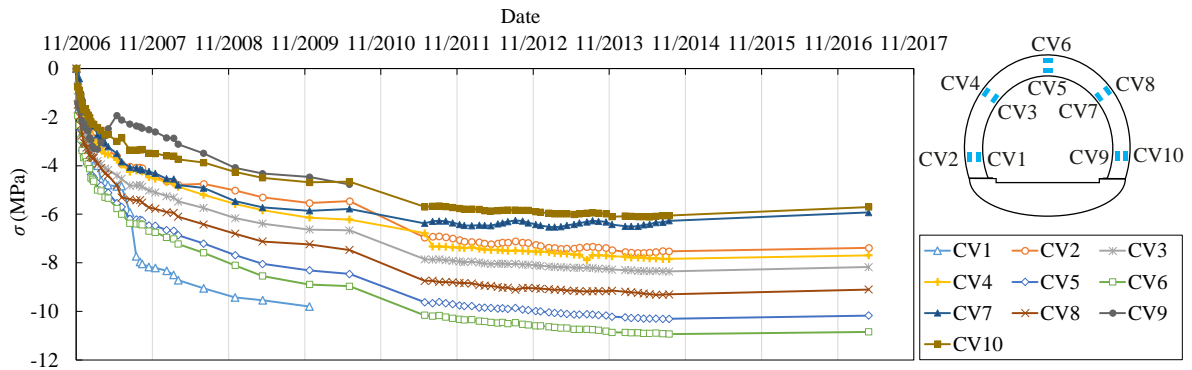


Figure 4.7: Stress measurement in the concrete ring at chainage 1383 m of SMP2

4.2.2 Numerical model

2D numerical modeling is performed with *FLAC3D* code in the present study. In order to model the reprofiling process between stage A and B, it is necessary to carry out the simulation in large-strain mode which allows to update the position of grid-points during the calculation. The real geometry of the tunnel section is simplified by considering a circular opening. Excavation of the upper part and the lower part of the section are modeled at the same time.

The tunnel face advance has great influence on the tunnel convergence. In 2D modeling, the tunnel face advance can be simulated by progressive reduction of the radial stress at the wall introducing the deconfinement rate λ .

In order to calculate the deconfinement rate λ , a 3D simulation is first performed using an elasto-plastic model with Mohr-Coulomb yield criterion and tension cut-off applying the obtained parameters of rock mass (Table 4.2): $E = 650$ MPa, $\nu = 0.3$, $c = 0.42$ MPa, $\phi = 23^\circ$, $\psi = 0^\circ$ and $\sigma_t = 8.5$ KPa. We assume that the deconfinement rate obtained by an elasto-plastic calculation can also be applied to the time-dependent modeling.

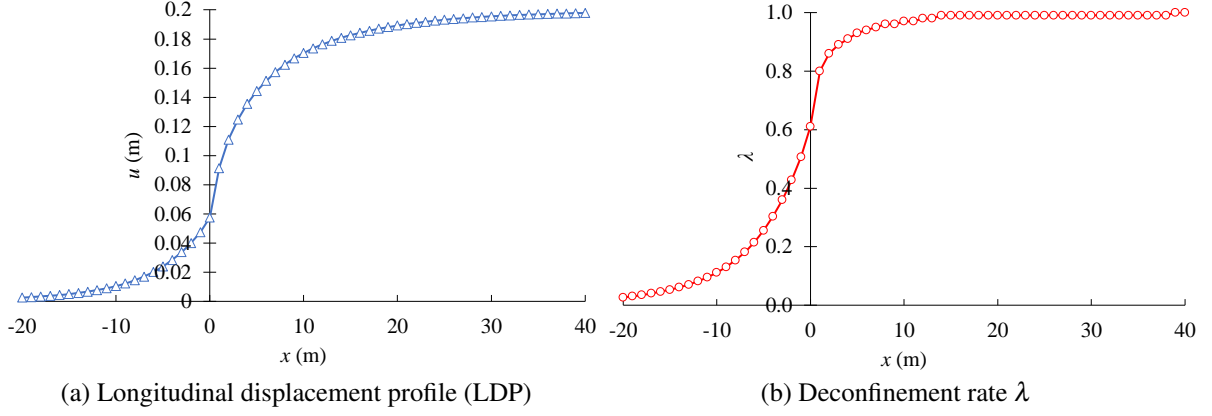


Figure 4.8: LDP and calculated deconfinement rate for the section at chainage 1383 m in SMP2

The longitudinal displacement profile (LDP) can be determined (Figure 4.8a). The deconfinement rate is then calculated (Figure 4.8b) with the following equations presented in Section 1.3.4:

For elastic response:

$$u = \lambda \frac{\sigma_0 R}{2G} \quad (4.3)$$

For the elasto-plastic response (see Equation 1.51):

$$\frac{2G}{\sigma_0} \frac{u}{R} = \lambda_e \left[F_1 + F_2 \left(\frac{R}{R_p} \right)^{K_p-1} + F_3 \left(\frac{R_p}{R} \right)^{K_\psi+1} \right] \quad (4.4)$$

Once the deconfinement rate is obtained, we can perform the 2D numerical simulations. The considered 2D mesh is shown in Figure 4.9. The model size is large enough (about $32 R$ where R is the tunnel radius) to avoid the influence of the model boundaries. The initial state of stress is considered as isotropic with $\sigma_0 = 8.5$ MPa and zero normal displacements are imposed on the model borders.

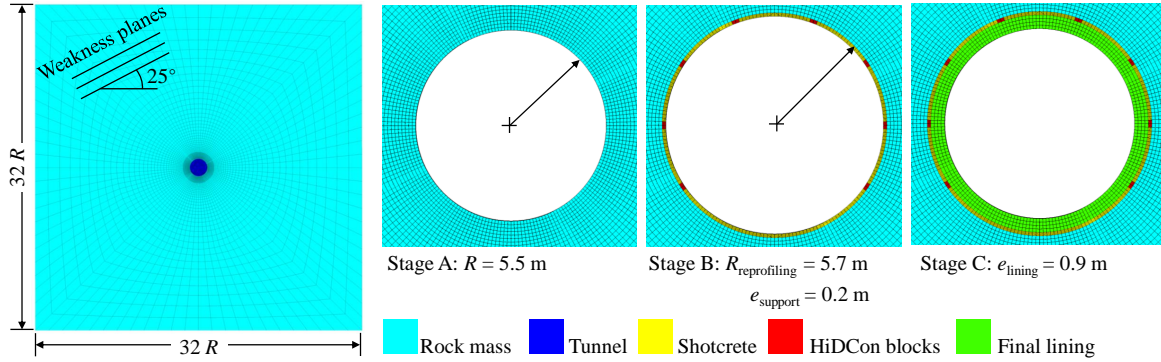


Figure 4.9: 2D mesh for the section at chainage 1383 m in SMP2

So as to represent the excavation and support procedures followed in the field, the computation is composed of four stages (Table 4.6). Modeling begins 32 days before the excavation of the considered section in order to take into account the influence of the tunnel face advance on the not-excavated part of the ground. The section is first opened with an equivalent radius of 5.5 m by deactivating the corresponding elements and the pressure $P_i = \sigma_0$ is applied on the tunnel wall in the normal direction. The tunnel face advance before and after the opening of studied section is modeled by decreasing progressively

the stress applied on the tunnel wall following the deconfinement rate function λ previously determined (Figure 4.8b). 94 days later corresponding to xx m from the face, the opened section becomes significantly smaller because of the large convergence. The section is then enlarged to a radius of 5.7 m and the elements of the yielding support system are activated which contains 8 HiDCon elements of 20 cm * 40 cm. At the end, the concrete ring with a thickness of 90 cm is activated and the time-dependent response are computed for more than 10 years.

Table 4.6: Four stages of numerical simulation

Stage	Date (mm/dd/yyyy)	Face (m)	t after excavation (days)	t computation (days)	λ (-)	
0	Beginning of simulation	04/03/2006	1368	*	0	
1	Section excavation	05/05/2006	1383	0	32	0.61
2	Reprofiling and support installation	08/07/2006	1418	94	126	1
3	Lining installation	10/01/2006	1446	149	181	*

The various elements introduced the numerical modeling are shown in Table 4.7. The rock mass is modeled by CVISC model with ubiquitous joints using the parameters obtained by [Tran-Manh et al. \(2015\)](#) for the section at chainage 1383 m (Table 4.2). The introduced weakness planes are parallel to the tunnel axis with an orientation of 25 degrees to the right top side of the galley. The interface between the rock mass and the yielding support and that between the yielding support and the final lining are assumed to be rigid.

Table 4.7: Summary of the elements introduced in the numerical modeling of SMP2

	Element	Modeling
Ground	Matrix mass	CVISC Model
	Weakness planes	Ubiquitous-joint model
Reinforcement	Bolts	Not introduced
Semi-rigid support	Steel ribs with sliding joints	Not introduced
	Shotcrete	Elastic
	HiDCon blocks	Double-yield model
Final lining	Concrete ring	Elastic
Interface	Ground / yielding support	Rigid
	Semi-rigid support / final lining	Rigid

The constitutive models and parameters values for the elements introduced in the numerical modeling of SMP2 are summarized in Table 4.8.

Table 4.8: Summary of the constitutive parameters in the numerical modeling of SMP2

Matrix mass	Elastic bulk modulus	K	(MPa)	541.67	
CVISC Model	Elastic shear modulus	G^M	(MPa)	250	
	Maxwell dynamic viscosity	η^M	(GPa.day)	13.75	
	Kelvin shear modulus	G^K	(MPa)	550	
	Kelvin viscosity	η^K	(GPa.day)	2.2	
	Cohesion	c	(MPa)	1.2	
	Friction angle	ϕ	($^\circ$)	26	
	Tension limit	σ_t	(kPa)	8.5	
	Dilation angle	ψ	($^\circ$)	0	
Weak planes	Dip		($^\circ$)	-25	
Ubiquitous-joint model	Dip direction		($^\circ$)	90	
	Joint cohesion	c_j	(MPa)	0.42	
	Joint friction angle	ϕ_j	($^\circ$)	23	
	Joint tension limit	σ_{tj}	(kPa)	8.5	
	Joint dilation angle	ψ_j	($^\circ$)	0	
	Shotcrete	Young's modulus	E	(GPa)	10
Elastic		Poisson's ratio	ν	(-)	0.2
HiDCon blocks	Young's modulus	E	(MPa)	550	
	Double-yield model	Poisson's ratio	ν	(-)	0
		Cohesion	c	(MPa)	10^{20}
	Tension limit	σ^t	(MPa)	0	
	Multiplier	R	(-)	1000	
	Cap pressure (with hardening)	p_c	(MPa)	2.83	
Concrete ring	Young's modulus	E	(GPa)	20	
	Elastic	Poisson's ratio	ν	(-)	0.2

4.2.3 Obtained results

The numerical results of displacement contour around the gallery before and after the reprofiling and installation of yielding support system for the section at chainage 1383 m of SMP2 are shown in Figure 4.10.

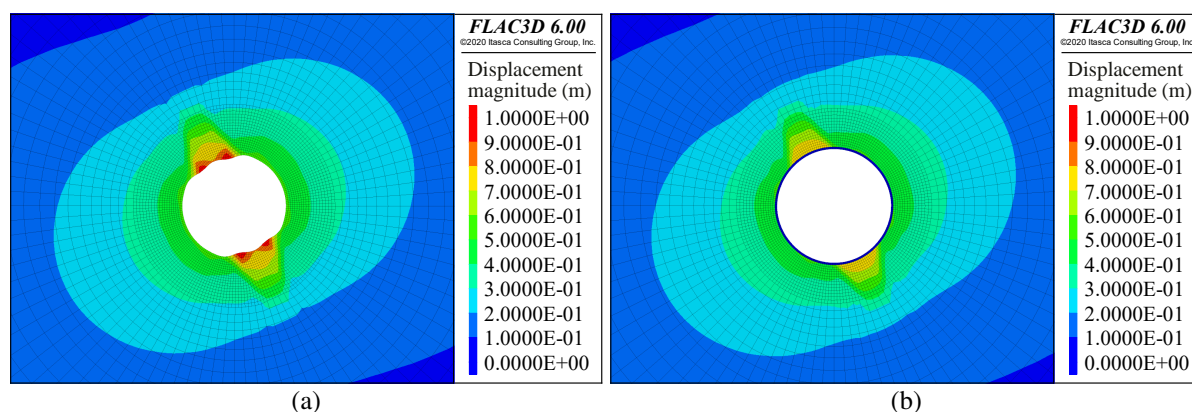


Figure 4.10: Displacement contour before (a) and after (b) reprofiling process 94 days after excavation

Before reprofiling, the convergence on the tunnel wall has reached near 1 m. The mesh has been highly deformed and the section is no longer circular. The strong anisotropy of the convergence as

observed in the field in a given direction is correctly reproduced thanks to the ubiquitous-joint approach. The reprofiling process is performed by removing the deformed elements, enlarging the tunnel section and installing the yielding support system.

The same values of the constitutive parameters are first kept to simulate the mid-term and long-term behavior. In this case, the convergence increases with a nearly constant slope because of the presence of Maxwell element in the CVISC model and the stress in the final lining reach values as high as 40 to 60 MPa after 10 years (Figure 4.11).

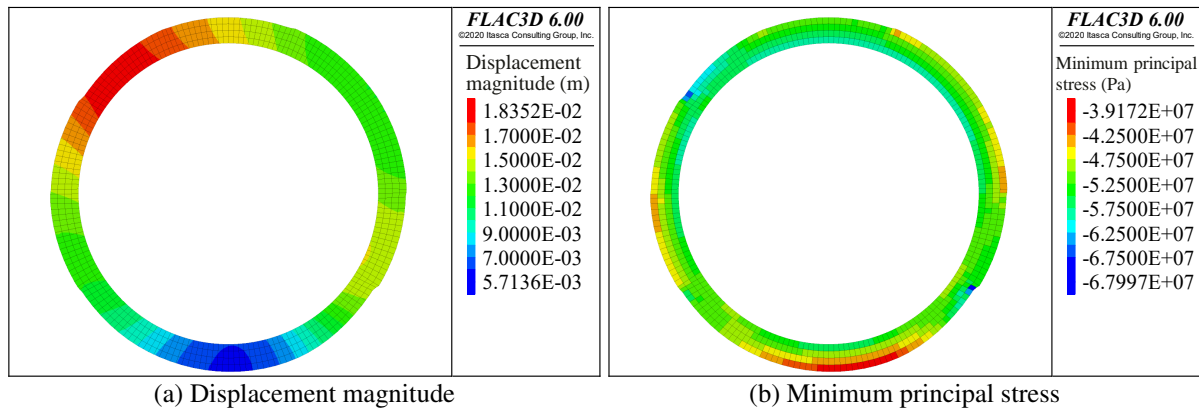


Figure 4.11: Displacement and minimum (maximum in absolute value) principal stress in the final lining

4.2.4 Time-dependency of the viscosity

This overestimation of the long-term stress in the lining is due to the assumption of a constant viscosity η^M of the Maxwell element in the CVISC model. In order to reproduce the stabilization of the stress in final lining as measured in field, the viscosity of Maxwell element η^M needs to be adjusted during the calculation: it is increased to 100 times after 3 months and 3000 times after 5 years to block the tunnel convergence. The obtained stress in the final lining is about 10 MPa at the end of the computation except in a few elements exhibiting a stress concentration because of the modeling of the HiDCon blocks in the yielding support and the interface between the yielding support and the final lining which is assumed to be rigid during the calculation.

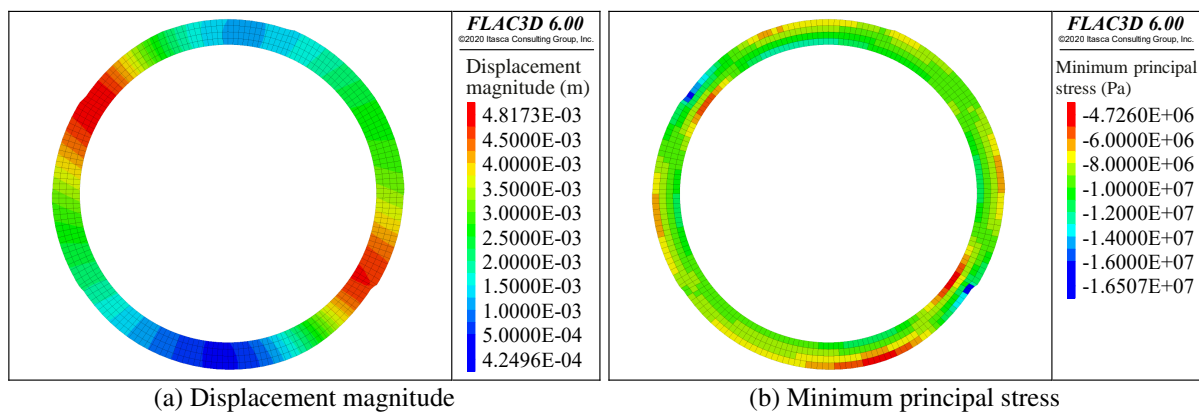


Figure 4.12: Displacement and minimum principal stress in the final lining after modification of η^M

In summary, the considered constitutive model can be applied to simulate the mid-term and long-term behavior while the viscosity of Maxwell element η^M needs to be increased by step over time in

order to stabilize and block the deformation of the ground after installation of the final lining. Increasing of η^M of the CVISC model during the numerical modeling after lining installation was also proposed by De La Fuente et al. (2019) in the case of Fréjus road tunnel.

In order to take into account the time-dependency of η^M , fractional derivative calculus is introduced. The newton dashpot of the Maxwell element in the deviatoric part of CVISC model is replaced by the Abel element (Figure 4.13).

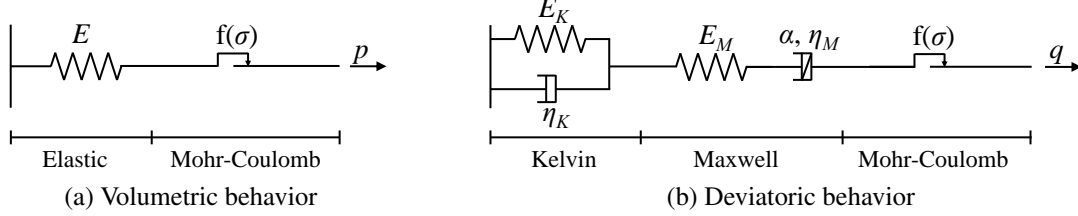


Figure 4.13: Fractional CVISC model

The classical Maxwell model for deviatoric creep is described as:

$$\dot{e}_{ij}^M = \frac{1}{2G^M} \dot{S}_{ij} + \frac{1}{2\eta^M} S_{ij} \quad (4.5)$$

The introduction of the fractional derivative calculus permits to replace the Maxwell viscosity η^M by another value η^* . Then, the increment of the deviatoric strain can be expressed as:

$$\dot{e}_{ij}^M = \frac{1}{2G^M} \dot{S}_{ij} + \frac{1}{2\eta^*} S_{ij} \quad (4.6)$$

where η^* is defined as:

$$\eta^* = \frac{\eta^M}{\alpha} \Gamma(1 + \alpha) \left(\frac{t}{\tau}\right)^{1-\alpha} \quad \text{and} \quad \tau = \frac{\eta^M}{G^M} \quad (4.7)$$

Practically, this modification of the CVISC model can be implemented with progressive change of η^* by the function: $\eta^* = \max(\eta^M, \eta^*)$.

η^* increases explicitly but more and more slowly. The parameter α is calibrated for the section at chainage 1383 m in SMP2: $\alpha = 0.07$. The variation of η^* on time t is shown in Figure 4.14.

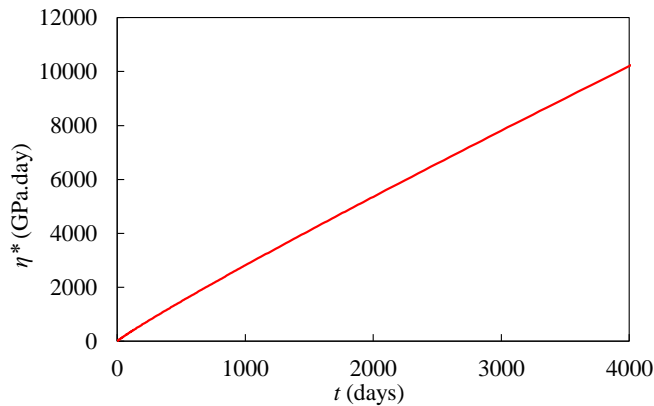


Figure 4.14: Variation of η^* versus computational time t

By introducing this modification, the range of mid-term and long-term stress in the final lining (Figure 4.7) can be well reproduced (Figure 4.15).

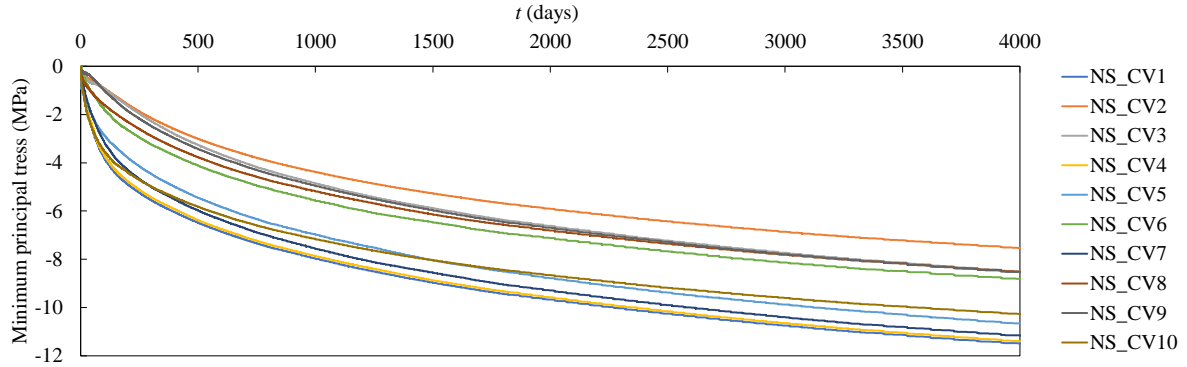


Figure 4.15: Numerical results of the stress in the final lining at chainage 1383 m in SMP2

4.3 SMP4-PS

2D numerical modeling is performed in small-strain mode for SMP4-PS based on the analysis of convergence data. SMP4 is much deeper and the initial state of stress is considered geostatic and isotropic with $\sigma_x = \sigma_y = \sigma_z = 16.2$ MPa. The constitutive model of the support systems used in the modeling are the same as in SMP2. As a unique direction of anisotropy cannot be identified in SMP4-PS, the rock mass is simulated with CVISC model without introducing weakness planes to study the average response. The constitutive parameters need to be adjusted as the rock at this greater depth is stiffer. The average excavation rate of SMP4-PS is about 0.6 m/day from chainage 10310 to 10410 m and tunneling is carried out on 2 stages:

- Stage A: the ground is reinforced by bolts; The upper part of the tunnel is first excavated and supported by steel ribs with sliding joints.
- Stage B: at 11 m from the tunnel face, the lower part of the tunnel is excavated and supported by steel ribs with sliding joints; the yielding support system is applied: 8 or 4 high deformable concrete elements are placed between the steel ribs and filled with shotcrete.

The convergence data available for SMP4-PS have been processed in Section 3.3. The mean convergence represented by the fitted circle is studied in the numerical simulations presented in the following.

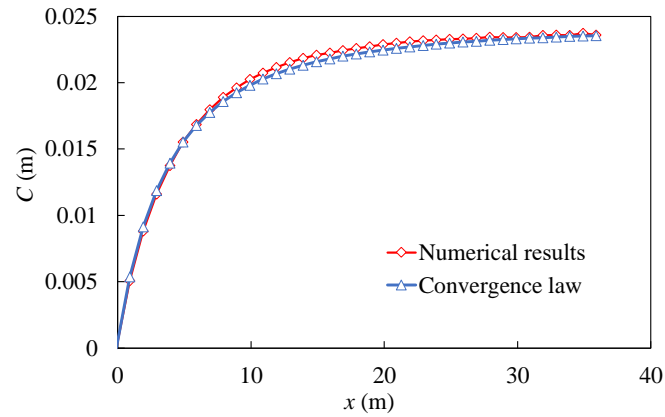
4.3.1 Numerical model

The parameters of the CVISC model that describes the rock mass behavior in SMP4 must be identified. The elasto-plastic parameters are first determined by fixing the same values for the Poisson's ratio ν , the friction angle ϕ , the tension limit σ_t and the dilation angle ψ as those of SMP2. The two remaining parameters (Young's modulus E and cohesion c) are fitted by using the time-independent part of the convergence law (Section 3.3):

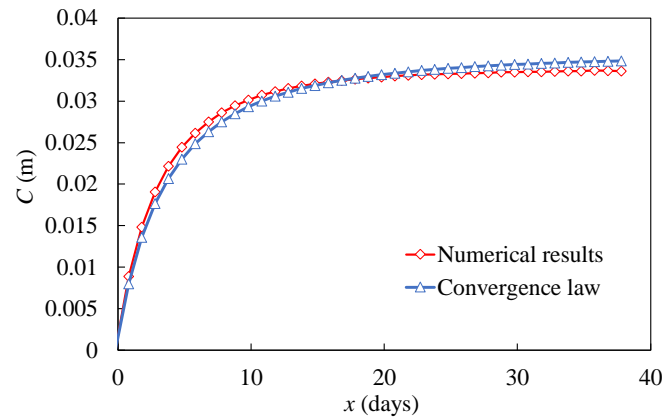
$$C(x) = C_{\infty x} \left[1 - \left(\frac{X}{X+x} \right)^2 \right] \quad (4.8)$$

For that 3D time-independent numerical modeling is performed by using the Mohr-Coulomb model.

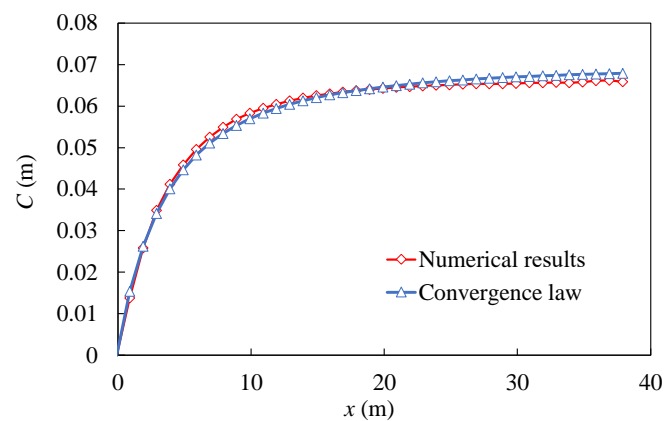
As for example the numerical results of the sections at chainages 10316, 10321 and 10326 m with the corresponding fitted values of E et c are shown in Figure 4.16 and compared with those of the convergence law. This method permits to separate the time-dependent and independent parts while fitting the constitutive parameters of the numerical model with the help of the studies of the convergence law.



(a) Chainage 10316 m: $E = 1625$ MPa, $c = 3.12$ MPa



(b) Chainage 10321 m: $E = 1625$ MPa, $c = 3.84$ MPa



(c) Chainage 10326 m: $E = 1625$ MPa, $c = 2.52$ MPa

Figure 4.16: Fitting of elasto-plastic parameters of SMP4-PS

The obtained elasto-plastic parameters are used to compute the deconfinement rate as done in SMP2. The results of the calculation of LDP curve and λ are shown in Figure 4.17. The deconfinement rate at the tunnel face is about 0.4 while at 1 m from the face, the deconfinement rate reaches values above

0.8. We assume that the deconfinement rate obtained with elasto-plastic calculation is applicable for the following time-dependent simulations.

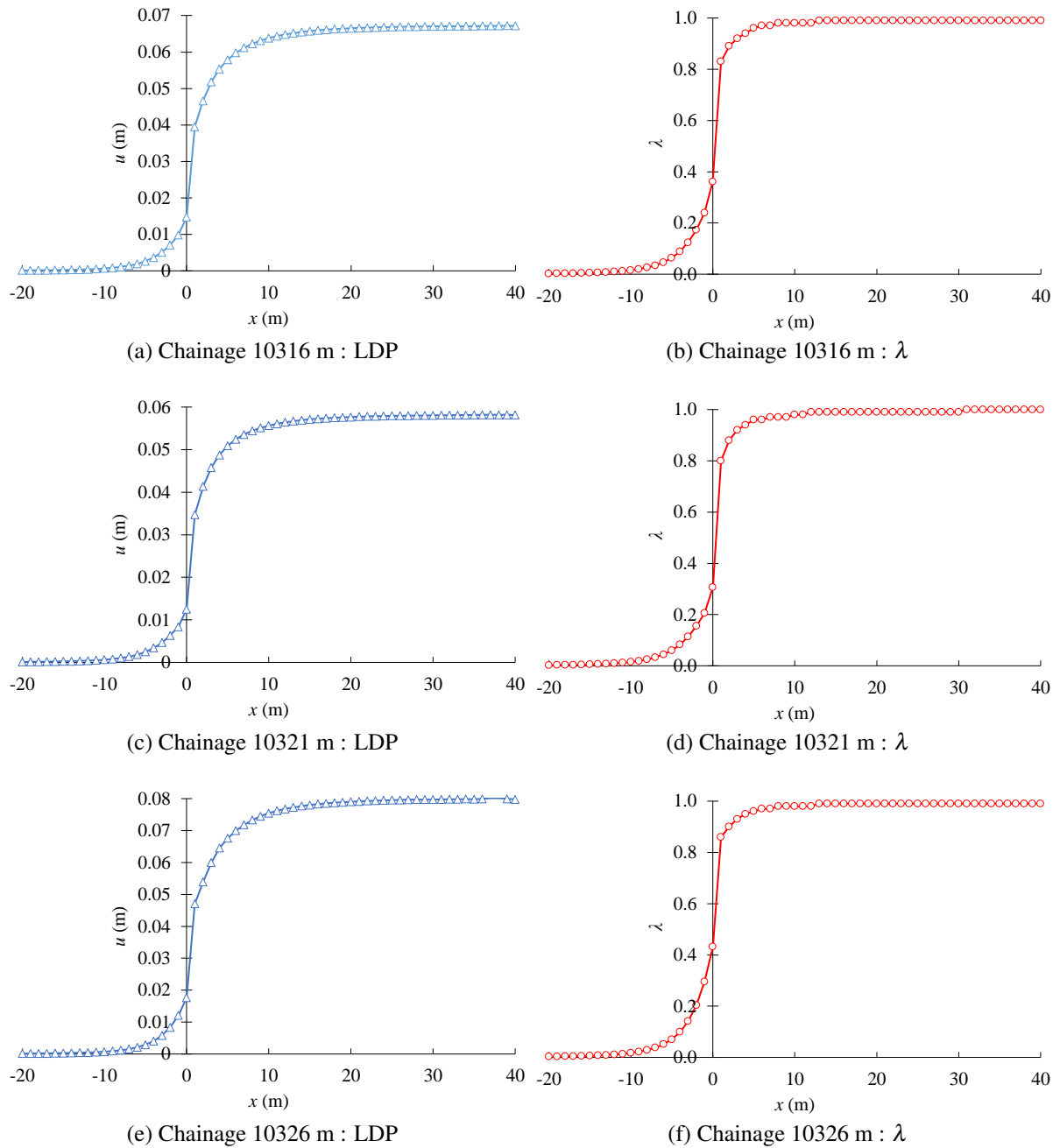


Figure 4.17: Longitudinal displacement profile and calculated deconfinement rate in SMP4-PS

Once the deconfinement rate and the elasto-plastic parameters are obtained, the time-dependent parameters of the CVISC model are identified as follows.

For simplicity, the real geometry of the tunnel section is not taken into account but simplified to a circle with an equivalent radius of 3.15 m (Figure 4.18). Only half of the section is modeled because of the symmetry of the model with respect to the horizontal direction. The model size is large enough to avoid the edge effects. The excavation and the support procedures are modeled in 2 stages: excavation of the full section and installation of the yielding support system at 11 m from the face.

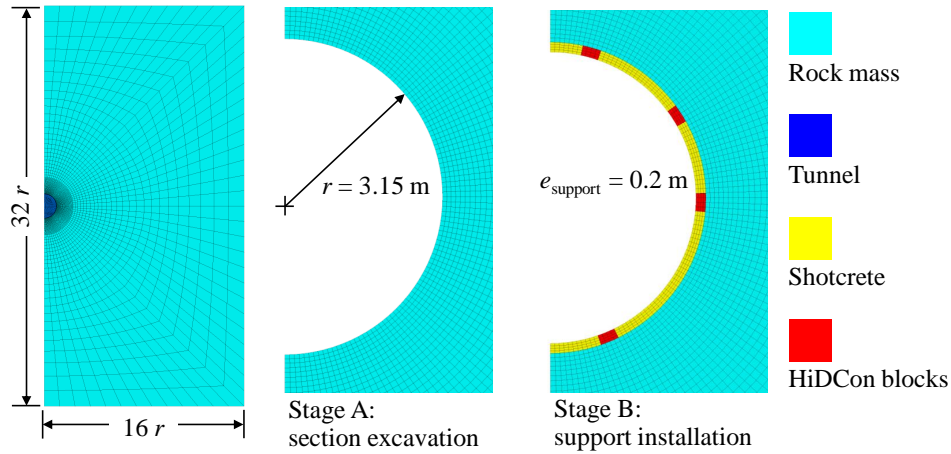


Figure 4.18: 2D mesh for numerical simulation of SMP4-PS

The constitutive models and parameters used to simulate the support system of SMP4-PS are the same as for SMP2. They are summarized in Table 4.9.

Table 4.9: Summary of the elements introduced in the numerical modeling of SMP4-PS

	Element	Modeling
Ground	Matrix mass	CVISC Model
Reinforcement	Bolts	Not introduced
Semi-rigid support	Steel ribs with sliding joints	Not introduced
	Shotcrete	Elastic
Final lining	HiDCon blocks	Double-yield model
	Concrete ring	Not installed
Interface	Ground / yielding support	Not introduced
	Semi-rigid support / final lining	Not introduced

The constitutive models and parameters values for the elements introduced in the numerical modeling of SMP4-PS are summarized in Table 4.10.

Table 4.10: Summary of the constitutive parameters in the numerical modeling of SMP4-PS

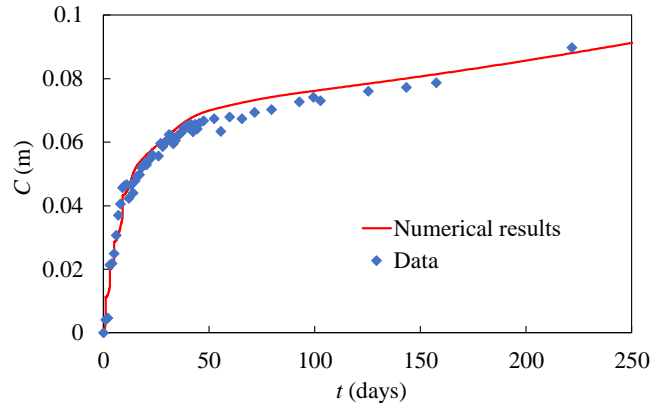
Shotcrete	Young's modulus	E	(GPa)	10
Elastic	Poisson's ratio	ν	(-)	0.2
HiDCon blocks	Young's modulus	E	(MPa)	550
Double-yield model	Poisson's ratio	ν	(-)	0
	Cohesion	c	(MPa)	10^{20}
	Tension limit	σ^t	(MPa)	0
	Multiplier	R	(-)	1000
	Cap pressure (with hardening)	p_c	(MPa)	2.83

4.3.2 Results

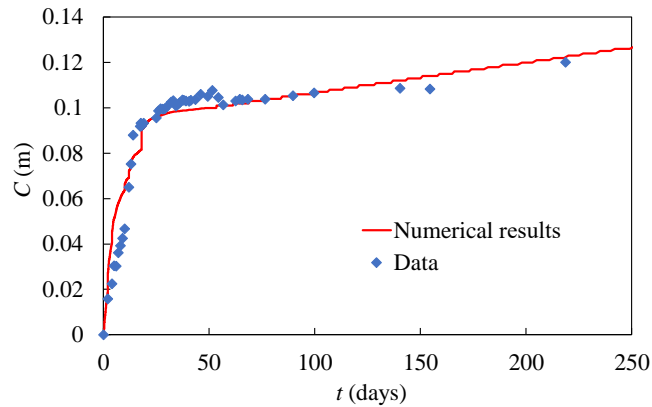
Numerical simulations have been performed to fit the mean convergence of SMP4-PS, which has previously been identified by fitting a circle of the section (Section 3.3). The calibration of the constitutive parameters of the CVISC model is shown for 3 different sections in Table 4.11. As seen in Figure 4.19, the convergence data are well reproduced for mid-term scale of more than 200 days.

Table 4.11: Obtained parameters of the CVISC model for SMP4-PS

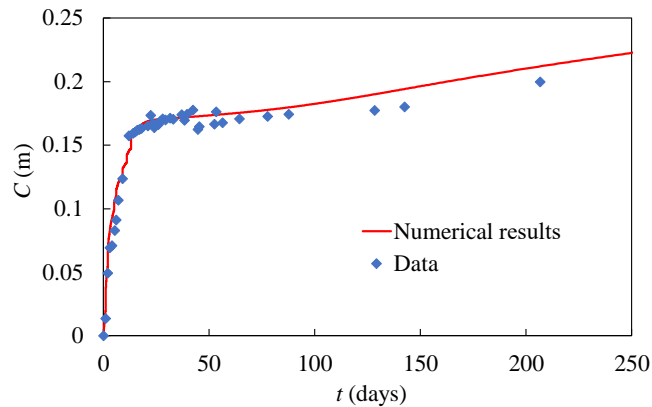
Chainage (m)	E (MPa)	ν (-)	G^K (MPa)	η^K (GPa.day)	η^M (GPa.day)	c (MPa)	ϕ ($^\circ$)	σ_t (kPa)	ψ ($^\circ$)
10316 T	1625	0.3	825	13.2	550	3.12	26	8.5	0
10321 C	1625	0.3	715	2.64	412.5	3.84	26	8.5	0
10326 T	1625	0.3	605	1.375	275	2.52	26	8.5	0



(a) Chainage 10316 m



(b) Chainage 10321 m



(c) Chainage 10326 m

Figure 4.19: Numerical simulation of mean behavior of SMP4-PS

Field measurements exhibit a strong heterogeneity of the ground along the tunnel which can be reproduced in the numerical simulations with the model parameters presented in Table 4.11. The cohesion of the section at chainage 10326 m is smaller than in the other two sections which is reflected in the much higher measured convergence in this section. The viscosity of Maxwell is also smaller because the convergence rate after the support installation is higher in this section.

The displacements magnitudes of the ground and the support system at 200 days after the support installation are shown in Figure 4.20.

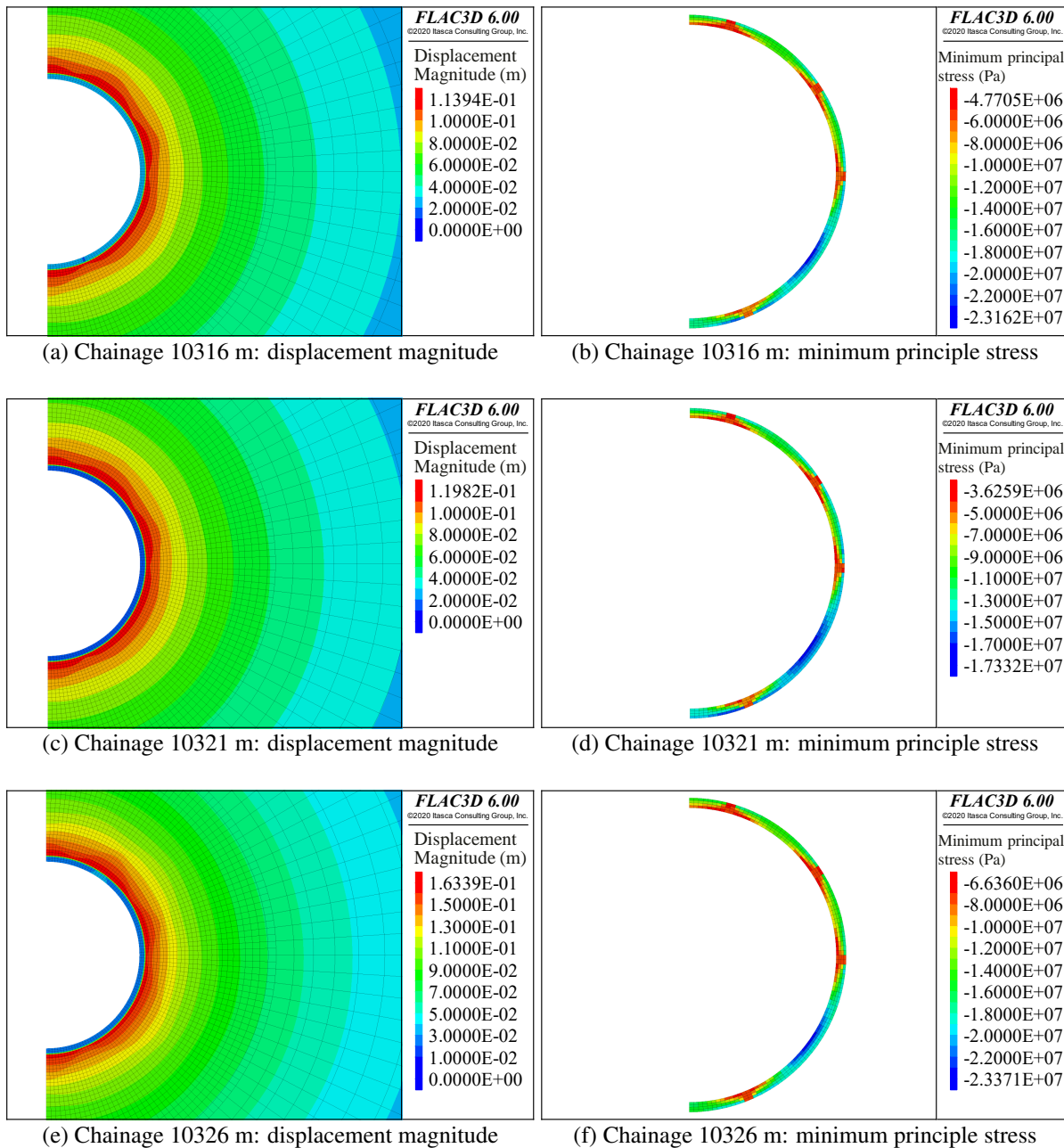


Figure 4.20: Numerical results at 200 days after support installation of SMP4-PS

In sections at chainage 10316 and 10321 m, as the convergence is rather small, the HiDCon blocks remain in the elastic domain with a maximum principal compressive stress (in absolute value) between 5 and 7 MPa. However, at chainage 10326 m where the convergence is higher, several elements of

the HiDCon blocks begin to yield. In the bottom right corner of the support system where no HiDCon element is installed, the stress in the shotcrete is much larger and reaches more than 20 MPa. The HiDCon blocks can decrease the stress level in the shotcrete and cause a slight anisotropy of the displacement magnitude.

From the numerical results, the strings convergence can also be computed. For example, the results of the section at chainage 10326 m are shown in Figure 4.21. The model parameters characterizing the mean behavior of the rock underestimate the convergence of strings D3 and D5 (whose shortening is larger than the averages convergence) and overestimate the strings D1, D4, D6, D7, D8 and D9 (whose shortening is smaller than the averages convergence).

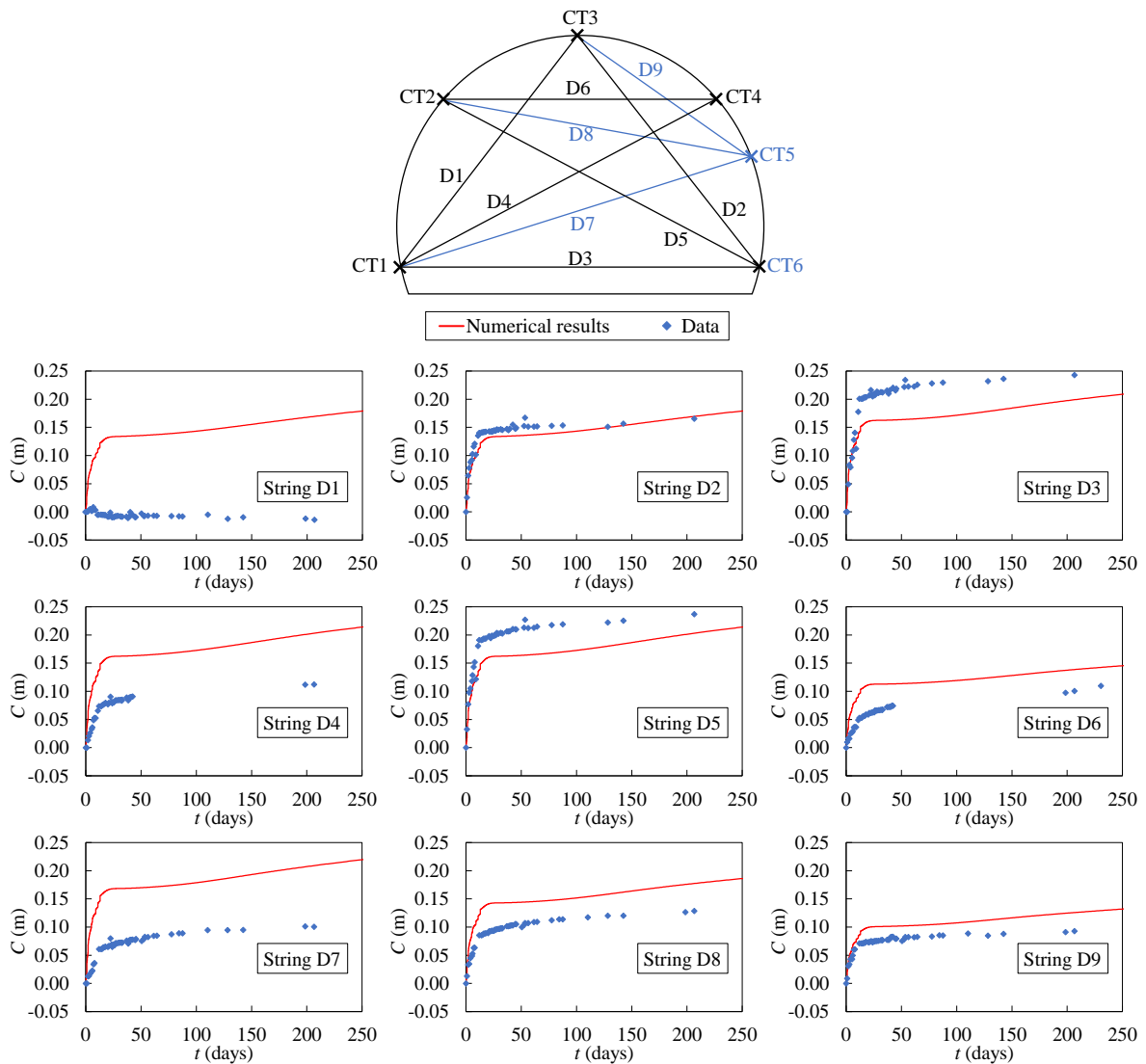


Figure 4.21: Numerical simulation of the strings at chainage 10326 m of SMP4-PS

4.4 SMP4-RPS

SMP4-PS has been enlarged to full section (SMP4-RPS) from chainage 10310 to 10410 m. 3D numerical modeling has been carried out to study the enlarged gallery. The numerical simulations are performed in small-strain mode because the field measurements exhibit rather small convergence. As

SMP4-RPS is excavated after SMP4-PS, it is necessary to model the excavation process for both two stages to take into account the influence of PS on RPS and evaluate the efficiency of the excavation on two stages. The convergence data recorded in the field have been processed in Section 3.4.

4.4.1 Stress measurements in the shotcrete

In addition to the convergence measurements, stress measurements have been recorded in the shotcrete lining in two sections at chainage 10325 and 10383 m (Section 2.3.5). The mid-term measurements in the upper part of the section at chainage 10383 m are used to compare with the numerical results (Figure 4.22).

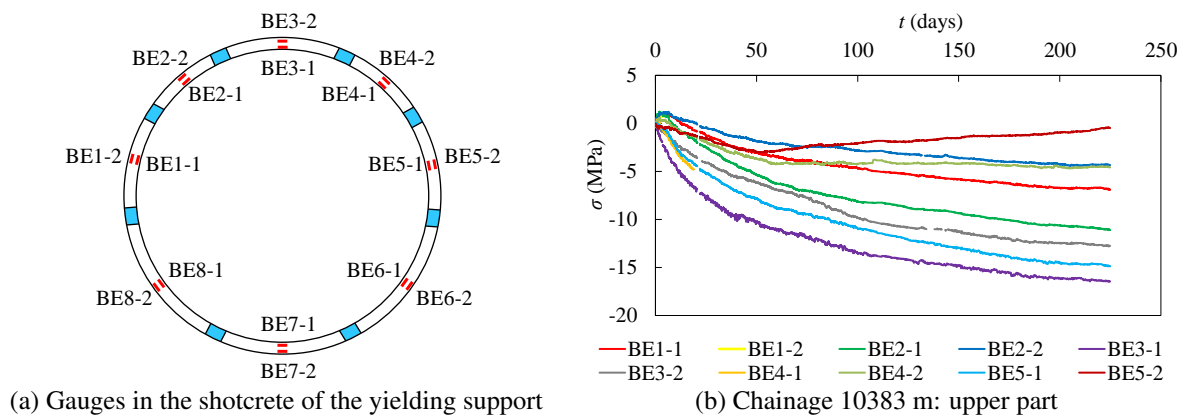


Figure 4.22: Stress measurements in the shotcrete in SMP4-RPS

4.4.2 Numerical model

The section at chainage 10344 m is first studied as it is situated sufficiently far from the extremities of the SMP4-RPS and the information about the tunnel face advance and the support installation are available. Step-by-step method is applied for the numerical modeling, which permits to take into account the exact information of the tunnel face advance and the support installation.

The 3D mesh is shown in Figure 4.23. The model is 98 m long and represents the tunnel from chainage 10300 to 10398 m of SMP4 to take into account the influence of tunnel face before and after the section under study and to avoid the border effects. The numerical modeling of the excavation process includes both the excavation of the small section and its enlargement. It is composed of four stages:

- PS-A: excavation of SMP4-PS;
- PS-B: support installation of SMP4-PS;
- RPS-A: enlargement of the excavated section (PS) to full size (RPS);
- RPS-B: support installation of SMP4-RPS.

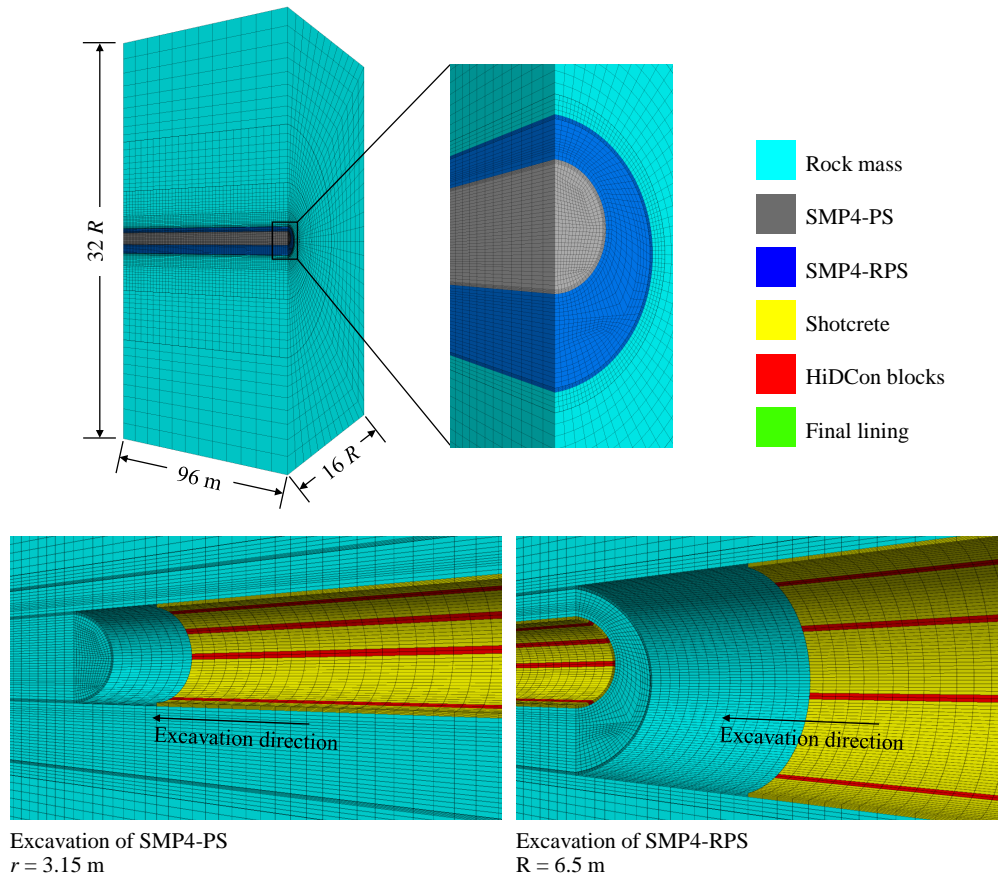


Figure 4.23: 3D mesh for numerical simulation of SMP4-RPS

The real tunnel face advance and support installation as described in the worksite reports are implemented in the model (Figure 4.24 and Table 4.12). When the tunnel face advance information lacks for a few sections, we assume that they follow the same procedure as the surrounding sections.

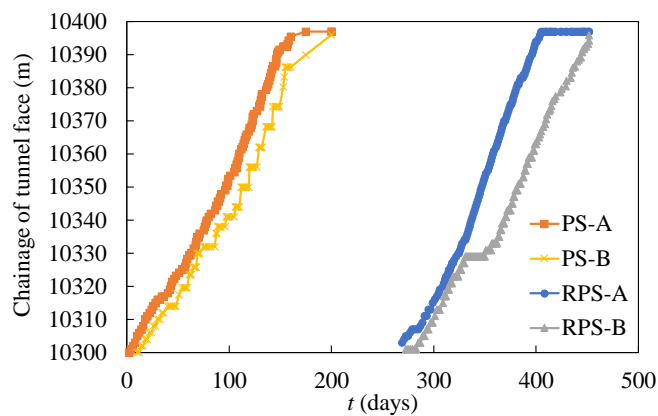


Figure 4.24: Tunnel face advance of SMP4-PS and SMP4-RPS

Table 4.12: Four excavation stages at chainage 10344 m in SMP4-RPS

Stage	Date (mm/dd/yyyy)	Face PS (m)	Face RPS (m)	Computation time (days)
PS-A	09/12/2018	10344	*	54
PS-B	10/01/2018	10356	*	73
RPS-A	05/23/2019	*	10344	307
RPS-B	06/26/2019	*	10375	341

The elements to be modeled in the present computations are summarized in Table 4.13.

Table 4.13: Summary of the elements introduced in the numerical modeling of SMP4-RPS

	Element	Modeling
Ground	Matrix mass	CVISC Model
Reinforcement	Bolts	Not introduced
Semi-rigid support	Steel ribs with sliding joints	Not introduced
	Shotcrete	Elastic
	HiDCon blocks	Double-yield model
Final lining	Concrete ring	Not installed
Interface	Ground / yielding support	Not introduced
	Semi-rigid support / final lining	Not introduced

The yielding support is modeled with the same models and properties as for SMP2 and SMP4-PS. The interface between the ground and the yielding support is not introduced in the computation as the preliminary numerical modeling shows nearly isotropic deformation.

The constitutive models and parameters values for the elements introduced in the numerical modeling of SMP4-PS are summarized in Table 4.14.

Table 4.14: Summary of the constitutive parameters in the numerical modeling of SMP4-RPS

Shotcrete	Young's modulus	E	(GPa)	10
Elastic	Poisson's ratio	ν	(-)	0.2
HiDCon blocks	Young's modulus	E	(MPa)	550
Double-yield model	Poisson's ratio	ν	(-)	0
	Cohesion	c	(MPa)	10^{20}
	Tension limit	σ^t	(MPa)	0
	Multiplier	R	(-)	1000
	Cap pressure (with hardening)	p_c	(MPa)	2.83

4.4.3 Numerical results

The typical values of the constitutive parameters have been obtained for SMP4-RPS (Table 4.15), which allows to reproduce the mean convergence data of the section up to mid-time scale at chainage 10344 m (Figure 4.25).

Table 4.15: Obtained parameters of the CVISC model for SMP4-RPS

Chainage (m)	E (MPa)	ν (-)	G^K (MPa)	η^K (GPa.day)	η^M (GPa.day)	c (MPa)	ϕ ($^\circ$)	σ_t (kPa)	ψ ($^\circ$)
10344 T	1625	0.3	550	15.4	756.25	2.76	26	8.5	0

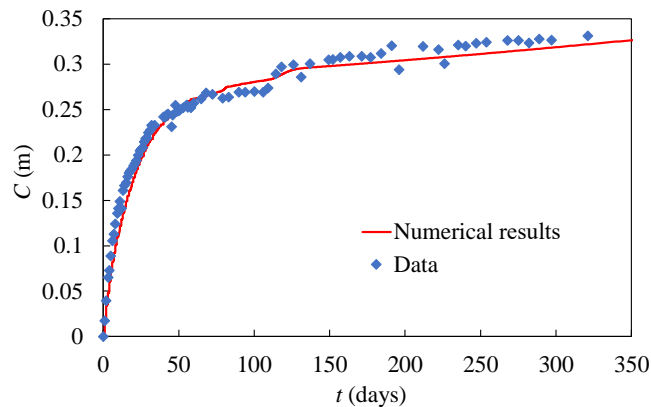
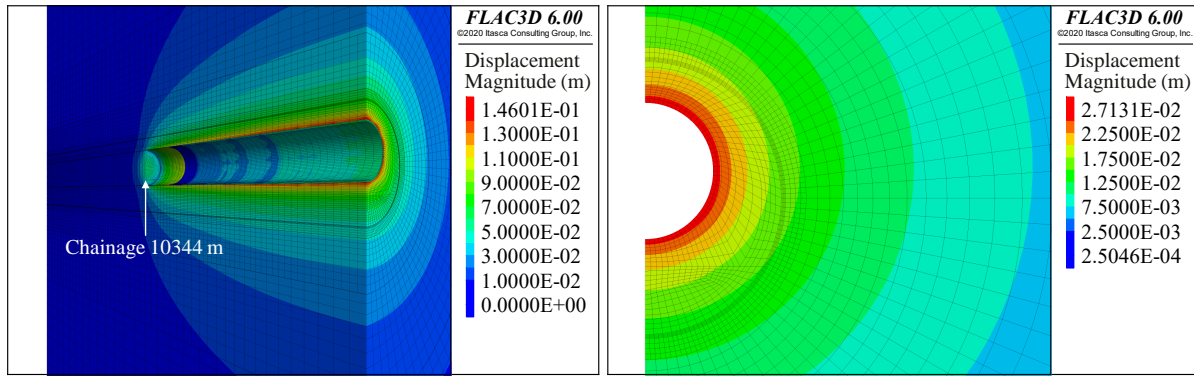
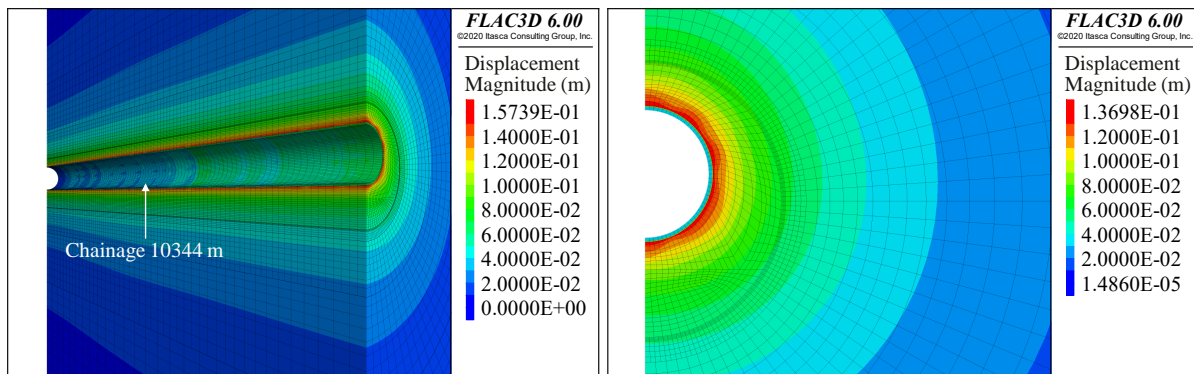


Figure 4.25: Numerical simulation of mean convergence of SMP4-RPS

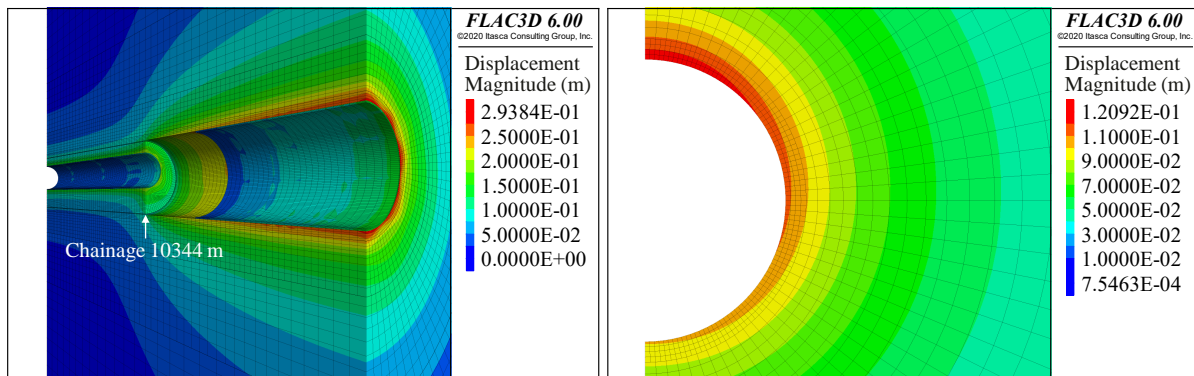
The displacement magnitude at chainage 10344 m are shown in Figure 4.26 at different stages of the excavation. The excavation of PS induces a quasi-isotropic displacement contour. However, the beginning of the excavation of RPS induces a significant anisotropy of the displacement around the tunnel because the excavated PS is not centered: it is located in the upper part of the RPS profile. The upper part of RPS shows larger displacement at the beginning and the deformation becomes less anisotropic later.



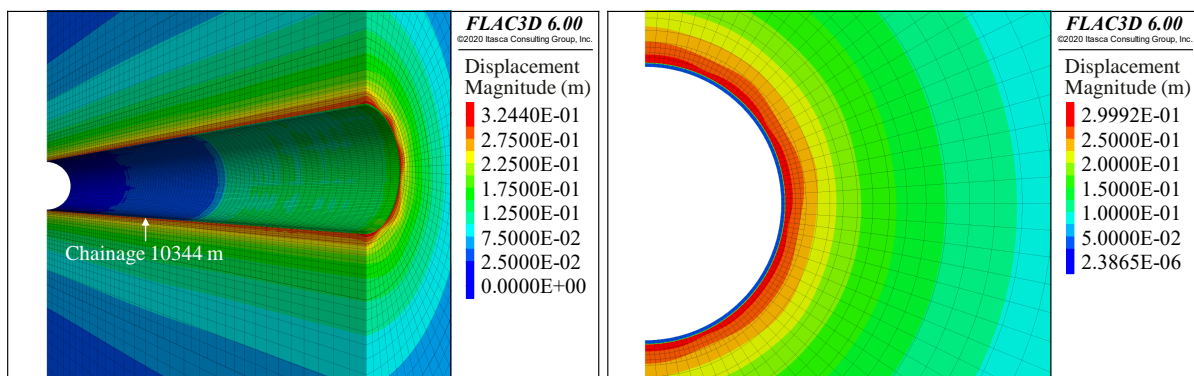
(a) When tunnel face is at chainage 10344 m for SMP4-PS



(b) At the end of the excavation and support installation of SMP4-PS



(c) When reprofiling is at chainage 10344 m for SMP4-RPS



(d) At the end of the reprofiling and support installation of SMP4-RPS

Figure 4.26: Displacement magnitude contour at chainage 10344 m for different excavation stages in SMP4-RPS

The computed stress in shotcrete of the support system is shown in Figure 4.27. The HiDCon blocks are elastic at the end of the excavation and several elements of the HiDCon blocks began to yield after 2 years because of the time-dependent deformation of the rock mass.

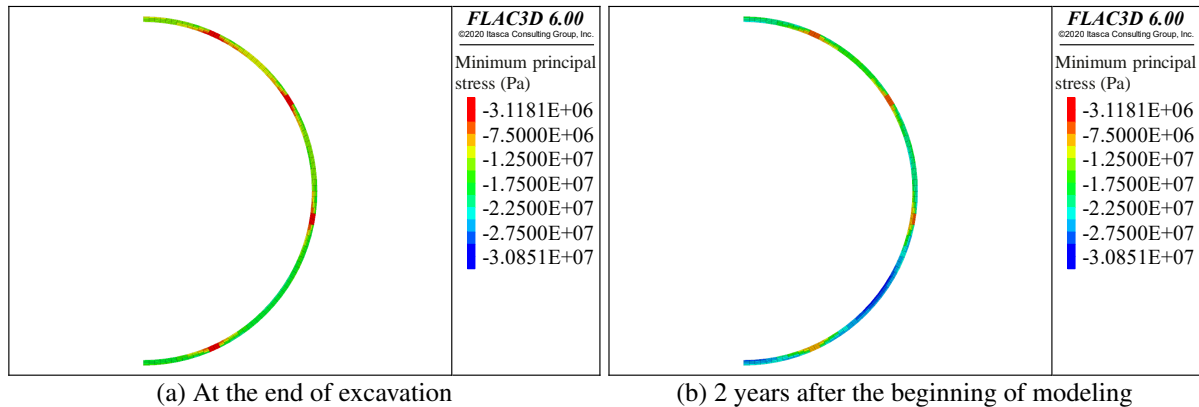


Figure 4.27: Stress contour of the shotcrete in SMP4-RPS

We focus on the first 250 days after the installation of the support system and study the hoop stress evolution. The numerical results of hoop stress of 16 elements are shown in Figure 4.28. The stress increases quickly at the beginning and then the increasing rate of the stress becomes almost constant because of the presence of Maxwell element in the CVISC model. Thus the minimum principal stress (maximum in absolute value) in the shotcrete after 100 days is overestimated as compared to the field data: 15 to 21 MPa at 200 days in the numerical modeling and less than 17 MPa in the field data.

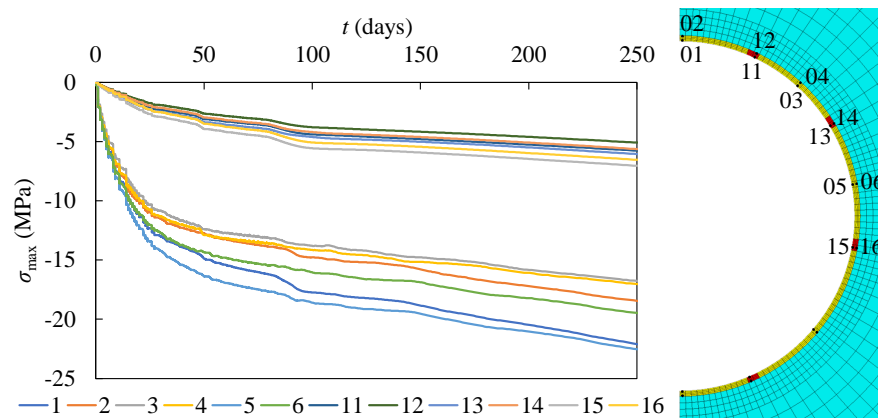


Figure 4.28: Hoop stress evolution of the shotcrete in SMP4-RPS

4.5 Summary

Numerical simulations have been carried out with *Flac3D* using the developed constitutive model in SMP2 (Tran-Manh, 2014).

The time-dependent and anisotropic behavior of SMP2 has been simulated in the present work by applying the considered model (the CVISC model combined with the ubiquitous-joint model) and by taking into account the specific support system. The mid-term and long-term hoop stress in the final lining is overestimated when the same values of parameters, calibrated from the short-term ground behavior (Tran-Manh, 2014), are applied. The viscosity of the Maxwell element in the constitutive model need to

be increased after installation the final lining to simulate the very low convergence rate. The fractional CVISC model is applied, which gives a good simulation of the long-term stress in the final lining.

As no dominant direction of anisotropy is identified in SMP4-PS and RPS, which are much deeper than SMP2 and excavated in another direction, the CVISC model is applied without introducing the ubiquitous joints. In the numerical modeling of different parts of SMP4, several parameters (ν , ϕ , σ_t and ψ) are fixed to the obtained values from SMP2. The other constitutive parameters are adjusted as the rock mass is much stiffer because of larger overburden (Table 4.16). The Young's modulus E and the viscosity of Maxwell element η^M obtained for SMP4 have much higher values than for SMP2.

Table 4.16: Summary of the obtained parameters for the CVISC model

Gallery	Chainage (m)	E (MPa)	ν (-)	G^K (MPa)	η^K (GPa.day)	η^M (GPa.day)	c (MPa)	ϕ (°)	σ_t (kPa)	ψ (°)
SMP2	1383	650	0.3	550	2.2	13.75	1.2	26	8.5	0
SMP4-PS	10316 T	1625	0.3	825	13.2	550	3.12	26	8.5	0
	10321 C	1625	0.3	715	2.64	412.5	3.84	26	8.5	0
	10326 T	1625	0.3	605	1.375	275	2.52	26	8.5	0
SMP4-RPS	10344 T	1625	0.3	550	15.4	756.25	2.76	26	8.5	0

Field observations have emphasized the strong heterogeneity of the rock mass. The complex geological context is accounted for in constitutive model by considering “average” values of the rock mass properties that can lead to an acceptable simulation of the global response of the ground. However, the local response of the individual geological units cannot be reproduced with the present approach.

The shotcrete in the temporary support system and the concrete ring as the final lining are simulated by elastic model with fixed mechanical properties lack of detailed information about the time-dependent characteristics of concrete.

The performance of the HiDCon elements installed in the yielding support system is highlighted by the numerical simulations, as they contribute to reduce significantly the stress in the shotcrete layer. Therefore, it provides an efficient solution for the support system of tunnels in highly squeezing ground.

The procedure of the numerical modeling and the obtained constitutive parameters can be applied and adjusted with the future field work and the new monitoring data, which contributes to the design of the further construction.

CONCLUSIONS AND FUTURE WORK

Conclusions

The current thesis work aims to study the time-dependent and anisotropic behavior observed during and after the excavation of SMP exploratory galleries of Lyon-Turin link under squeezing condition on the basis of extensive monitoring programs. The developed procedure of analyses of the ground response after tunneling in SMP2 has been applied for further time scale and for the condition encountered in SMP4, which is much deeper and excavated in another direction. The excavation of different parts of SMP4 is performed with large size section (GS) or small size section (PS) and reprofiling of PS to full size (RPS).

Data processing

The recorded cross-section convergence data are much smaller and squeezing is less pronounced in SMP4 than that in SMP2 even though the gallery is much deeper. The developed methods of data processing and obtained parameters values of the semi-empirical convergence law for SMP2 are successfully applied to SMP4 with several adaptations:

- In the geometrical processing of the anisotropic convergence, when a preferred direction of deformation can be identified, the deformation of the cross-section is fitted by an ellipse and the convergence of the minor and major axes can be fitted independently. When no dominant direction of anisotropy can be identified, the deformation of the cross-section is simply fitted by a circle and the convergence of the circle diameter is fitted by the convergence law.
- The obtained parameters values of the convergence law of SMP2 are applied considering the size effect, which permit to predict long-term convergence of the tunnel wall by fitting a single parameter related to $C_{\infty x}$ “instantaneous” convergence.
- If the tunnel is excavated and supported in two stages during the convergence measurements, fitting of the convergence law also needs to be carried out separately for two stages.

In SMP4-GS, the material heterogeneity is taken into account and the anisotropy of section closure is identified by the identification of a preferred orientation of the tunnel deformation for each section. With the parameters obtained from SMP2, the convergence can be reproduced for the first studied sections and only the first twenty days of convergence measurements are sufficient for the prediction of long-term convergence. However, when the tunnel approaches the collapsed section at chainage 10303 m, the convergence becomes much stronger and higher value of the parameter T (i.e. characteristic time related to the time-dependent properties of the system) in the convergence law is required to fit the convergence data. This high value of parameter T is seen as an indicator of the collapse.

In SMP4-PS and RPS, the measured convergences are much smaller than in SMP4-GS. A single

orientation cannot be identified for the anisotropic convergence because the rock mass is highly heterogeneous. The mean convergence is fitted by a circle shape of the deformed section, and the anisotropic convergence is represented by the shortening of different strings. The mean convergence and strings convergence are reproduced by fitting the convergence law following the two stages of excavation and support installation keeping the same values of the parameters as for SMP4-GS except C_{∞} , which is fitted separately for two stages of each section.

The long-term convergences normalized by the tunnel diameter of SMP4-PS and SMP4-RPS are compared, and three zones are identified. In the first and third zones, the normalized predicted convergences are similar for these two profiles. However, in the second zone, the normalized convergence is larger for SMP4-RPS than for SMP4-PS. This reflects the heterogeneity of the rock mass not only in longitudinal direction but also in the radial direction. Comparison of the predicted convergence using the convergence law shows that the excavation method with small size section and reprofiling does not have significant advantages in reducing the long-term convergence.

Numerical modeling

Based on the constitutive model developed for SMP2 and the obtained typical values of the mechanical parameters, numerical simulations have been carried out with *Flac3D* code.

The time-dependent and anisotropic behavior of SMP2 has been simulated in large-strain mode with a 2D model. The constitutive model based on CVISC viscoelastic-plastic law combined with the ubiquitous-joint approach as proposed by Tran-Manh (2014) is used. The whole process of tunnel excavation and support installation includes the reprofiling phase. Keeping the same model parameters as those calibrated for the short-term response (Stage 1 of the excavation) by Tran-Manh (2014) leads to over-estimate the stresses in the final lining in the long term. This is remedied by considering a higher value of the viscosity of the Maxwell element in the CVISC model at the installation of the final lining. Another option is explored which consists in resorting to a fractional Maxwell element which gives a good simulation of the mid-term and long-term responses with the same set of model parameters. However, the implementation of CVISC in *Flac3D* is for the moment restricted to 2D problems.

As no dominant direction can be identified in SMP4-PS and RPS, 2D and 3D numerical modeling has been carried out with the CVISC model without introducing the ubiquitous-joint approach to analyze the average behavior of heterogeneous rock mass in SMP4, which is much deeper and excavated in another direction. The rate-independent constitutive parameters of the rock mass can be determined with the help of the parameter C_{∞} of the convergence law. As the rock mass is much stiffer than for SMP2, the constitutive parameters as fitted for SMP2 cannot be used and need to be adjusted. A set of model parameters is proposed for the short-term and mid-term response of the rock mass. Different parameter values reflect the material heterogeneity in both longitudinal and radial direction.

Thanks to the 3D numerical modeling taking into account the excavation procedure, support installation and reprofiling process of SMP4, the hoop stress in the shotcrete of the temporary support system is simulated. The highly deformable elements (HiDCon) installed in the temporary support are modeled using the double-yield model available in *Flac3D*. The performance of the HiDCon elements is demonstrated in the numerical simulations as they lead to a significant reduction of the stresses in the shotcrete layer.

Future work

As the construction works of SMP4 and the in-situ monitoring programs are currently in progress, the analyses can be completed when more field data are collected. The field data processing procedure, the numerical tools and the obtained values of parameters can be applied for the further part of SMP4 which is excavated with full size section. As mentioned in the thesis of [Tran-Manh \(2014\)](#), future studies of the convergence law and numerical simulation might allow to find an empirical relation between the parameters of the convergence law and the mechanical parameters of the rock mass.

The current studies of the survey gallery at the axis of the Southern tube of base tunnel can give indications for the construction of the future Northern tube distanced from 35 to 40 m. The applied support method shows advantages when crossing squeezing formation and could be applied for the Northern tube. The data processing procedure and the numerical models can be re-used and adjusted.

Several improvements could be proposed for future numerical studies.

In the 2D modeling, the excavation of the cross-section and the influence of the tunnel face advance are taken into account by introducing the deconfinement rate λ , which is calculated by a simple elastoplastic numerical simulation and assumed the same in a viscoelastic-plastic modeling. In order to validate this assumption, further studies are needed as the assumed evolution of the deconfinement rate has a major influence on the short-term response. The influence of the support installation on the deconfinement rate could also be introduced as it is done in the implicit convergence-confinement methods.

Further studies are also required for the implementation of fractional derivative viscous models in 3D numerical models. This appears as a promising way to account for evolution of the viscosity of the rock with stress and strain.

In the present work, the concrete (shotcrete in the temporary support and concrete ring of the final lining) is simulated with linear elastic model. Time-dependency of the mechanical properties of the support system needs to be accounted for and could be implemented in the current model. Study of the behavior of support structure contributes to the design of construction.

Field monitoring plays an important role for the analysis of the ground behavior. In the numerical of the yielding support system with HiDCon elements in SMP4, the stress in the shotcrete layer of only one section is validated while the information about the stress or stain in the HiDCon elements is not available. The modeling of the yielding support system can be completed with more recorded data for the future field work.

REFERENCES

- Addante, M. T. (2016). *Anisotropic Closure in Squeezing Ground* (Master Thesis). Politecnico di Torino, Ecole des Ponts ParisTech.
- AFTES. (2005). *Méthodes d'auscultation des ouvrages souterrains*. Tunnels et Espace souterrain.
- Aydan, O., Akagi, T., and Kawamoto, T. (1993). The squeezing potential of rocks around tunnels; Theory and prediction. *Rock Mechanics and Rock Engineering*, 26(2), 137–163. doi: 10.1007/BF01023620
- Barla, G. (1995). Squeezing rocks in tunnels. *ISRM News Journal*, 3/4, 44–49.
- Barla, G. (2001). Tunnelling under squeezing rock conditions. *Eurosummer-School in Tunnel Mechanics, Innsbruck, nsbruckpp*(July), 169–268. doi: 10.1111/j.1600-0447.2009.01439.x
- Barla, G., Barla, M., Bonini, M., and Debernardi, D. (2007). *Lessons learned during the excavation of the Saint Martin La Porte access gallery along the Lyon-Turin Base tunnel*. (Tech. Rep.).
- Barla, G., Barla, M., Bonini, M., and Debernardi, D. (2014). Guidelines for tbn tunnelling in squeezing conditions – a case study. *Geotechnique Letters*, 4(April-June), 83–87. doi: 10.1680/geolett.13.00065
- Barla, G., Bonini, M., and Debernardi, D. (2010). Time Dependent Deformations in Squeezing Tunnels. *International Journal of Geoengineering Case Histories*, 2(1), 40. doi: 10.4417/IJGCH-02-01-03
- Barla, G., Bonini, M., and Semeraro, M. (2011). Analysis of the behaviour of a yield-control support system in squeezing rock. *Tunnelling and Underground Space Technology*, 26(1), 146–154.
- Barla, G., Debernardi, D., and Sterpi, D. (2012). Time-dependent modeling of tunnels in squeezing conditions. *International Journal of geomechanics*, 12(6), 697–710. doi: 10.1061/(ASCE)GM.1943-5622.0000163.
- Barton, N., Lien, R., and Lunde, J. (1974). Engineering classification of rock masses for the design of tunnel support. *Rock Mechanics Felsmechanik Mécanique des Roches*, 6(4), 189–236. doi: 10.1007/BF01239496
- Bernaudo, D., and Rousset, G. (1992). La “nouvelle méthode implicite” pour l’étude du dimensionnement des tunnels. *Revue Française de Géotechnique*(60), 5–26. doi: 10.1051/geotech/1992060005
- Bernaudo, D., and Rousset, G. (1996). the ‘New Implicit Method’ for Tunnel Analysis. *International Journal for Numerical and Analytical Methods in Geomechanics*, 20(9), 673–690.
- Bieniawski, Z. T. (1973). Engineering Classification of Jointed Rock Masses. *Civ Eng S Afr*, 15(12), 335–343.
- Bieniawski, Z. T. (1989). *Engineering rock mass classifications: a complete manual for engineers and geologists in mining, civil, and petroleum engineering*. John Wiley & Sons.
- Bobet, A., and Einstein, H. H. (2011). Tunnel reinforcement with rockbolts. *Tunnelling and Underground Space Technology*, 26(1), 100–123. doi: 10.1016/j.tust.2010.06.006
- Bonini, M., and Barla, G. (2012). The Saint Martin La Porte access adit (Lyon-Turin Base Tunnel) revisited. *Tunnelling and Underground Space Technology*, 30, 38–54. doi: 10.1016/j.tust.2012.02.004

- Bonini, M., Debernardi, D., Barla, M., and Barla, G. (2009). The mechanical behaviour of clay shales and implications on the design of tunnels. *Rock Mechanics and Rock Engineering*, 42(2), 361–388. doi: 10.1007/s00603-007-0147-6
- De La Fuente, M. (2018). *Tunneling under squeezing conditions : Effect of the excavation method* (PhD thesis). Université Paris-Est.
- De La Fuente, M., Sulem, J., Taherzadeh, R., and Subrin, D. (2019). Tunneling in Squeezing Ground : Effect of the Excavation Method. *Rock Mechanics and Rock Engineering*. doi: 10.1007/s00603-019-01931-4
- Debernardi, D. (2008). *Viscoplastic behaviour and design of tunnels* (PhD thesis). Politecnico di Torino.
- Debernardi, D., and Barla, G. (2009). New viscoplastic model for design analysis of tunnels in squeezing conditions. *Rock Mechanics and Rock Engineering*, 42(2), 259–288. doi: 10.1007/s00603-009-0174-6
- Deere, D. U. (1964). Technical description of rock cores for engineering purpose. *Rock Mechanics and Engineering Geology*, 1(1), 17-22.
- Deere, D. U., and Deere, D. W. (1988). The rock quality designation (RQD) index in practice. In *Rock classification systems for engineering purposes*. ASTM International.
- Descocudres, F., Giani, G., and Brino, L. (2015). Il tunnel di base del Moncenisio per la nuova linea ferroviaria Torino-Lione: aspetti geomeccanici e confronto con i grandi trafori svizzeri. *Gallerie e Grandi Opere Sotterranee*(115), 21–31.
- Duveau, G., Shao, J. F., and Henry, J. P. (1998). Assessment of some failure criteria for strongly anisotropic geomaterials. *Mechanics of Cohesive-Frictional Materials*, 3(1), 1–26. doi: 10.1002/(SICI)1099-1484(199801)3:1<1::AID-CFM38>3.0.CO;2-7
- Einstein, H. (1989). Design and analysis of underground structures in swelling and squeezing rocks. In *Developments in geotechnical engineering* (Vol. 59, pp. 203–262). Elsevier.
- Fjær, E., and Nes, O. M. (2013). Strength anisotropy of Mancos shale. In *47th us rock mechanics/geomechanics symposium*.
- Fujita, M. (1978). Seikan undersea tunnel. In *Tunnelling under difficult conditions*.
- Gioda, G. (1981). A finite element solution of non-linear creep problems in rocks. *International Journal of Rock Mechanics and Mining Sciences & Geomechanics Abstracts*, 18(1), 35–46. doi: 10.1016/0148-9062(81)90264-3
- Gioda, G. (1982). On the non-linear ‘squeezing’ effects around circular tunnels. *International Journal for Numerical and Analytical Methods in Geomechanics*, 6(1), 21–46.
- Gioda, G., and Cividini, A. (1996). Numerical methods for the analysis of tunnel performance in squeezing rocks. *Rock Mechanics and Rock Engineering*, 29(4), 171–193. doi: 10.1007/BF01042531
- Goel, R. K. (2000). Tunnelling in squeezing ground conditions. *Rivista Italiana di Geotecnica*, 1, 35–40.
- Goel, R. K., Jethwa, J., and Paithankar, A. (1995). Tunnelling through the young Himalayas—a case history of the Maneri-Uttarkashi power tunnel. *Engineering Geology*, 39(1-2), 31–44.
- Gol’denblat, I. I., and Kopnov, V. A. (1966). Strength of glass-reinforced plastics in the complex stress state. *Polymer Mechanics*, 1(2), 54–59. doi: 10.1007/BF00860685
- Guayacán-Carrillo, L. M. (2016). *Analysis of long-term closure in drifts excavated in Callovo-Oxfordian claystone: roles of anisotropy and hydromechanical couplings* (PhD thesis). Université Paris-Est.
- Guayacán-Carrillo, L.-M., Sulem, J., Seyed, D. M., Ghabezloo, S., and Armand, G. (2018). Size effect on the time-dependent closure of drifts in Callovo-Oxfordian claystone. *International Journal of Geomechanics*, 18(10), 04018128.
- Guayacán-Carrillo, L.-M., Sulem, J., Seyed, D. M., Ghabezloo, S., Noiret, A., and Armand, G. (2016). Analysis of long-term anisotropic convergence in drifts excavated in Callovo-Oxfordian claystone.

- Rock Mechanics and Rock Engineering*, 49(1), 97–114.
- Hasanpour, R., Rostami, J., and Barla, G. (2015). Impact of Advance Rate on Entrapment Risk of a Double-Shielded TBM in Squeezing Ground. *Rock Mechanics and Rock Engineering*, 48(3), 1115–1130. doi: 10.1007/s00603-014-0645-2
- Heise, F., and Herbst, F. (1913). Förderung. In *Lehrbuch der Bergbaukunde* (pp. 281–525). Springer.
- Hill, R. (1948). A Theory of the Yielding and Plastic Flow of Anisotropic Metals. *Proceedings of the Royal Society A: Mathematical, Physical and Engineering Sciences*, 193(1033), 281–297. doi: 10.1098/rspa.1948.0045
- Hill, R. (1949). The Theory of Plane Plastic Strain for Anisotropic Metals. *Proceedings of the Royal Society of London. Series A, Mathematical and Physical Sciences*, 198(1054), 428–437. doi: 10.1098/rspa.1949.0110
- Hill, R. (1950). *The mathematical Theory of Plasticity*. doi: 10.1002/9780470694626.ch6
- Hoek, E. (1994). *Strength of rock and rock masses*.
- Hoek, E. (2001). Big tunnels in bad rock. *Journal of Geotechnical and Geoenvironmental Engineering*, 127(9), 726–740.
- Hoek, E., and Brown, E. (1980). *Underground Excavations in Rock*.
- Hoek, E., Carranza-Torres, C., and Corkum, B. (2002). Hoek-brown failure criterion – 2002 edition. In *Proceedings of narms-tac* (pp. 267–273). doi: 10.1016/0148-9062(74)91782-3
- Hoek, E., and Marinos, P. (2000). Predicting tunnel squeezing problems in weak heterogeneous rock masses. *Tunnels and Tunnelling International*, 32(11), 45–51.
- Hoek, E., Marinos, P., and Benissi, M. (1998). Applicability of the geological strength index (GSI) classification for very weak and sheared rock masses. The case of the Athens Schist Formation. *Bulletin of Engineering Geology and the Environment*, 57(2), 151–160. doi: 10.1007/s100640050031
- Itasca. (2017). Fast lagrangian analysis of continua (FLAC3D v6.00) [Computer software manual]. Itasca Consulting Group Inc., USA.
- Jaeger, J. C. (1960). Shear Failure of Anisotropic Rocks. *Geological Magazine*, 97(01), 65. doi: 10.1017/S0016756800061100
- Jethwa, J., Singh, B., and Singh, B. (1984). Estimation of ultimate rock pressure for tunnel linings under squeezing rock conditions—a new approach. In *Design and performance of underground excavations: Isrm symposium—cambridge, uk, 3–6 september 1984* (pp. 231–238).
- Kabwe, E., Karakus, M., and Chanda, E. K. (2020). Creep constitutive model considering the overstress theory with an associative viscoplastic flow rule. *Computers and Geotechnics*, 124(December 2019), 103629. doi: 10.1016/j.compgeo.2020.103629
- Kovári, K. (1986). Rock deformation problems when using full-facing cutting equipment in rock, part 2. *Tunnel*, 4(86), 289–298.
- Kovári, K., and Staus, J. (1996). Basic considerations on tunnelling in squeezing ground. *Rock Mechanics and Rock Engineering*, 29(4), 203–210. doi: 10.1007/BF01042533
- Lombardi, G. (1977). Un modele pour le tunnel. In *Journees de l'afes*.
- Mainardi, F. (2010). *Fractional Calculus and Waves in Linear Viscoelasticity*. IMPERIAL COLLEGE PRESS. doi: 10.1142/p614
- Mainardi, F., and Spada, G. (2011). Creep, relaxation and viscosity properties for basic fractional models in rheology. *European Physical Journal: Special Topics*, 193(1), 133–160. doi: 10.1140/epjst/e2011-01387-1
- Mathieu, E. (2008). At the mercy of the mountain. *T & T international(OCT)*, 21–24.
- McLamore, R., and Gray, K. E. (1967). The mechanical behavior of anisotropic sedimentary rocks. *Journal of Manufacturing Science and Engineering, Transactions of the ASME*, 89(1), 62–73. doi: 10.1115/1.3610013

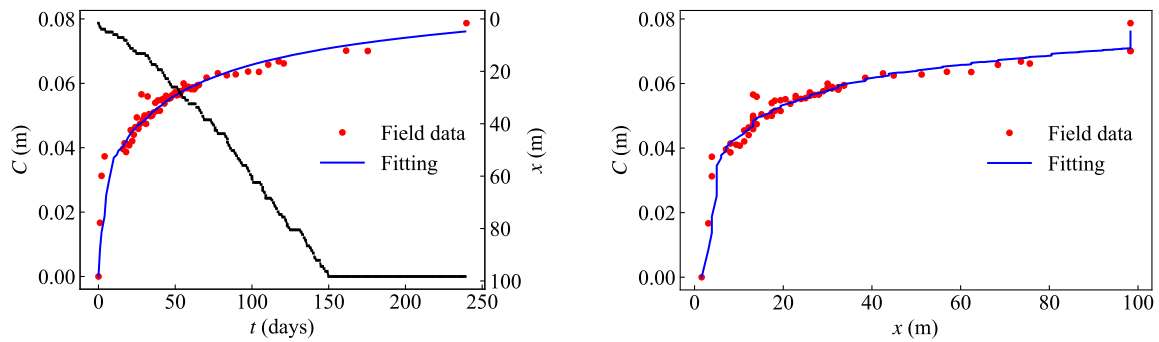
- Monin, N., Brino, L., and Chabert, A. (2014). Le tunnel de base de la nouvelle liaison ferroviaire Lyon-Turin: retour d'expérience des ouvrages de reconnaissance. In *Congrès International AFTES 2014, Lyon, 13-15 October*.
- Muir Wood, A. M. (1972). Tunnels for roads and motorways. *Quarterly Journal of Engineering Geology*, 5(1-2), 111–126. doi: 10.1144/GSL.QJEG.1972.005.01.12
- NGI. (2015). *Using the Q-system, Rock mass classification and support design*.
- Nguyen-Minh, D., and Guo, C. (1996). Recent progress in convergence confinement method. In *Isrm international symposium-eurock 96*. (pp. 855–860).
- Oka, F., Kimoto, S., Kobayashi, H., and Adachi, T. (2002). Anisotropic Behavior of Soft Sedimentary Rock and a Constitutive Model. *SOILS AND FOUNDATIONS*, 42(5), 59–70.
- O'Rourke, T. D. (1984). *Guidelines for tunnel lining design*. ASCE, New York.
- Palmstrom, A. (1982). The volumetric joint count—a useful and simple measure of the degree of rock mass jointing. In *International association of engineering geology. international congress. 4* (pp. 221–228).
- Panet, M. (1995). *Le calcul des tunnels par la méthode convergence-confinement*. Presses ENPC.
- Pariseau, W. G. (1968). PLASTICITY THEORY FOR ANISOTROPIC ROCKS AND SOILS. In *The 10th u.s. symposium on rock mechanics (usrms)*.
- Perzyna, P. (1966). Fundamental problems in viscoplasticity. In *Advances in applied mechanics* (Vol. 9, pp. 243–377). Elsevier.
- Pietruszczak, S., and Mroz, Z. (2000). Formulation of anisotropic failure criteria incorporating a microstructure tensor. *Computers and Geotechnics*, 26(2), 105–112. doi: 10.1016/S0266-352X(99)00034-8
- Ramoni, M., and Anagnostou, G. (2008). Reference : TBM drives in squeezing ground – Shield-rock interaction. *Building underground for the future; AFTES International Congress, Monaco*(October), 163.172.
- Rettighieri, M., Treilclot, J., Mathieu, E., Barla, G., and Panet, M. (2008). Difficultés liées aux fortes convergences rencontrées lors du creusement de la descenderie de Saint Martin La Porte. In *Congrès international de monaco* (pp. 395–403).
- Russo, G., Repetto, L., Piraud, J., and Lavignerie, R. (2009). Back-analysis of the extreme squeezing conditions in the exploratory adit to the Lyon-Turin base tunnel. In *Proceedings of the 3rd canus rock mechanics symposium*.
- Semnani, S. J., White, J. A., and Borja, R. I. (2016, dec). Thermoplasticity and strain localization in transversely isotropic materials based on anisotropic critical state plasticity. *International Journal for Numerical and Analytical Methods in Geomechanics*, 40(18), 2423–2449. doi: 10.1002/nag.2536
- Singh, B., and Goel, R. K. (1999). *Rock mass classification: a practical approach in civil engineering* (Vol. 46). Elsevier.
- Singh, B., Jethwa, J. L., Dube, A. K., and Singh, B. (1992). Correlation between observed support pressure and rock mass quality. *Tunnelling and Underground Space Technology*, 7(1), 59–74. doi: 10.1016/0886-7798(92)90114-W
- Steiner, W. (1996). Tunnelling in squeezing rocks: Case histories. *Rock Mechanics and Rock Engineering*, 29(4), 211–246. doi: 10.1007/BF01042534
- Stepi, D., and Gioda, G. (2009). Visco-Plastic behaviour around advancing tunnels in squeezing rock. *Rock Mechanics and Rock Engineering*, 42(2), 319–339. doi: 10.1007/s00603-007-0137-8
- Subrin, D., Vu, T. M., Sulem, J., Robert, A., Monin, N., and Brino, L. (2009). Geometrical treatment of convergence and levelling data for the description of the anisotropic behaviour of carboniferous

- coal schists met in the St-Martin-La-Porte access gallery. In *AITES-ITA World Tunnel Congress, Budapest, 23-28 May*.
- Sulem, J. (1983). *Comportement différé des galeries profondes* (PhD thesis). Ecole Nationale des Ponts et Chaussées.
- Sulem, J., Panet, M., and Guenot, A. (1987a). An analytical solution for time-dependent displacements in a circular tunnel. *International journal of rock mechanics and mining sciences & geomechanics abstracts*, 24(3), 155–164.
- Sulem, J., Panet, M., and Guenot, A. (1987b). Closure analysis in deep tunnels. *International journal of rock mechanics and mining sciences & geomechanics abstracts*, 24(3), 145–154.
- Terzaghi, K. (1946). *Rock defects and loads on tunnel supports*. Harvard University.
- Tran-Manh, H., Sulem, J., Subrin, D., and Billiaux, D. (2015). Anisotropic Time-Dependent Modeling of Tunnel Excavation in Squeezing Ground. *Rock Mechanics and Rock Engineering*, 48(6), 2301–2317. doi: 10.1007/s00603-015-0717-y
- Tran-Manh, H. (2014). *Comportement des tunnels en terrain poussant* (PhD thesis). Université Paris-Est.
- Triclot, J., Rettighieri, M., and Barla, G. (2007). Large deformations in squeezing ground in the saint-martin la porte gallery along the lyon-turin base tunnel. *Underground space—the 4th dimension of metropolises*. Taylor & Francis Group, London.
- Tsai, S. W., and Wu, E. M. (1971). A General Theory of Strength for Anisotropic Materials. *Journal of Composite Materials*, 5(1), 58–80. doi: 10.1177/002199837100500106
- Vu, T. M. (2010). *Comportement des tunnels en terrains tectonisés - Application à la liaison ferroviaire Lyon-Turin* (PhD thesis). Université Paris-Est.
- Vu, T. M., Sulem, J., Subrin, D., Monin, N., and Lascols, J. (2013). Anisotropic closure in squeezing rocks: The example of Saint-Martin-La-Porte access gallery. *Rock Mechanics and Rock Engineering*, 46(2), 231–246. doi: 10.1007/s00603-012-0320-4
- Windsor, C. R., and Thompson, A. G. (1994). Rock reinforcement—technology, testing, design and evaluation. *Comprehensive Rock Engineering, Principles, Practice & Projects; Hudson, JA, Ed*, 451–484.

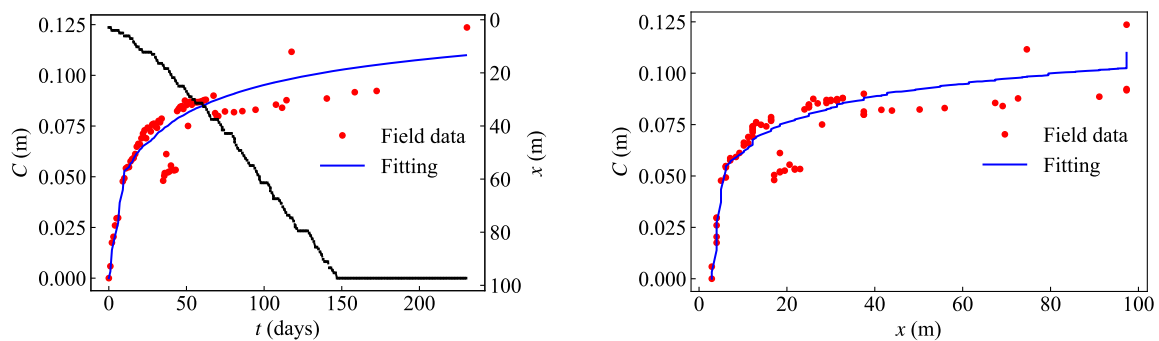
APPENDIX A

AVERAGE CONVERGENCE OF THE SECTIONS IN SMP4-PS

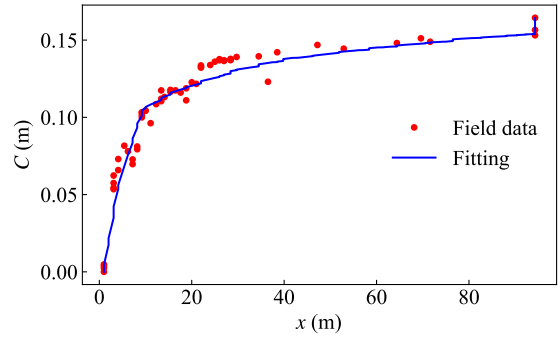
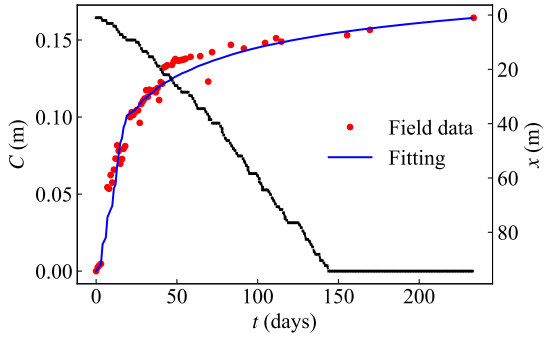
The detailed fitting results of the average convergence of the sections in SMP4-PS are summarized in this appendix. The proposed parameters values of the convergence law for every section are shown in Table 3.8. The black lines in the figures represent the tunnel face advance.



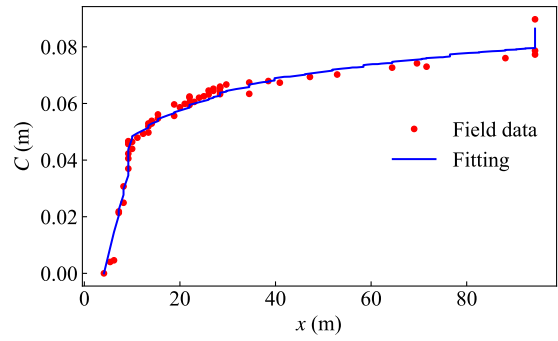
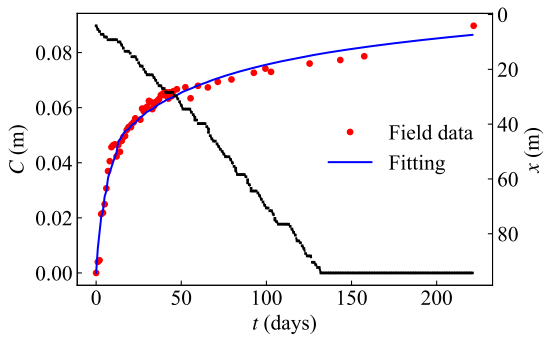
Chainage 10312 m (C)



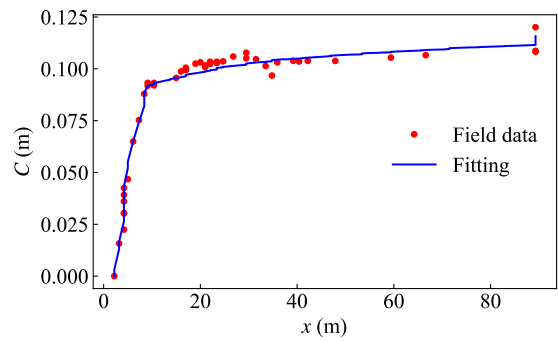
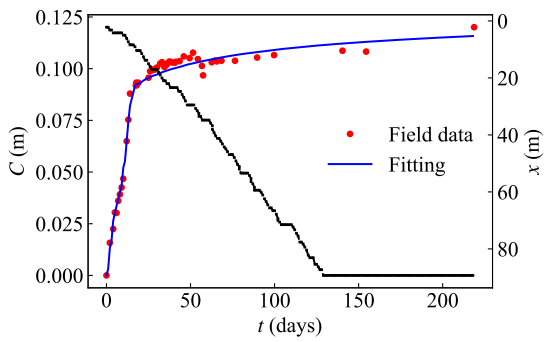
Chainage 10313 m (T)



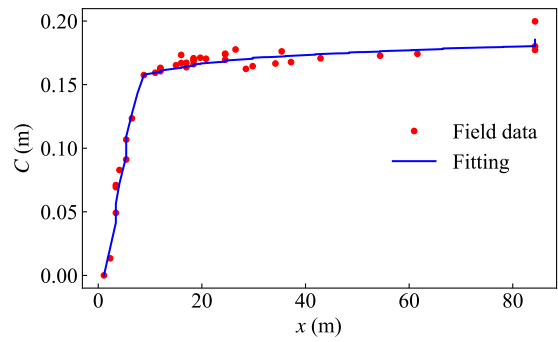
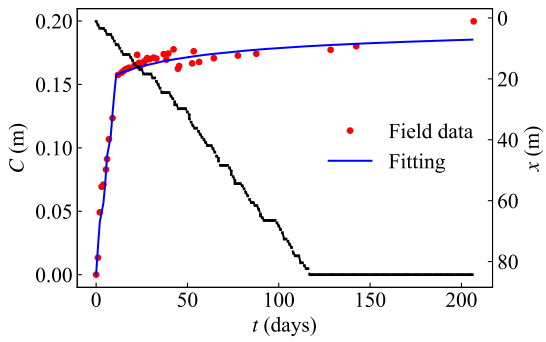
Chainage 10316 m (C)



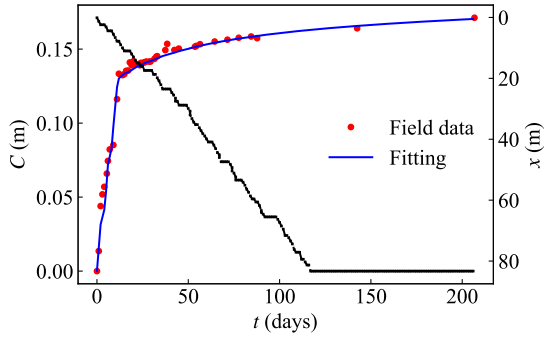
Chainage 10316 m (T)



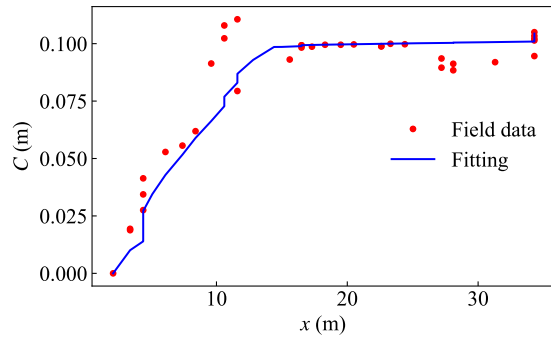
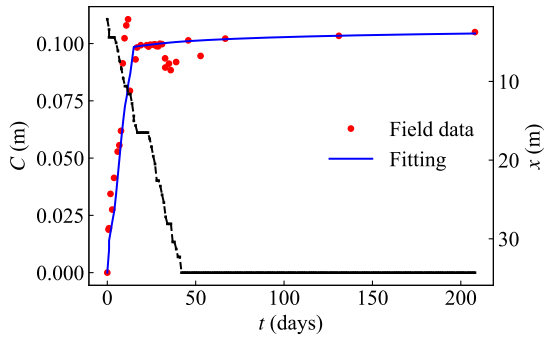
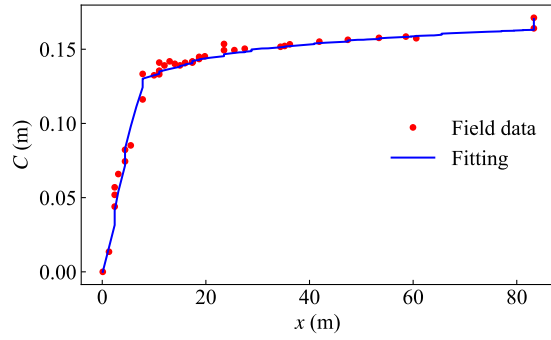
Chainage 10321 m (C)



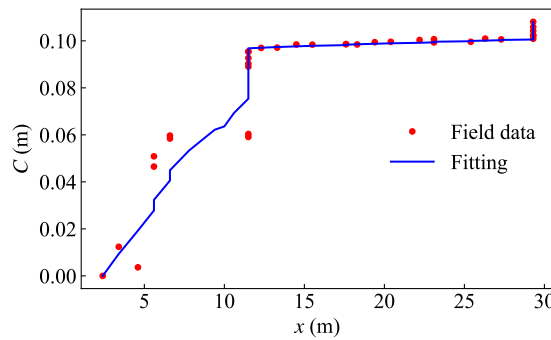
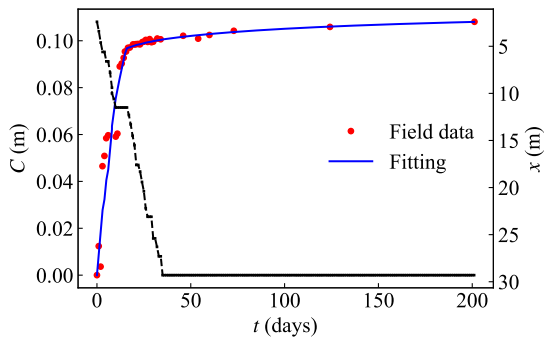
Chainage 10326 m (T)



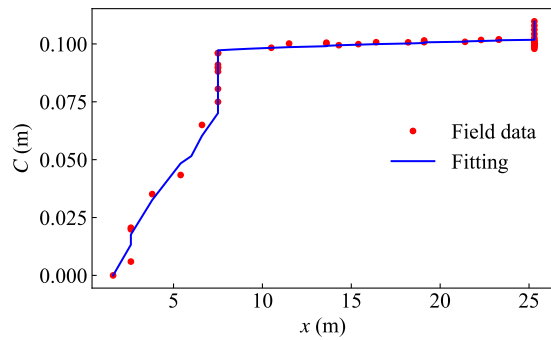
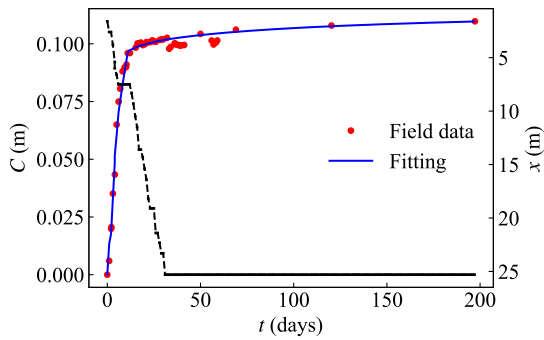
Chainage 10327 m (C)



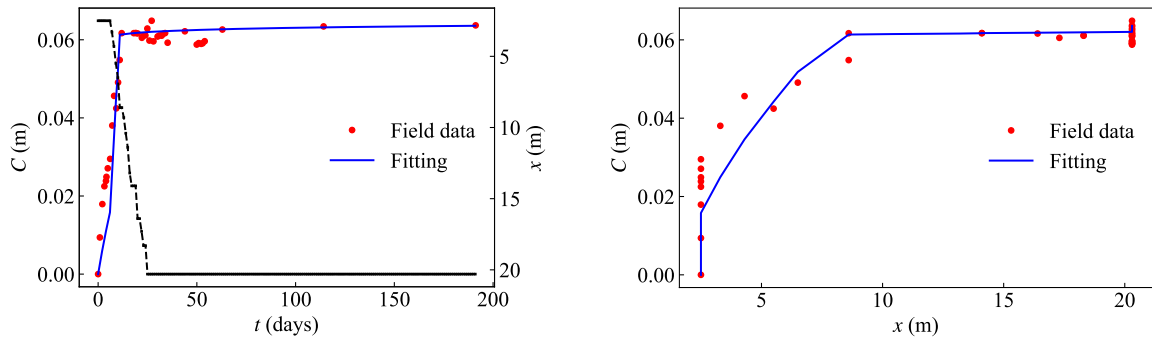
Chainage 10376 m (B)



Chainage 10381 m (B)



Chainage 10385 m (B)



Chainage 10390 m (B)

Figure A.1: Mean convergence fitting of the sections in SMP4-PS (The black lines show the tunnel face advance.)

APPENDIX B

STRING CONVERGENCE OF THE SECTIONS IN SMP4-PS

The detailed fitting results of the strings convergence of the sections in SMP4-PS are summarized in this appendix. The proposed parameters values of the convergence law for every section are shown in Table 3.9. The black lines in the figures represent the tunnel face advance.

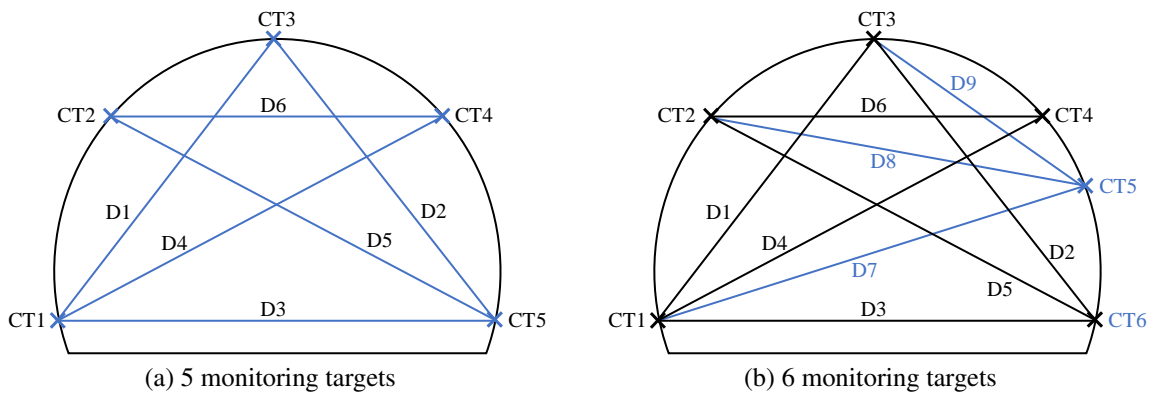


Figure B.1: Strings used for convergence measurements in SMP4-PS (The black lines show the tunnel face advance.)

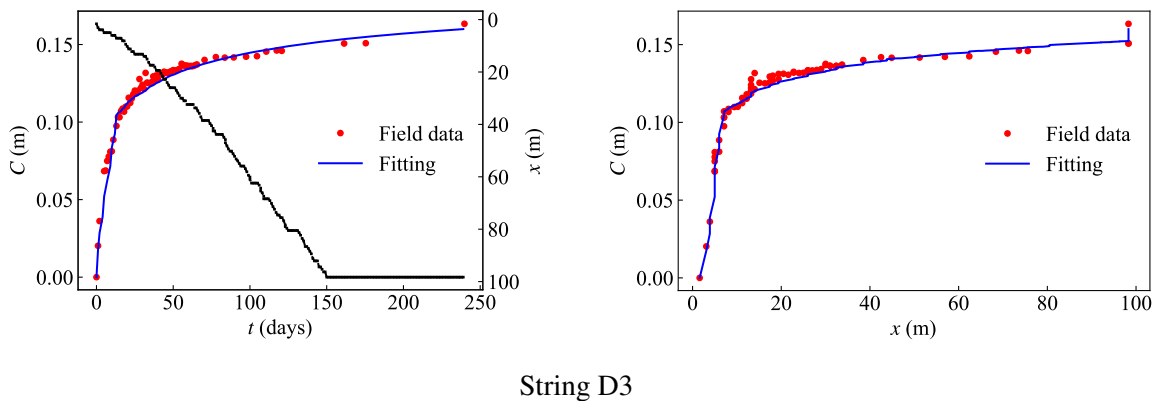
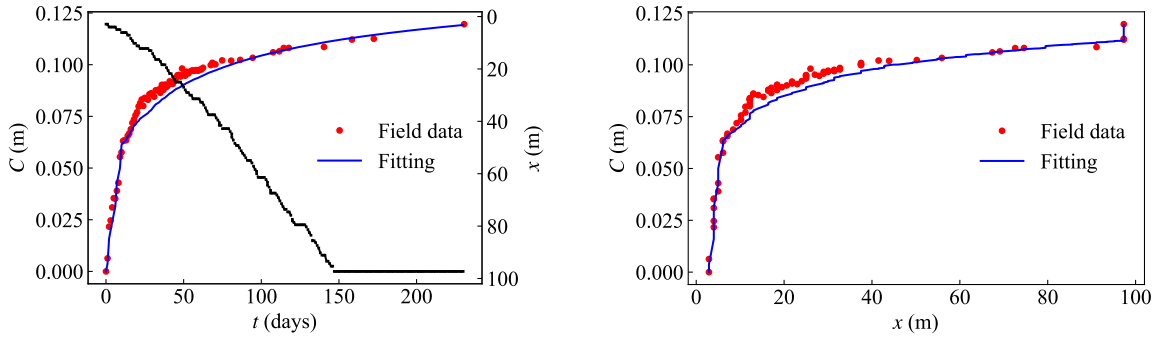
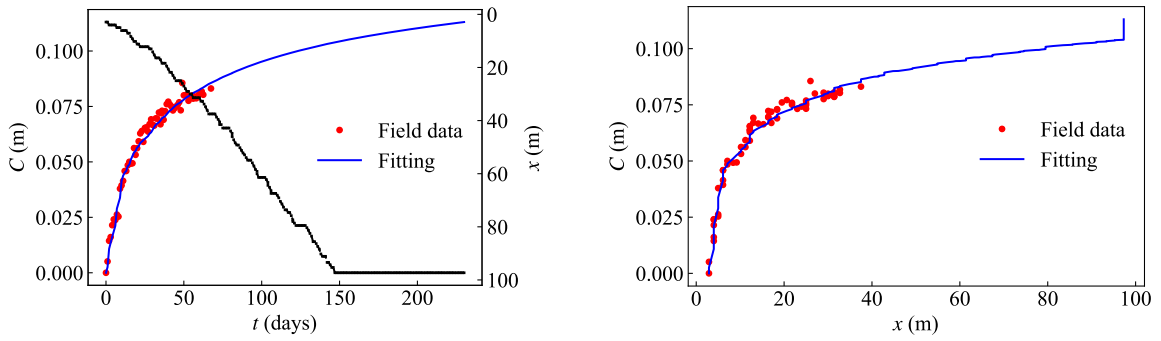


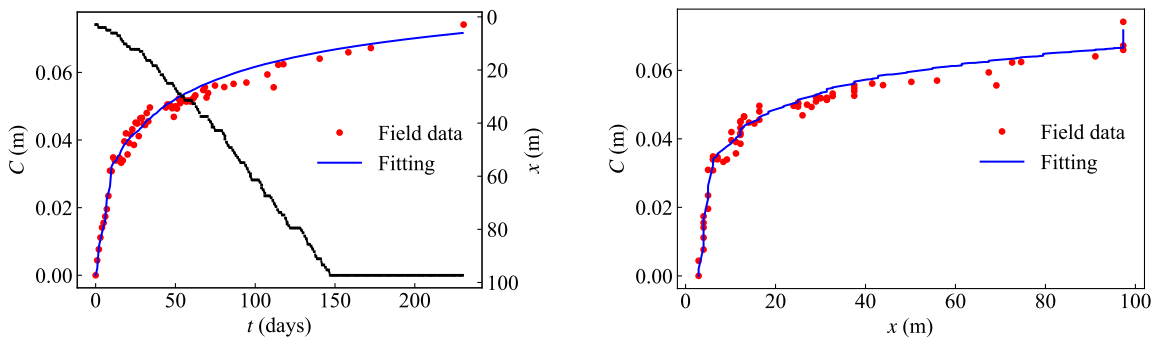
Figure B.2: Strings convergence fitting of the section at chainage 10312 m (C) in SMP4-PS (The black lines show the tunnel face advance.)



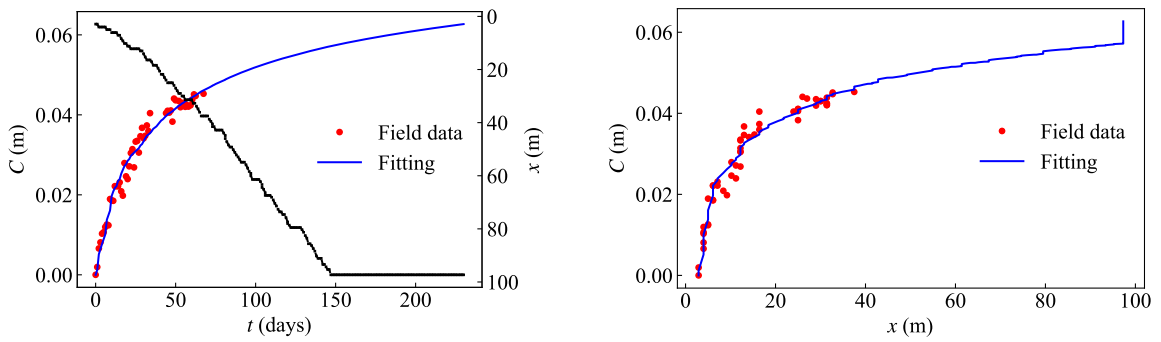
String D3



String D4

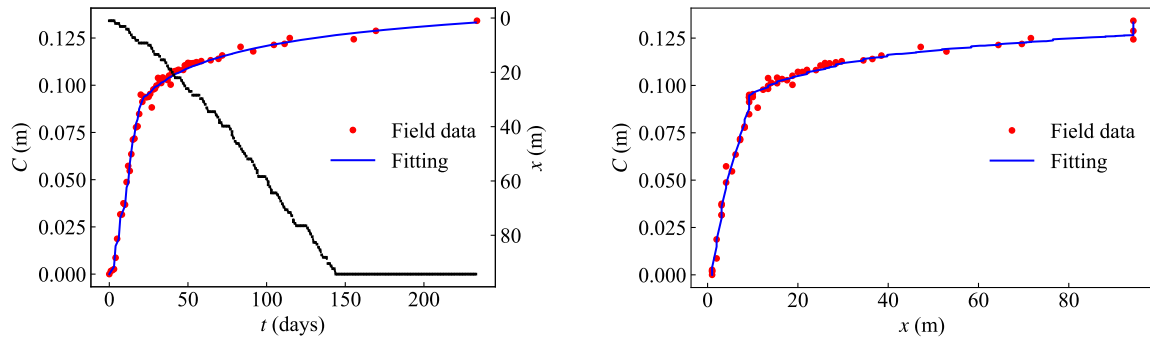


String D5

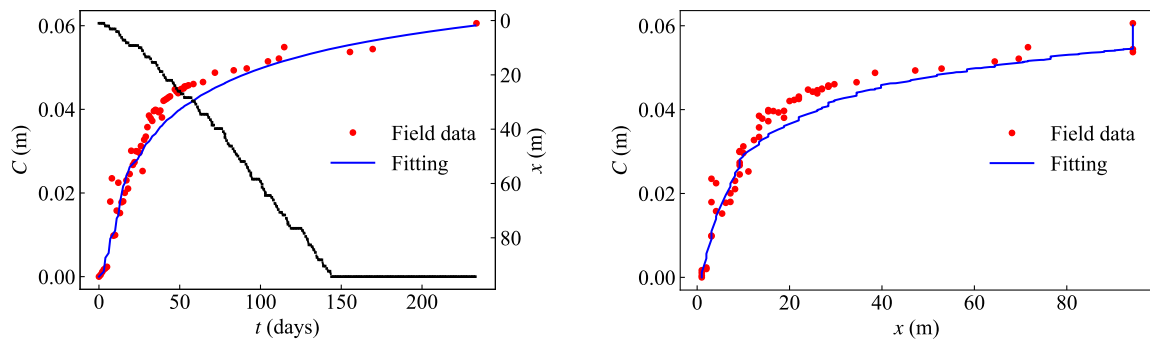


String D6

Figure B.3: Strings convergence fitting of the section at chainage 10313 m (T) in SMP4-PS (The black lines show the tunnel face advance.)

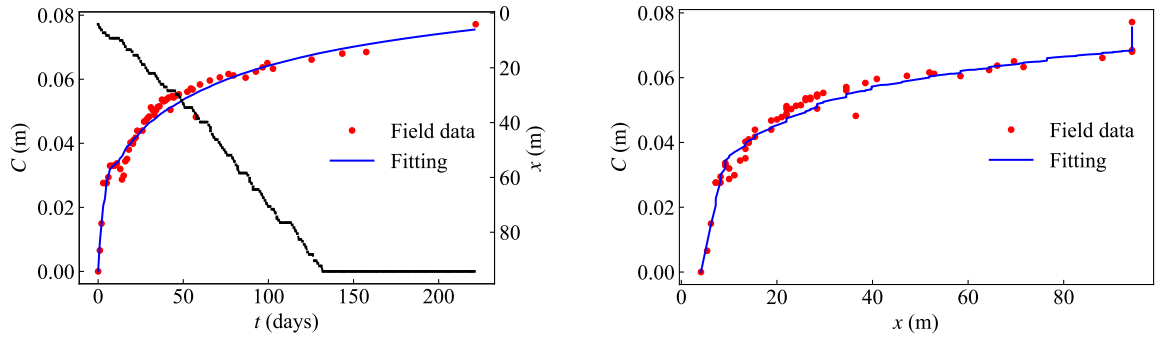


String D5

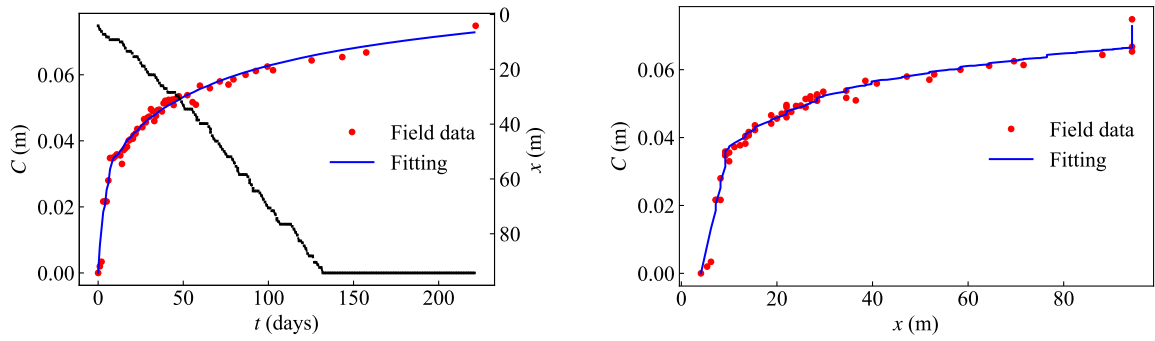


String D6

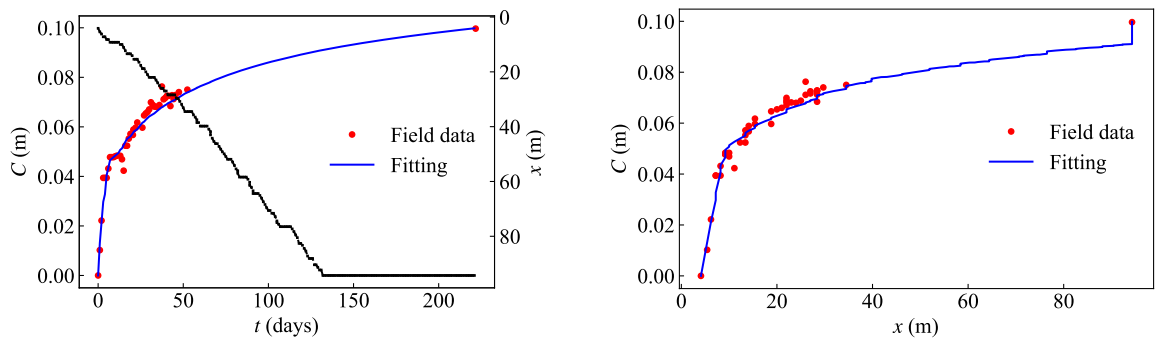
Figure B.4: Strings convergence fitting of the section at chainage 10316 m (C) in SMP4-PS (The black lines show the tunnel face advance.)



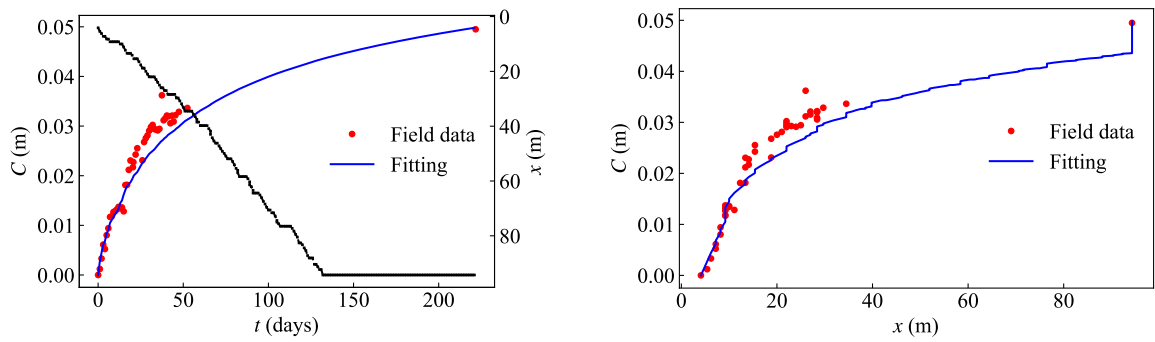
String D1



String D3

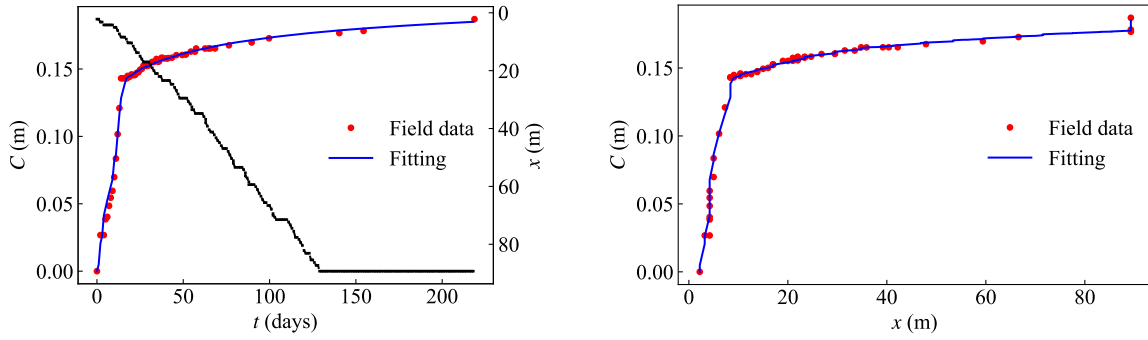


String D4

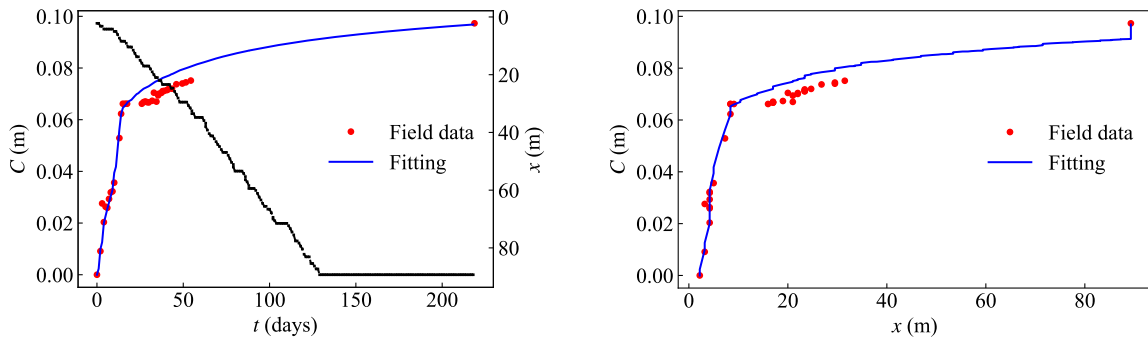


String D6

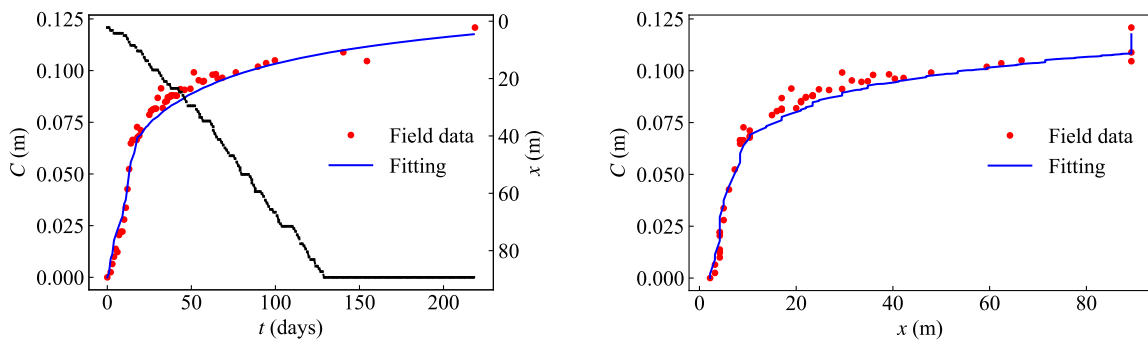
Figure B.5: Strings convergence fitting of the section at chainage 10316 m (T) in SMP4-PS (The black lines show the tunnel face advance.)



String D3

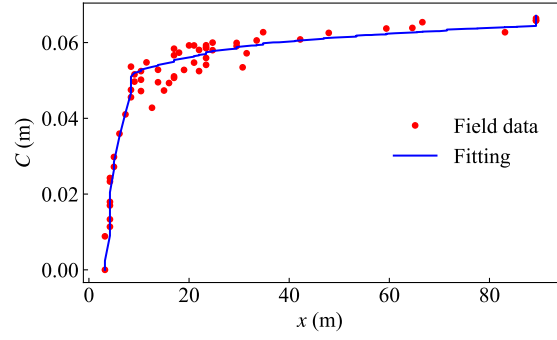
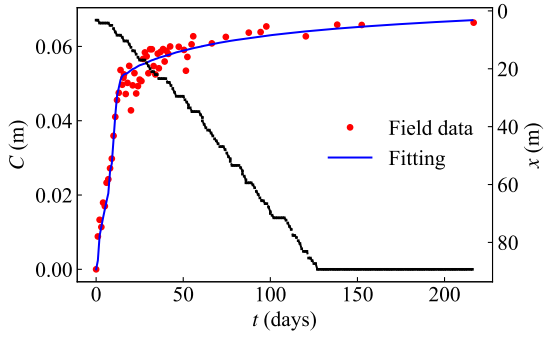


String D4

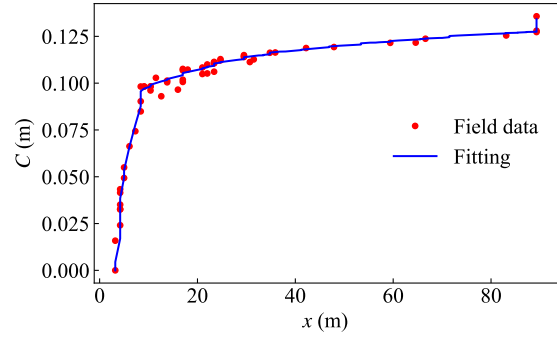
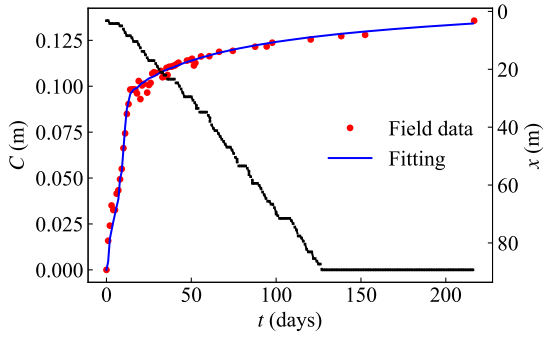


String D7

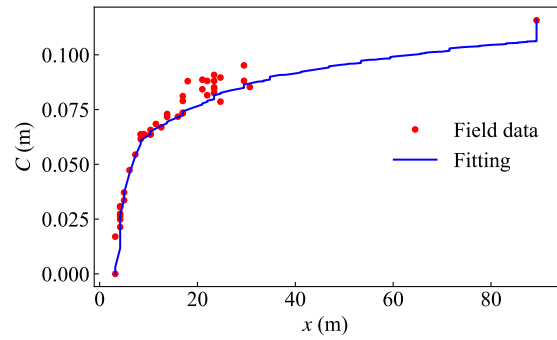
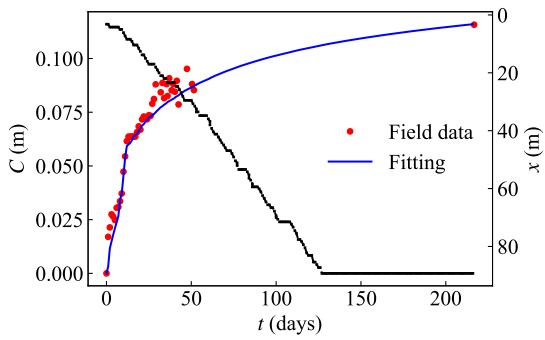
Figure B.6: Strings convergence fitting of the section at chainage 10321 m (C) in SMP4-PS (The black lines show the tunnel face advance.)



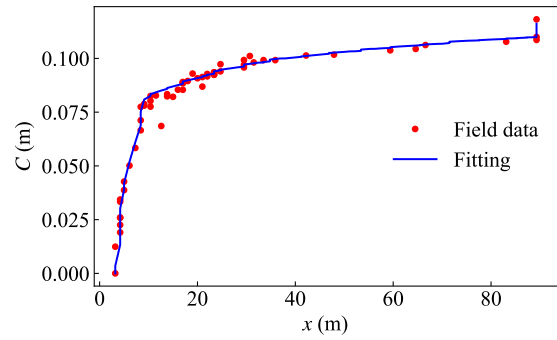
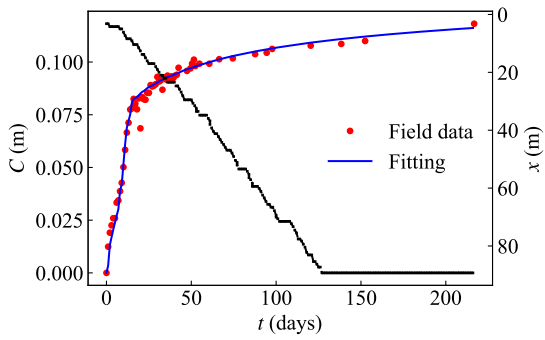
String D2



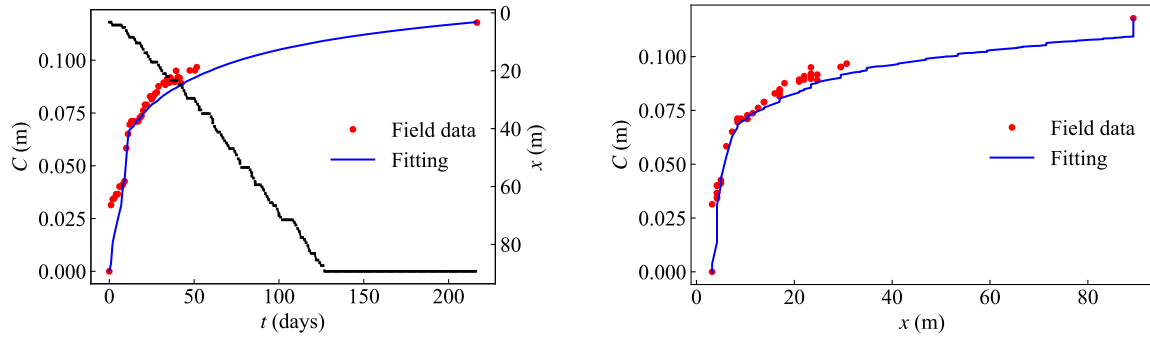
String D3



String D4

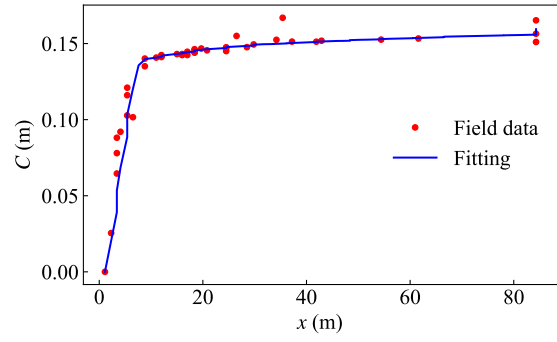
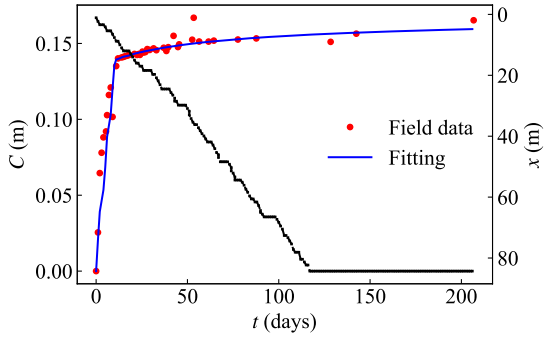


String D5

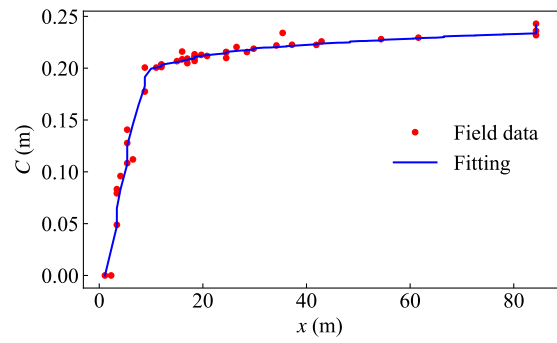
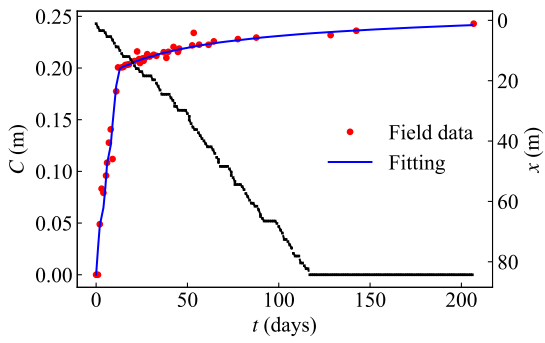


String D6

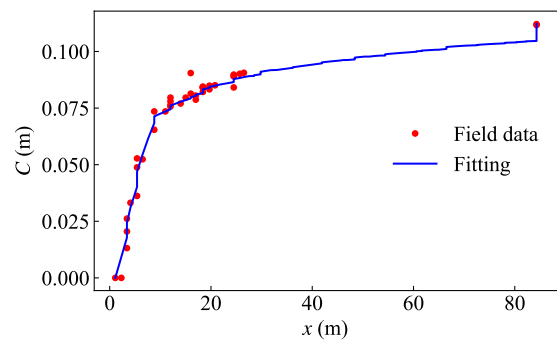
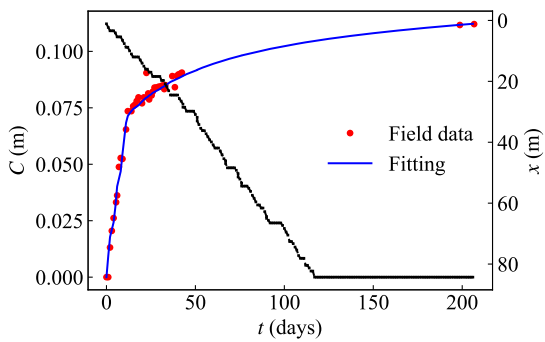
Figure B.7: Strings convergence fitting of the section at chainage 10321 m (T) in SMP4-PS (The black lines show the tunnel face advance.)



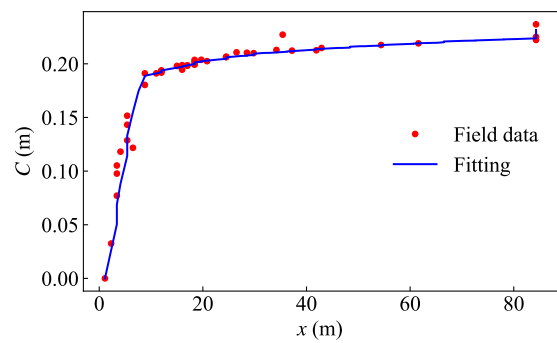
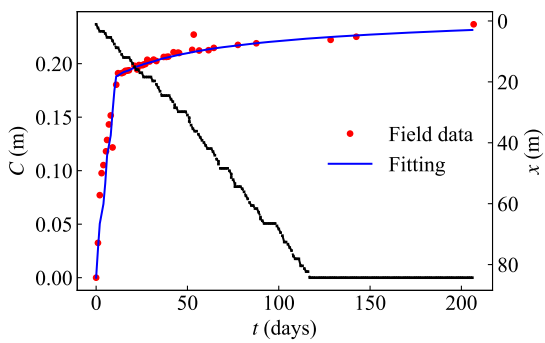
String D2



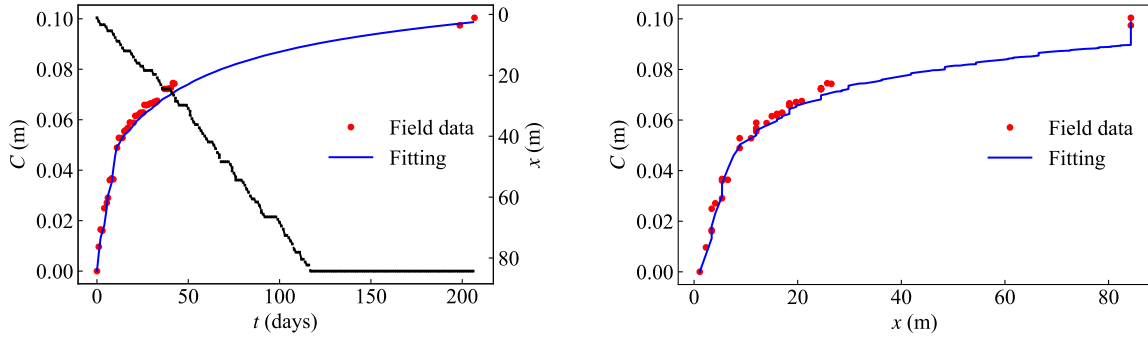
String D3



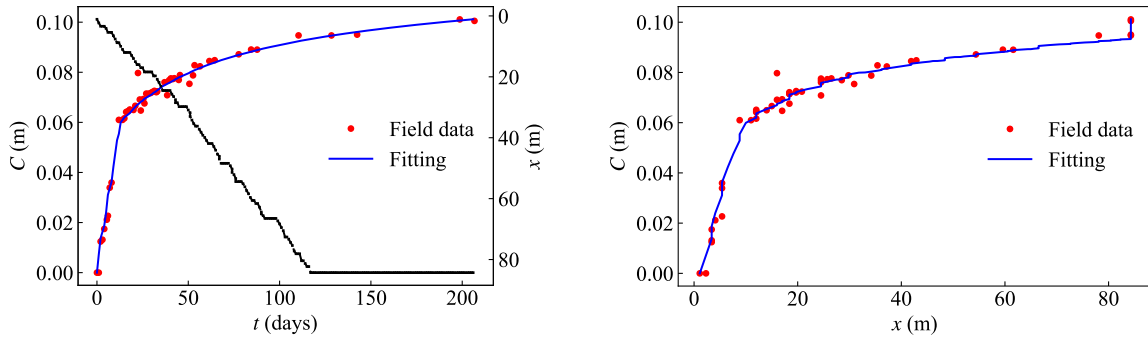
String D4



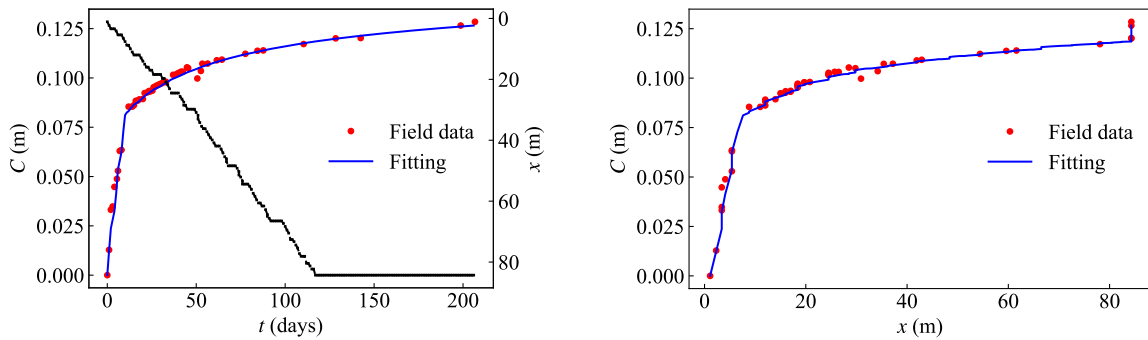
String D5



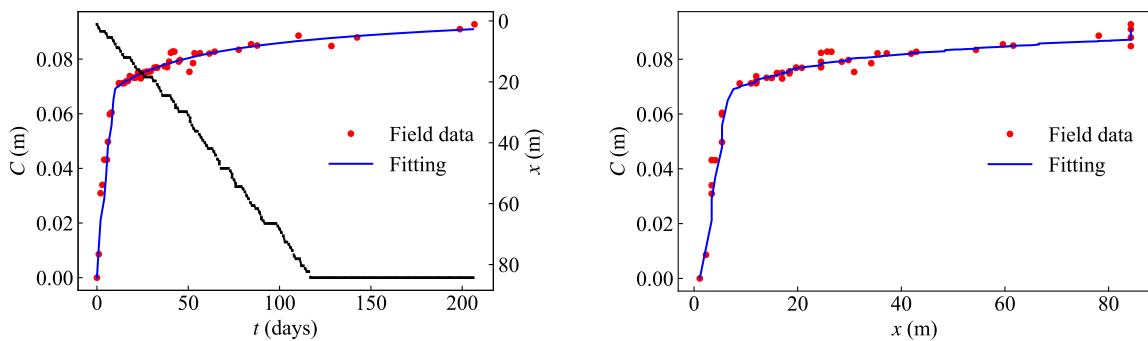
String D6



String D7

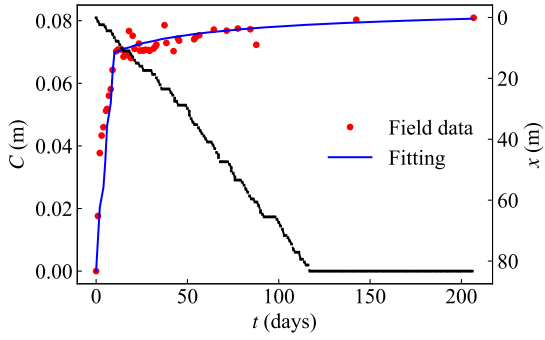


String D8

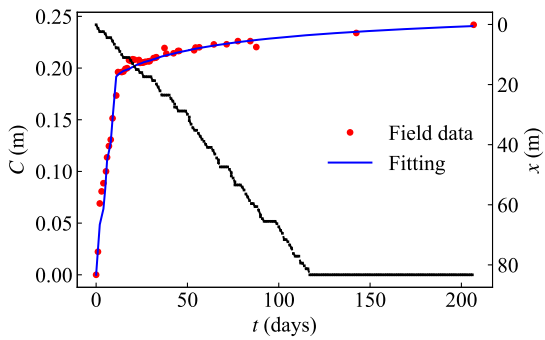


String D9

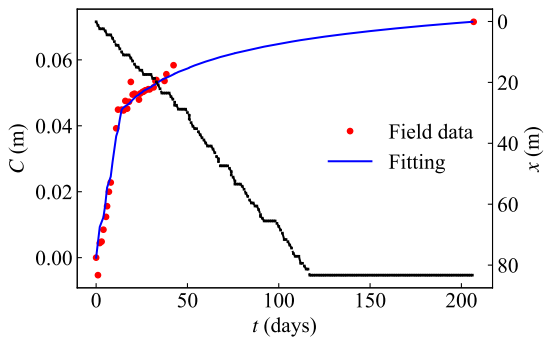
Figure B.8: Strings convergence fitting of the section at chainage 10326 m (T) in SMP4-PS (The black lines show the tunnel face advance.)



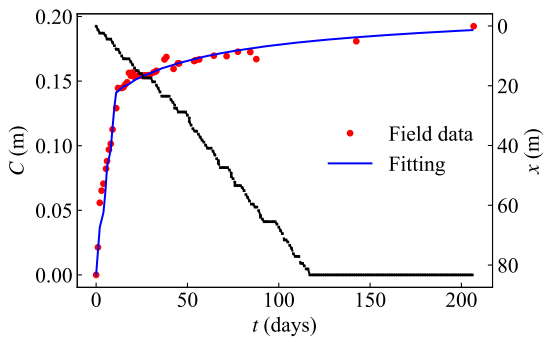
String D2



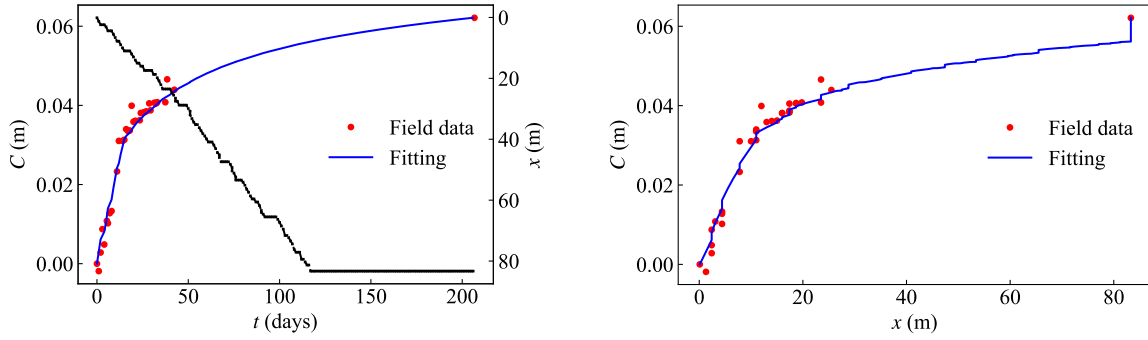
String D3



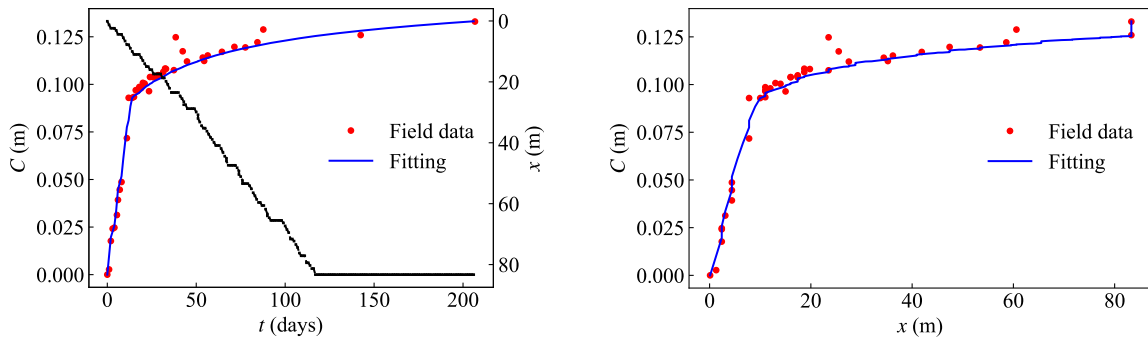
String D4



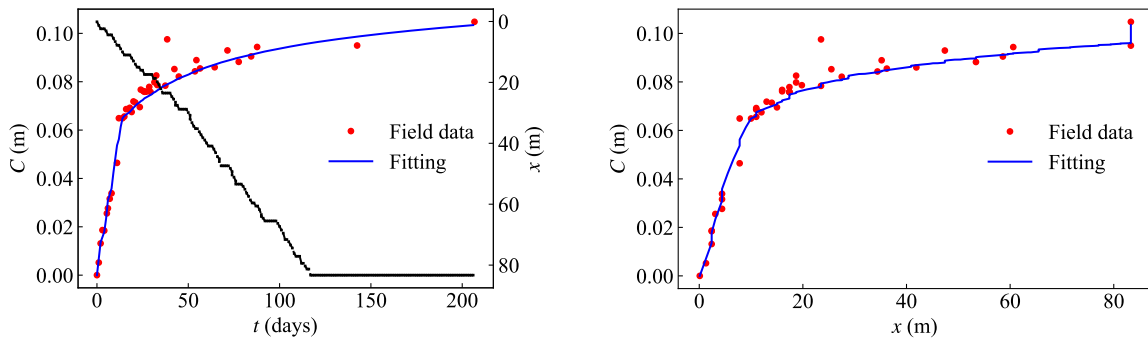
String D5



String D6

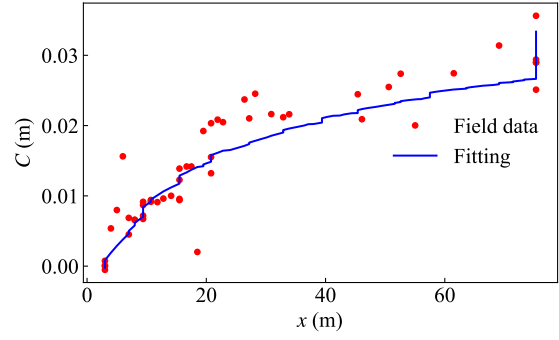
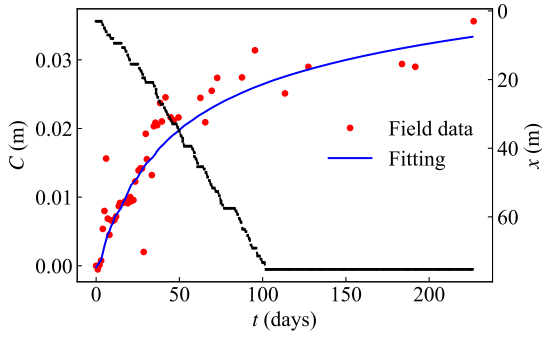


String D7

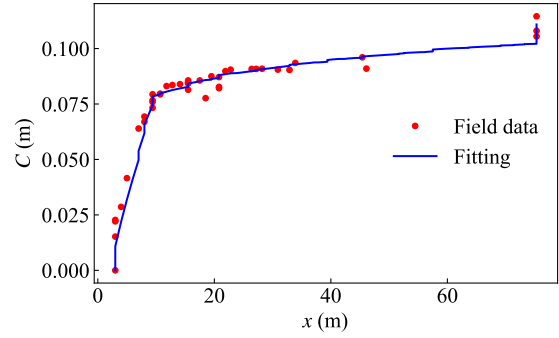
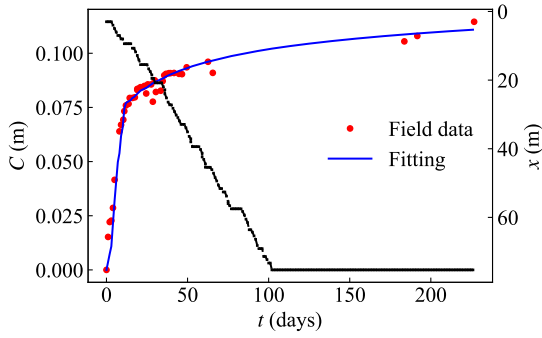


String D8

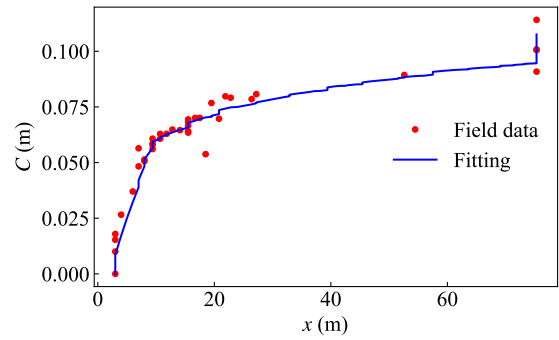
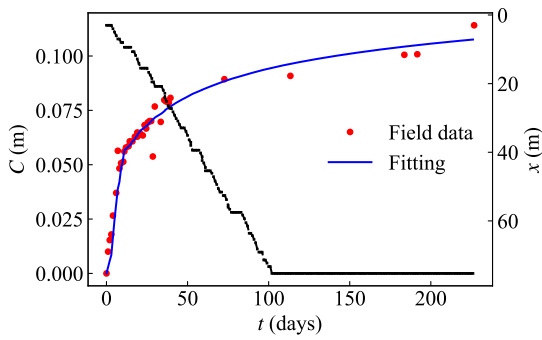
Figure B.9: Strings convergence fitting of the section at chainage 10327 m (C) in SMP4-PS (The black lines show the tunnel face advance.)



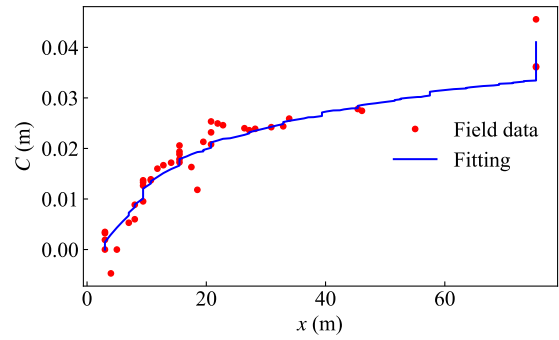
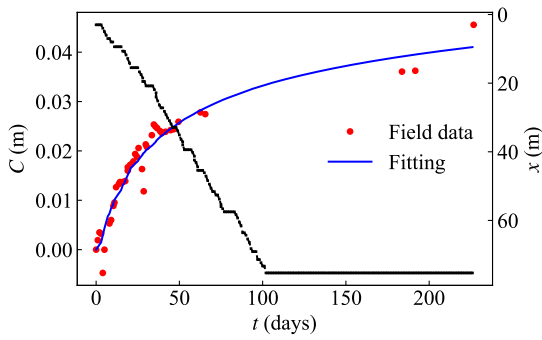
String D1



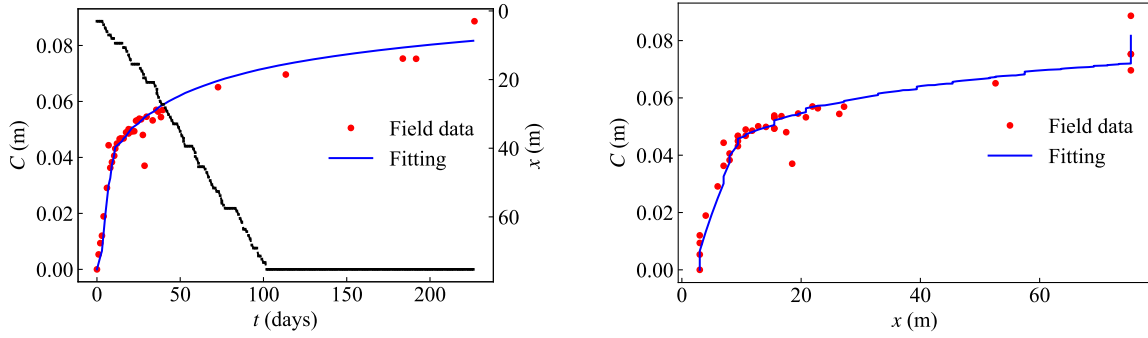
String D3



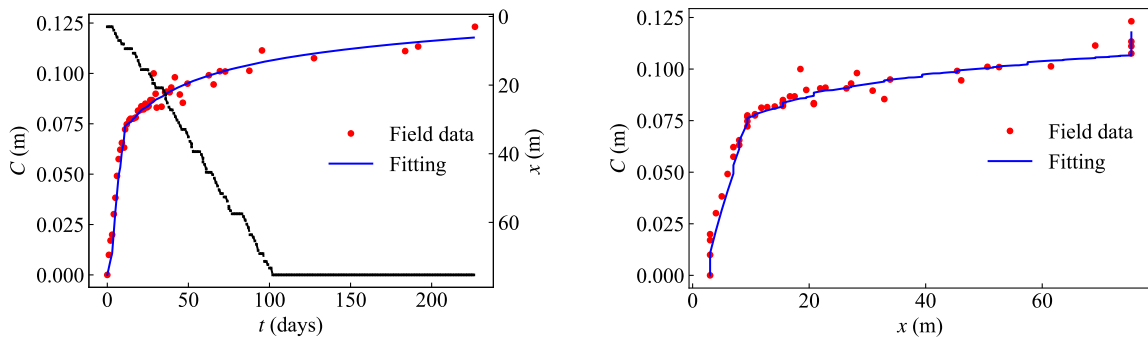
String D4



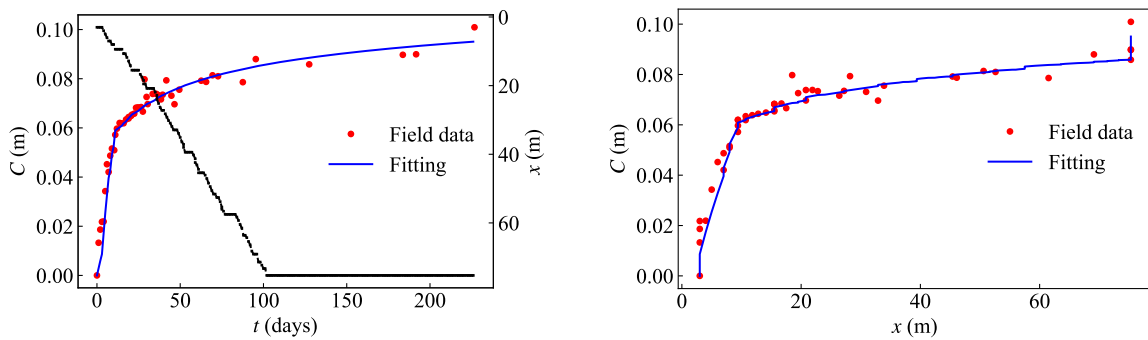
String D5



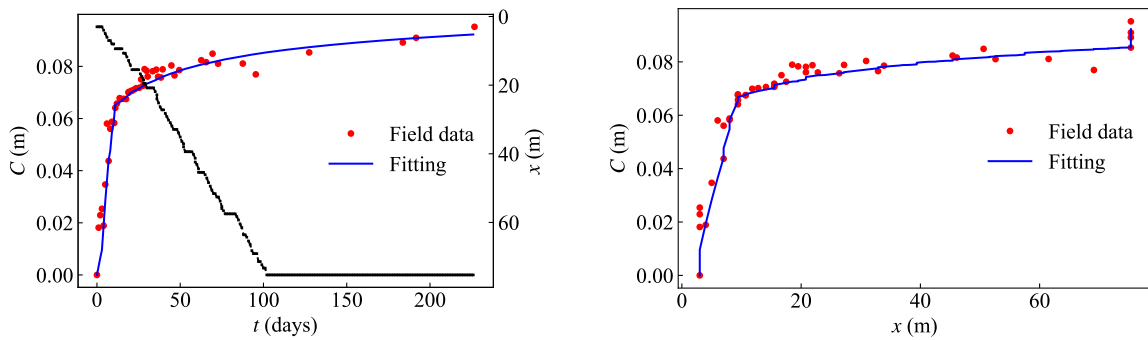
String D6



String D7

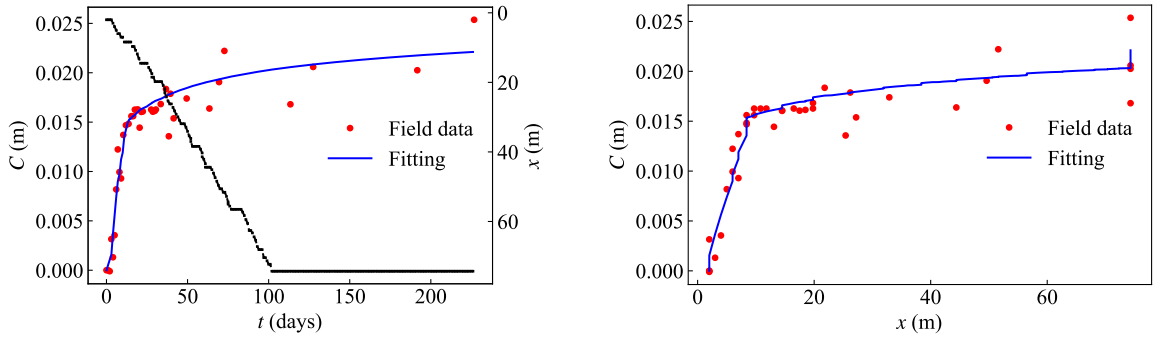


String D8

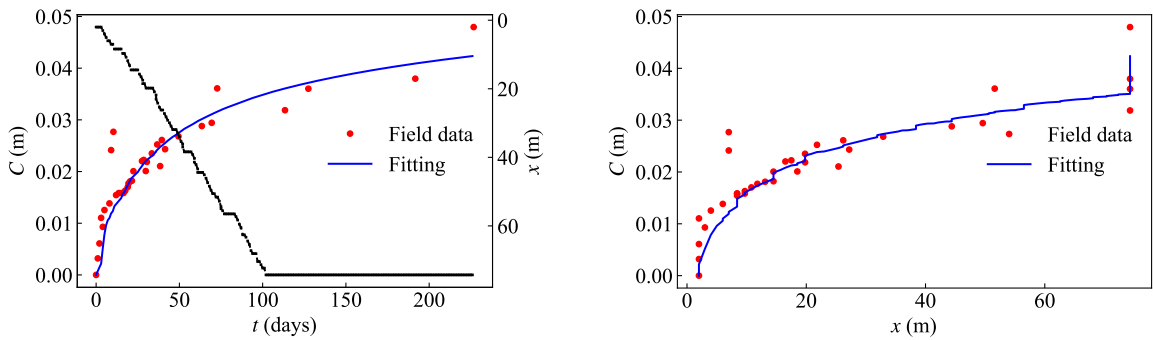


String D9

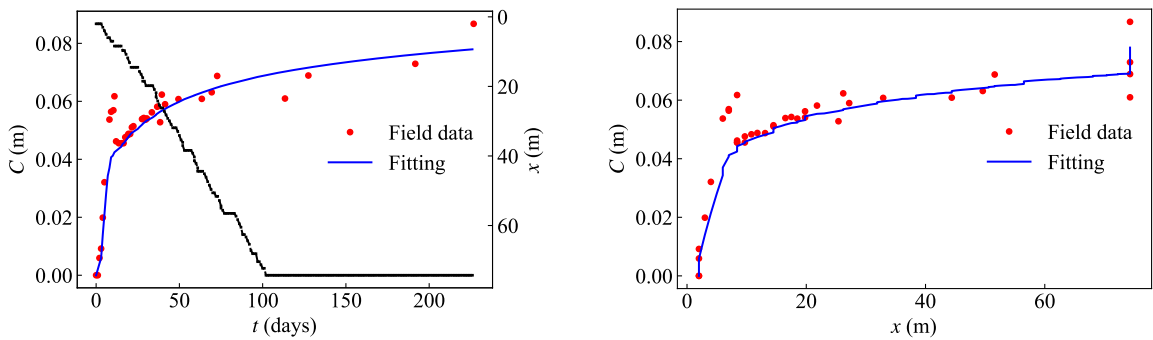
Figure B.10: Strings convergence fitting of the section at chainage 10335 m (T) in SMP4-PS (The black lines show the tunnel face advance.)



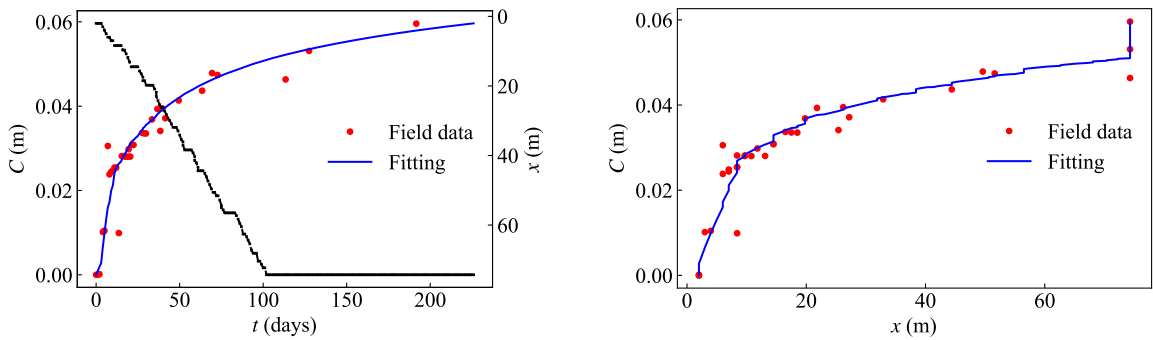
String D1



String D2

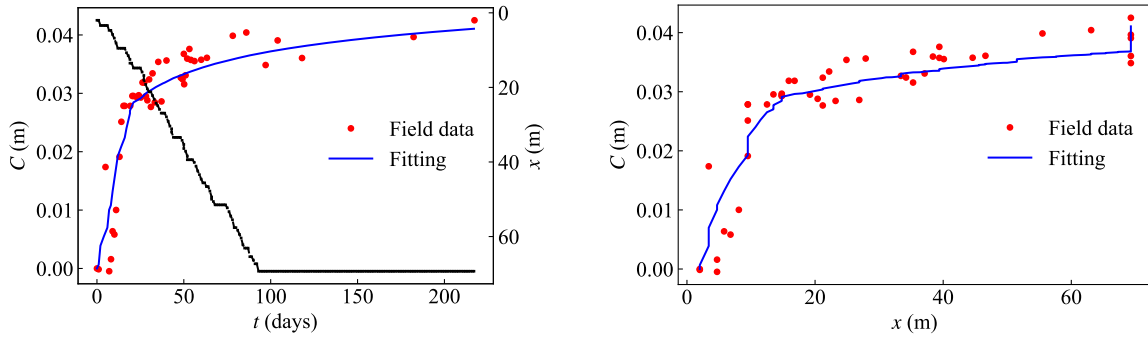


String D3

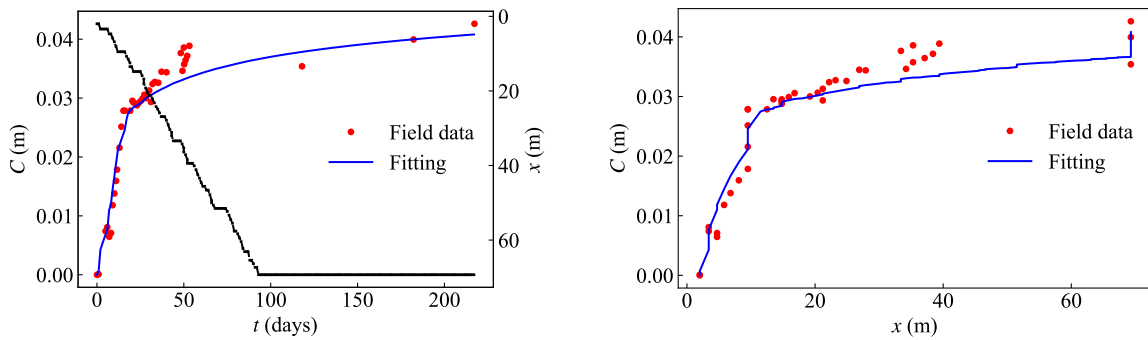


String D7

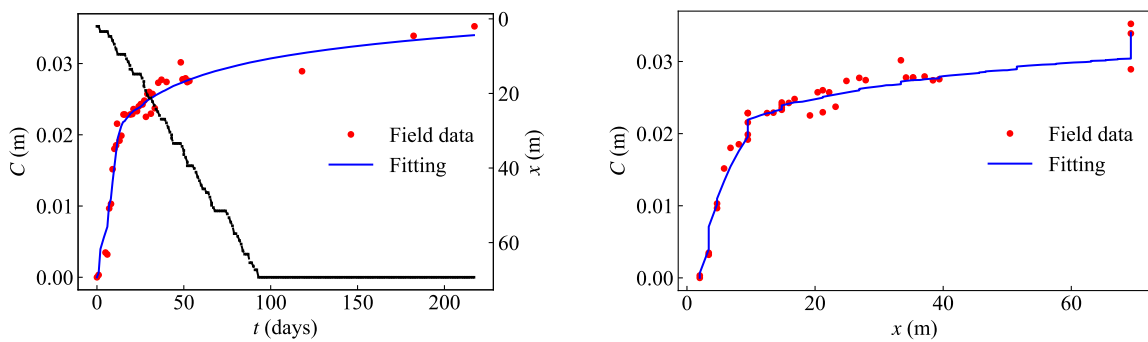
Figure B.11: Strings convergence fitting of the section at chainage 10336 m (C) in SMP4-PS (The black lines show the tunnel face advance.)



String D4

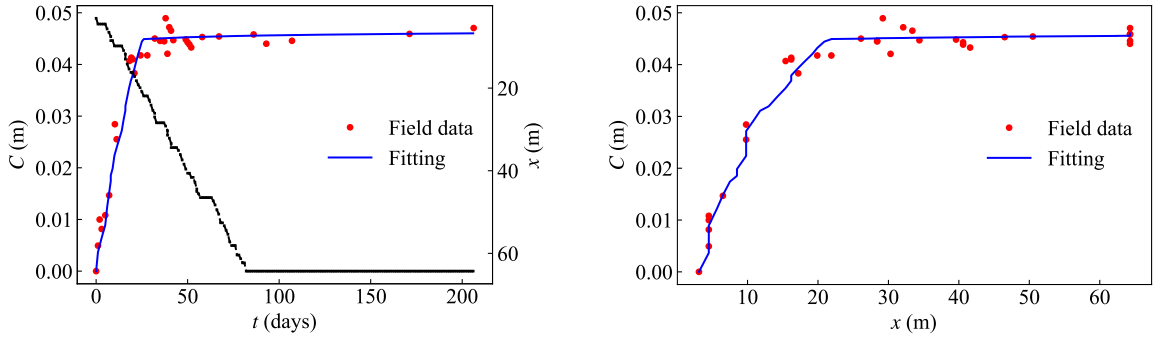


String D7

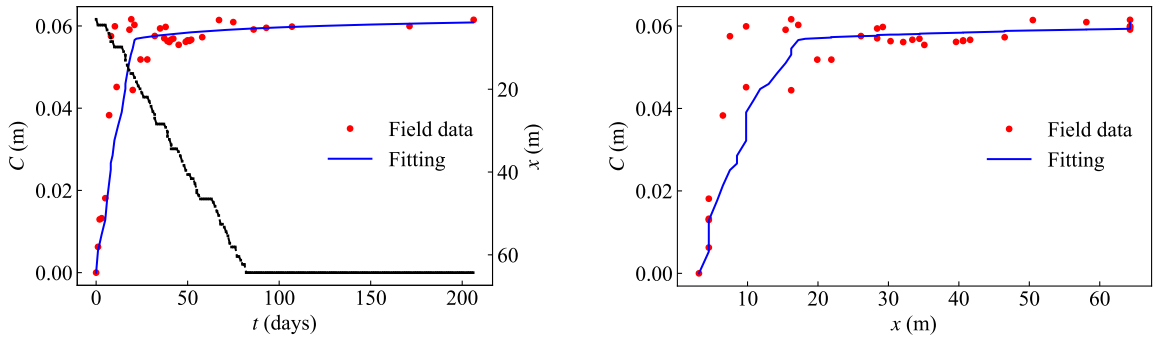


String D8

Figure B.12: Strings convergence fitting of the section at chainage 10341 m (T) in SMP4-PS (The black lines show the tunnel face advance.)

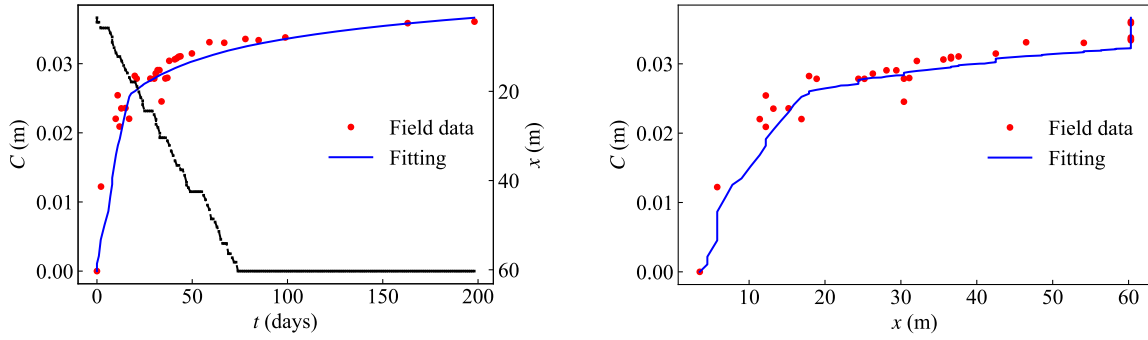


String D2

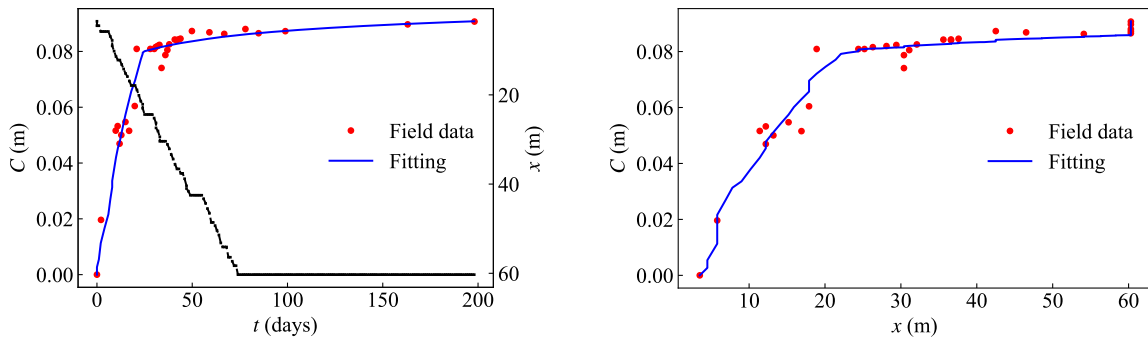


String D3

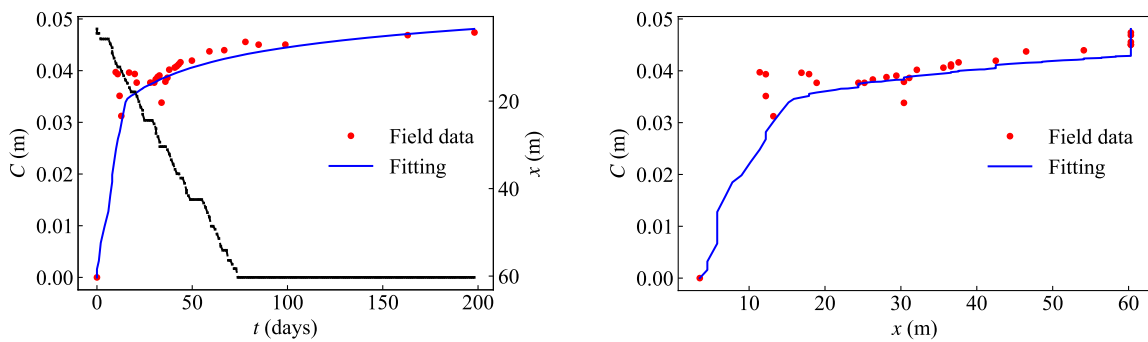
Figure B.13: Strings convergence fitting of the section at chainage 10346 m (T) in SMP4-PS (The black lines show the tunnel face advance.)



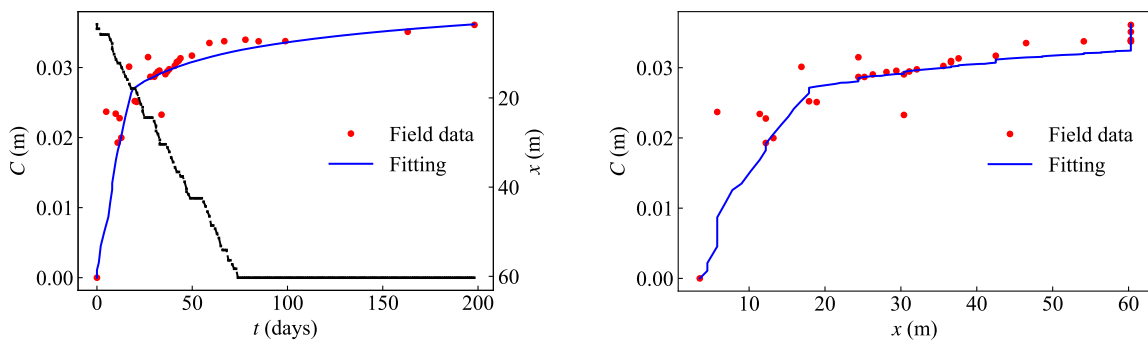
String D2



String D3

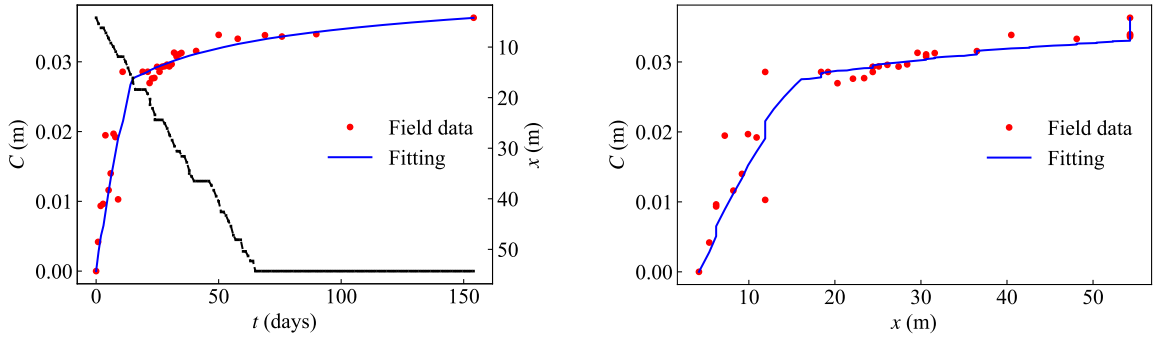


String D5

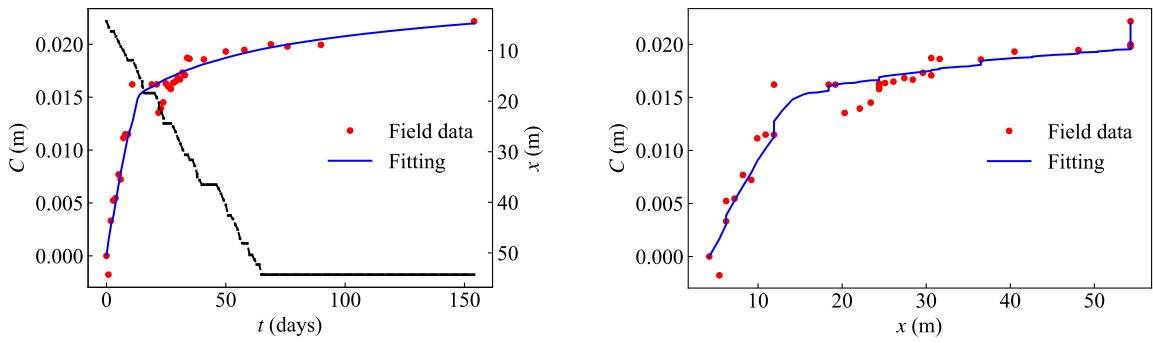


String D6

Figure B.14: Strings convergence fitting of the section at chainage 10350 m (T) in SMP4-PS (The black lines show the tunnel face advance.)

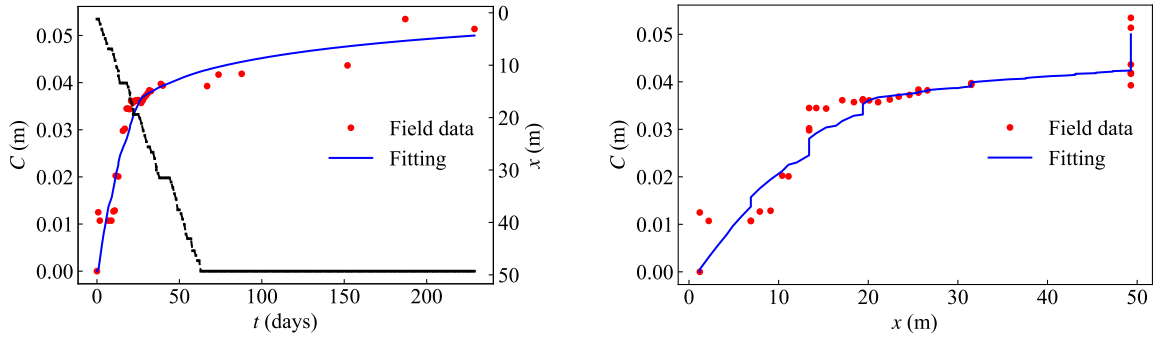


String D5

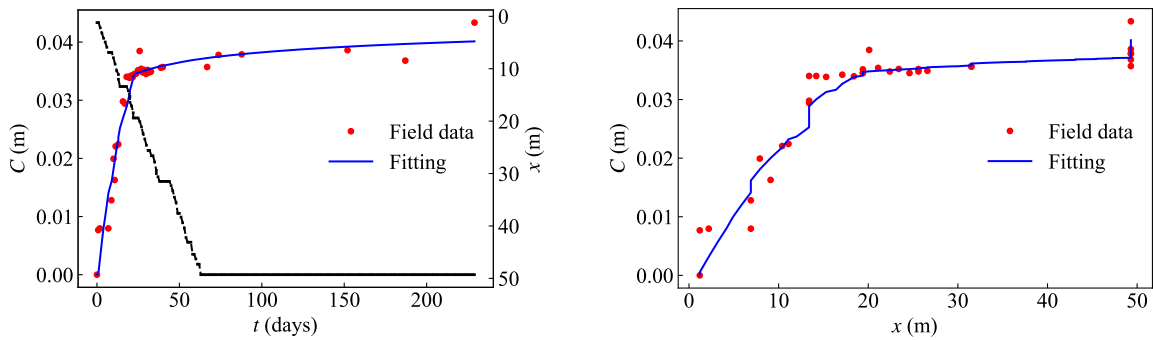


String D6

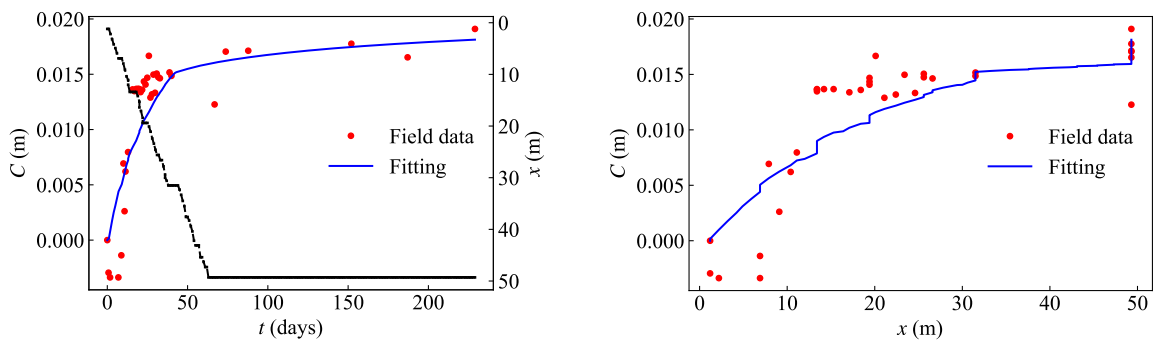
Figure B.15: Strings convergence fitting of the section at chainage 10356 m (T) in SMP4-PS (The black lines show the tunnel face advance.)



String D3

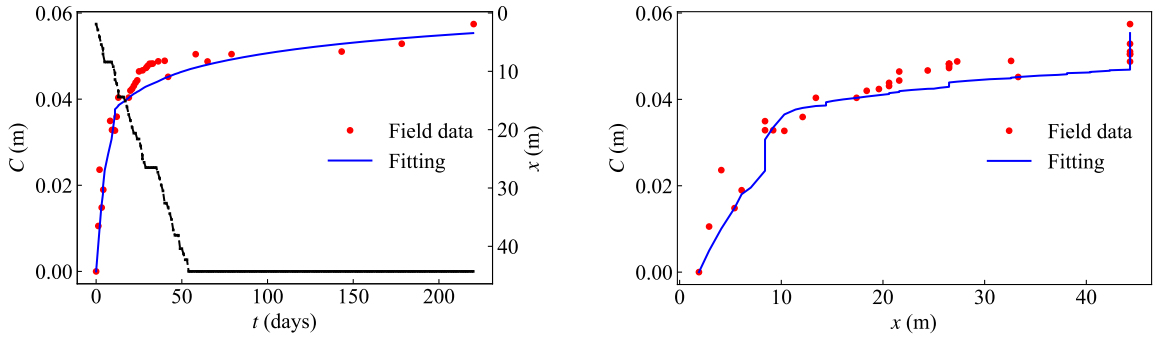


String D4

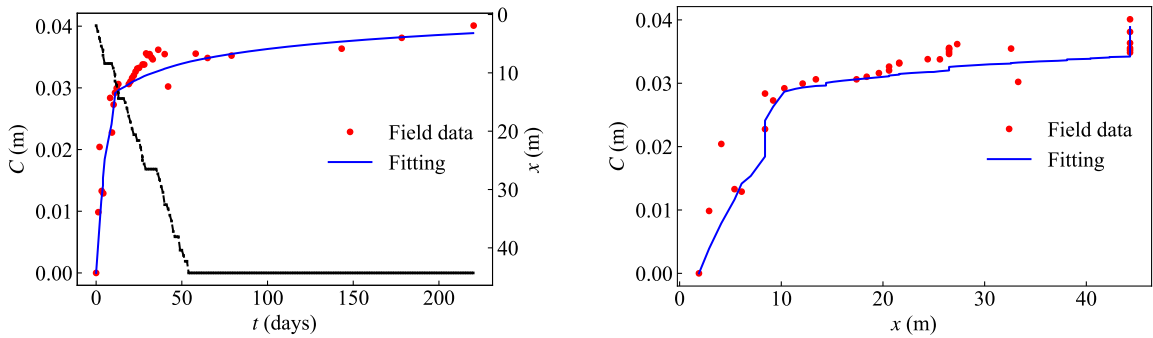


String D6

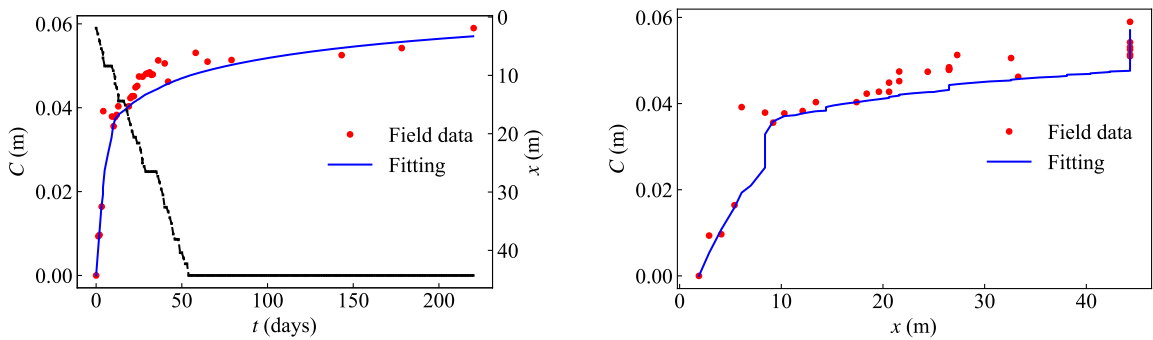
Figure B.16: Strings convergence fitting of the section at chainage 10361 m (T) in SMP4-PS (The black lines show the tunnel face advance.)



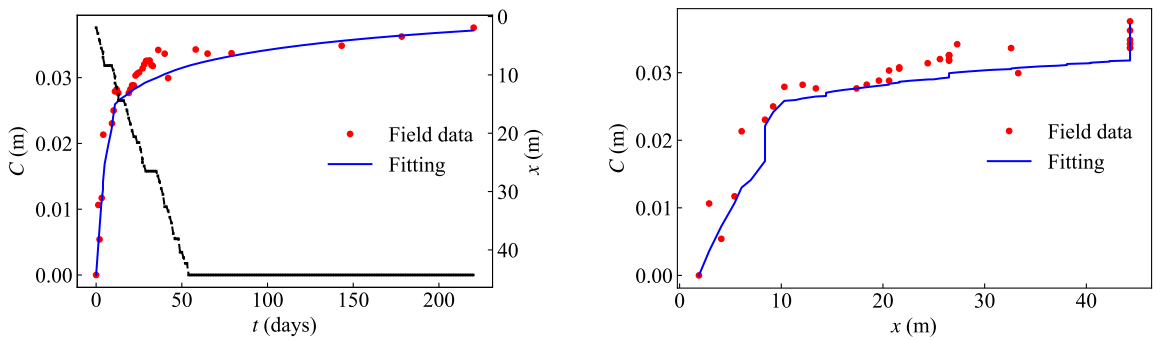
String D3



String D4

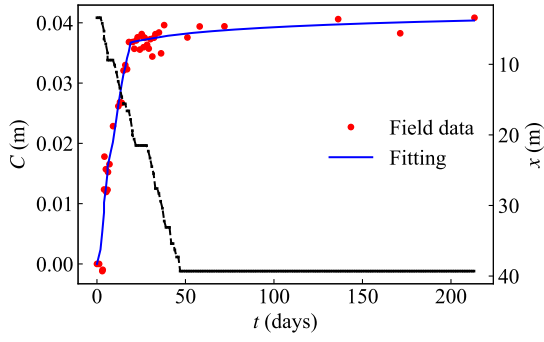


String D5

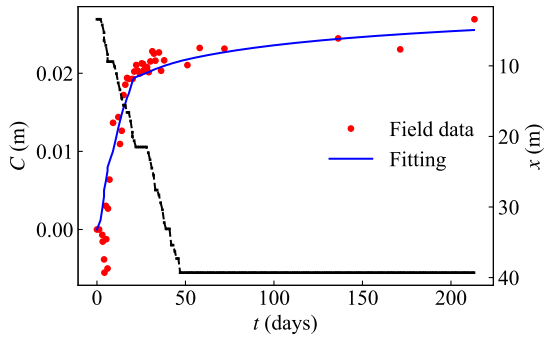


String D6

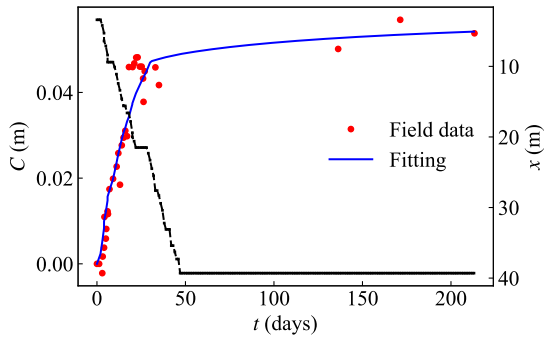
Figure B.17: Strings convergence fitting of the section at chainage 10366 m (T) in SMP4-PS (The black lines show the tunnel face advance.)



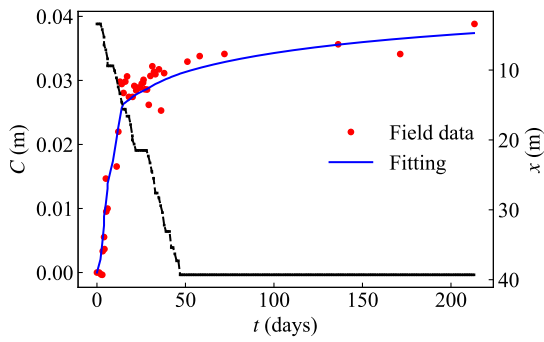
String D1



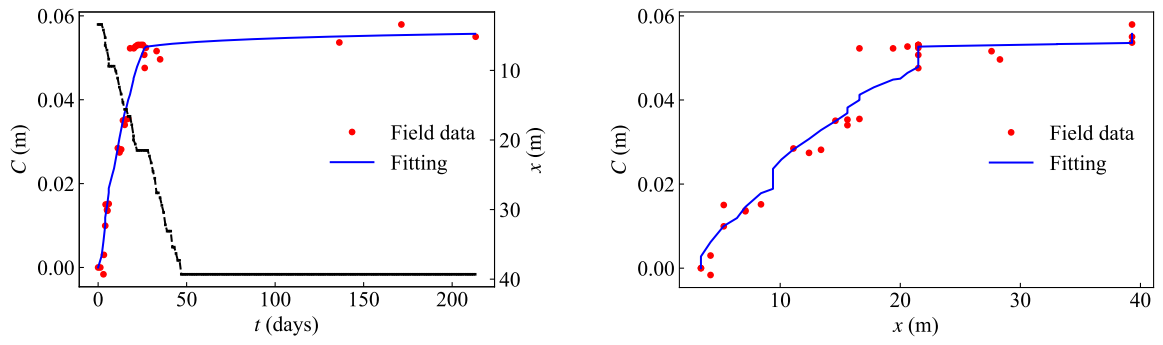
String D2



String D4

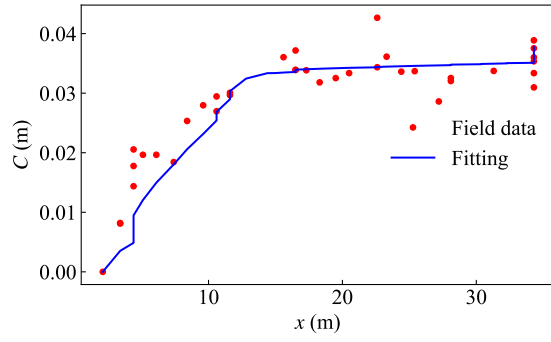
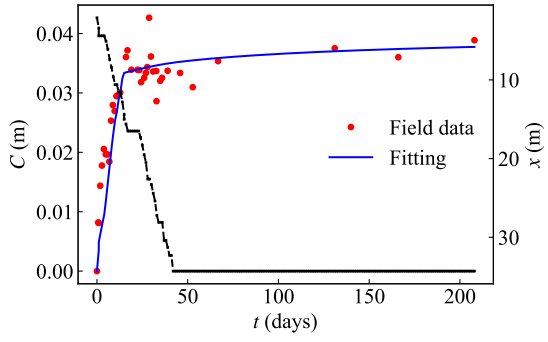


String D5

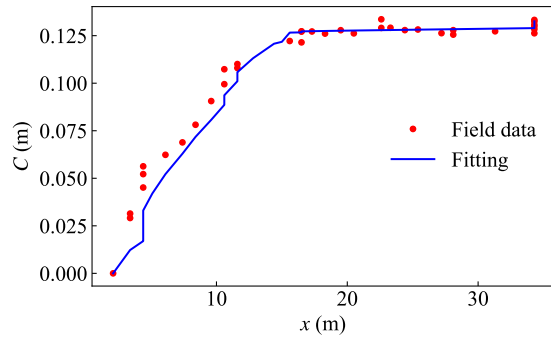
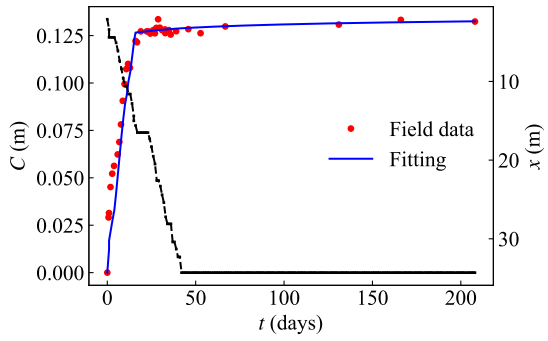


String D6

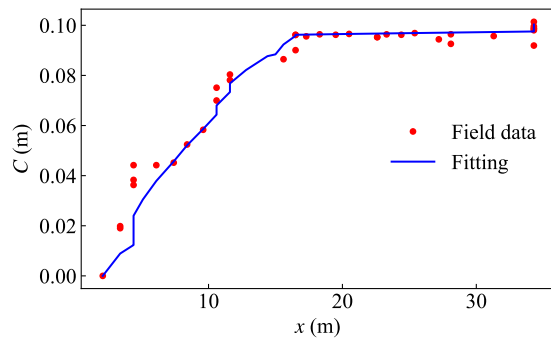
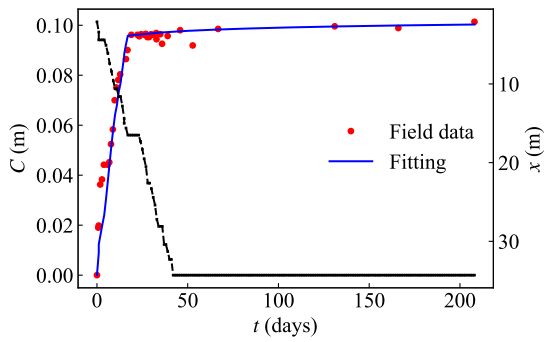
Figure B.18: Strings convergence fitting of the section at chainage 10371 m (B) in SMP4-PS (The black lines show the tunnel face advance.)



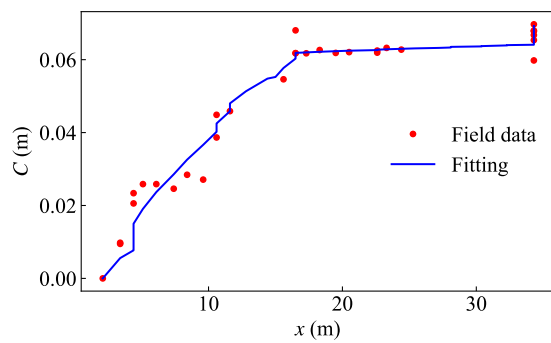
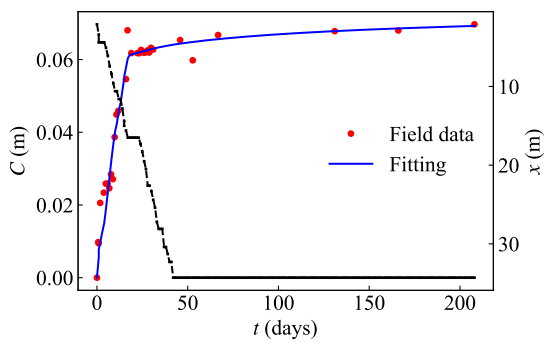
String D1



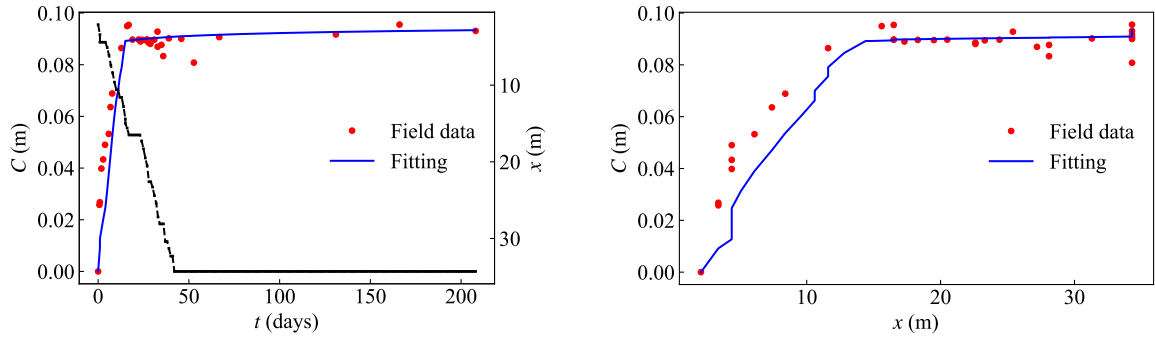
String D2



String D3

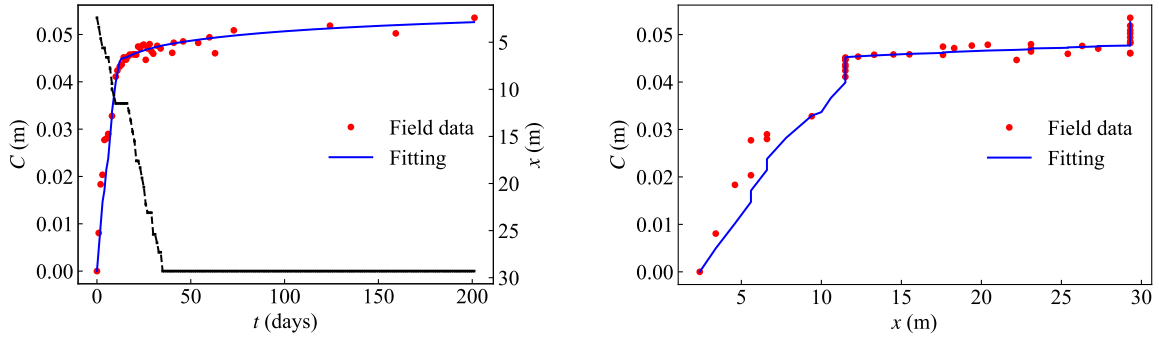


String D4

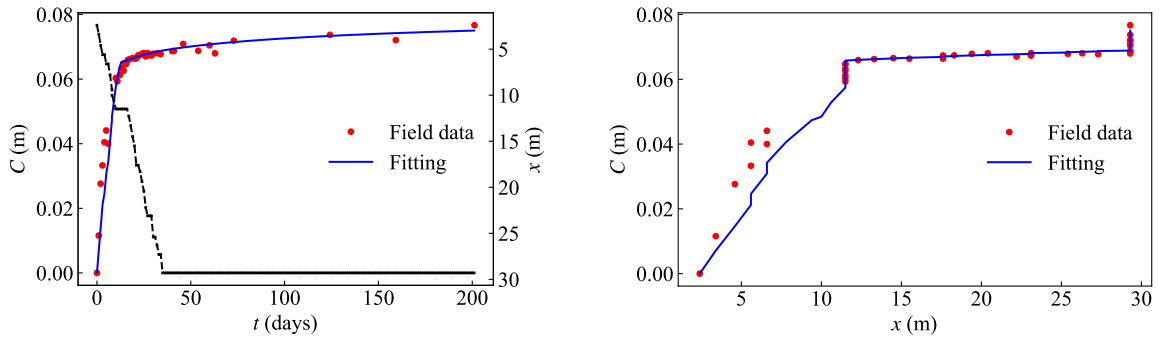


String D5

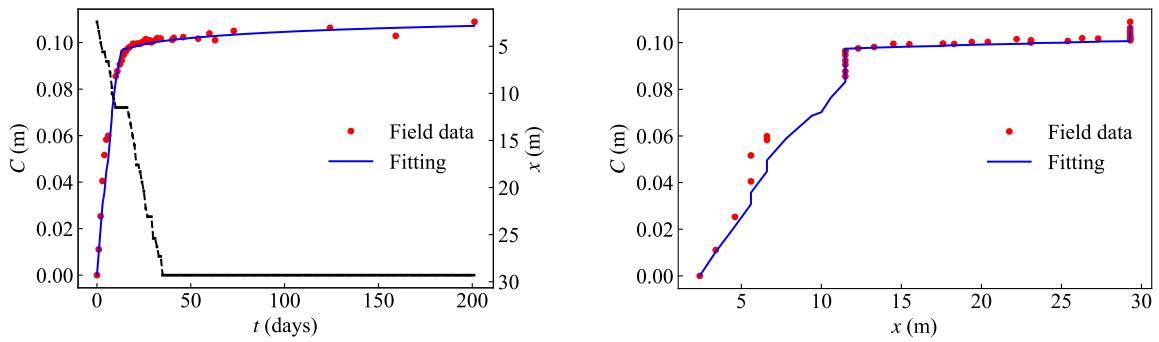
Figure B.19: Strings convergence fitting of the section at chainage 10376 m (B) in SMP4-PS (The black lines show the tunnel face advance.)



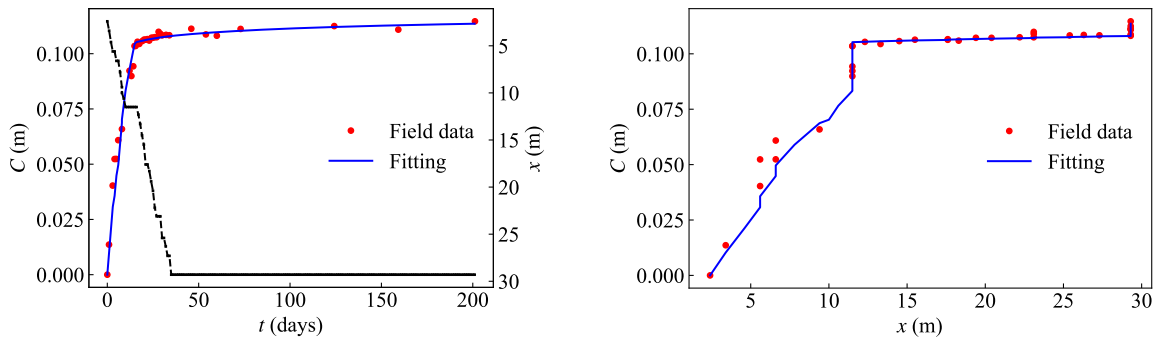
String D1



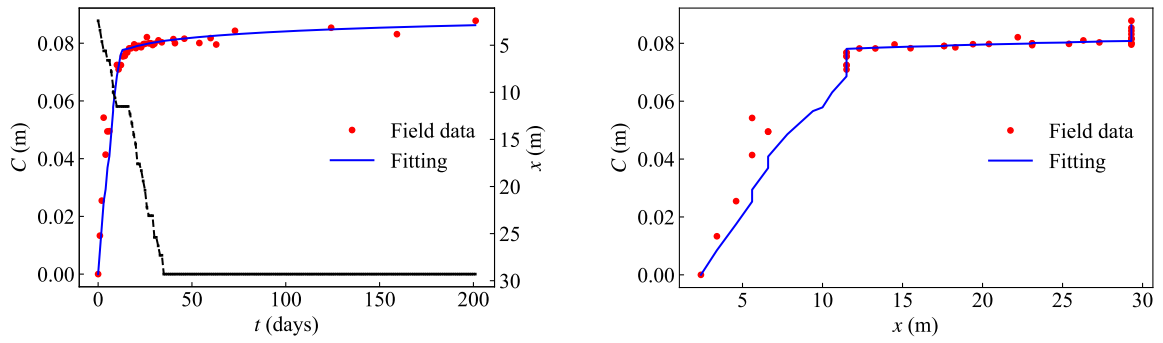
String D2



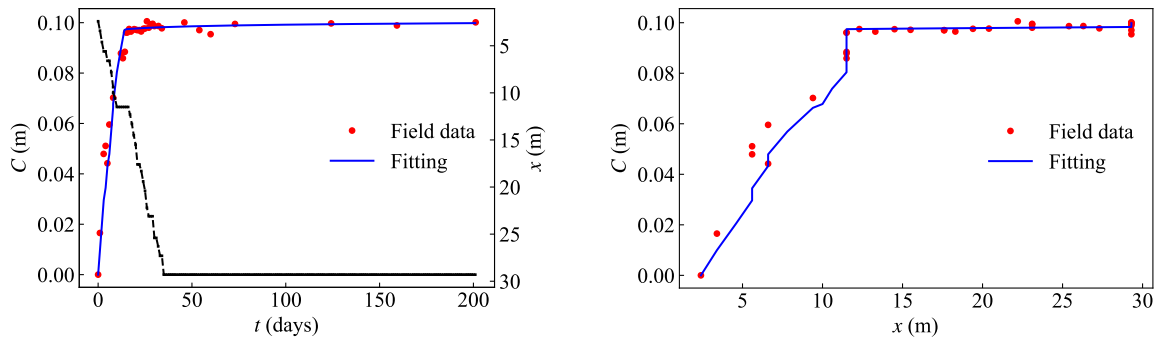
String D3



String D4

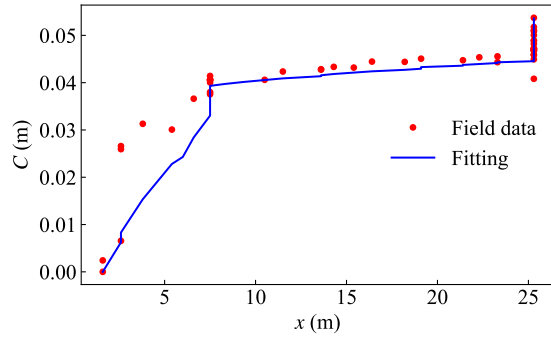
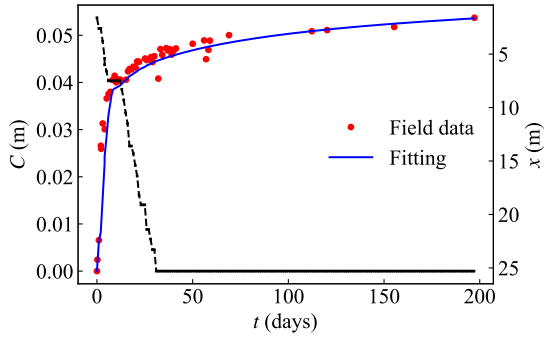


String D5

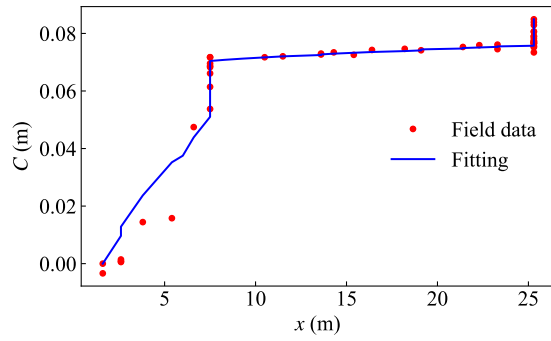
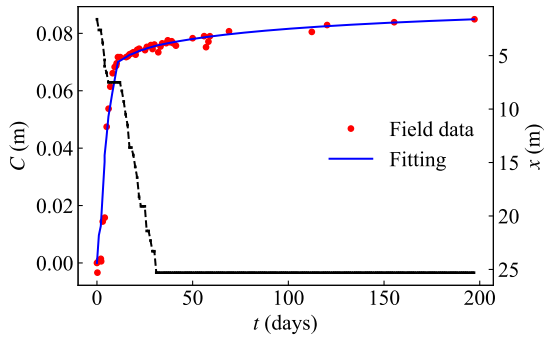


String D6

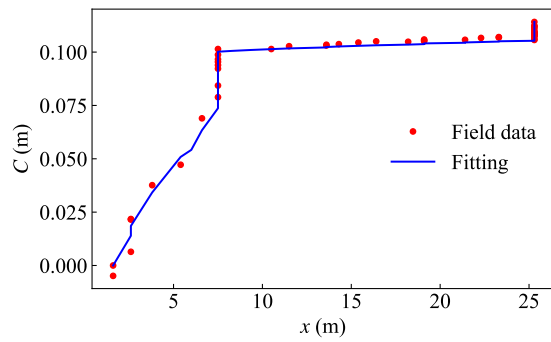
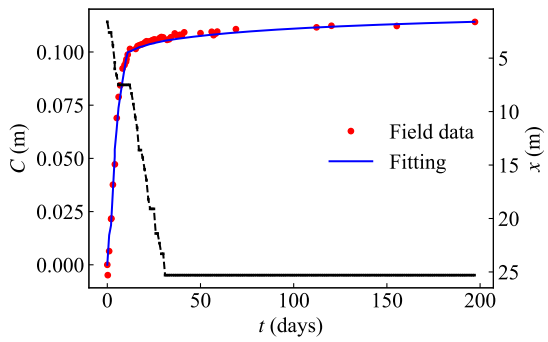
Figure B.20: Strings convergence fitting of the section at chainage 10381 m (B) in SMP4-PS (The black lines show the tunnel face advance.)



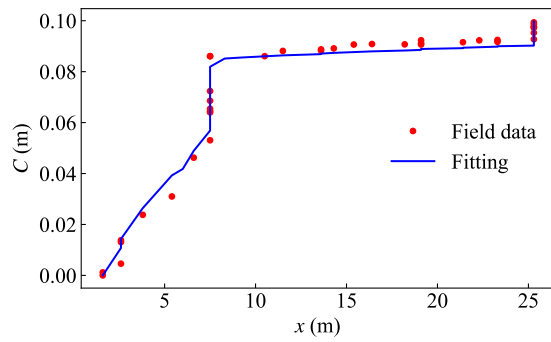
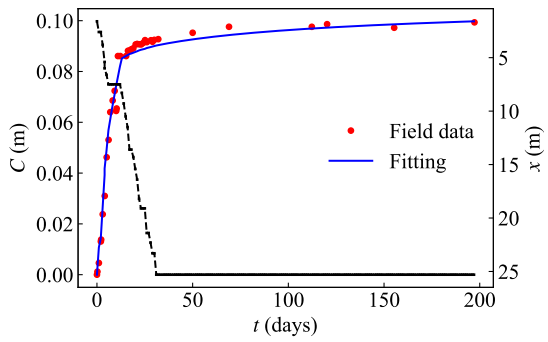
String D1



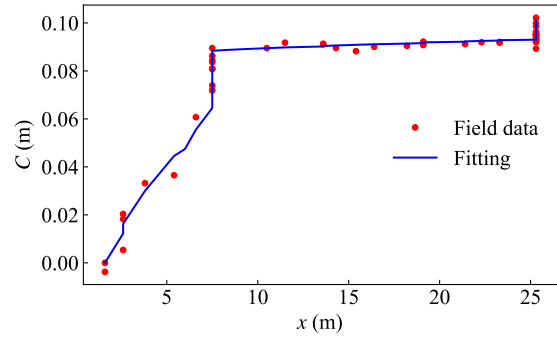
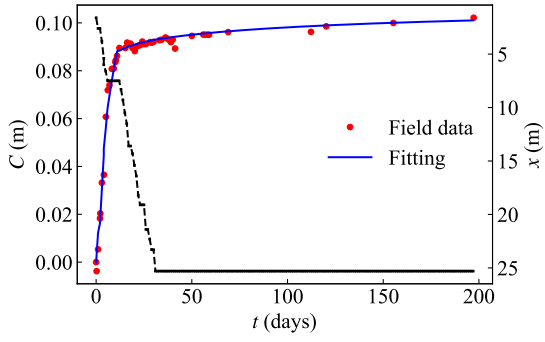
String D2



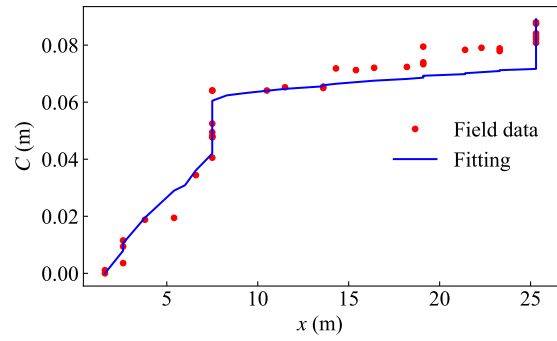
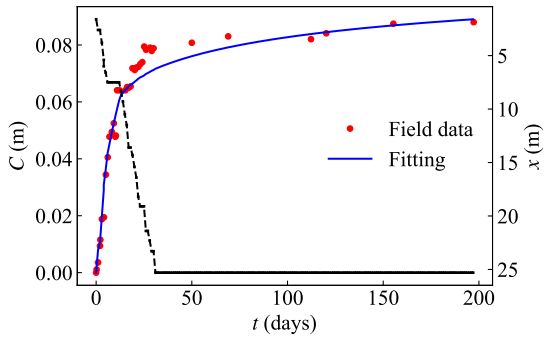
String D3



String D4

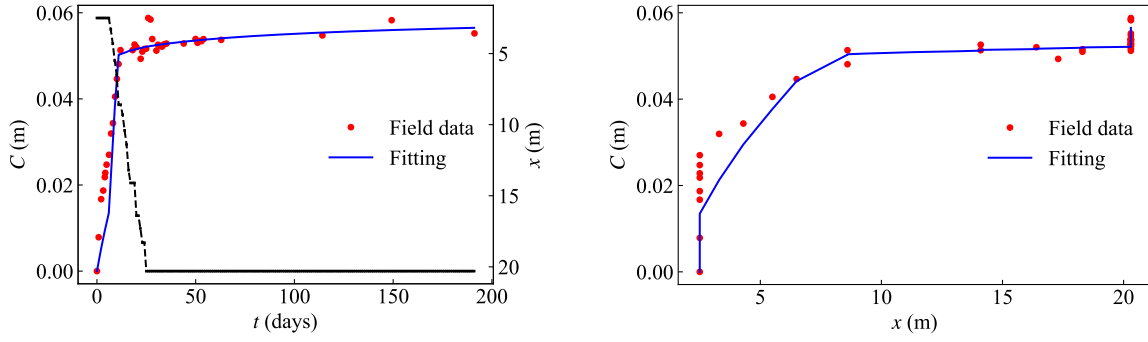


String D5

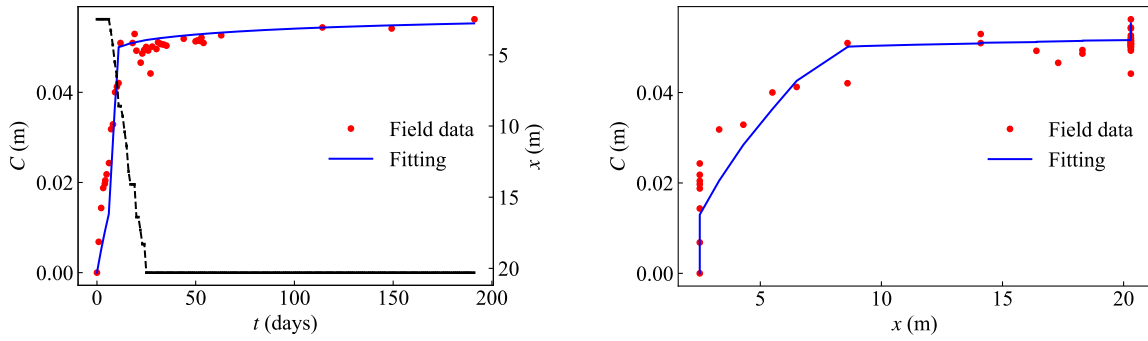


String D6

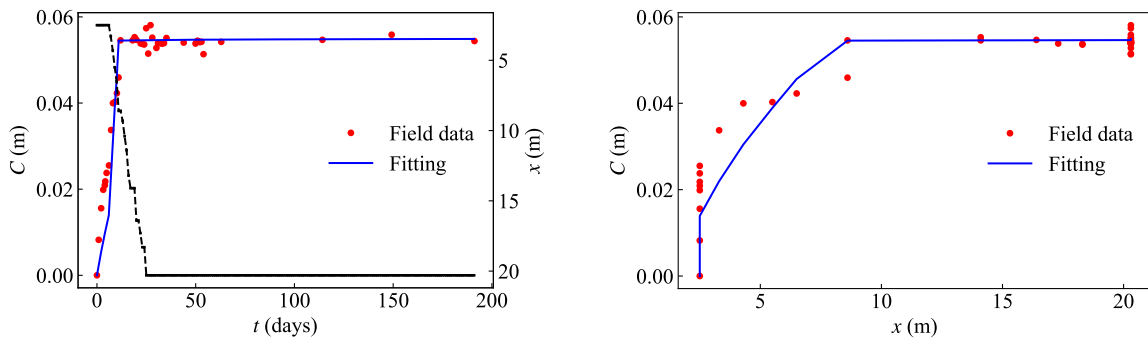
Figure B.21: Strings convergence fitting of the section at chainage 10385 m (B) in SMP4-PS (The black lines show the tunnel face advance.)



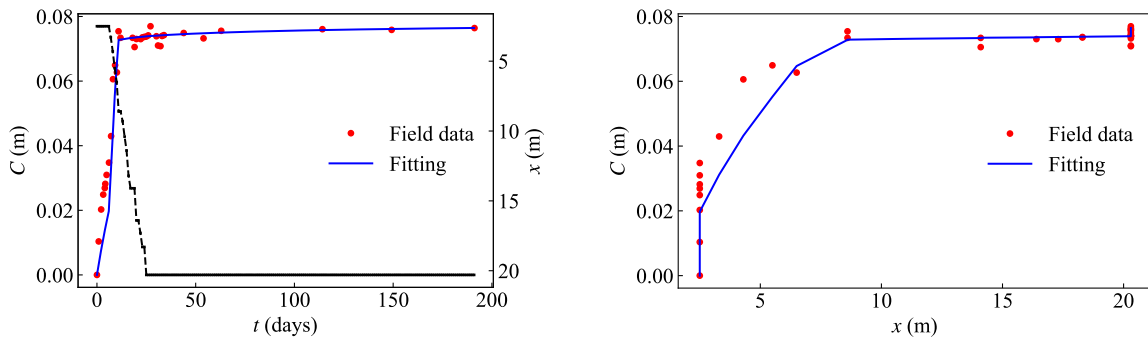
String D1



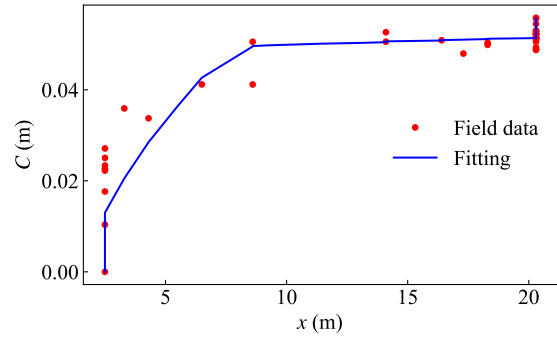
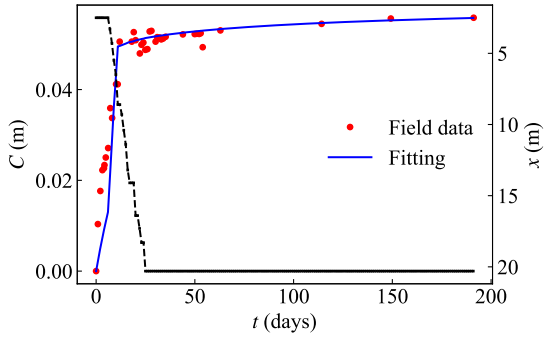
String D2



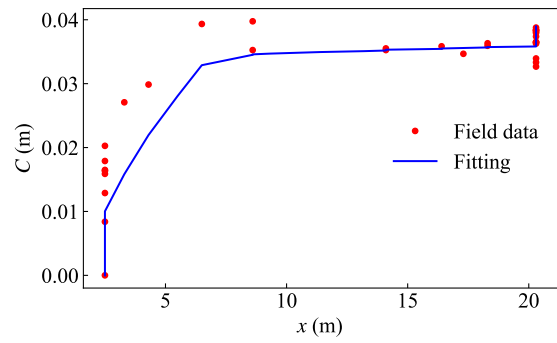
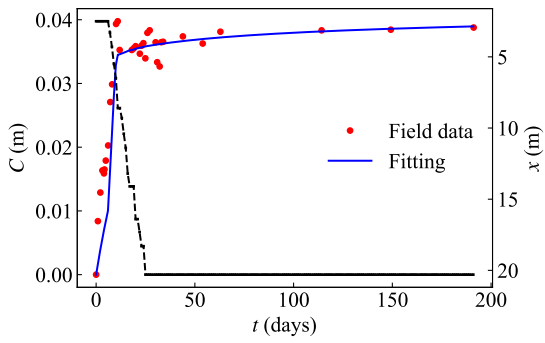
String D3



String D4



String D5



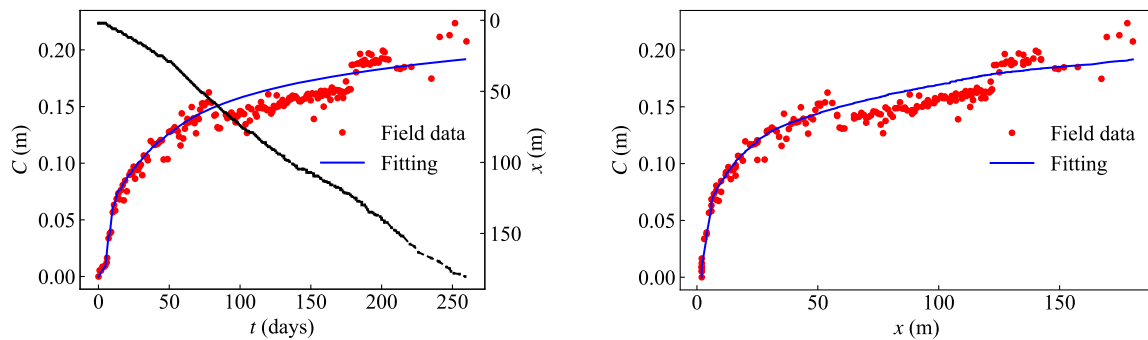
String D6

Figure B.22: Strings convergence fitting of the section at chainage 10390 m (B) in SMP4-PS (The black lines show the tunnel face advance.)

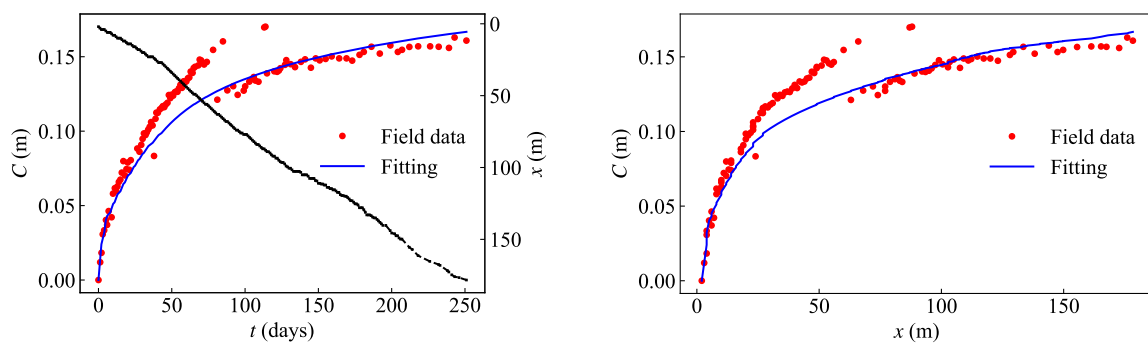
APPENDIX C

AVERAGE CONVERGENCE OF THE SECTIONS IN SMP4-RPS

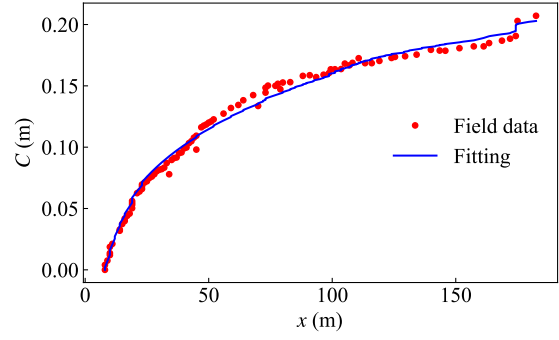
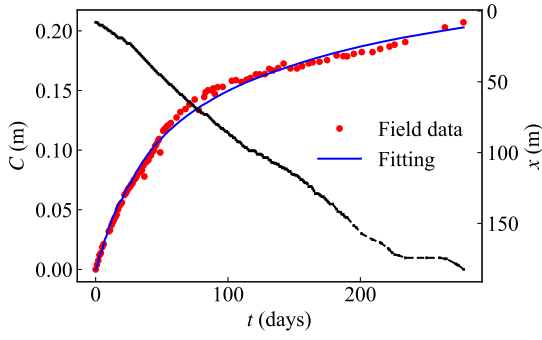
The detailed fitting results of the average convergence of the sections in SMP4-RPS are summarized in this appendix. The proposed parameters values of the convergence law for every section are shown in Table 3.10. The black lines in the figures represent the tunnel face advance.



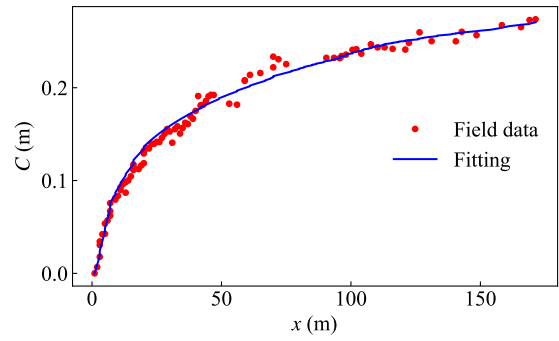
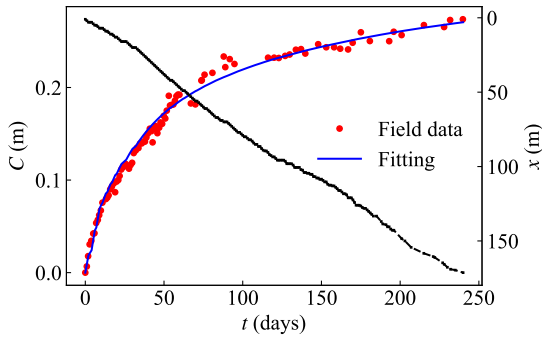
Chainage 10305 m (B)



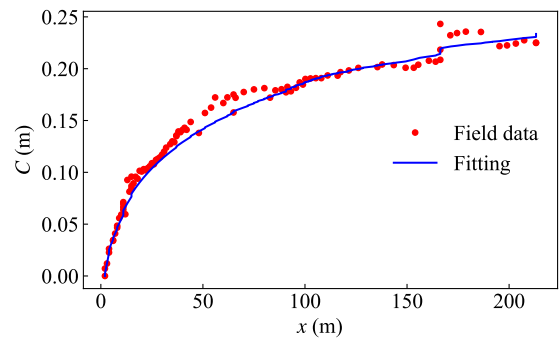
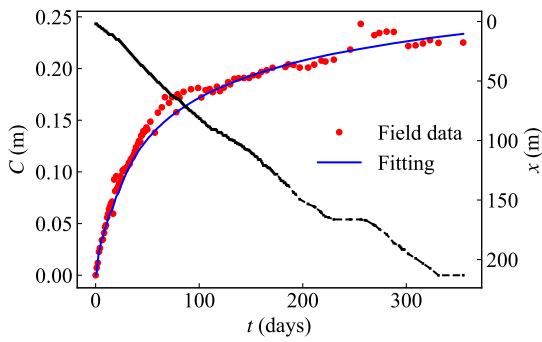
Chainage 10307 m (B)



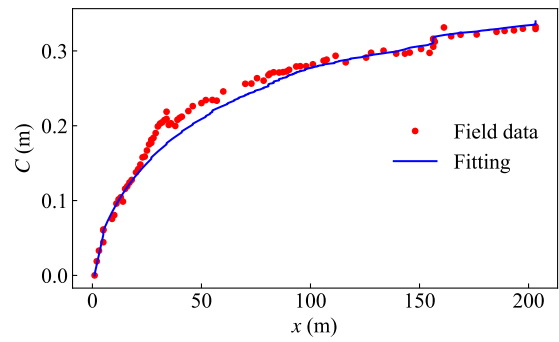
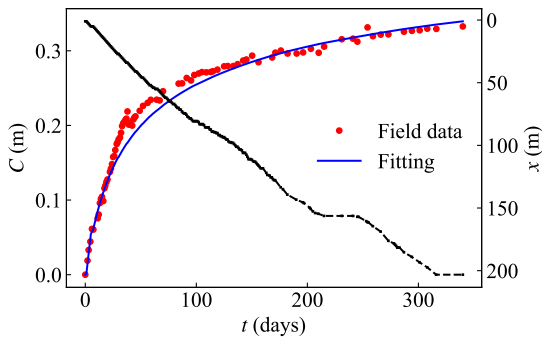
Chainage 10311 m (B)



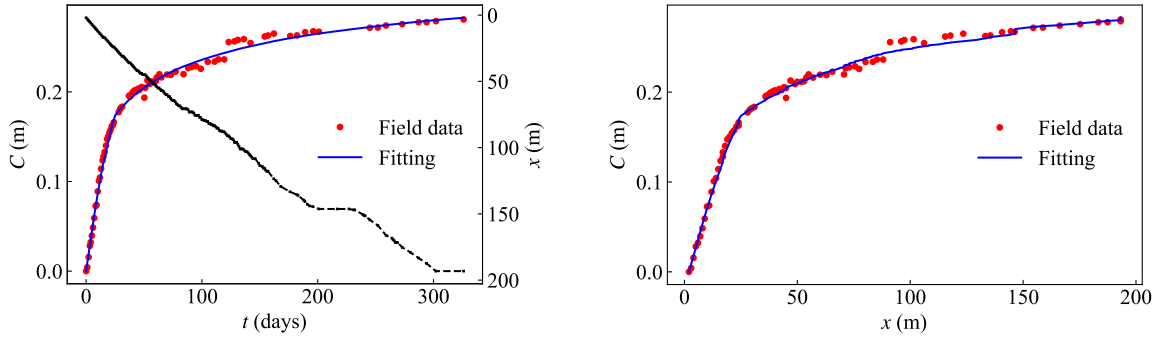
Chainage 10314 m (B)



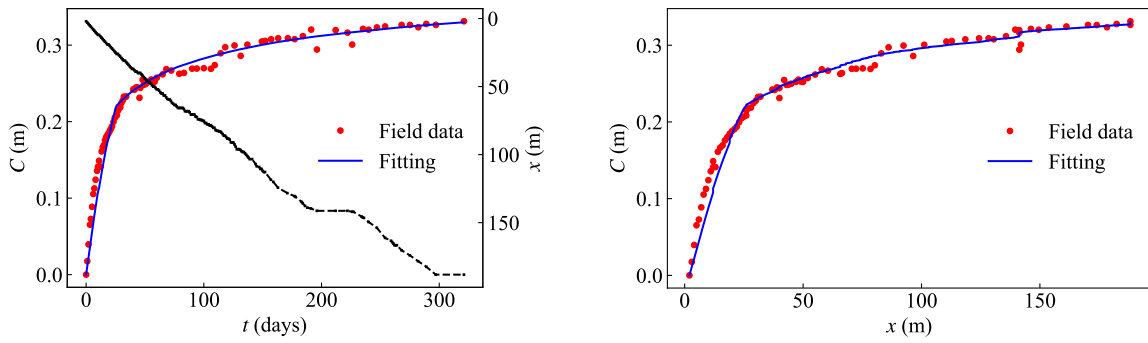
Chainage 10319 m (B)



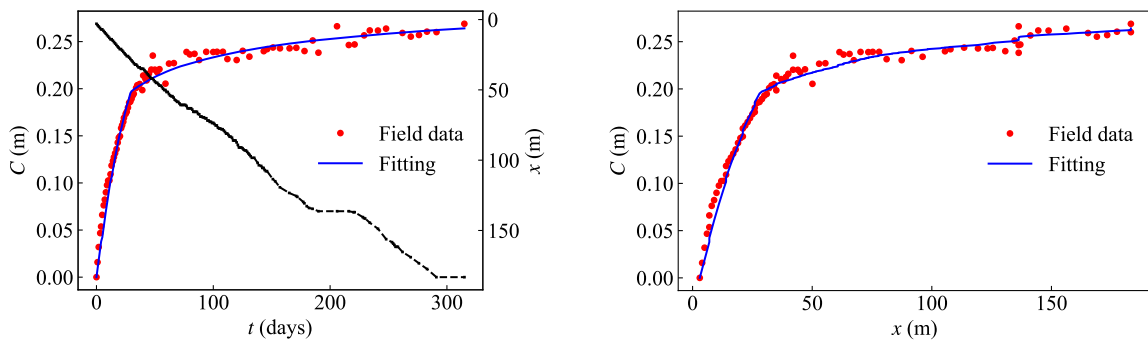
Chainage 10329 m (B)



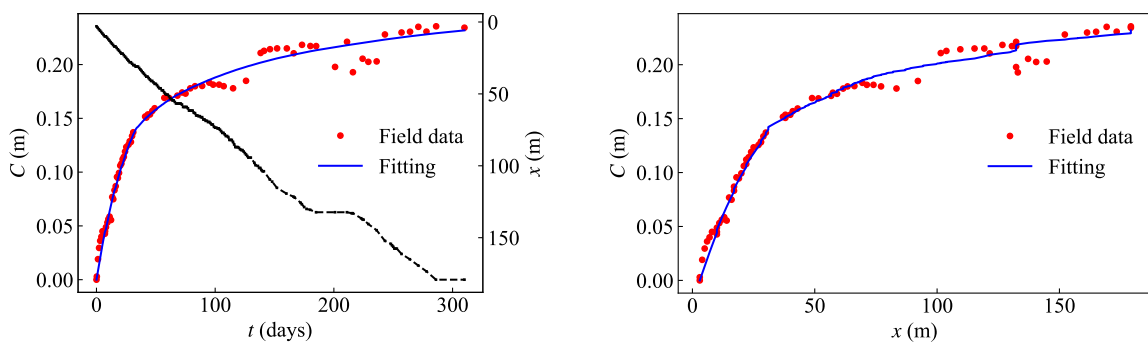
Chainage 10339 m (B)



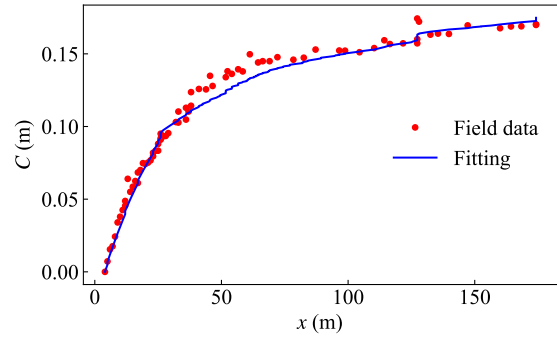
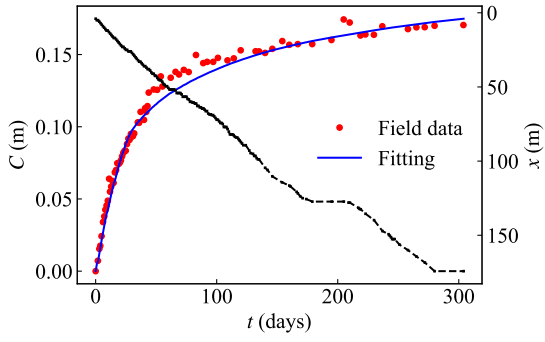
Chainage 10344 m (B)



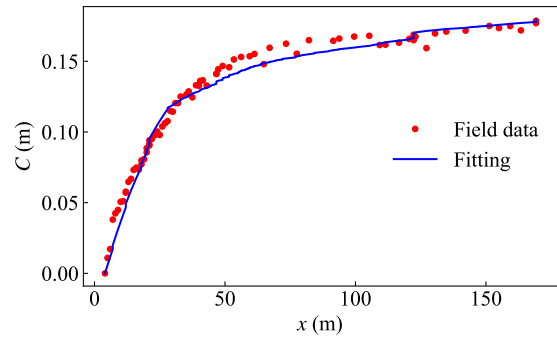
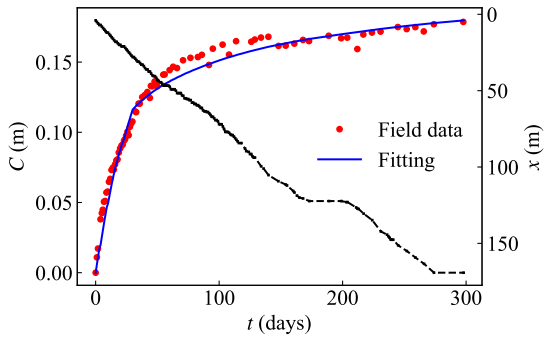
Chainage 10349 m (B)



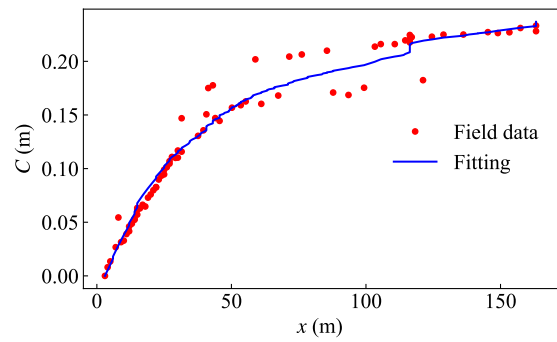
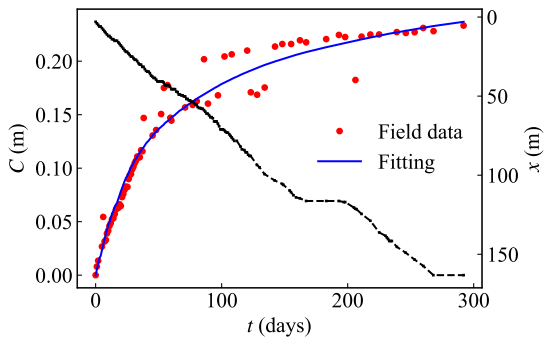
Chainage 10353 m (B)



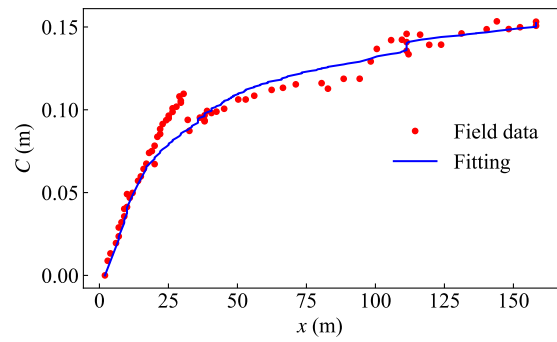
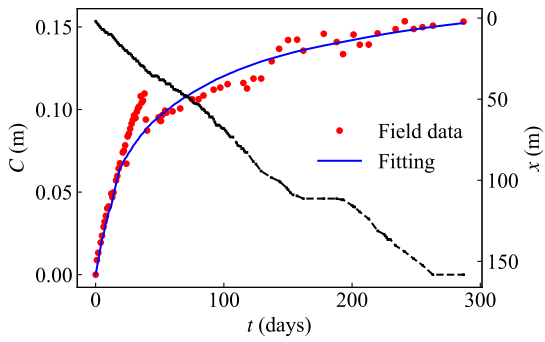
Chainage 10358 m (B)



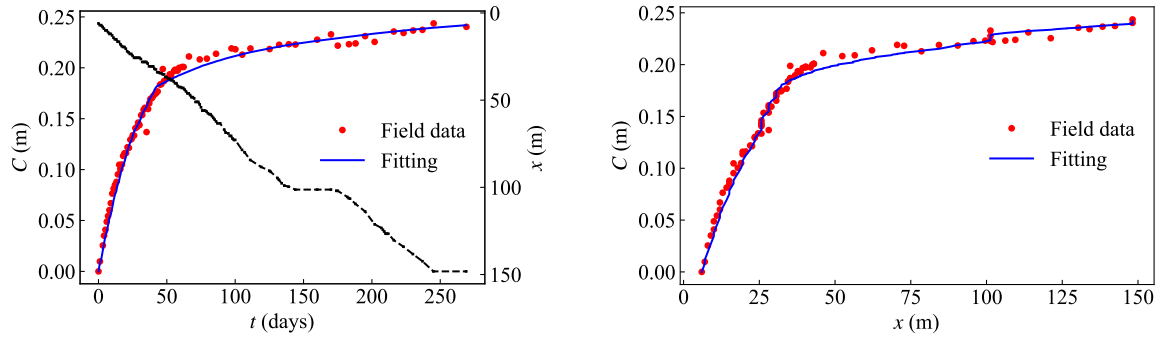
Chainage 10363 m (B)



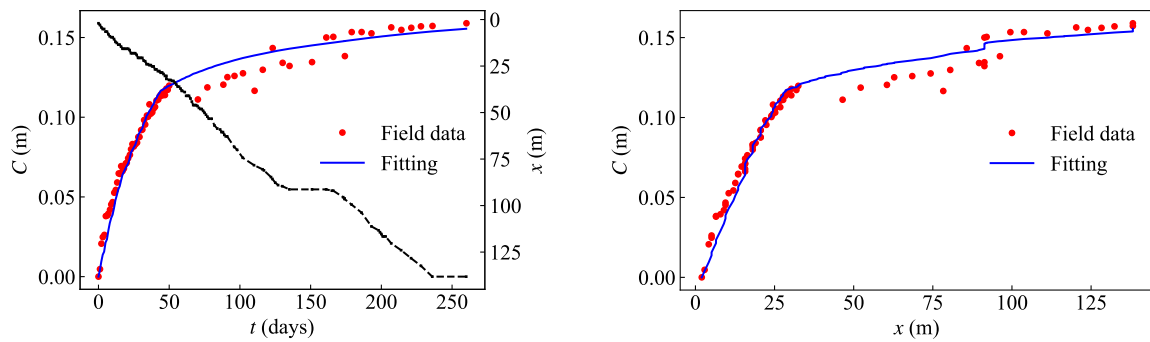
Chainage 10369 m (B)



Chainage 10374 m (B)



Chainage 10384 m (B)



Chainage 10394 m (B)

Figure C.1: Mean convergence fitting of the sections in SMP4-RPS (The black lines show the tunnel face advance.)

APPENDIX D

STRING CONVERGENCE OF THE SECTIONS IN SMP4-RPS

The detailed fitting results of the strings convergence of the sections in SMP4-RPS are summarized in this appendix. The proposed parameters values of the convergence law for every section are shown in Table 3.11. The black lines in the figures represent the tunnel face advance.

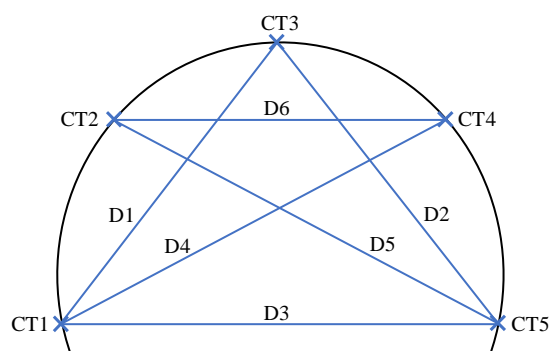
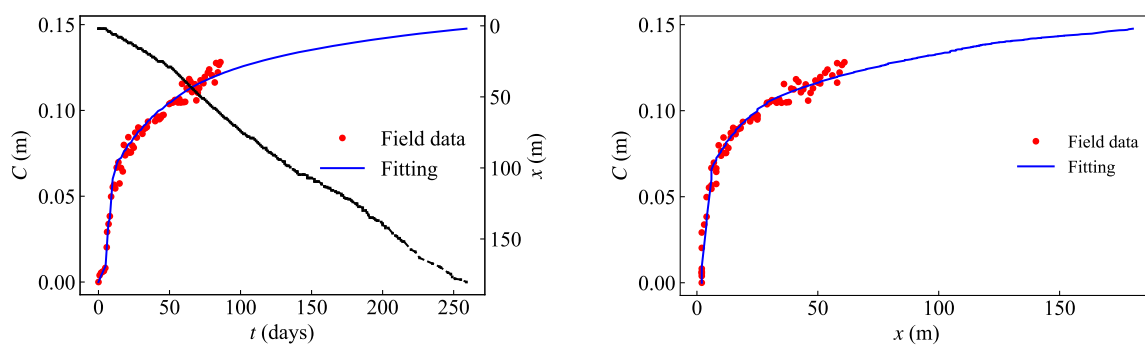
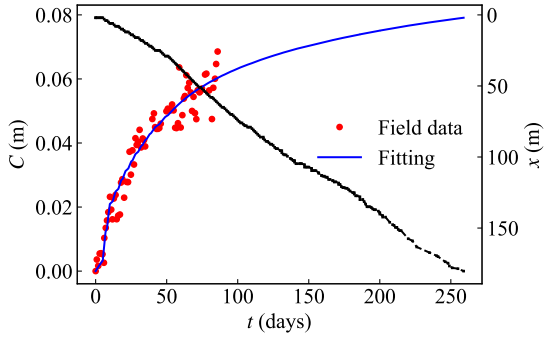


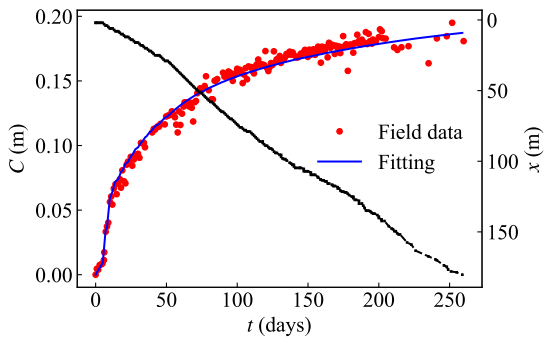
Figure D.1: Strings used for convergence measurements in SMP4-RPS (The black lines show the tunnel face advance.)



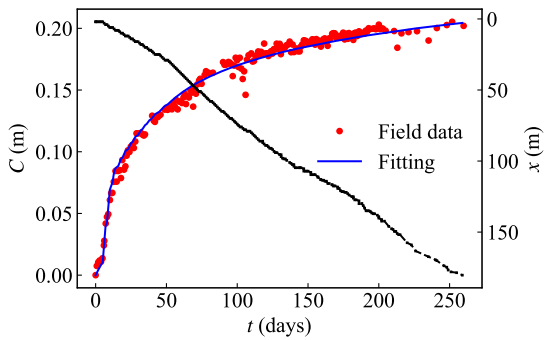
String D1



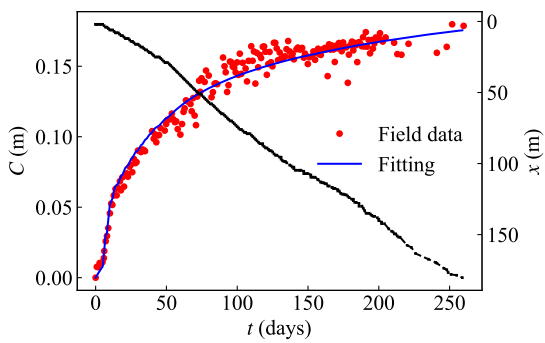
String D2



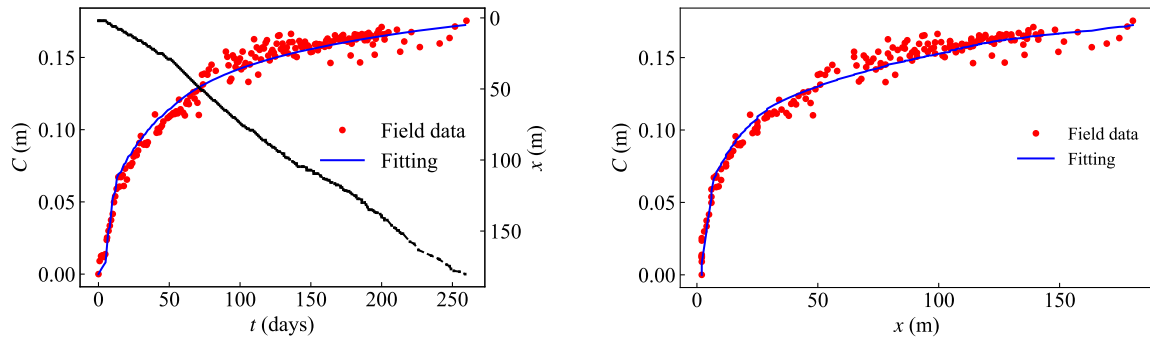
String D3



String D4

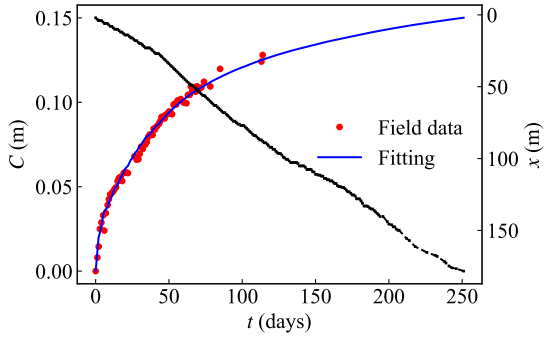


String D5

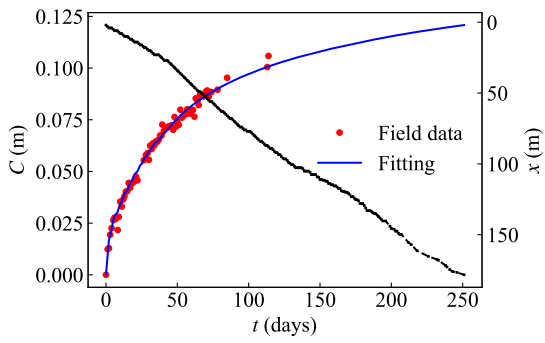


String D6

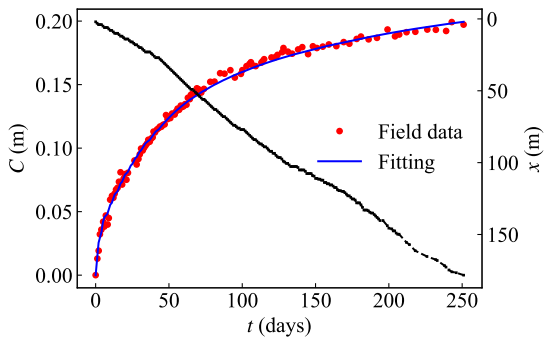
Figure D.2: Strings convergence fitting of the section at chainage 10305 m (B) in SMP4-RPS (The black lines show the tunnel face advance.)



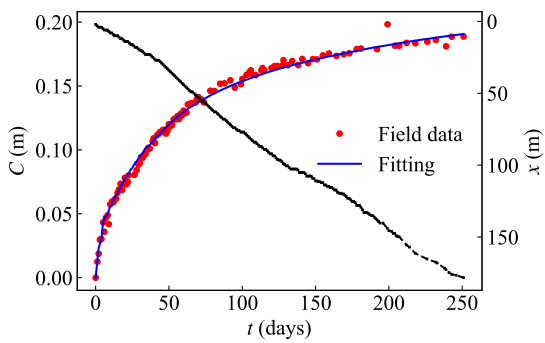
String D1



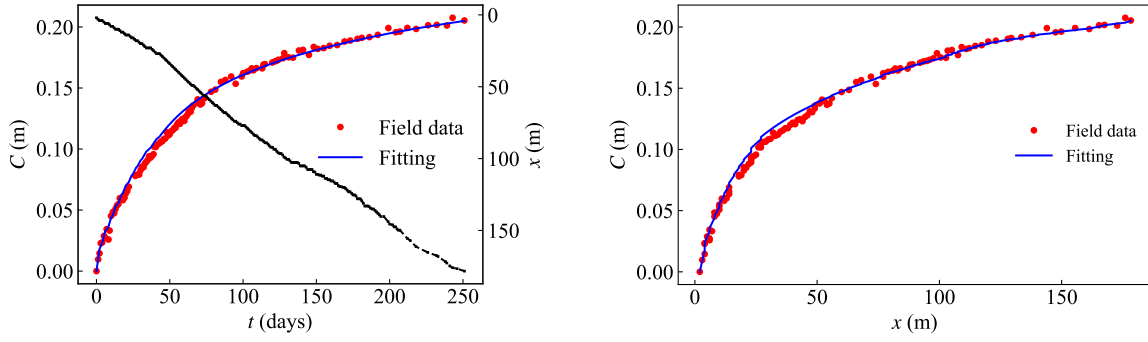
String D2



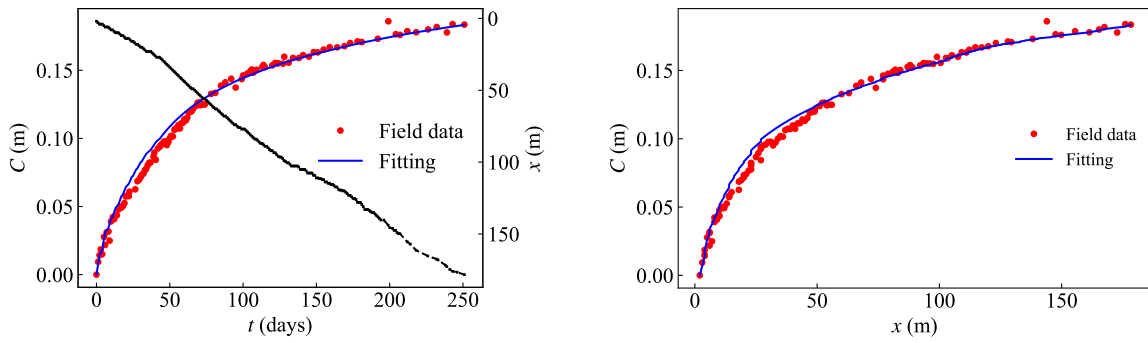
String D3



String D4

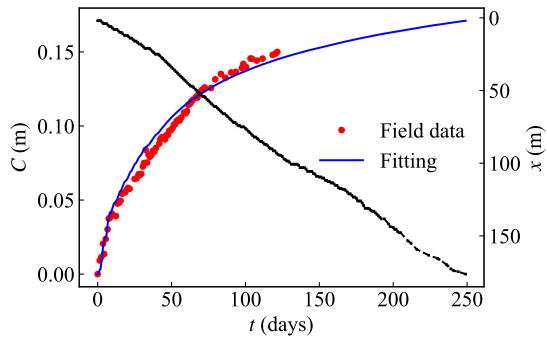


String D5

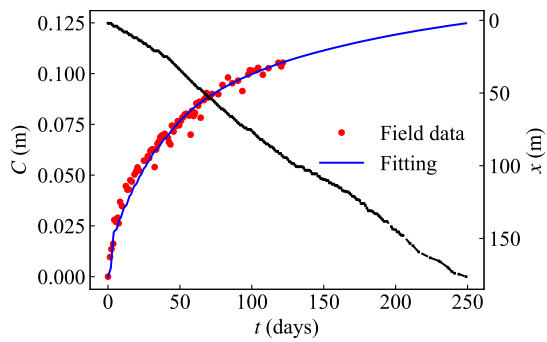


String D6

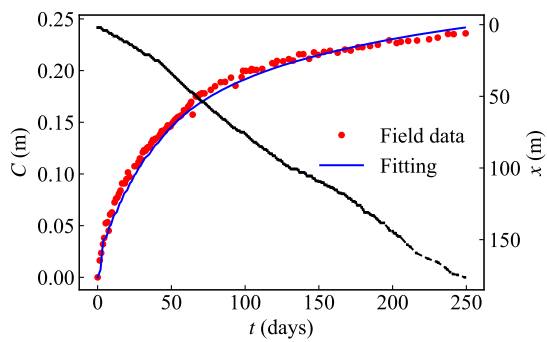
Figure D.3: Strings convergence fitting of the section at chainage 10307 m (B) in SMP4-RPS (The black lines show the tunnel face advance.)



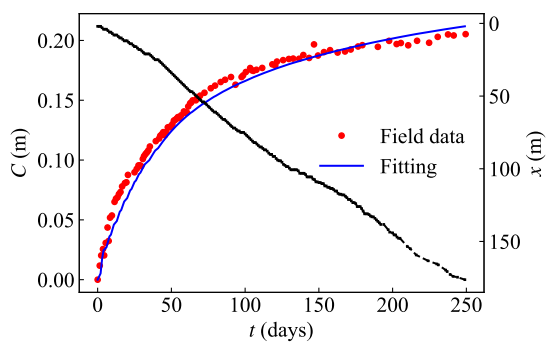
String D1



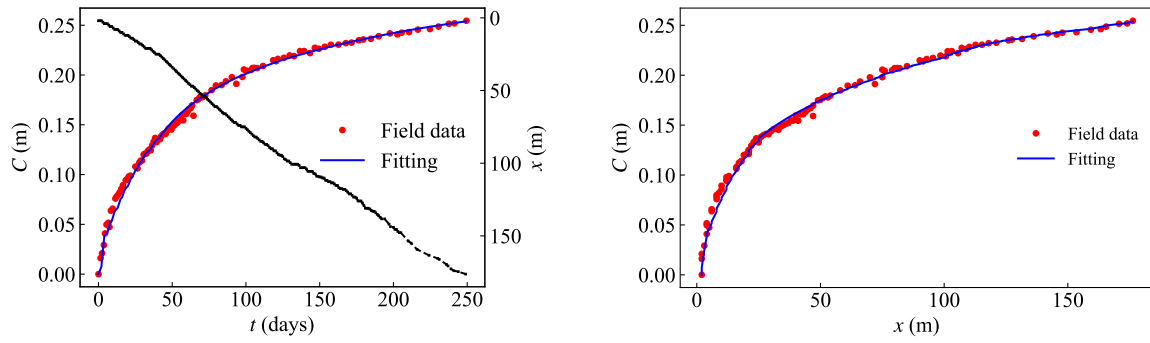
String D2



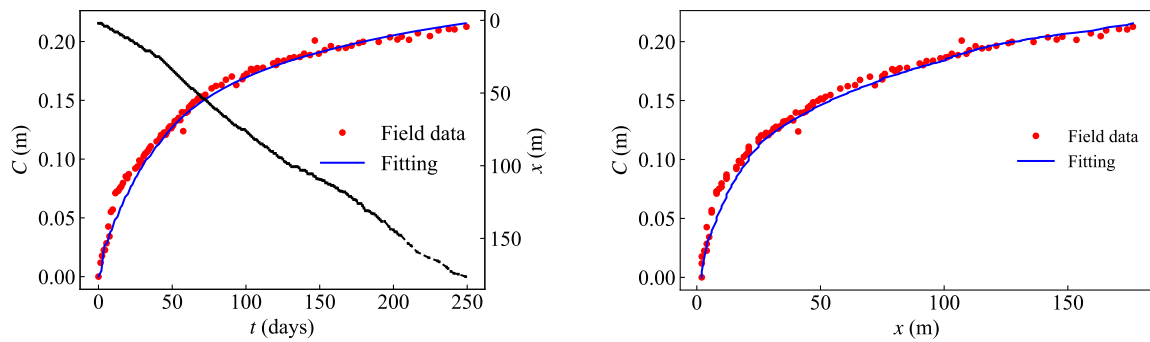
String D3



String D4

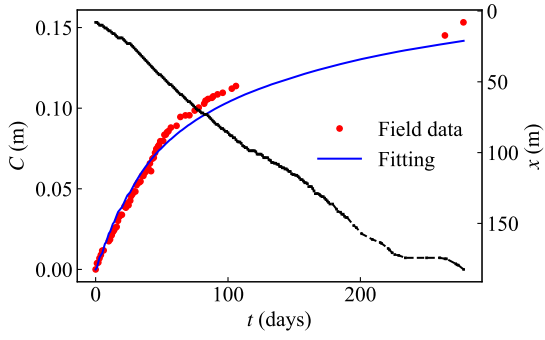


String D5

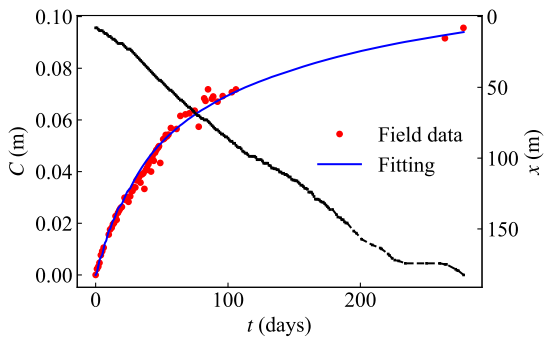


String D6

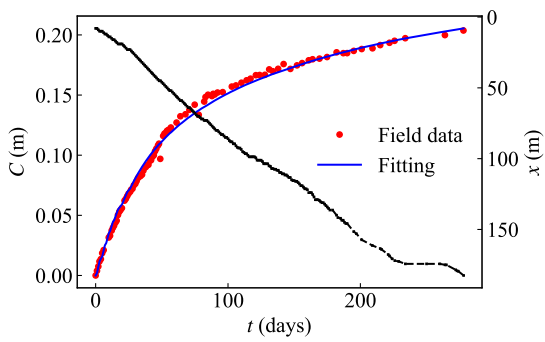
Figure D.4: Strings convergence fitting of the section at chainage 10309 m (B) in SMP4-RPS (The black lines show the tunnel face advance.)



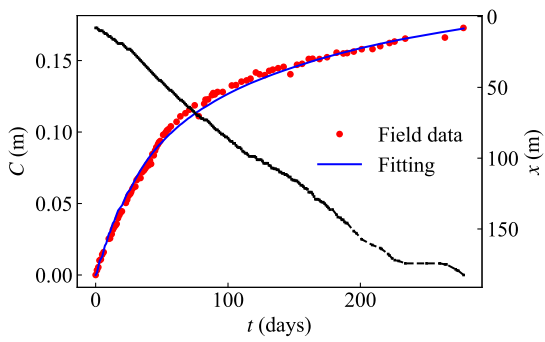
String D1



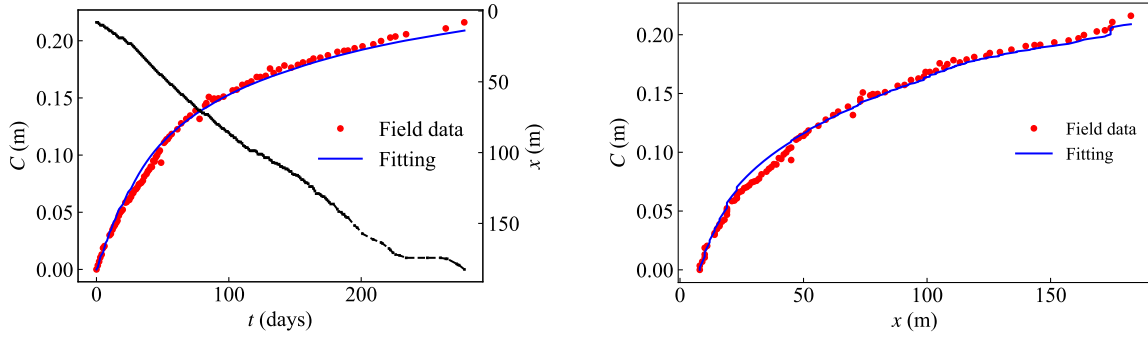
String D2



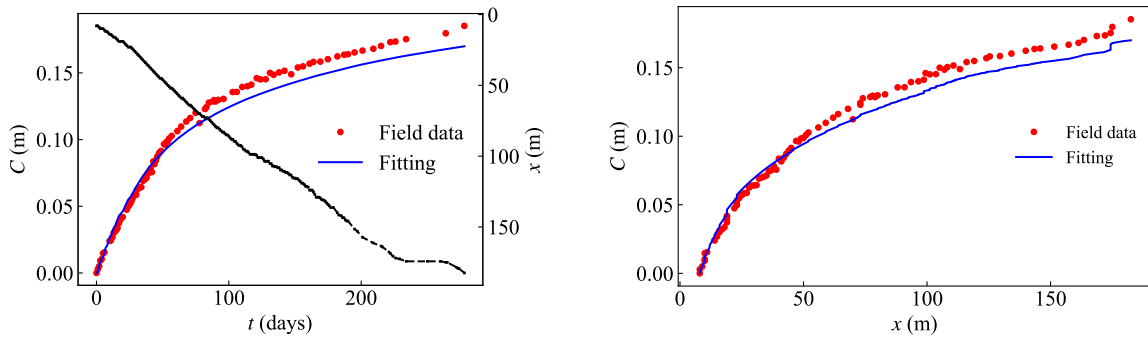
String D3



String D4

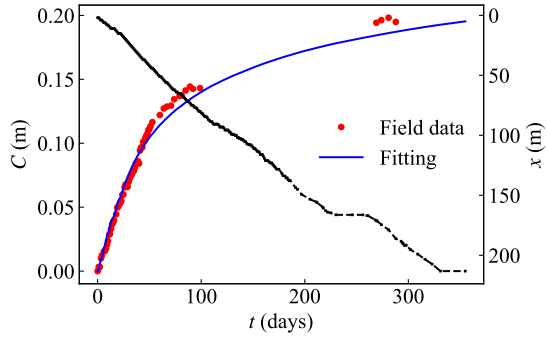


String D5

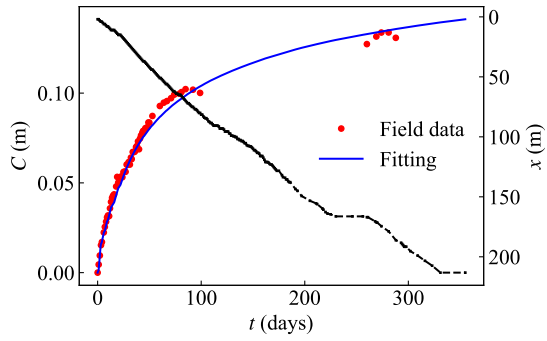


String D6

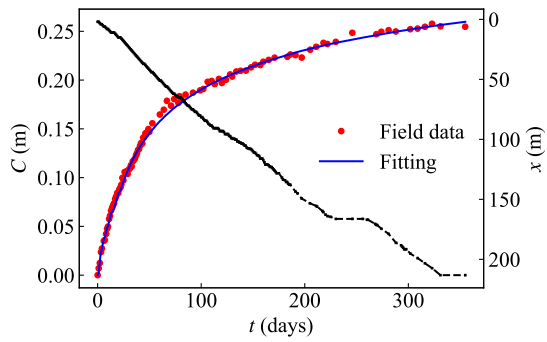
Figure D.5: Strings convergence fitting of the section at chainage 10311 m (B) in SMP4-RPS (The black lines show the tunnel face advance.)



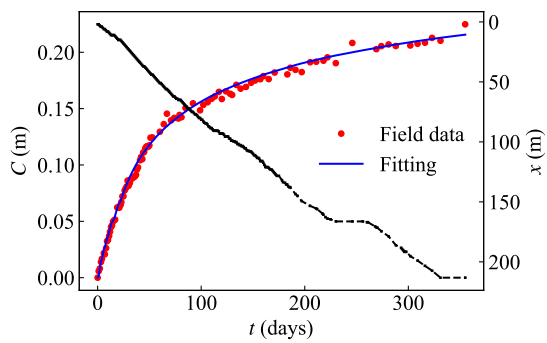
String D1



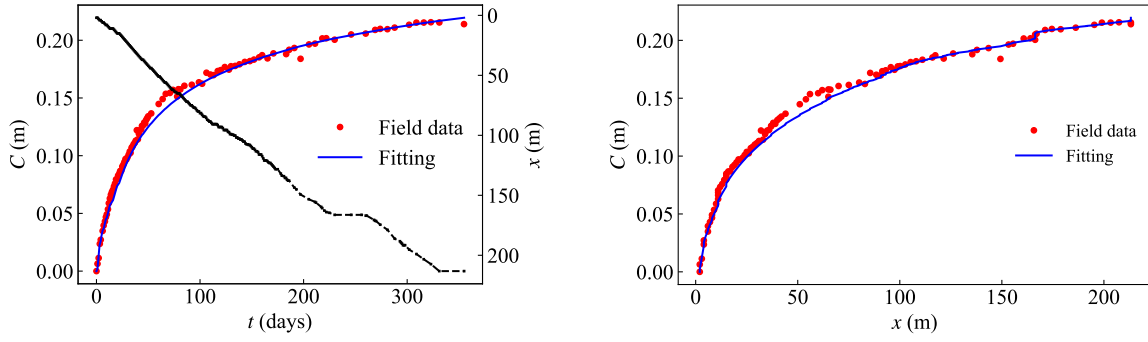
String D2



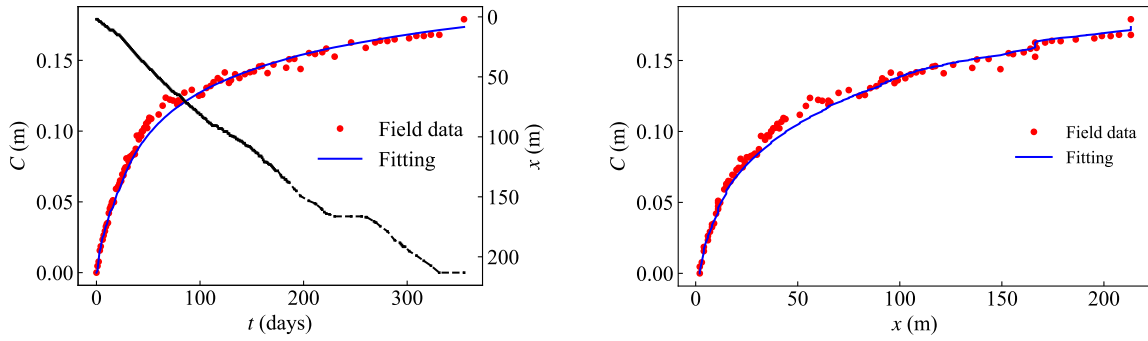
String D3



String D4

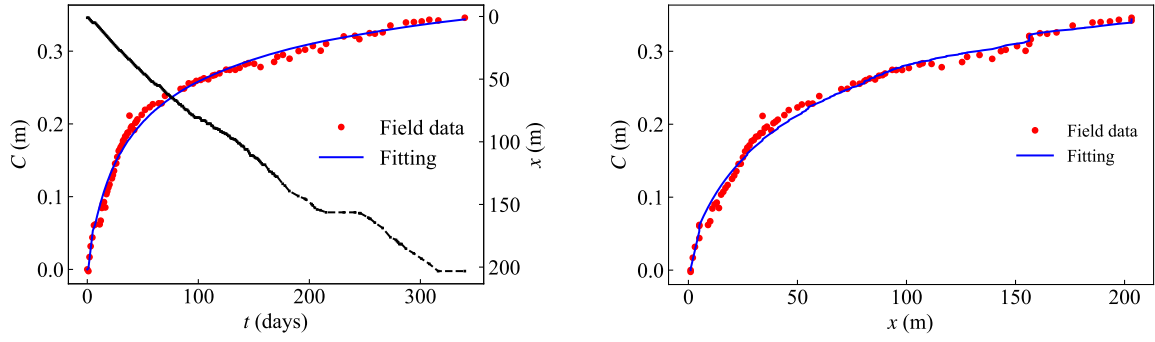


String D5

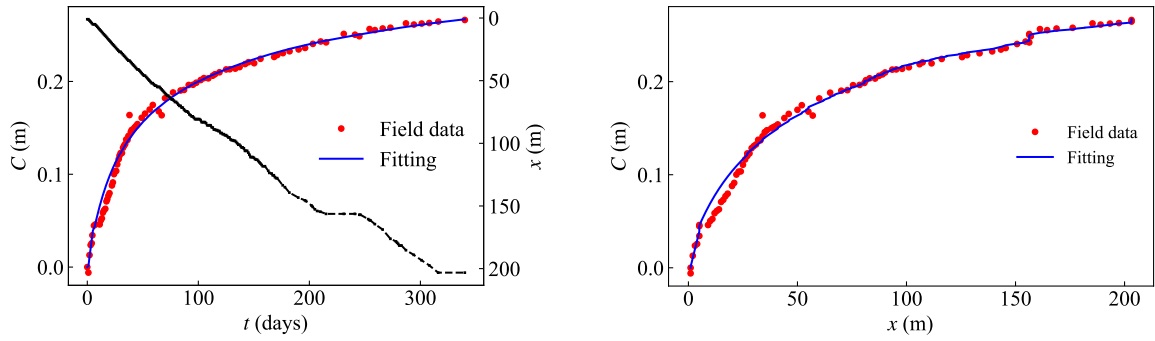


String D6

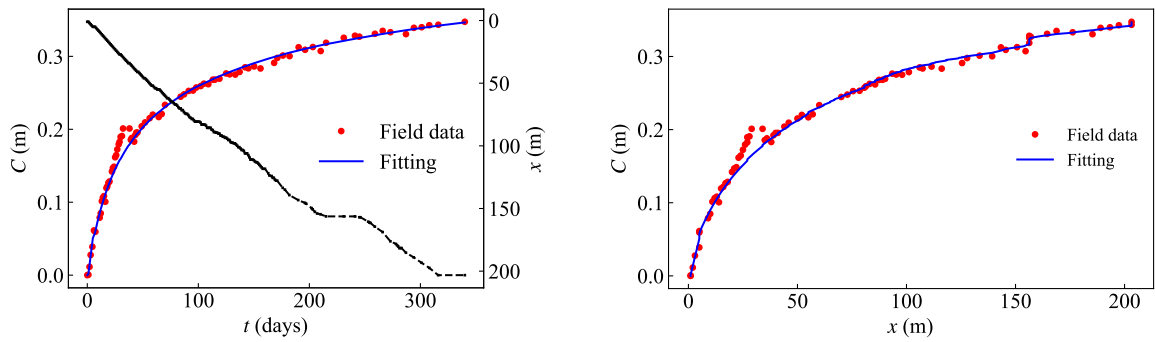
Figure D.6: Strings convergence fitting of the section at chainage 10319 m (B) in SMP4-RPS (The black lines show the tunnel face advance.)



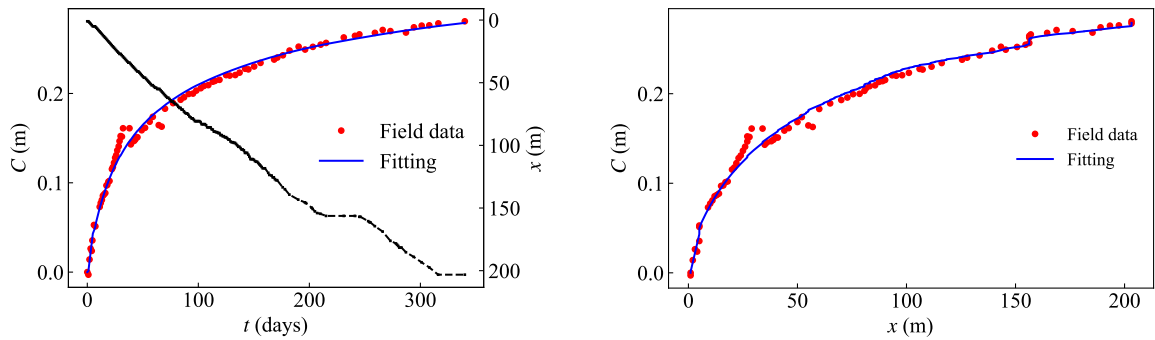
String D3



String D4

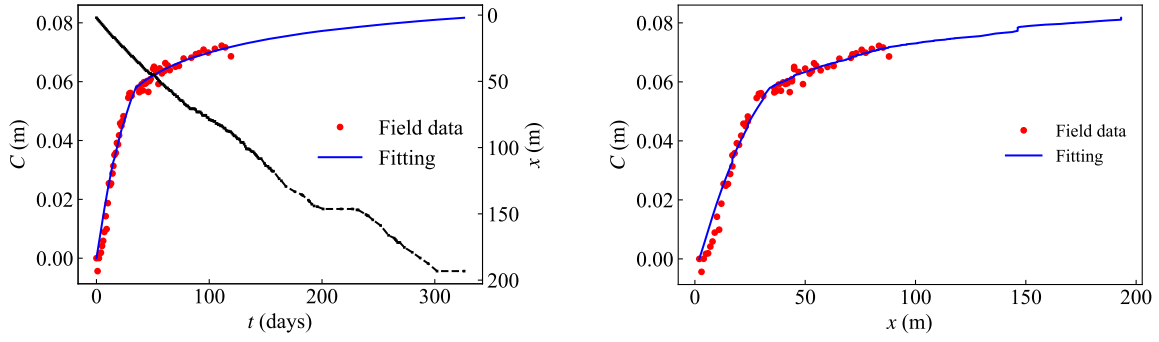


String D5

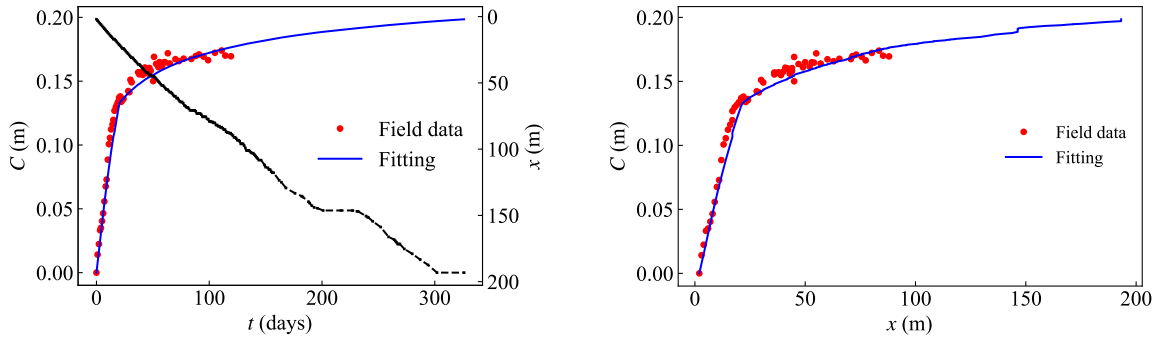


String D6

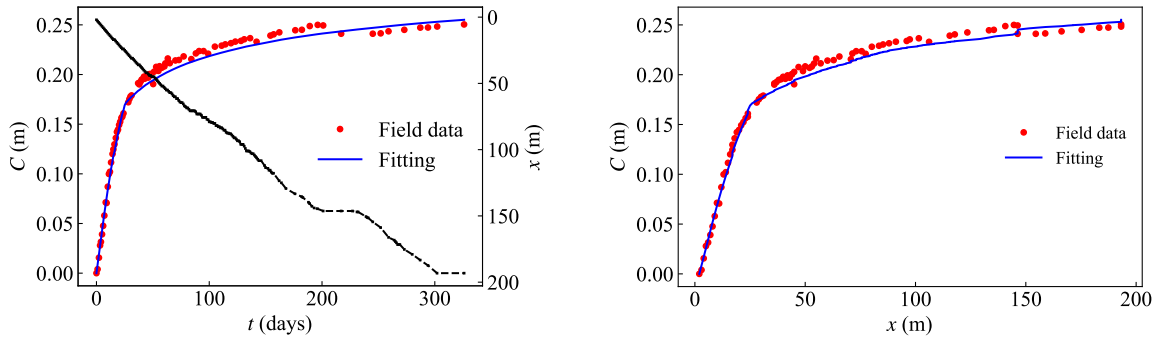
Figure D.7: Strings convergence fitting of the section at chainage 10329 m (B) in SMP4-RPS (The black lines show the tunnel face advance.)



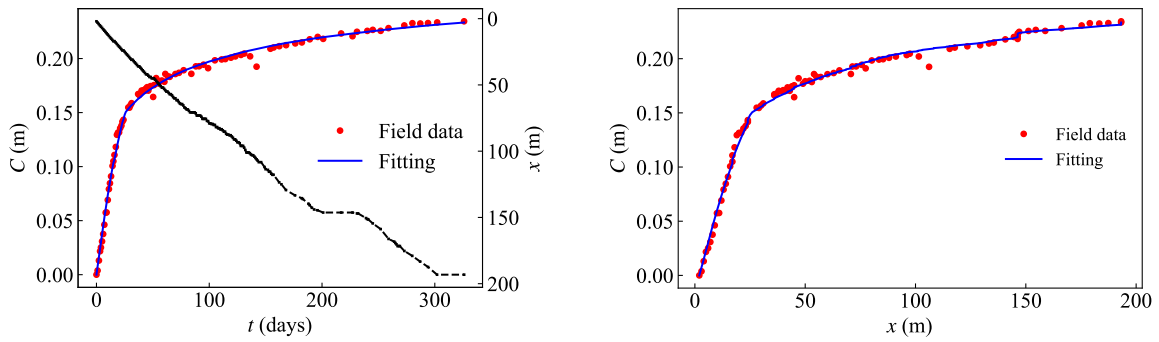
String D1



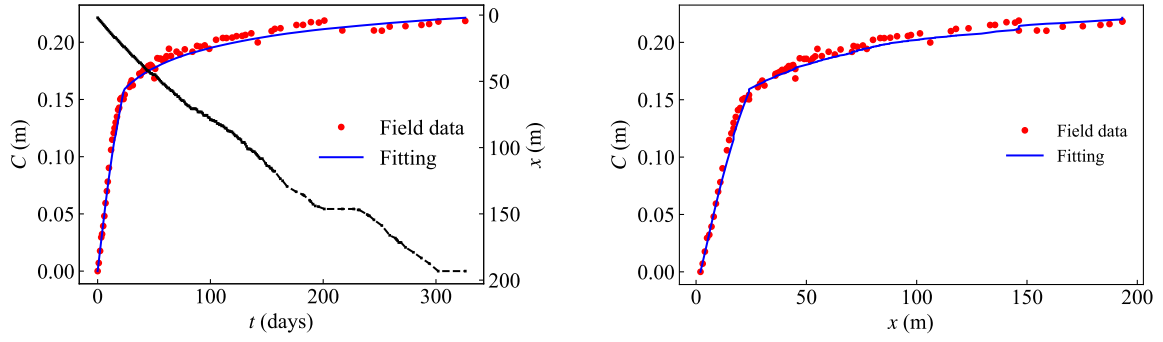
String D2



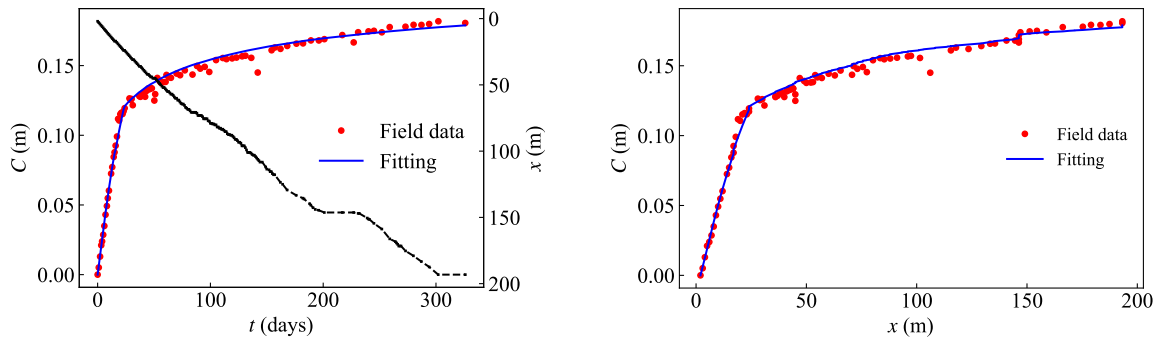
String D3



String D4

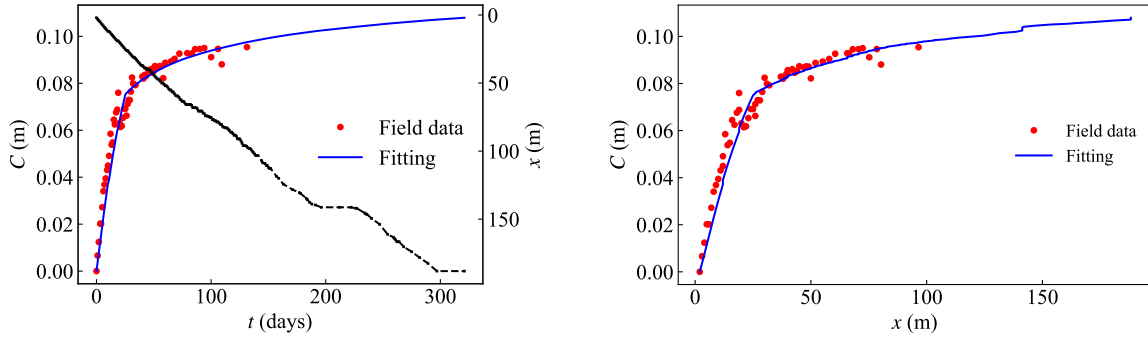


String D5

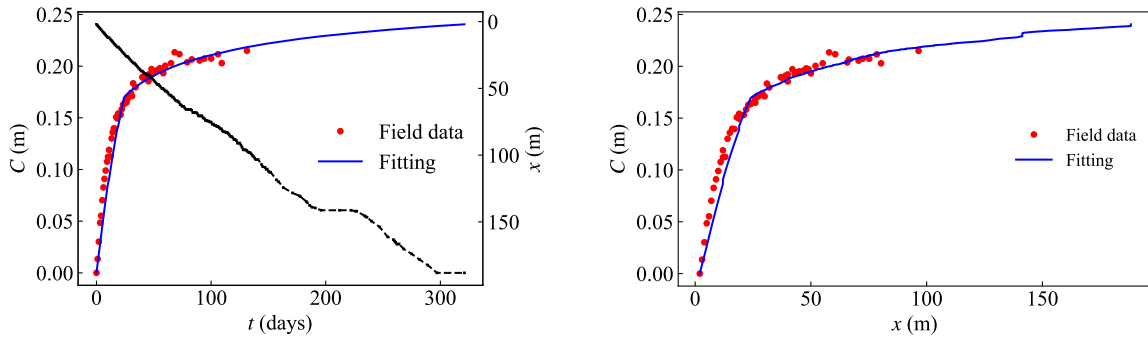


String D6

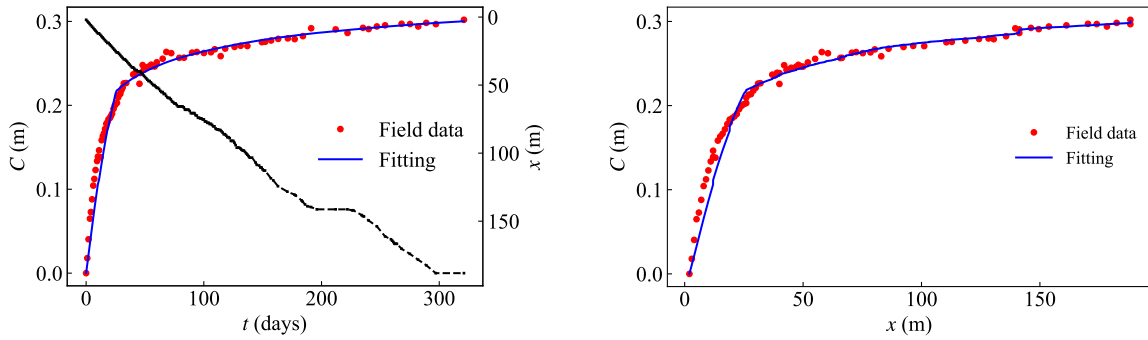
Figure D.8: Strings convergence fitting of the section at chainage 10339 m (B) in SMP4-RPS (The black lines show the tunnel face advance.)



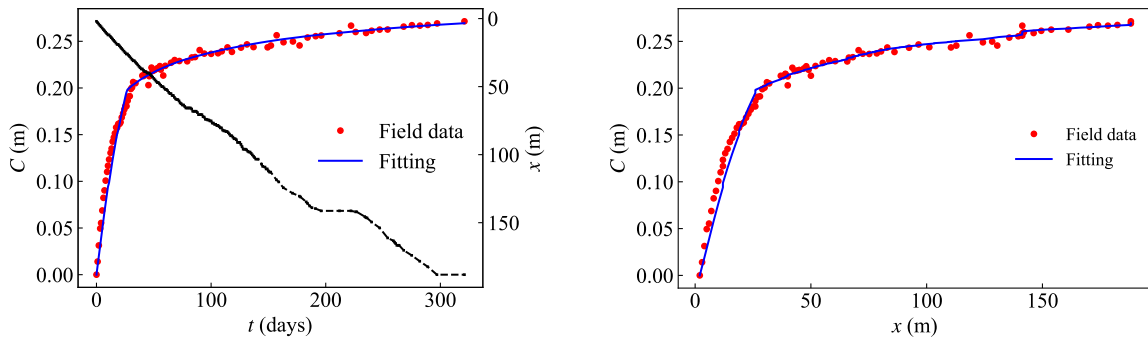
String D1



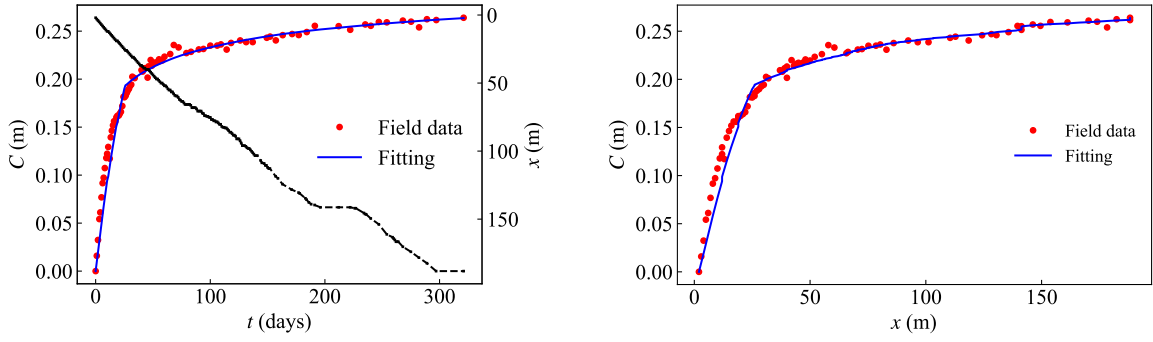
String D2



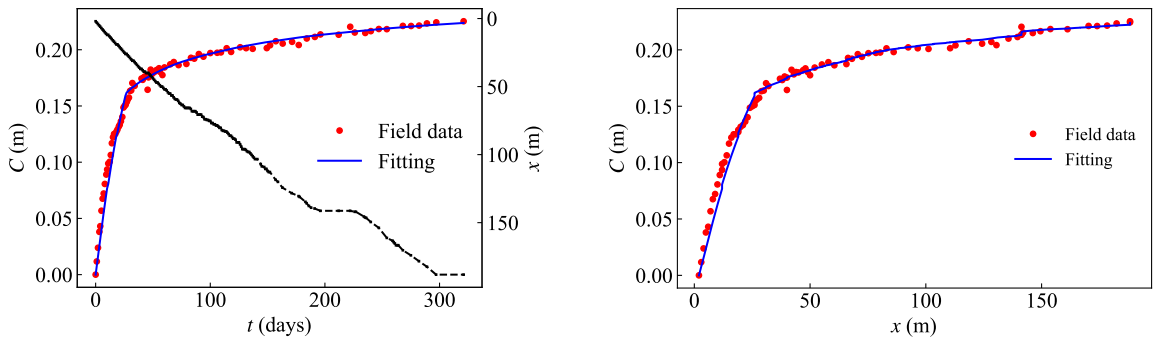
String D3



String D4

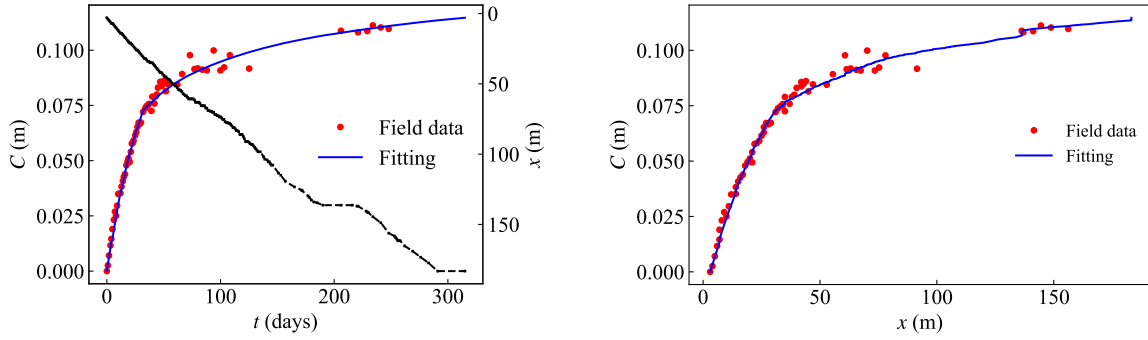


String D5

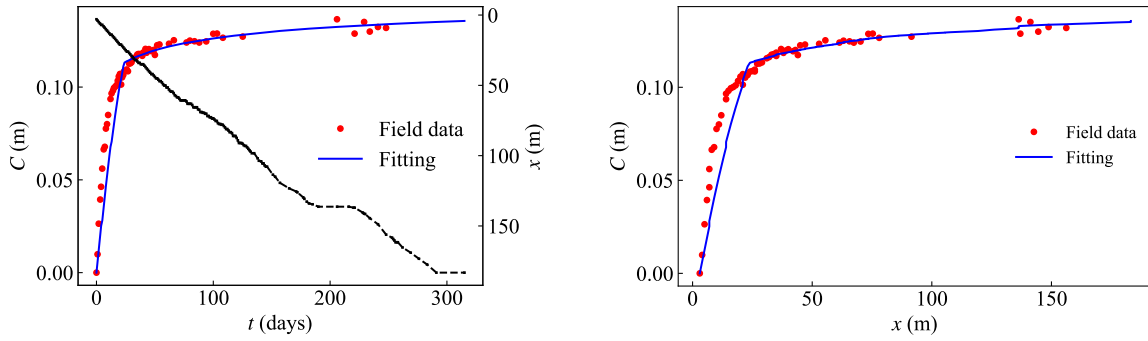


String D6

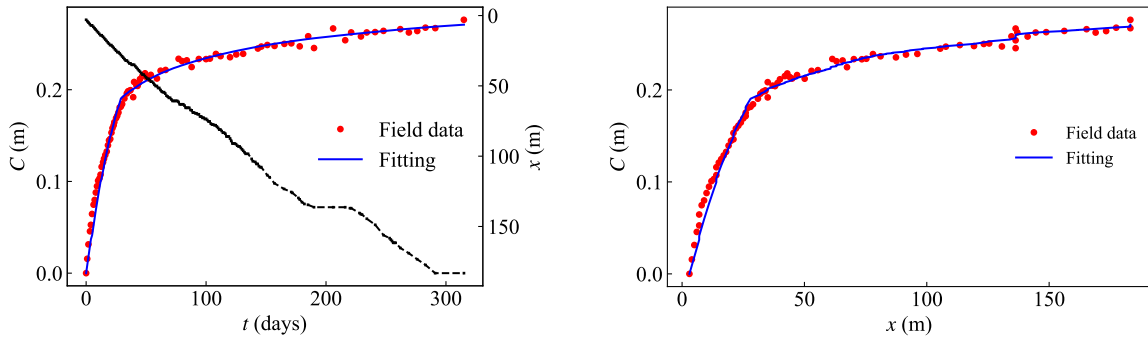
Figure D.9: Strings convergence fitting of the section at chainage 10344 m (B) in SMP4-RPS (The black lines show the tunnel face advance.)



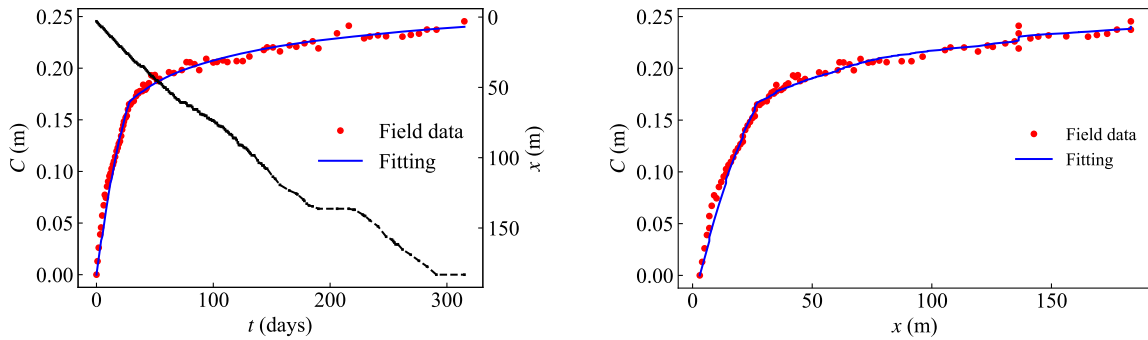
String D1



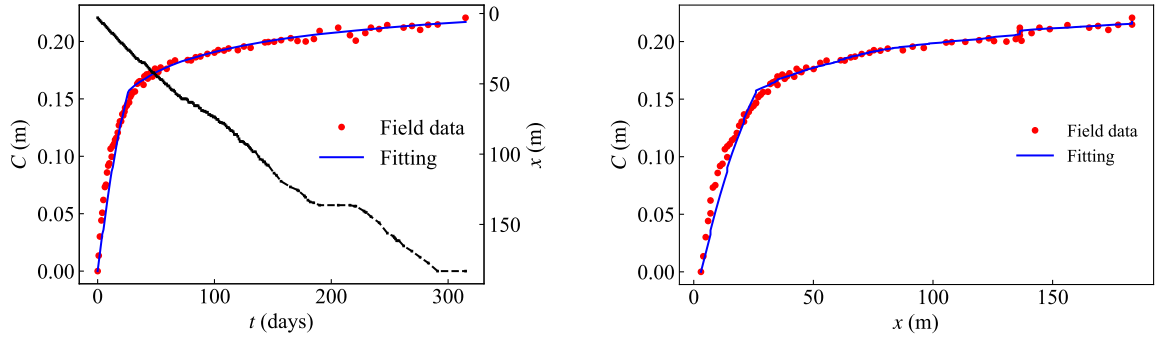
String D2



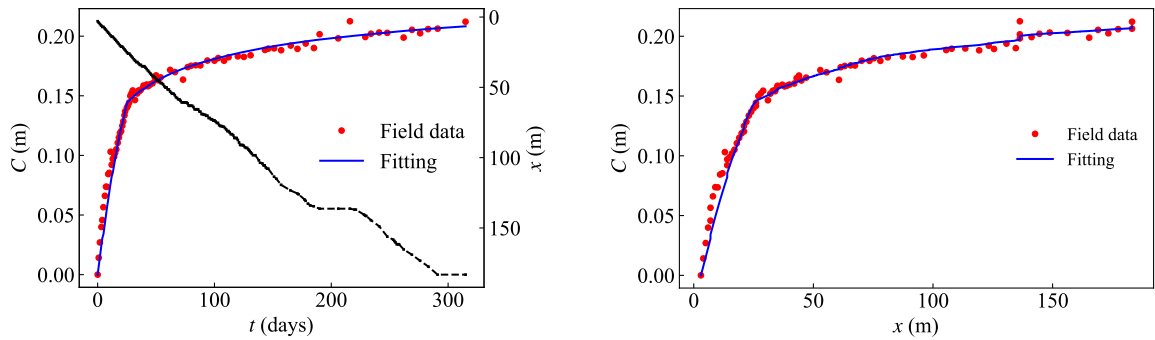
String D3



String D4

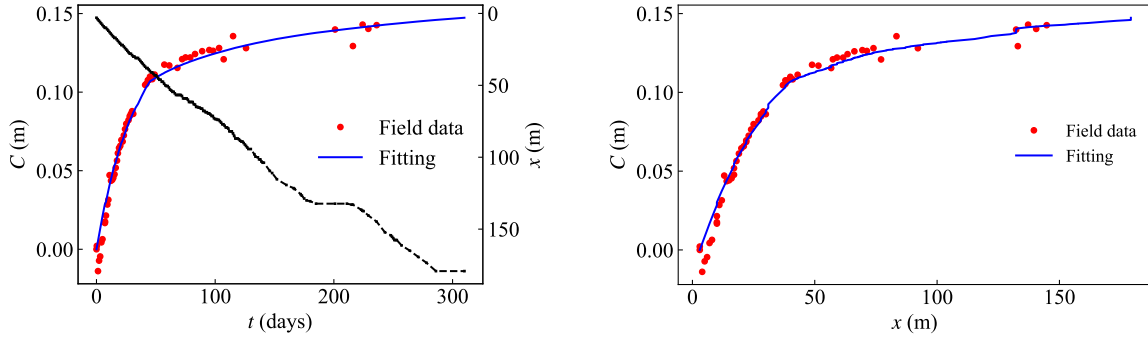


String D5

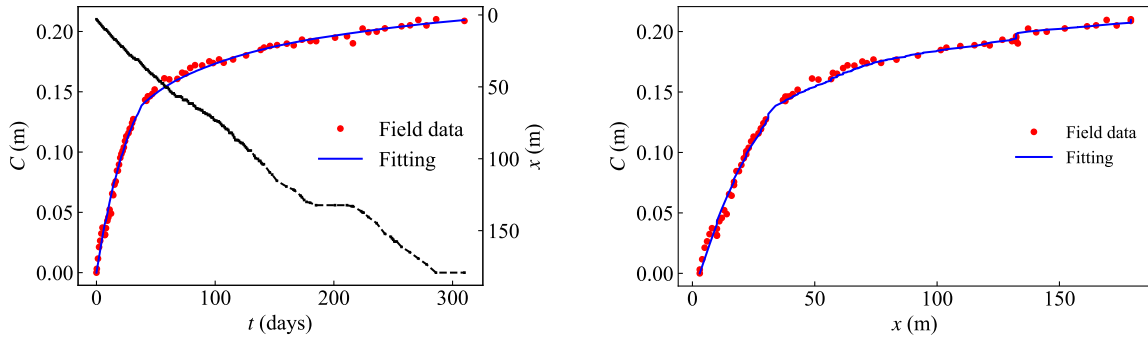


String D6

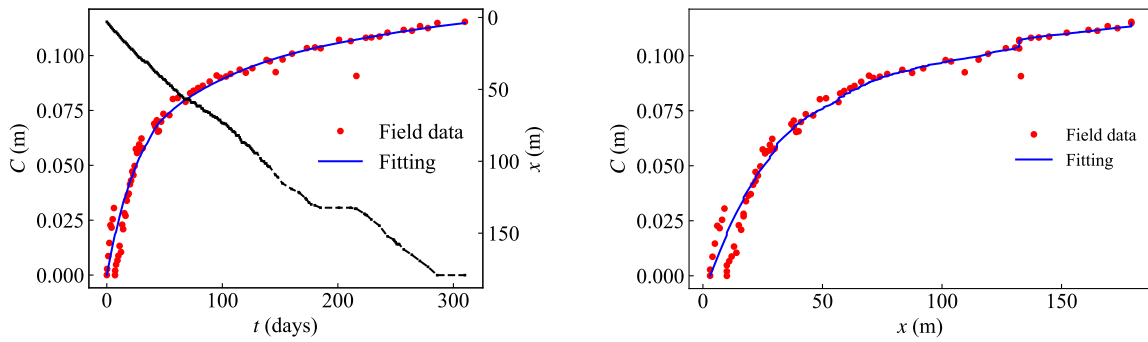
Figure D.10: Strings convergence fitting of the section at chainage 10349 m (B) in SMP4-RPS (The black lines show the tunnel face advance.)



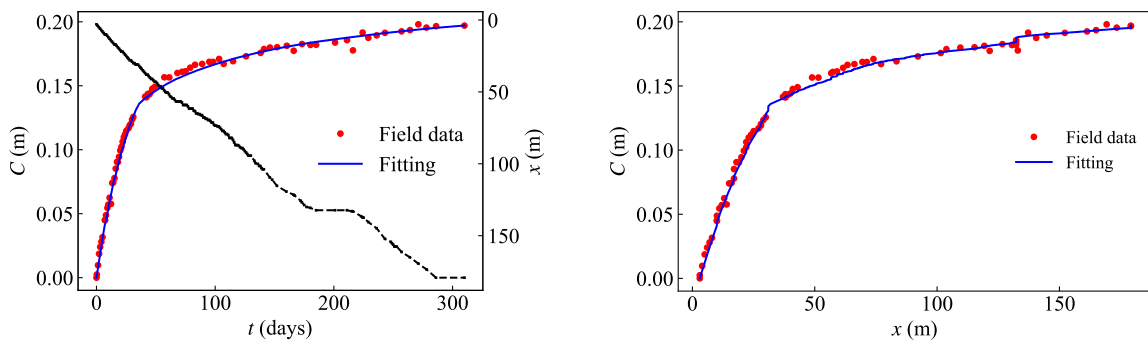
String D2



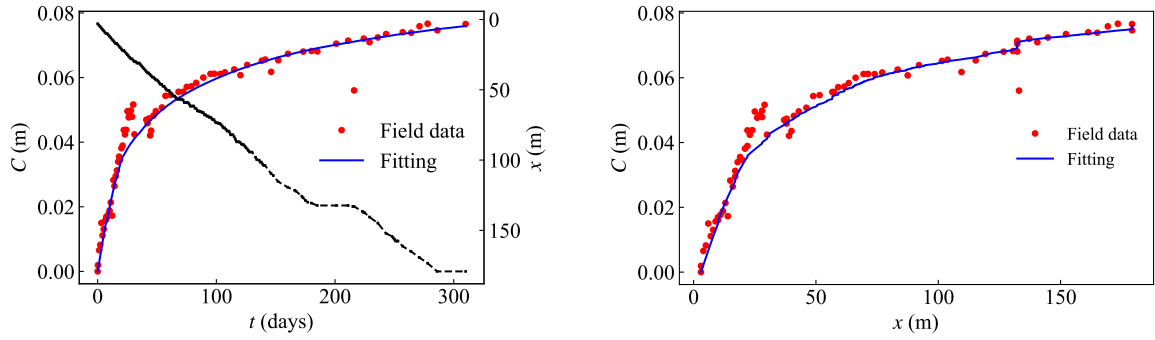
String D3



String D4

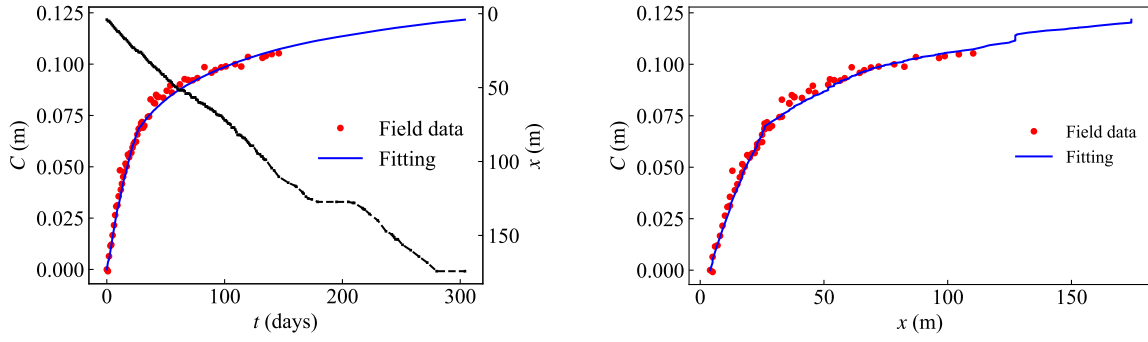


String D5

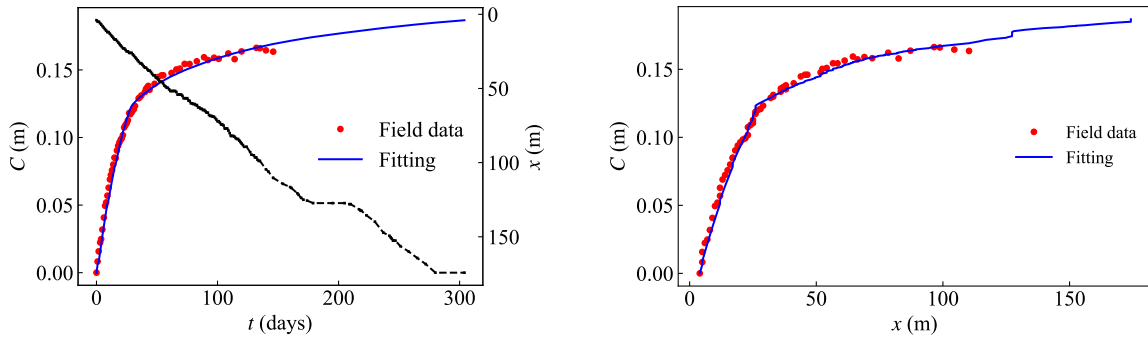


String D6

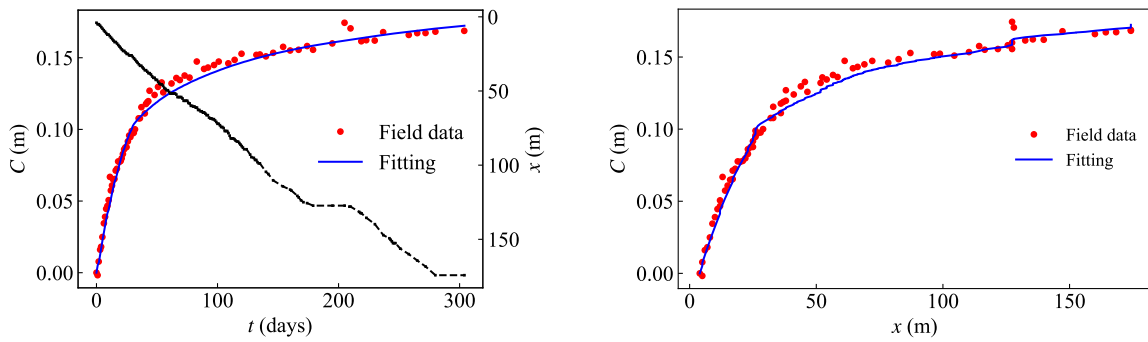
Figure D.11: Strings convergence fitting of the section at chainage 10353 m (B) in SMP4-RPS (The black lines show the tunnel face advance.)



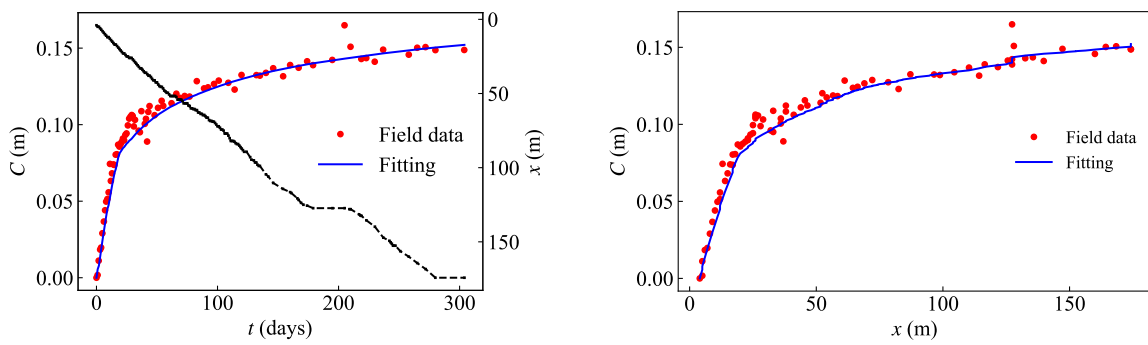
String D1



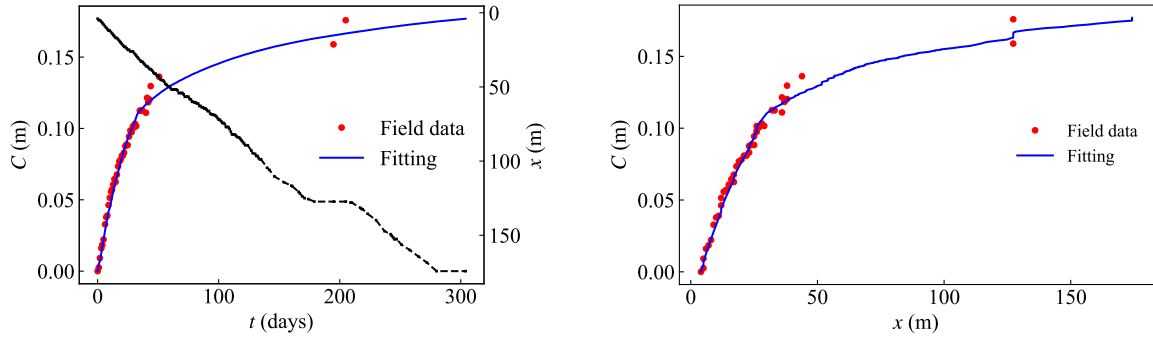
String D2



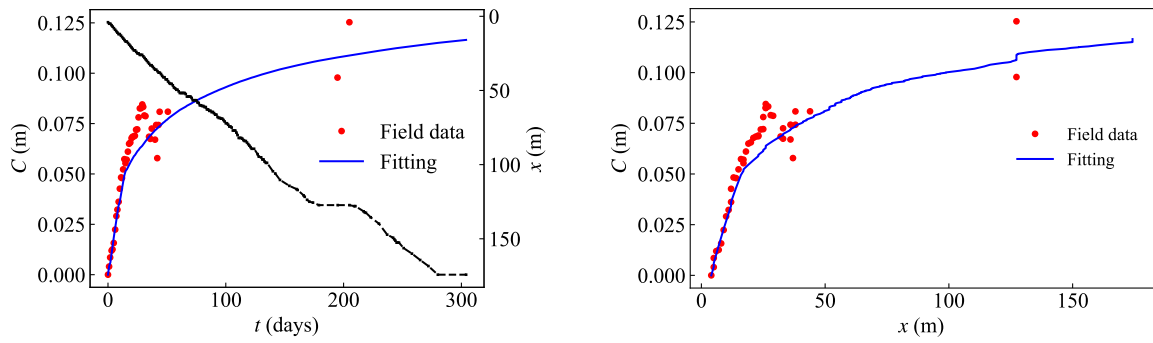
String D3



String D4

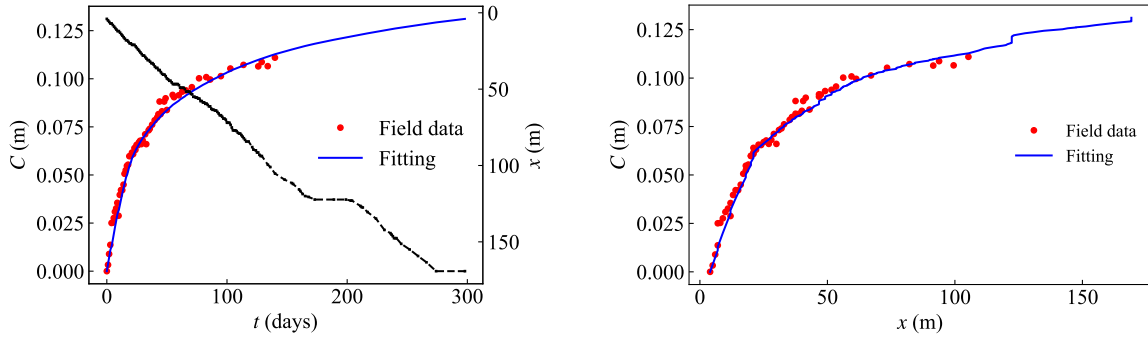


String D5

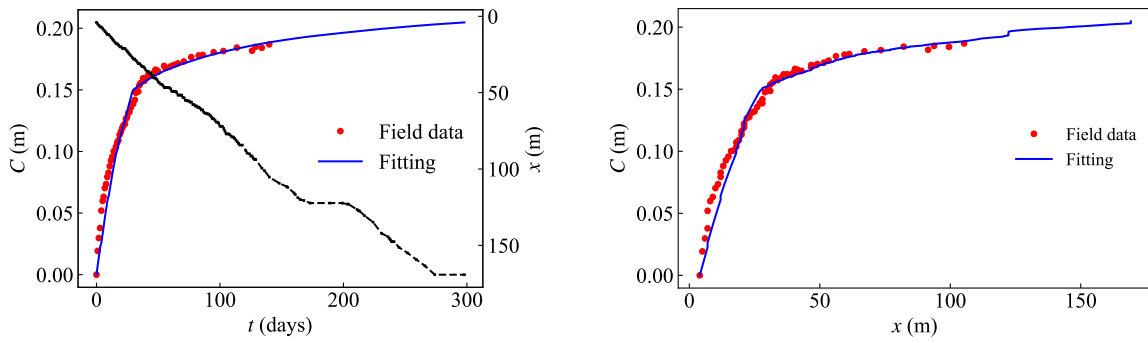


String D6

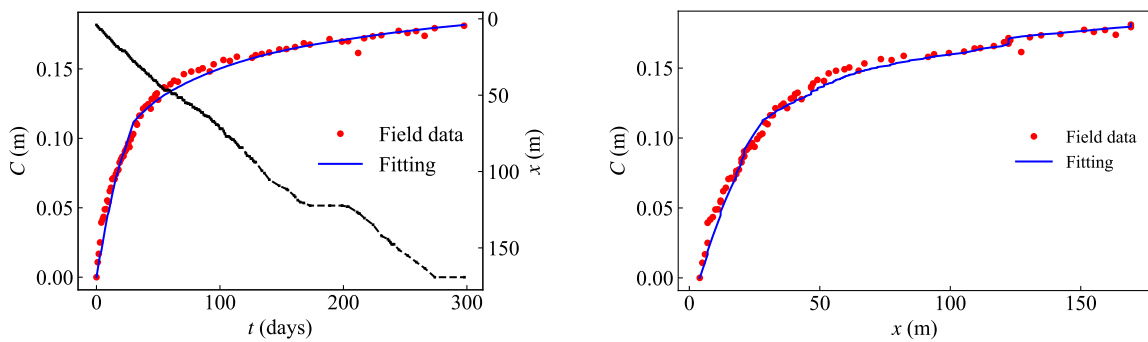
Figure D.12: Strings convergence fitting of the section at chainage 10358 m (B) in SMP4-RPS (The black lines show the tunnel face advance.)



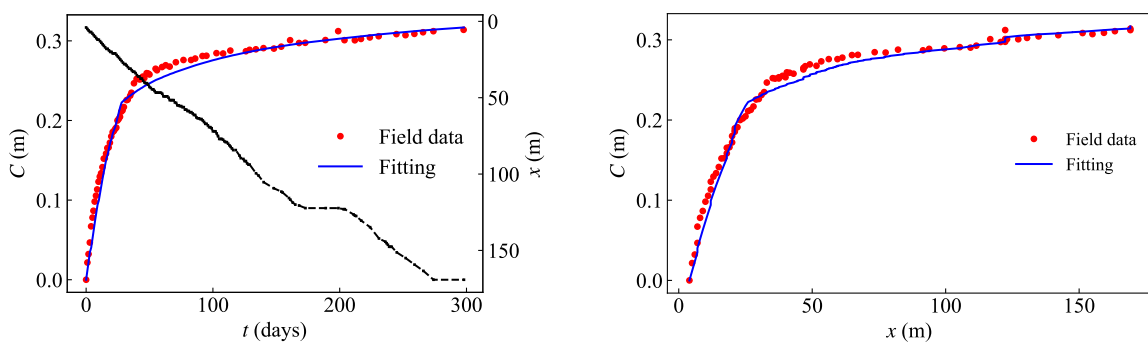
String D1



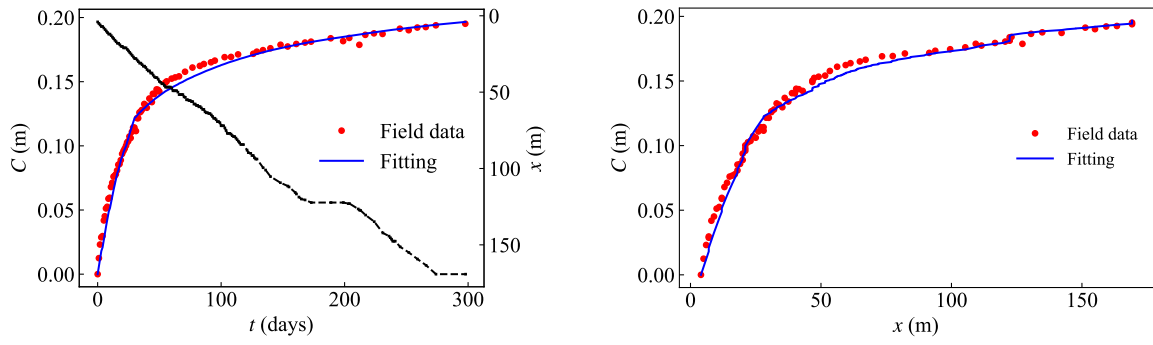
String D2



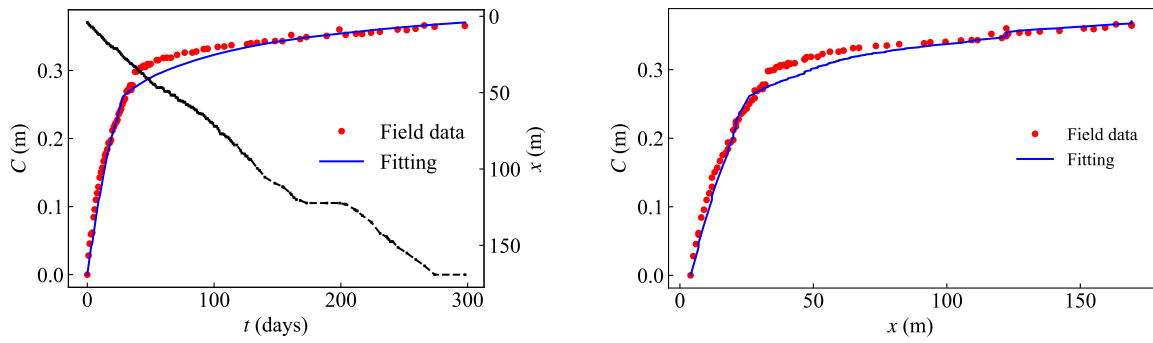
String D3



String D4

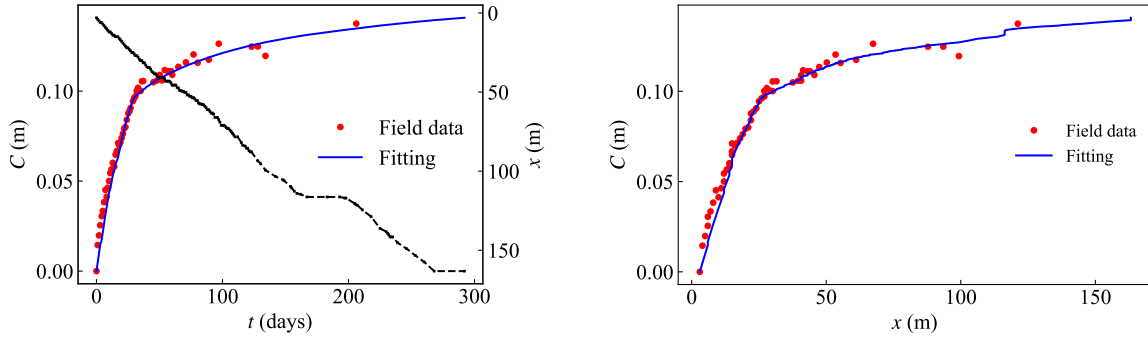


String D5

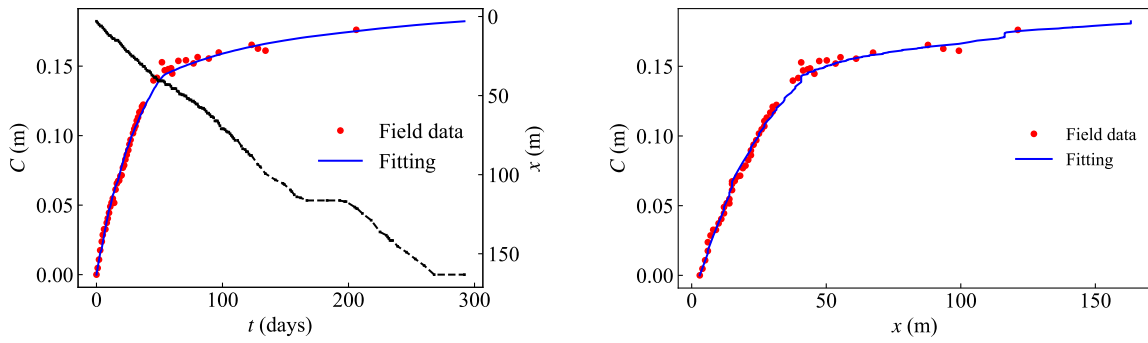


String D6

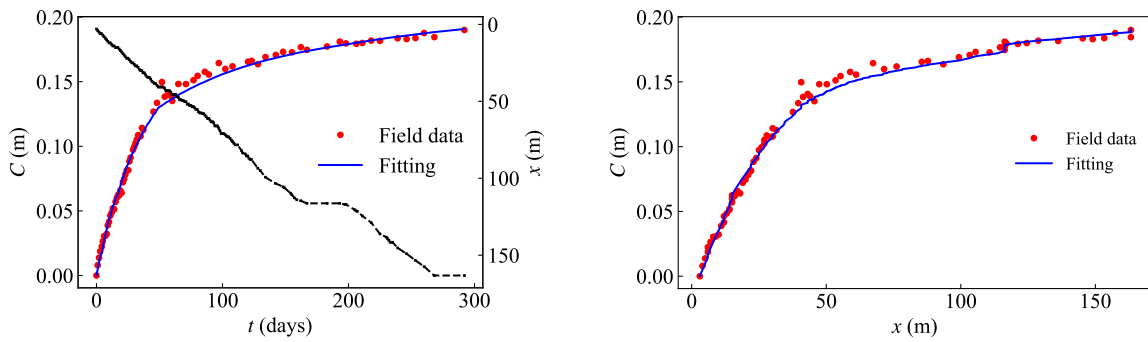
Figure D.13: Strings convergence fitting of the section at chainage 10363 m (B) in SMP4-RPS (The black lines show the tunnel face advance.)



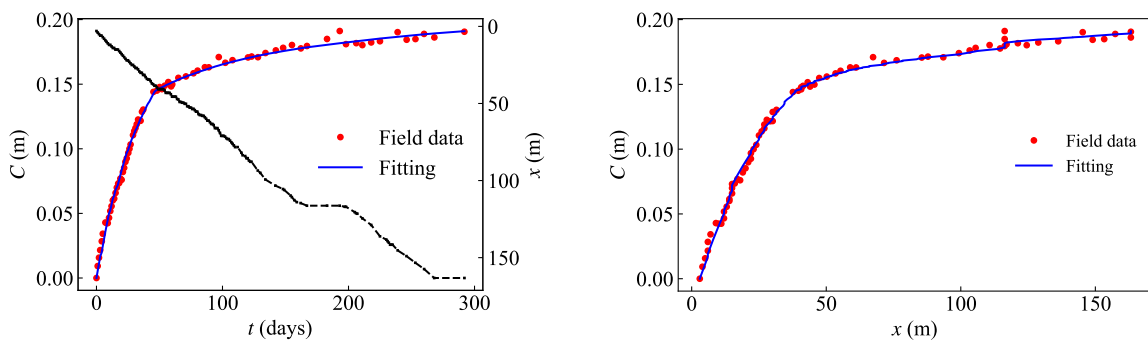
String D1



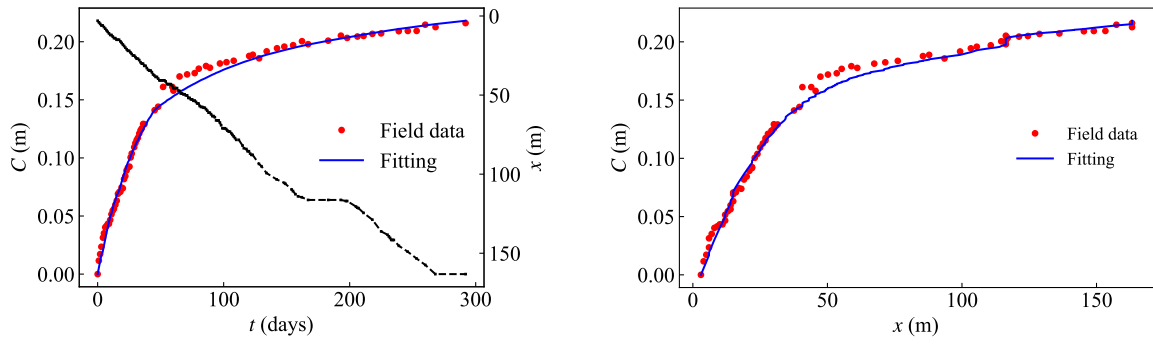
String D2



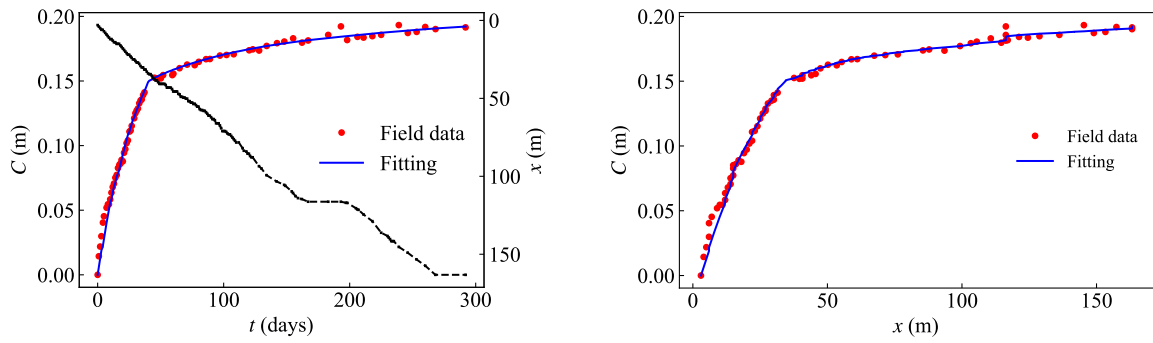
String D3



String D4

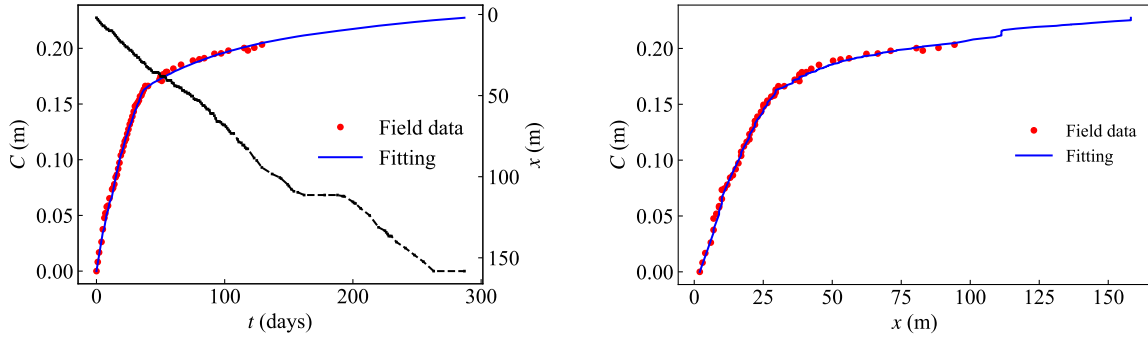


String D5

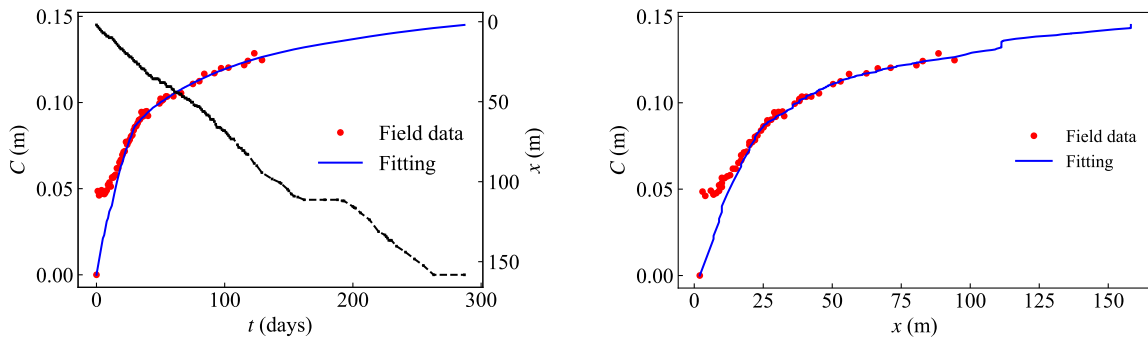


String D6

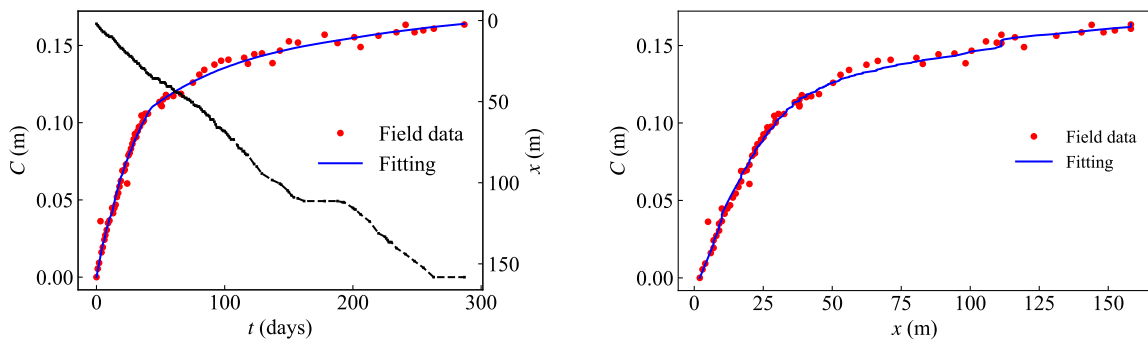
Figure D.14: Strings convergence fitting of the section at chainage 10369 m (B) in SMP4-RPS (The black lines show the tunnel face advance.)



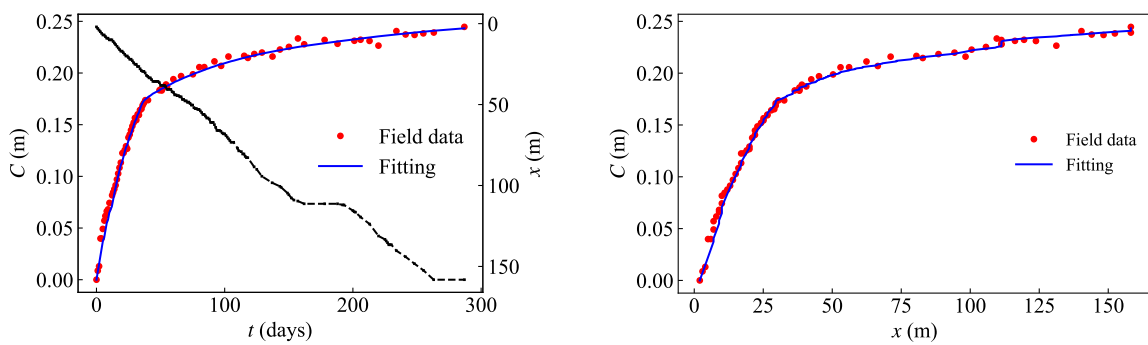
String D1



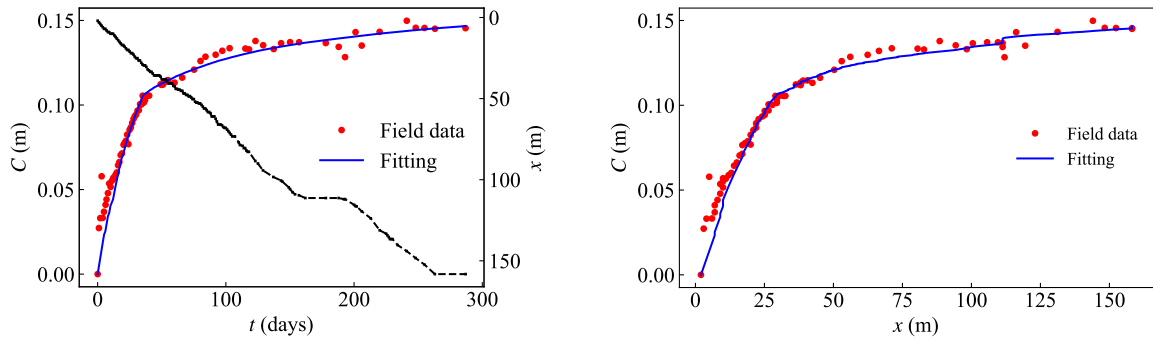
String D2



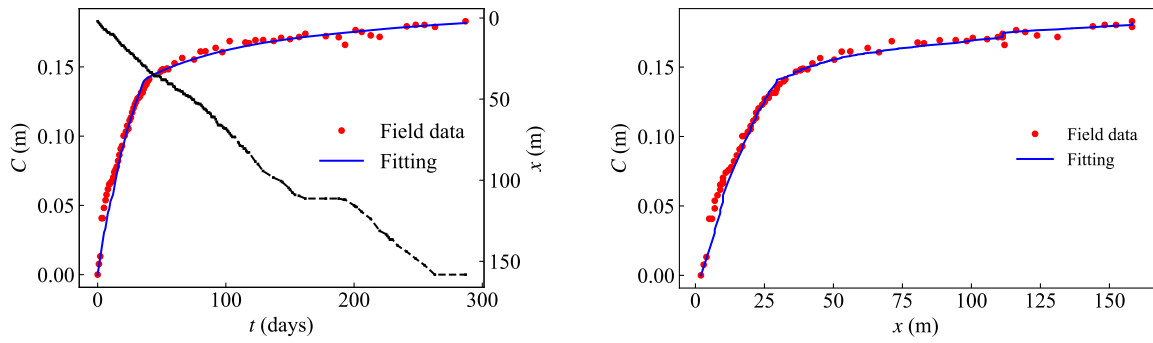
String D3



String D4

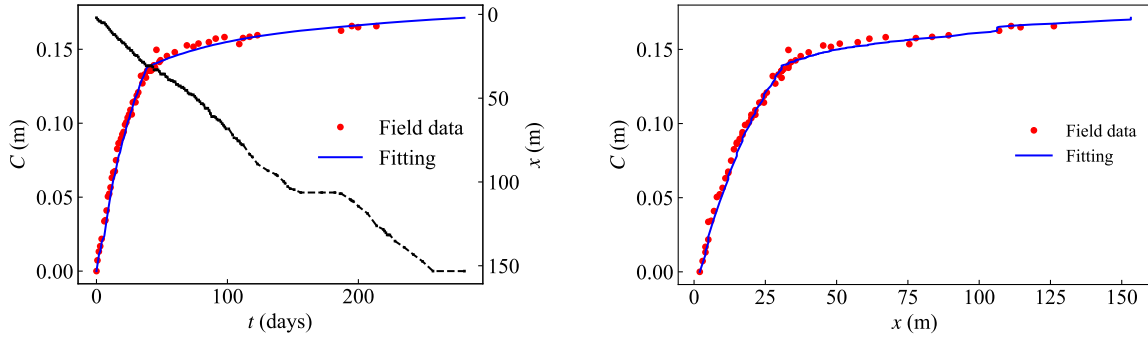


String D5

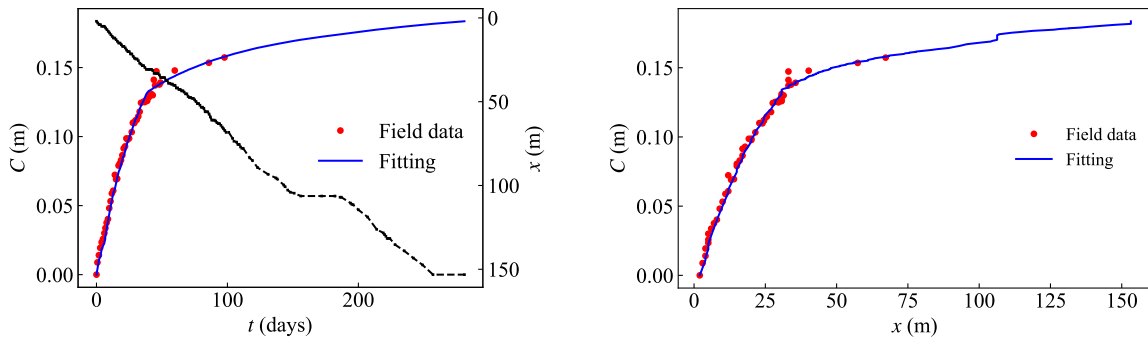


String D6

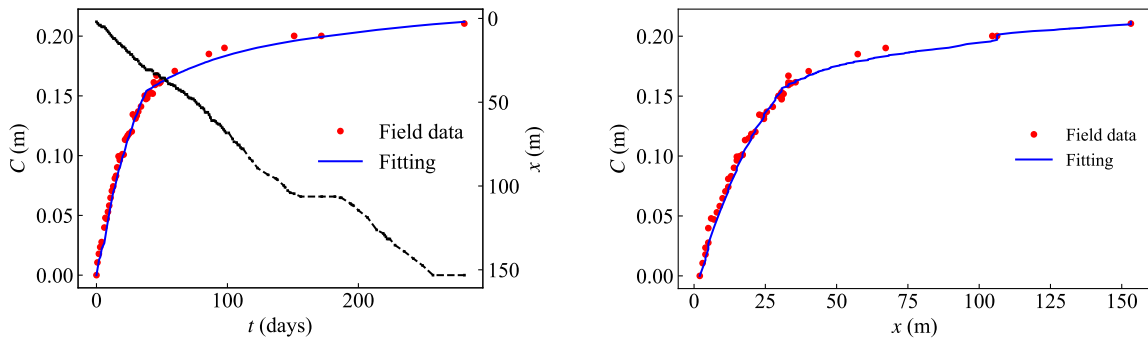
Figure D.15: Strings convergence fitting of the section at chainage 10374 m (B) in SMP4-RPS (The black lines show the tunnel face advance.)



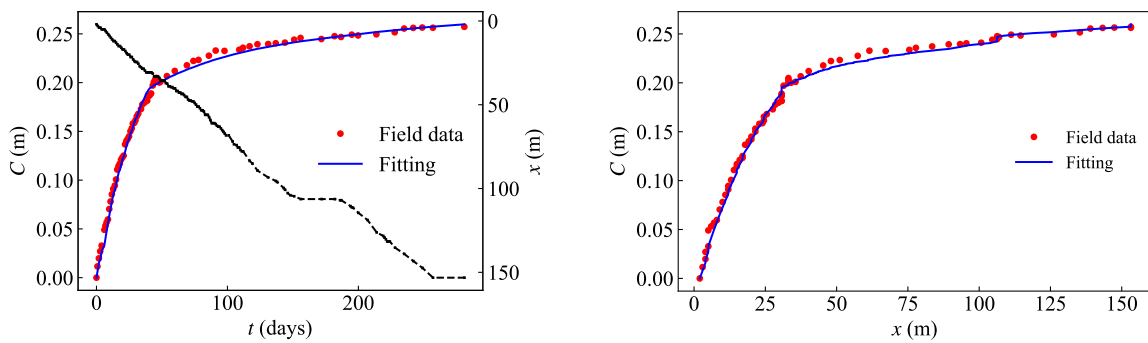
String D1



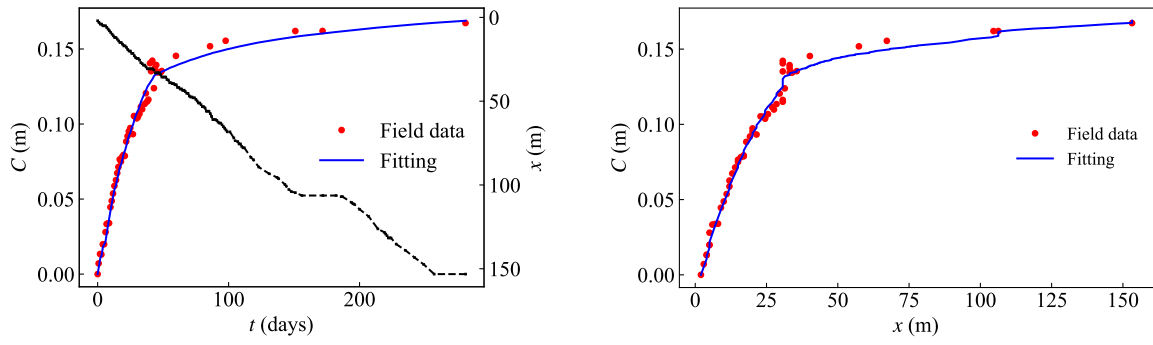
String D2



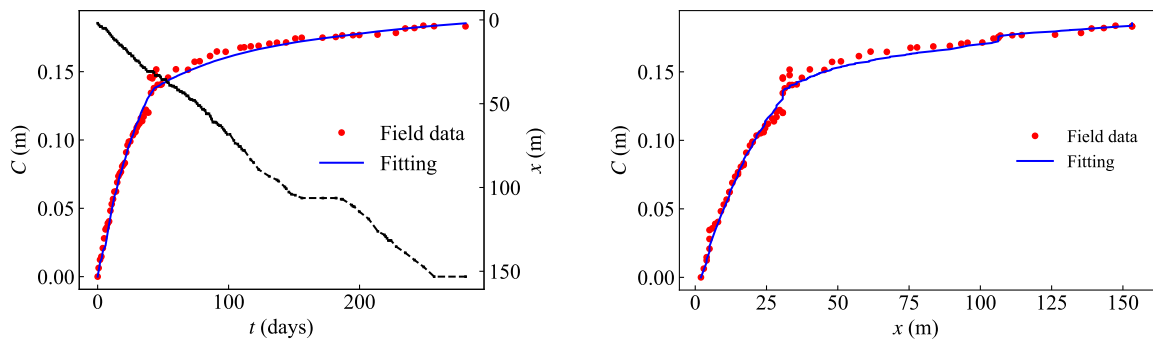
String D3



String D4

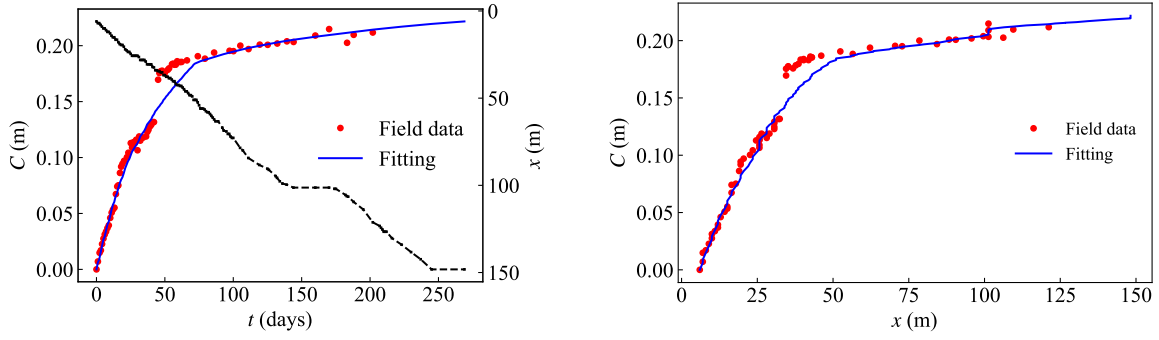


String D5

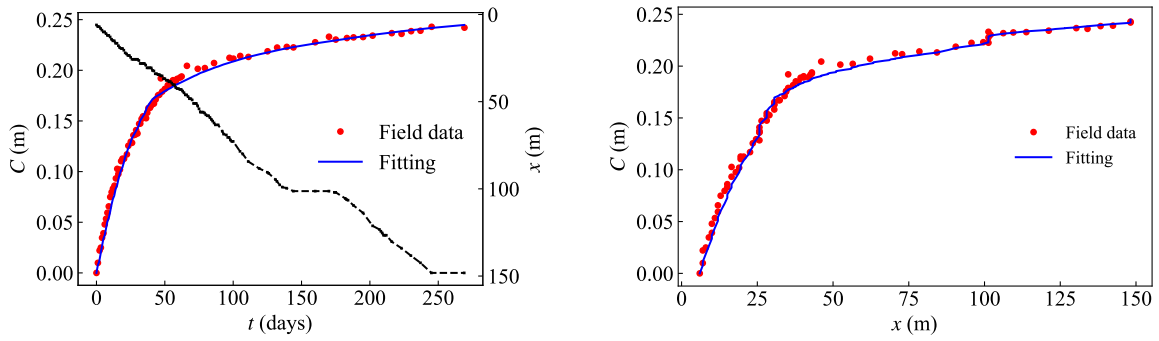


String D6

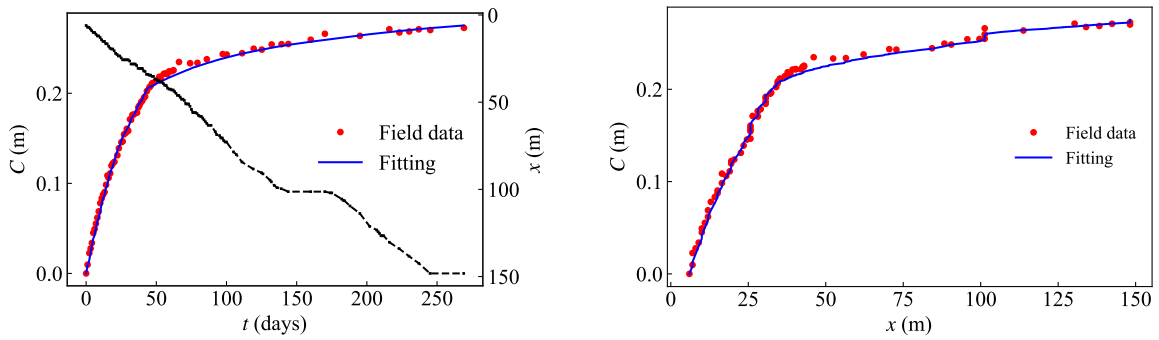
Figure D.16: Strings convergence fitting of the section at chainage 10379 m (B) in SMP4-RPS (The black lines show the tunnel face advance.)



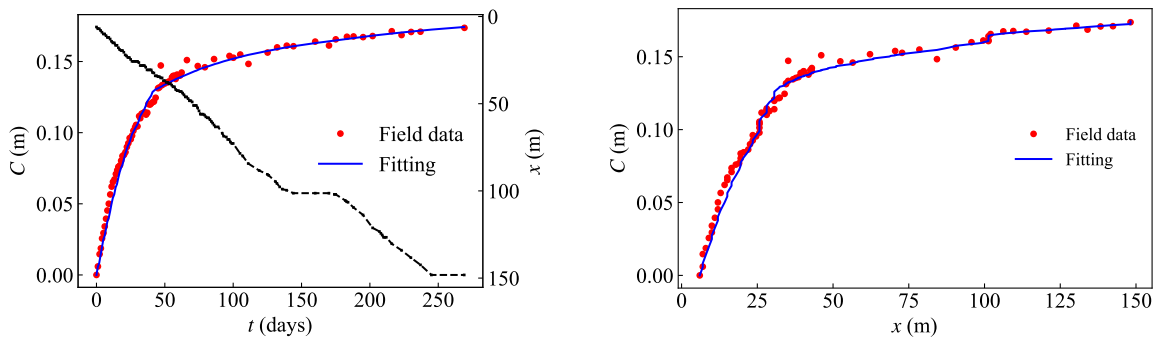
String D1



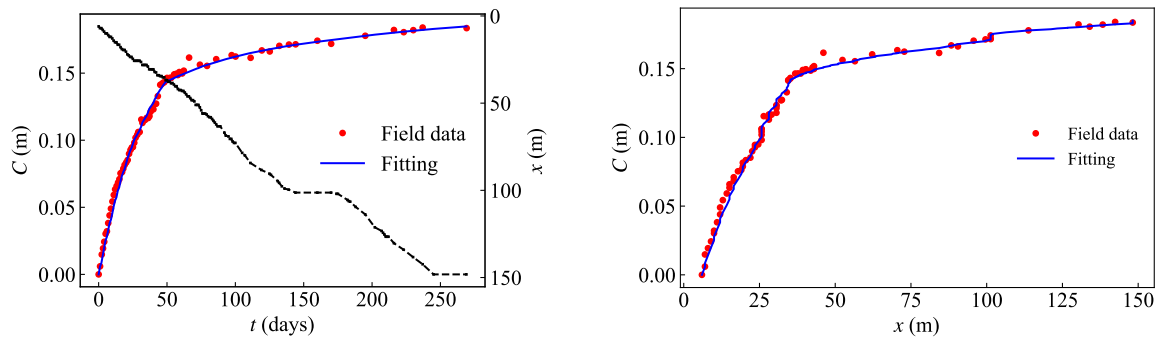
String D3



String D4



String D5



String D6

Figure D.17: Strings convergence fitting of the section at chainage 10384 m (B) in SMP4-RPS (The black lines show the tunnel face advance.)